

**AN INVESTIGATION OF NOVEL UHF MICROSTRIP FRACTAL
PATCH ANTENNAE FOR AN RFID DOORWAY READER SYSTEM**

SAVEEN MANILKA BANDARA JAYASOORIYA

A thesis submitted in partial fulfilment of the requirement of Staffordshire
University for the degree of Doctor of Philosophy

November 2019

Dedication:

To the utmost of my life, my Lord and Saviour Jesus Christ who lives in me through the Holy Ghost, to the glory of God the Father.

“I returned, and saw under the sun, that the race is not to the swift, nor the battle to the strong, neither yet bread to the wise, nor yet riches to men of understanding, nor yet favour to men of skill; but time and chance happeneth to them all”.

– Ecclesiastes ix:xi [KJV]

“Engineers need to be constantly reminded that all engineering failures result from faulty judgements rather than faulty calculations. They must think and communicate visually.”

– Eugene S. Ferguson, ‘Engineering and the Mind’s Eye’, 1992.

Abstract

The applications of Radio Frequency Identification (RFID) technology has expanded drastically after the arrival of data revolution and coming age of human-free industry: Industry 4.0. The focus has been reduction of installation costs by developing plug and play systems when transitioning from traditional manual-scan systems to fully automated systems with improved efficiency.

The main contributor to efficiency of an RFID system is the reader antenna. Microstrip patch antennae are found to be most suitable for RFID applications. Miniaturisation of the antenna without compromising its efficiency has been one of the central concerns in the last few decades. For fixed reader RFID antennae, maintaining enough gain while having the ability to read tags moving in any orientation and speed as well as blind spots when clustered together have been major challenges in the industry.

The work proposed in this thesis aims to design miniaturised novel modified fractal antennae suitable for an RFID doorway reader system, operating at UK's RFID UHF band, 870MHz. The work proposed combines novel miniaturising and gain enhancement techniques to meet desired requirements. Fractal patterns are used to increase the electrical length of the antenna while maintaining its physical size and obtain multiband behaviour thus reading tags slightly off-tuned with the help of RFID reader's Frequency hopping technique. Antennae are made on high dielectric constant substrates, RF60A for further miniaturisation. Several geometry techniques including copper wall construction and 90 degree delayed two port feeders are used for gain enhancement, narrow beamwidth and circular polarisation. CST Microwave Studio Suite simulations demonstrate that a commercially available directivity (5dBi) compared to market research and published research papers have been achieved. RFID testing on manufactured prototypes demonstrated that antenna designs are suitable

for a fully automated doorway reader system to obtain 100% detection efficiency with precise manufacturing and fine tuning.

Acknowledgements

To Mum and Dad who made it all possible. Words fail to articulate the depths of parental love towards the only child of which I stand in awe.

Dr. Ian Taylor my external and former principal supervisor who handpicked me during my MSc industrial placement and encouraged me to pursue a PhD in fractal antennae thus laying the foundation for this project. He also deserves the credit of this work and much that follows.

The late Mr. Mark Wilkins of Bibliotheca Library solutions (Intellident) for equipping me in the art of antenna design.

Dr. Chris Gould my principal supervisor the gracious gentleman who took me from where Ian left towards the finish line. Without his support, guidance and instruction at such a crucial time this work wouldn't have been a success.

The highly esteemed Professor Sarath B. Tennakoon the man who was there to save me each time I misbehaved, who also had faith in me thus making provision for experimental work in this project without which this would have been another theoretical investigation.

Dr. Abdel-Hamid Soliman, Director of engineering researchers also known as the father of the house, for his thoughtfulness, encouragement, and advice to strengthen my work and help during March '19 crisis.

Special thanks to my dear friend Philip Else for his generous support, clever solutions in overcoming challenges during PCB fabrication.

Mr. Paul Thomas for his RF expertise during a frustrated antenna tuning process.

Mr. Hirantha Kaluarachchi for volunteering in antenna performance testing.

Being the custodian of the family blessing, I'm humbled by the tremendous selfless support given to me by my family members and loved ones during this long and arduous academic journey. It's a great blessing to be raised by a God-fearing family which take honour in serving the Lord and His Church faithfully.

Last but not the least my confrères in engineering research of S103 Mellor building the habitat of intellectual vagabonds, which was practically our home away from home. I extend my sincere thanks to Ernest, Masum, Anas, Monday, Samir and Daniel for their valuable support and comradeship also appreciating that harmonious working environment during my stay.

Table of Contents

Contents

Abstract.....	i
Acknowledgements.....	iii
List of Figures	vii
List of Tables	xii
Nomenclature	xiv
1 Introduction	1
1.1 Background and motivation.....	1
1.1.1 RFID security systems.....	2
1.1.2 RFID reader systems.....	3
1.2 Aims and Objectives.....	7
1.3 Significance of research	8
1.4 Scope and limitations of research.....	9
1.5 Research methodology	9
1.6 Thesis overview and structure.....	10
2 Review of RFID Technology and Systems.....	13
2.1 Introduction	13
2.2 RFID overview	13
2.3 RFID Frequencies and Standards	15
2.4 RFID tag classification	16
2.5 Challenges in RFID pertaining to a doorway reader system.....	17
2.6 Summary	19
3 Review of Microstrip Antenna	20
3.1 Introduction	20
3.2 Overview of Microstrip Antenna	20
3.3 Antenna miniaturising techniques.....	27
3.4 Fractals and its applications to antennae	30
3.5 Fractal Antenna used in RFID reader antennae.....	36
3.6 Potential commercially available designs for a doorway reader antenna	44
3.7 Summary	45
4 Development of a doorway reader antenna: proposed designs and simulation results	47
4.1 Introduction	47
4.1.1 Antenna requirement for doorway reader application	48
4.1.2 Available designs and their performance	49
4.1.3 Proposed solution	49

4.2	Minkowski-Like Pre-Fractal (MLPF)-based antenna	50
4.2.1	Introduction to the fractal and its construction	50
4.2.2	Proposed Design and Simulation Results.....	54
4.3	Tau Fractal based antenna.....	76
4.3.1	Introduction to the fractal and its construction	76
4.3.2	Proposed Design and Simulation Results.....	78
4.4	Space Filling Tree (SFT) Fractal Antenna.....	91
4.4.1	Introduction to the fractal and its construction	91
4.4.2	Proposed Design and Simulations.....	95
4.5	Maltese Cross Fractal Antenna	110
4.5.1	Introduction to the fractal and its construction	110
4.5.2	Proposed Design and Simulations.....	113
4.6	Summary	122
5	Development of doorway reader antenna: more proposed designs and simulation results.	124
5.1	Inverted Tau Fractal Antenna (Inv Tau)	125
5.1.1	Introduction to the fractal and its construction (Inv Tau)	125
5.1.2	Proposed design and Simulation results.....	130
5.2	Stanley Fractal Antenna	134
5.2.1	Introduction to the fractal and its construction	134
5.2.2	Proposed design and simulation results	138
5.3	Jerusalem Cross fractal antenna	142
5.3.1	Introduction to the fractal and its construction	142
5.3.2	Proposed design and simulation results	144
5.4	Summary of simulated results of proposed models.....	148
6	Prototype build and test	154
6.1	Introduction	154
6.2	Calculations and design of power divider with extra 90-degree feeder at one port	155
6.2.1	Calculations of stripline widths and quarter wavelengths.....	156
6.2.2	Wilkinson Power divider on PCB.....	161
6.3	Antenna prototype build.....	169
6.4	Antenna performance testing.....	175
6.4.1	Test variables and methodology.....	175
6.4.2	Test set up.....	182
6.4.3	Results.....	188
6.5	Summary	192
7	Applications of RFID doorway readers.....	195
7.1	Doorway reader applications for Healthcare.....	195

7.2	Doorway reader applications for retail.....	200
7.3	Doorway reader applications for airports.....	200
7.4	Doorway reader applications for Smart Manufacturing.....	201
7.5	For smart waste management.....	201
7.6	Summary.....	202
8	Discussion, Conclusions and further work.....	203
8.1	Discussion.....	203
8.2	Conclusions.....	209
8.3	Further work.....	210
8.3.1	Mits PCB milling machine's limitations.....	211
8.3.2	Accuracy of copper wall constructed around the antennae.....	212
8.3.3	Issues with feeding mechanism of the radiating patch.....	213
8.3.4	Errors in Wilkinson power divider's copper pads.....	215
8.3.5	Port impedances Z11 and Z22.....	216
8.3.6	Burden of stub tuning.....	216
8.3.7	Using a four-port feeder.....	219
	REFERENCES.....	221
	APPENDIX A.....	229
	APPENDIX B.....	233
	APPENDIX C.....	237

List of Figures

Fig. 1-1: RFID Security gate mounted on the floor [9].....3

Fig. 1-2: Bibliotheca's selfCheck™ [10]4

Fig. 1-3: Nordic ID handheld RFID reader [11]4

Fig. 1-4: Intellident Quarter Portal™ [12]5

Fig. 1-5: Bibliotheca Smart Stock™ and Smart blade230™ [15].....5

Fig. 1-6: Bibliotheca's flex AHM™ [15].....6

Fig. 2-1: Capabilities required of RFID systems [16].....14

Fig. 3-1: Microstrip line feed and coaxial feed of a patch antenna [40]21

Fig. 3-2: Effective length of patch due to fringing effect [40].....22

Fig. 3-3: Antenna Circular-polarising techniques [16], [40]26

Fig. 3-4: Wilkinson Power Divider [45]27

Fig. 3-5: Patch and measured S11 in design [72].....37

Fig. 3-6: 3D radiation patterns of [72]37

Fig. 3-7: Radiation pattern for Rectangular patch in [73]38

Fig. 3-8: Radiation pattern for Rectangular patch in [73]38

Fig. 3-9: Radiation pattern for [74]39

Fig. 3-10: Antennae with different fractal iterations in [75].....40

Fig. 3-11: Final design of [75].....40

Fig. 3-12: Circular polarised radiation observed by surface currents in [75]41

Fig. 3-13: Simulated and measured radiation pattern for [75]41

Fig. 3-14: E field radiation patterns of repeater antenna in [76]42

Fig. 3-15: Proposed antenna for enclosure [77]42

Fig. 3-16: Folded ground plane antenna with 90-degree phase feeding [79]43

Fig. 3-17: Circular polarised behaviour seen by E plane at 90 degree intervals [79].....44

Fig. 4-1: Proposed antennae mounted on a doorframe.....49

Fig. 4-2: Iterations of a Minkowski like pre fractals [58]51

Fig. 4-3: MLPF fractal used to miniaturise antenna with irregular slots curved for circular polarisation [59].....51

Fig. 4-4: Proposed 1st iteration of MLPF antenna52

Fig. 4-5: Proposed 2nd iteration of MLPF antenna.....53

Fig. 4-6: Proposed 3rd iteration of MLPF antenna53

Fig. 4-7: 1st iteration of MLPF antenna in CST.....54

Fig. 4-8: S11 against frequency for the simulated 1st iteration of MLPF antenna.....55

Fig. 4-9: VSWR against frequency for the simulated 1st iteration of MLPF antenna.....55

Fig. 4-10: Coaxial port was shifted to get a blip near to 870 MHz, resonating at 1022.2 MHz with S11=-10.4 dB.....56

Fig. 4-11: Coaxial port was shifted to get a blip near to 870 MHz, resonating at 1022.2 MHz with VSWR=1.865256

Fig. 4-12: E (Absolute) Farfield radiation pattern for frequency $f=1022.2$ MHz57

Fig. 4-13: E (Absolute) Farfield radiation pattern for frequency $f= 2141.6$ MHz.....57

Fig. 4-14: E (Absolute) Farfield radiation pattern for frequency $f= 2741.9$ MHz.....58

Fig. 4-15: E (Absolute) Farfield radiation pattern for 906 MHz at $\phi=0$ and $\phi=90$ degree cut59

Fig. 4-16: Surface currents of the design showing linearly polarised antenna60

Fig. 4-17: 2nd iteration of MLPF antenna in CST.....61

Fig. 4-18: E (Absolute) Farfield radiation pattern at 848.2 MHz both $\phi=0$ and $\phi=90$ degree cuts62

Fig. 4-19: E (Absolute) Farfield radiation pattern at 885.9 MHz both $\phi=0$ and $\phi=90$ degree cuts63

Fig. 4-20: 3 rd iteration of MLPF antenna in CST	63
Fig. 4-21: Two coaxial feeding ports on the patch coming via ground plane and dielectric layer	65
Fig. 4-22: E (Absolute) Farfield radiation pattern at 868.5 MHz both phi=0 and phi=90 degree cuts	66
Fig. 4-23: Surface currents on the radiating patch showing circular polarised behaviour	66
Fig. 4-24: Farfield 3D radiation pattern at 868.5 MHz	67
Fig. 4-25: Wall construction around the antenna	67
Fig. 4-26: E (Absolute) Farfield radiation pattern at 859 MHz both phi=0 and phi=90 degree cuts. The beam widths are shown in Table 4-11.....	70
Fig. 4-27: 3D radiation pattern of antenna demonstrating a circularly polarised narrow directed beam	70
Fig. 4-28: Coaxial outer core added to coaxial ports.....	71
Fig. 4-29: S11 against frequency resonating at 874.3 MHz with bandwidth of 5 MHz.....	73
Fig. 4-30: E (Absolute) Farfield radiation pattern for 874.3 MHz at phi=0 and phi=90-degree cuts	74
Fig. 4-31: E plane co polar and cross polar cuts on radiation pattern	74
Fig. 4-32: H plane co polar and cross-polar cuts on radiation pattern	75
Fig. 4-33: 3D radiation pattern of final MLPF antenna.....	75
Fig. 4-34: Surface currents on patch	75
Fig. 4-35: Proposed 1st iteration of TAU fractal antenna.....	76
Fig. 4-36: Proposed 2nd iteration of TAU fractal antenna	77
Fig. 4-37: Proposed 3rd iteration of TAU fractal antenna.....	78
Fig. 4-38: 3rd iteration of TAU fractal antenna in CST	79
Fig. 4-39: 2nd iteration of TAU fractal antenna in CST.....	79
Fig. 4-40: S11 against frequency resonating at 880.1 MHz.....	82
Fig. 4-41: 3rd iteration of TAU fractal antenna in CST	82
Fig. 4-42: E (Absolute) Farfield radiation pattern at 874.3 MHz both at phi=0 and phi=90 degree cuts.....	84
Fig. 4-43: Wall construction around the antenna	84
Fig. 4-44: Wall construction of Tau fractal antenna	85
Fig. 4-45: E (Absolute) Farfield radiation pattern at 877 MHz with copper wall	86
Fig. 4-46: 3D radiation pattern at 877 MHz with copper wall.....	86
Fig. 4-47: surface currents at 877 MHz demonstrating circular polarisation	86
Fig. 4-48: S11 against frequency defining bandwidth of 5 MHz.....	89
Fig. 4-49: E plane co-polar and cross-polar cuts.....	89
Fig. 4-50: H plane co and cross polar cuts	90
Fig. 4-51: 3D radiation pattern of TAU fractal antenna.....	90
Fig. 4-52: Surface currents on Tau fractal antenna.....	90
Fig. 4-53: Proposed fractal arm slot with dimensions.....	91
Fig. 4-54: Cross bar fractal places at the centre of the patch	92
Fig. 4-55: Four cross bars placed at the four quadrants of the patch.....	93
Fig. 4-56: Effective patch area which can be used after the four cross bars are placed	94
Fig. 4-57: Proposed 1st iteration of the SFT fractal antenna	95
Fig. 4-58: Proposed 2nd iteration of the SFT fractal antenna.....	95
Fig. 4-59: 1st iteration of SFT fractal antenna in CST	98
Fig. 4-60: S11 against frequency showing 1132.4 MHz as resonant frequency having an S11 of -10.86 dB.....	99
Fig. 4-61: 2 nd iteration of SFT fractal antenna in CST	99

Fig. 4-62: E (Absolute) Farfield radiation patterns at 1126.6 MHz both $\phi=0$ and $\phi=90$ degree cuts	100
Fig. 4-63: variation of k, which changes factor of which the next iteration's length is added (3 rd iteration of SFT fractal antenna in CST)	102
Fig. 4-64: Wall construction around the SFT fractal antenna	104
Fig. 4-65: E (Absolute) Farfield results of the SFT fractal antenna with wall at 880 MHz both $\phi=0$ and $\phi=90$ degree cuts.....	105
Fig. 4-66: 3D radiation pattern.....	106
Fig. 4-67: Surface currents on SFT 3 rd iteration antenna demonstrating circular polarisation	106
Fig. 4-68: Coaxial ports moved closer to centre from (12,12) to (8,8).....	107
Fig. 4-69: Return loss S11 at 871.4 MHz with a bandwidth of 6 MHz.....	108
Fig. 4-70: E (Absolute) Farfield radiation patterns for $\phi=0$ and $\phi=90$ -degree cuts.....	109
Fig. 4-71: E plane co-polar and cross-polar cuts.....	109
Fig. 4-72: H plane co-polar and cross-polar cuts	110
Fig. 4-73: Surface current patterns on SFT antenna.....	110
Fig. 4-74: Proposed Maltese Cross depicting lengths and flare angles	111
Fig. 4-75: Proposed Maltese cross fractal with vertical and horizontal lengths	112
Fig. 4-76: Proposed 1 st and 2 nd iterations of the Maltese cross fractal antenna.....	112
Fig. 4-77: Proposed Maltese Cross antenna in CST (1st, 2nd and 3rd iteration of the fractal)	113
Fig. 4-78: S11 parameter against frequency showing 1129.5 MHz as resonance and S11 as -18.5789 dB on Maltese Cross 1 st iteration	114
Fig. 4-79: E (Absolute) Farfield radiation pattern of 3 rd iteration of Maltese cross fractal with wall constructed around.....	116
Fig. 4-80: 3D radiation pattern of Maltese cross 3 rd iteration fractal antenna with wall construction.....	117
Fig. 4-81: Surface currents on radiating patch of the 3 rd iteration of Maltese cross fractal demonstrating circular polarised behaviour	117
Fig. 4-82: Return loss S11 and Bandwidth 4 MHz	120
Fig. 4-83: E (Absolute) Farfield radiation pattern $\phi=0$ and $\phi=90$ degree cuts.....	120
Fig. 4-84: E plane radiation pattern co-polar and cross-polar cuts.....	121
Fig. 4-85: H plane radiation pattern co-polar and cross-polar cuts	121
Fig. 4-86: surface currents on Maltese cross fractal antenna	121
Fig. 5-1: Spread factor or Lacunarity of Tau and Inverted Tau fractal.....	126
Fig. 5-2: Proposed 1st iteration of Inverted Tau fractal antenna	126
Fig. 5-3: Framework for 2nd iteration of Inverted Tau fractal	127
Fig. 5-4: 2nd iteration of the Inverted Tau fractal	128
Fig. 5-5: Framework for 3rd iteration of Inverted Tau fractal.....	129
Fig. 5-6: 3rd iteration of Inverted Tau fractal	129
Fig. 5-7: CST models of 2nd and 3rd iteration of Inverted Tau Fractal antennae	130
Fig. 5-8: S11 against frequency of Inverted Tau fractal antenna having a bandwidth of 4 MHz.	132
Fig. 5-9: E (Absolute) Farfield radiation patterns at $\phi=0$ and $\phi=90$ degrees	132
Fig. 5-10: E plane co-polar and cross polar radiation patterns	133
Fig. 5-11: H plane co-polar and cross-polar radiation patterns	133
Fig. 5-12: Surface currents of Inverted Tau fractal antenna (3rd iteration) from 0 degrees to 315 degrees in 45-degree intervals	133
Fig. 5-13: Comparison of Maltese Cross and Stanley fractal elements.....	134
Fig. 5-14: 1st iteration of Stanley fractal antenna.....	135

Fig. 5-15: 2nd iteration of Stanley fractal antenna	135
Fig. 5-16: 3rd iteration of Stanley fractal antenna.....	136
Fig. 5-17: Stanley fractal element and its variable dimensions	137
Fig. 5-18: first three iterations of proposed Stanley fractal modelled in CST Microwave Studio	138
Fig. 5-19: Return loss S11 against frequency with a bandwidth of 6 MHz	140
Fig. 5-20: E (Absolute) Farfield radiation patterns at phi=0 and phi=90 degree cuts.....	140
Fig. 5-21: E plane radiation pattern Co-polar and Cross-polar cuts.....	141
Fig. 5-22: H plane radiation pattern co-polar and cross-polar cuts	141
Fig. 5-23: Surface currents of Stanley fractal antenna from 0 degrees to 315 degrees in 45-degree intervals.....	141
Fig. 5-24: Jerusalem cross element	142
Fig. 5-25: Proposed fractal antenna	143
Fig. 5-26: CST model of Jerusalem cross fractal antenna	144
Fig. 5-27: S11 against frequency with a bandwidth of 5 MHz	146
Fig. 5-28: E (Absolute) Farfield radiation patterns for phi=0 and phi=90 degree cuts	146
Fig. 5-29: E plane radiation pattern co-polar and cross-polar cuts.....	147
Fig. 5-30: H plane radiation pattern co-polar and cross-polar cuts	147
Fig. 5-31: Surface currents on Jerusalem cross fractal antenna	147
Fig. 5-32: Change of polarisation from LHCP to RHCP by changing 90-degree feed	150
Fig. 6-1: Power splitter set up	155
Fig. 6-2: Stripline wilkinson power divider.....	156
Fig. 6-3: Rogers Impedance calculator computing 70.7 ohm stripline width.....	159
Fig. 6-4: Rogers Impedance calculator computing 50-ohm stripline width	159
Fig. 6-5: Stripline dimensions for Wilkinson Power Divider	161
Fig. 6-6: Wilkinson Power divider circuit.....	162
Fig. 6-7: Wilkinson ring splitter circuit.....	163
Fig. 6-8: Relationship between angle and radius.....	164
Fig. 6-9: Numerical solution obtained by Mathcad for radius r=16.19 mm	166
Fig. 6-10: Final dimensions of Wilkinson power divider	166
Fig. 6-11: SMA end launch connector	167
Fig. 6-12: Gerber for Wilkinson power divider circuit.....	167
Fig. 6-13: S11 S12 and S13 response for proposed ring splitter	168
Fig. 6-14: Manufactured Wilkinson power divider with 100-ohm resistor	168
Fig. 6-15: Full Wilkinson set up with extra quarter wavelength	169
Fig. 6-16: Gerber files for MLPF, TAU, SFT and Jerusalem Cross fractal antennae	169
Fig. 6-17: Mits PCB milling machine	170
Fig. 6-18: Milled PCB antenna TAU, Jerusalem cross, MLPF and SFT.....	171
Fig. 6-19: Copper wall built around the antenna	172
Fig. 6-20: Individual port impedances (Z11 and Z22) measurement set up	173
Fig. 6-21: Impedance, return loss and VSWR measurements with Wilkinson power divider and quarter wavelength set up	174
Fig. 6-22: Stub tuned antennae with copper walls ready for testing	175
Fig. 6-23: Wooden doorframe used to antenna testing.....	176
Fig. 6-24: Walking route (marked in red) of the test subject.....	176
Fig. 6-25: Antenna locations on doorframe and radiation patterns covering chest to knee height.....	177
Fig. 6-26: Car mobile phone holder used as a bracket to hold antenna to the doorframe	178
Fig. 6-27: File carrying orientations	179

Fig. 6-28: Files may be clustered together in three different ways (Face to face, back to back and face to back).....	179
Fig. 6-29: Doorway reader test set up comprising of power divider and FEIG LUR1002 reader	183
Fig. 6-30: Doorway reader test set up comprising of power divider and FEIG LRU 1002 RFID reader	184
Fig. 6-31: LRU1002 reader operating in buffered read mode detecting tags passing through the doorway.....	185
Fig. 6-32: Control antenna (Mobilemark).....	187
Figure 7-1: NHS Patient Record Journey by Restore Records Management [97]	197
Fig. 8-1: manufactured antenna by Mits PCB milling machine depicting surface roughness	211
Fig. 8-2: Top 2 board produced with 30 degree milling bits whilst bottom 2 boards where produces of 60-degree bits	212
Fig. 8-3: Gap between copper wall and antenna ground plane	213
Fig. 8-4: Ports too close to each other.....	214
Fig. 8-5: MMCX straight plug PCB mount and MMCX to RG58 converter	214
Fig. 8-6: Wilkinson power divider dimensions	215
Fig. 8-7: Proposed Wilkinson circuit divider with quarter wavelength element embedded to splitter	216
Fig. 8-8: Tuning antennae using copper taped pasted on radiating patch.....	217
Fig. 8-9: Depicting suggested pads for trimmer capacitors for effective tuning	218
Fig. 8-10: Wilkinson divider with embedded quarter wavelength arm to feed antenna	218
Fig. 8-11: Four port feed with 0, 90, 180- and 270-degree time phase shift delays	219

List of Tables

Table 3-1: Various dielectric materials and their performance in a standard patch antenna as in [48]29

Table 3-2: Dimensions and antenna parameters of commercially available RFID antenna for Doorway reader application.....45

Table 4-1: MLPF, Tau, SFT and Maltese cross fractals.....47

Table 4-2: Design criteria for an RFID doorway reader antenna50

Table 4-3: Variation in Resonant Frequency, S11 and VSWR with Coaxial port coordinate58

Table 4-4: S11, VSWR and Directivity at 906 MHz59

Table 4-5: S11 and VSWR at 786 MHz in 2nd iteration of MLPF fractal antenna61

Table 4-6: Antenna parameter with scaling of the patch size.....62

Table 4-7: Resonant frequencies with patch size being scaled to obtain the required frequency64

Table 4-8: Antenna parameters when patch size = 46 mm64

Table 4-9: Antenna parameters for 868.5 MHz65

Table 4-10: Variation of patch size, slot lengths, widths and coaxial coordinates with antenna parameters.....69

Table 4-11: 3dB beamwidths at 859 MHz both $\phi=0$ and $\phi=90$ degree cuts.....70

Table 4-12: Changes in Coaxial wire mesh, copper wall height and thickness72

Table 4-13: Re-simulating with high accuracy -30.0 dB73

Table 4-14: Antenna parameters with varying dimension parameters to obtain a frequency close to 870 MHz81

Table 4-15: Antenna parameters at 880.1 MHz.....83

Table 4-16: Antenna parameters when a two port 90 degree phase feeder is applied.....83

Table 4-17: Results for the model with wall construction.....85

Table 4-18: Variation of coaxial port location.....87

Table 4-19: Variation of 3rd iteration dimensions and ground plane88

Table 4-20: Tau fractal antenna results.....88

Table 4-21: S11 and VSWR for 1132.4 MHz on SFT 1st iteration antenna design.....98

Table 4-22: Antenna parameters for 1126.6 MHz on SFT 2nd iteration fractal antenna.....100

Table 4-23: Antenna parameters with varying patch size101

Table 4-24: Antenna parameters with varying k and coaxial port coordinate103

Table 4-25: Antenna parameters with varying SFT slot length Fl.....104

Table 4-26: Antenna parameter results at 880 MHz with wall constructed around it.....105

Table 4-27: variation of coax ports and retuning of SFT fractal antenna108

Table 4-28: S11 and VSWR at 1129.5 MHz on Maltese cross 1st iteration.....114

Table 4-29: Antenna parameter variation with 1st, 2nd and 3rd iterations of the Maltese Cross fractal115

Table 4-30: Antenna parameters at 894.6 MHz on Maltese Cross fractal 3rd iteration with wall construction.....116

Table 4-31: Variation of flare lengths119

Table 4-32: Maltese Cross fractal final design119

Table 4-33: Final dimensions of MLPF, Tau, SFT and Maltese Cross antennae.....123

Table 5-1: Inv Tau, Stanley and Jerusalem Cross fractal125

Table 5-2: Inverted Tau simulation results.....131

Table 5-3: Simulation results for Stanley fractal antenna.....139

Table 5-4: Simulation results for Jerusalem cross fractal antenna145

Table 5-5: Final dimensions of Inv Tau, Stanley and Jerusalem Cross.....148

Table 5-6: Antenna performances of final designs149

Table 5-7: Z11 port impedances of antenna designs.....150

Table 5-8: Miniaturisation due to high dielectric substrate	151
Table 5-9: Axial Ratios of simulated antenna design.....	153
Table 6-1: Stripline widths for 70.7-ohm and 50-ohm lines by Method 1.....	157
Table 6-2: Stripline widths for 70.7 ohm and 50-ohm lines by Method 2.....	158
Table 6-3: Measured antenna parameters at 870 MHz.....	174
Table 6-4: Sample size estimation for 95% confidence interval	181
Table 6-5: Feasible sample size estimation.....	181
Table 6-6: Antenna parameters for MobileMark PN8-868LCP-1C-WHT-12 antenna	186
Table 6-7: MLPF performance table	188
Table 6-8: Tau performance table.....	189
Table 6-9: SFT performance table.....	190
Table 6-10: Jerusalem cross performance table	191
Table 6-11: Performance table for Control	192
Table 8-1: Simulated results for a four-port Jerusalem cross fractal antenna	219

Nomenclature

cm	Centimetres
CST	Computer Simulation Technology
dB	decibels
dBi	decibel isotropic
EPC	Electronic Product Code
ETSI	European Telecommunication Standard Institute
FCC	Federal Communication Commission
FF	Far Field
GHz	Giga Hertz
HF	High Frequency
IoT	Internet of Things
kHz	kilo Hertz
LF	Low Frequency
MHz	Mega Hertz
Mm	Millimetres
NF	Near Field
NHS	National Health Service
PCB	Printed Circuit Board
RF	Radio Frequency
RFID	Radio Frequency Identification
SHF	Super High Frequency
SFT	Space Filling Tree
SMA	SubMiniature version A
TLM	Transmission Line Matrix
UHF	Ultra High Frequency
VSWR	Voltage Standing Wave Ratio

1 Introduction

1.1 Background and motivation

The basic concept of radiofrequency identification (RFID) has been around for over 50 years, it has been developed during the period of 2nd world war, in today's industry its applications are widely used in healthcare, enterprise and society. The RFID technology has enabled many industries to increase their efficiency whilst reducing cost and increasing revenue [1]. Though RFID systems are most commonly used in the supply chain and logistics industry there are other smart applications which will be beneficial in the coming industrial revolution in fully automated manufacturing and asset tracking: Industry 4.0. [2].

One such challenge remains unsolved which is to develop a fully automated doorway reader system for document tracking applications. This includes automated check-in and check-out of items in and out of an office environment as well as to track said items within the office building. An example potential application is the need for this challenge arises mainly from the National Health Service (NHS) trusts where most patient records are not digitised yet. It is reported that there are over half a million missing patient records putting thousands of lives at risk with an attempt to cover up. [3], [4], [5], [6], [7], [8].

The need arises for a doorway reader system to be implemented in a building where each door passage is fixed with an antenna for the purpose of tracking RFID tagged documents. By using this system, the customer may locate the necessary files and hence solve the issue of file misplacement within the building. For such an antenna to be effectively implemented in an existing office environment with minimal work of installation, the antenna needs to be miniaturised such that it may fit into a standard

doorframe. Such an RFID antenna needs to have an 100% efficiency of detecting RFID tagged objects passing through the door passage with an operational region confined only to the door passage. This is done at line of sight from the RFID reader. Currently there are two main RFID systems in operation.

1. RFID security systems
2. RFID reader systems

1.1.1 RFID security systems

In a security system, the main objective is to detect un-checked transponders moving in or out of a defined environment. This is done by reading data stored on the RFID tag. RFID security system antennae usually comprises large gate-like high power antennae mounted to the floor panel as shown in Fig. 1-1. Installation costs for these antennae are high and they contribute to obstruction of foot traffic of the building ingress and egress. [9]



Fig. 1-1: RFID Security gate mounted on the floor [9]

1.1.2 RFID reader systems

In an RFID reader system, the objective is to both read or write data to the transponder. In contrast to RFID security systems, RFID reader systems remain manual with human involvement during its operation. Types of such RFID readers are listed below:

- a. Self-check kiosk, where an RFID antenna is placed on a kiosk. Users may check in and check out tagged books or documents as shown in Fig. 1-2. [10]



Fig. 1-2: Bibliotheca's selfCheck™ [10]

- b. RFID handheld readers where office staff may scan tagged items manually and portals with large antenna where staff may scan large items (pallets) stacked by a forklift. Nordic Handheld readers are shown in Fig.1-3. [11] and a Quarter portal is shown in Fig. 1-4. [12]



Fig. 1-3: Nordic ID handheld RFID reader [11]



Fig. 1-4: Intelligent Quarter Portal™ [12]

c. Shelves or tunnels with antenna on separation blades [13], [14] where documents may be placed, automatic sorting bins with conveyer belts and storage tunnels where large stocks of tagged items may be read with high power antennae as shown in Fig. 1-5 and Fig. 1-6. which are Bibliotheca products. [15]



Fig. 1-5: Bibliotheca Smart Stock™ and Smart blade230™ [15]



Fig. 1-6: Bibliotheca's flex AHM™ [15]

None of the above systems are fully automated and require user or staff intervention for operation. The RFID antenna for a document tracking system should function without any manual intervention while it tracks the location of the tagged document in an office/hospital environment. The above systems are not suitable, nor their antennae could be used for this requirement.

One of the main aspects of an RFID system is the antenna, both on the transmitter and transponder. Much research has been done over the years to develop them as their requirements differ from one application to another [16]. Today the main constraint of an RFID reader antenna is its size against performance as in directivity, gain and beam width. In most applications both reader and tag antennae need to be low profile whether it is designed for manufacturing, healthcare or service industry. Hence various techniques to miniaturise an antenna have been considered in the literature. One such method is using a fractal pattern. This increases the electrical length of the antenna

which effectively reduces the resonant frequency, and in order to tune the antenna back to its desired frequency, the structure needs to be scaled down resulting in miniaturisation [17], [18]. This is discussed in further detail in chapter 3.

Fractal antennae have been used over many years mainly for RFID transponder (tag) antennae as well as RFID reader antennae, the main aim being to make them low profile. Although fractals used on an antenna for miniaturising purposes are studied in detail, the effect of RFID read/write efficiency due to diffractals on the electromagnetic beam when a fractal pattern is applied is uncommon in published literature [17], [19], [20], [21]. As the multiband characteristics on a fractal antenna might contribute to reading the blind spots in an RFID system [22], [23], [24] as well as help read detuned tags in a tag cluster with the help of 'frequency hopping' provided by the RFID reader [9], [10], [11], [25].

1.2 Aims and Objectives

The aim of this research is to develop a near to farfield microstrip patch antenna and investigate the performance when a fractal pattern is applied, for the purpose of miniaturisation whilst optimising its gain, directivity and beam width in order to produce a novel microstrip antenna suitable for an Ultra High Frequency (UHF) RFID doorway reader system operating at 870 MHz. In order to achieve the aim of the research the following objectives were set:

- Carry out a literature survey to gain an understanding of the state of the art which include:
 - Current fractal patterns which are implemented on antenna designs and their performance
 - Geometry techniques
 - Other miniaturising techniques used

- Circular polarisation and antenna feeding techniques
- Analyse and design fractals on a standard microstrip antenna – 7 novel designs were considered in the investigation
- Evaluate and optimise 7 designed antennae by simulations using software: CST Microwave Studio for best antenna performance
- Build antenna prototypes of best performing simulated models using a Printed Circuit Board (PCB) milling machine
- Performance testing of prototypes on a doorframe with an RFID reader as a proof of concept for designs being viable for an RFID doorway reader system

1.3 Significance of research

As mentioned in section 1.1 there is a technological gap in the market for a fully automated document tracking system and its main challenge is size and performance of the antenna. Challenges include detecting tagged documents moving in different orientations and speeds, detecting clustered documents overcoming blind spots at the same time confining the operational region to the door passage. Simply mounting a high gain antenna with an high power reader is not suitable due to the constraints mentioned above (i.e. to mount an antenna on a doorframe without obstructing the door mechanism if the antenna is larger than the width of the doorframe). An RFID door portal has been developed recently and is commercially available [26]. However, due to mechanical and financial constraints, implementation of such an high power portal to each door passage in an office building is not feasible. This research investigates the application of fractal patterns applied to a compact microstrip patch antenna for an RFID doorway reader system to miniaturise as well as to improve its performance, also designing it such that the installation work is set to a minimum so

that it could be implemented to any office/work environment without disrupting its ongoing activity.

NHS specifically would benefit from this application for tracking patient records within the trust and any other institution with high document mobility.

1.4 Scope and limitations of research

This research focuses on design development and performance testing of novel RFID antennae suitable to be implemented for a doorway reader application. For this purpose, 7 fractals were applied on compact microstrip patch antennae. An extensive simulation was done for wider cases of geometry techniques for miniaturisation, gain enhancement and to obtain a narrow beam width. Feeding techniques were studied with single and two ports. The effect of a copper wall built around the antenna boundary for gain enhancement was also considered in the simulations. Most feasible designs were selected and prototyped for performance testing. Theoretical design of a Wilkinson power divider is considered in the investigation for feeding the antenna.

Prototyping limitations such as precision manufacturing of the PCB milling machine affected the selection of these designs. The copper walls were built by hand and hence the antenna impedances were not the same values as in simulated results. This had to be compensated with extra stub tuning which was performed on the patch to retune the antenna. Sample size for performance testing was set to a lower value for practical purposes. Due to commercially available SMA RG58 connectors' pad size, the strip width of the 50-ohm pads of the Wilkinson power divider had to be reduced.

1.5 Research methodology

Methodology adopted in this project consists of extensive simulations and experiments. The research started with a discussion on RFID regulations, classifications and challenges pertaining to a doorway reader system followed by an

analytical study of the theory of microstrip patch antennae. A literature survey of existing technical development of miniaturising, port feeding, circular polarisation techniques were studied to get an understanding of state of the art also comparing potential commercially available antennae suitable for this application.

Extensive step by step result oriented simulations were performed on 7 proposed antenna designs to achieve criteria required for an RFID doorway reader antenna using transmission line matrix (TLM) solver of CST Microwave Studio Suite 2014. Due to the complex nature of solving Maxwell equations, these simulations were performed in an iterative process to achieve the desired results. Numerical computations were performed using PTC Mathcad Prime 5.0 throughout this research. These models were validated by building prototypes and testing them on a wooden doorframe. EAGLE PCB maker was used to design printed circuit boards for Wilkinson power divider. All models were fabricated using Mits PCB milling machine. Antenna testing was performed using an industrially available FEIG LRU1002 UHF RFID reader operating at 2 watts.

1.6 Thesis overview and structure

This thesis comprises eight chapters: (1) Introduction, (2) Review of RFID technology and systems, (3) Review of Microstrip antenna, (4) Development of a doorway reader antenna: proposed designs and simulated results, (5) Development of a doorway reader antenna: more proposed designs and simulated results (6) Prototype build and test (7) Applications of RFID Doorway Readers and (8) Discussion, conclusions and further work.

Chapter one (1) is the introduction written to provide background information for the reader regarding the technological gap, the aim and objective of research and methodology.

Chapter two (2) - Comprises a literature review on the current RFID technology: its definitions, standards, classifications with potential applications and their challenges with respect to a doorway reader.

Chapter three (3) - gives a review of microstrip antennae, definitions and design parameters, feeding techniques of a microstrip antenna both general and to obtain circular polarisation, Wilkinson power dividers relevant for two port feeders. This chapter also provides a literature review of fractal antennae currently published and other miniaturising techniques used to obtain a compact antenna. Finally, this chapter discusses both published and commercially available designs which are used for RFID reader antennae and their performance.

Chapter four (4) - this chapter takes through the design analysis and simulation of results of the 4 proposed fractal patterns perforated on a standard patch antenna. The construction of the fractal algorithms and their parameters are discussed in this chapter. Step by step simulations have demonstrated that novel commercially viable designs have been achieved,

Chapter Five (5) – this chapter takes through design analysis and simulation of results of 3 more proposed fractal patterns perforated on a standard patch antenna. Knowledge gained from chapter 4 is used here to quickly obtain the desired output which will be tested practically using an RFID reader on a doorframe in Chapter five.

Chapter six (6) – this chapter takes through the prototype build, antenna tuning, impedance matching and performance testing using an RFID reader as a proof of concept that antennae selected from chapter four are suitable for a doorway reader antenna.

Chapter seven (7) – this chapter discusses applications of RFID doorway readers as proposed in this thesis on a wide field.

Chapter eight (8) – Thesis concludes with chapter six with general discussion, conclusions and recommendations drawn from simulation work as well as from performance tests for further work.

2 Review of RFID Technology and Systems

2.1 Introduction

This chapter provides a review of RFID systems, definitions, protocol, tag classifications challenges and applications. The overview of RFID discusses the advantages of RFID against traditional barcode systems and transition challenges towards fully automated manufacturing and service: Industry 4.0. The chapter further discusses RFID frequency bands and types of transponder tags used for different application and its rationale. Finally, the chapter concludes by discussing current challenges pertaining to an automated doorway reader system and potential applications of doorway reader systems in logistics and healthcare.

2.2 RFID overview

An RFID system can be defined as a wireless communication system in which the radio link between the reader and the tag are furnished by the modulated back-scattered waves [27]. In recent years after the boom of Internet of Things (IoT) the focus has shifted to asset tracking. In general, an RFID system should be able to have the ability to encode tags, attach encoded tags to assets, track the movement of tagged assets, integrate and share asset information to business application and to develop self-organisation of intelligent devices. In the present era of IoT an RFID system is capable of them all. The evolution of RFID capabilities is depicted in Fig. 2-1. [16].

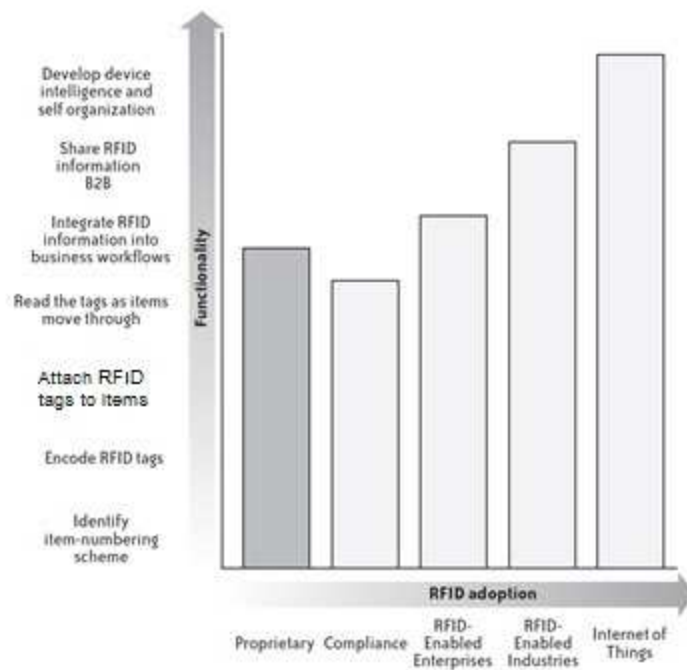


Fig. 2-1: Capabilities required of RFID systems [16]

In comparison to barcodes, RFID systems are expensive. There are many disadvantages of barcodes compared to RFID systems. Barcode labels and barcode readers are easily damaged by environment or abrasion or even obscured by dirt, labels, etc. In comparison to RFID tags, only small amounts of information can be encoded in them and cannot be changed. These can only be read at a very close range individually whereas an RFID system has the capacity to read multiple tags at a considerable range [28]. In addition, unlike barcode readers, RFID systems require no line of sight is required and can operate without human intervention having the ability to be re-written with a 1-10 year lifespan [16].

Since RFID systems remove all human errors from processes and provided data in digital format, there is high accuracy and reliability. RFID gives complete end-to-end visibility of the entire supply chain. In industry, RFID minimises lead times and reduces admin overheads due to human error, managing fleet assets better than humans and reduces or eliminates expensive holding areas. Unlike barcodes each product

movement automatically builds a transaction history giving traceability of items for recalls or emergency testing if needed [29].

Unlike barcodes, RFID tags have their own unique serial number which communicates with the reader, with memory for storing information, intelligent sensors (temperature or impact) and encryption if required for security purposes [28].

2.3 RFID Frequencies and Standards

Operational frequencies of an RFID system can be categorised into four frequency bands:

- | | |
|-------------------------------|-----------------------|
| 1. Low Frequency (LF) | 125 kHz and 134.2 kHz |
| 2. High Frequency (HF) | 13.56 MHz |
| 3. Ultra-High Frequency (UHF) | 865-868 MHz (UK) |
| 4. Super High Frequency (SHF) | 2.45 GHz |

Different frequencies are advantageous for different purposes. Low frequency signals are capable of travelling through water and a rough terrain and is widely accepted by many suppliers as it's relatively inexpensive. The quality of LF is that unlike higher frequencies, it works well around metal and is susceptible to electrical noise, thus making it suitable for vehicle immobilisation, access control, animal identification and metal container tracking.

High Frequency have a modest range of around 1 metre. They are largely affected by materials near the tags detuning them, however HF tags are unaffected by metals in close proximity. These are widely used in libraries and smart cards, also in logistics and retail markets.

Ultra-High Frequency signals have a long range of less than 10m and are an emerging technology. UHF systems have the ability to read many tags at a high speed suitable for

people counter application as well as document tracking. Supply chain management, retail inventory control and pharmaceuticals are its markets.

Super High Frequency signals have a long range and are ideal for tracking vehicles, drones and military applications [29].

The two major standards which regulate RFID are Federal Communication Commission (FCC) and European Telecommunications Standards Institute (ETSI). According to (Global Standard) GS1, the UK falls under ETSI standards which limits maximum radiated power from the antenna to 2 watts (33 dBm) under the Effective Radiated Power (ERP) scale. The operating frequencies allowed are 865-868 MHz (4 channel plan) at 2W ERP and 915-921 MHz at 4W ERP [30].

2.4 RFID tag classification

In a typical RFID system, tags communicate wirelessly at radio frequencies and most tags operate from the power extracted from the radio waves transmitted by an RFID reader. There are three kinds of tags:

1. Passive tags have no internal power source and operate from the power extracted from the reader
2. Semi-passive tags operate using the reader signal to cause a response from the tag however, semi-passive tags have a battery not to generate a response but to power electronics that are used in conjunction with off-board sensors such as a thermal sensor.
3. Active tags are battery-powered for transmission of signal back to the reader.

RFID tags are broken down to classes each having specific capability and backward compatible to previous class. Each higher class has the lower class's capability and characteristics with new capabilities [31].

EPC Class 0 tags (Generation 1) are tags which can be written once and read many times (WORM) These are factory programmable and cannot be programmed on installation.

EPC Class 1 tags (Generation1 and Generation 2) are WORM tags however they can be read by readers of a different manufacturer. EPC Class 1 Generation 2 can be written many times and read many times (Write Many Read Many, WMRM) having a better tag identification with 96 bits for EPC number and 160 for memory allowing the RFID reader to eliminate duplication in the field. Generation 2 tags read 10 times faster than Generation 1. There is a kill command which can make the tag permanently non-responsive.

EPC Class 1 Generation 2 tags also known as EPC global can be read at any frequency between 860-960 MHz. EPC Gen 2 860 MHz to 868 MHz. These are the most commonly used for UHF applications.

EPC Class 3 are battery-assisted passive tags (semi-passive). However, these are not yet fully defined.

EPC Class 4 are active tags which contains a battery to initiate communication with readers.

2.5 Challenges in RFID pertaining to a doorway reader system

One of the major challenges in an RFID system is tag collision resulting in low identification rates and shorter reading range (or the need for high RF power). A collision is said to have occurred when more than one tag sends their signal to the reader at the same time resulting in delay. This happens when active tags are used in an RFID system. In a passive tagged system, the antenna in the RFID reader transmits an electromagnetic signal to the tags and the antenna in the tag not only receives the signal but also harvests the energy from the electromagnetic field and stores it in a

capacitor. When the capacitor has built up sufficient energy it begins to release it to the tag's antenna (made out of a very thin coil). The tags coil then releases an encoded radio wave constituting information on the memory chip of the tag which the RFID reader then decodes. Passive tags operate by the energy consumed (typically 100mW). This is then resolved by the RFID reader software. Several anti-collision algorithms have been developed over the years [32], [33], [34], [35], [36].

Blind or weak spots in an RFID system occur when more tags are stacked together. This applies to a doorway reader application when an individual is carrying a pile of tagged documents, tagged books or even pushing a trolley filled with tagged documents. This phenomenon has not been theoretically analysed or been quantitatively measured. It is also demonstrated that the profiles of weak spots are strongly determined by the separation between the tags and that these are not monotonically distributed along the stack [37]. Research has been done to design no surface dead zone antennae for Near Field (NF) RFID applications [22], [38], [39].

When two or more passive tags are clustered together their coils (antennae) contribute to mutual coupling, detuning them making them unreadable. One of the techniques used to rectify this is 'Frequency hopping spread spectrum' (FHSS). In this technique the RFID reader transmits electromagnetic signals by swiftly switching the carrier signals through the available ETSI frequency channels. The transmitted signal is narrowband, and the full bandwidth is less than 1 MHz hopping 75 or more non-overlapping channels in half a minute or less. By doing so the reader allows itself to read detuned tags which are either clustered or shielded with a metal surface particularly in UHF due to its sensitivity [1], [16], [28].

Another challenge in Near Field (NF) RFID system is that their applications not only require to enhance performance, but also requires them to confine the operational region also known as the read range of the antenna so that the system should operate

in the assigned limited volume [22]. The doorway reader application is one such application that requires the antenna to read the items travelling via the region of entry of the door and not read any other tags in the vicinity of the door frame. For example, in a library a doorway reader should only read the items passing through the passage and not those which are on nearby shelves.

2.6 Summary

The study carried out on RFID standards, classifications and applications revealed that in order to implement an automated doorway reader system for a high volume document tracking application, the most suitable method of implementation is by using a near field (NF) antenna with passive tagged assets operating at Ultra High Frequency band for effective detection, speed and accuracy. The study revealed that UHF band has a high read/write rate on RFID tags and are more effective than commonly used HF gate applications. The use of passive tags is applicable considering the volume of assets for a low-cost system noting that Near field antennae could easily detect passive tags at a close range as discussed in this chapter. However, the main challenge remains which is the effective RFID tag detection when tags are clustered together and detuned due to mutual coupling of the coils resulting in blind spots, as well as confining the operational region of the antenna to the door passage. Applications of fractals have been considered mostly in farfield antennae which are governed differently than near field antenna. Application of fractals to near field antennae will miniaturise the antenna to a feasible size which could fit into a doorframe as well as increase tag detection rate due to diffractal behaviour of the backscattered electromagnetic beam after encountering fractals. Study of Microstrip antenna with fractals needs to be studied in detail to understand its applications. This is carried out in Chapter three.

3 Review of Microstrip Antenna

3.1 Introduction

Since the most suitable antenna design for an RFID doorway reader system is a microstrip antenna this chapter focuses on fundamental principles of antenna technology, miniaturising techniques currently used in industry and feeding techniques to obtain a circular polarised beam to overcome the hurdle of tag orientation. A comparison of various substrate material used with different dielectric constants is also presented. An extensive study on fractal antennae, their principle of operation and its contribution to miniaturisation is done in this chapter. Application of fractal antennae in RFID technology with a comparison of commercially available antennae which are potential for a doorway reader is also studied.

3.2 Overview of Microstrip Antenna

An antenna is a device which is used to transform a guided wave into a radiated wave or vice versa.

Microstrip is a type of open waveguide structure. Microstrip antennae (also known as patch antenna) are used in low profile, low cost and high-performance applications. These antennae are conformable to both planar and non-planar surfaces. A basic microstrip or patch antenna consists of a radiating patch, a ground plane (sometimes called the reflector) and a dielectric layer in between. The radiator is then fed by a microstrip line, a coaxial connector or by an aperture-coupled feed along with the ground plane. The main advantages of using microstrip antennae are them being low profile, inexpensive to manufacture using printed circuit technology and can easily be mounted.

When feeding a patch antenna with a microstrip line feed, it is easy to fabricate as the feed line itself is a conducting strip with finely matched impedance. However,

considering the fact that microstrip antennae are by nature low in efficiency, this reduces its gain further also limiting the bandwidth. Coaxial line feeds on the other hand do not come in the way of the electromagnetic beam. The inner conductor of the coaxial cable goes through the ground plane and the dielectric to the patch whilst the outer conductor is soldered to the ground plane [40], [41]. A strip line fed microstrip antenna comprising of a ground plane patch and dielectric substrate are shown in Fig. 3-1(a) and a circular patch microstrip antenna fed by a coaxial port is shown in Fig. 3-1(b).

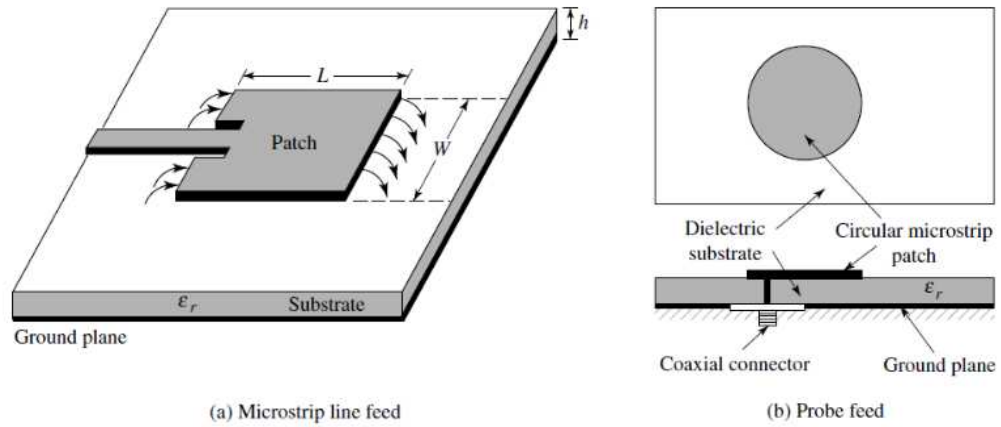


Fig. 3-1: Microstrip line feed and coaxial feed of a patch antenna [40]

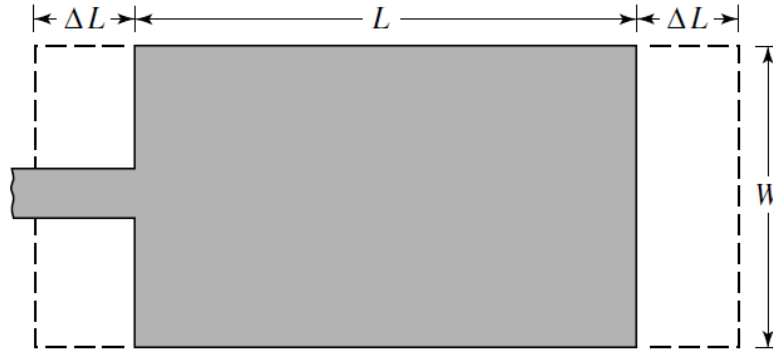
The calculations for the dimensions of a standard patch antenna can be found in [40], [42], [43], [44]. A standard patch antenna having a length of L in millimetres and width of W in millimetres with a dielectric thickness of H in millimetres where a ground plane is attached to the dielectric is said to be a compact thin patch antenna if the patch width is greater than thickness.

$$W > H \quad (1)$$

Since some of the wave travels in the dielectric substrate and air, the effective dielectric constant $\epsilon_{r_{eff}}$ for a dielectric constant ϵ_r is given by:

$$\epsilon_{reff} = \frac{\epsilon_r + 1}{2} + \frac{\epsilon_r - 1}{2} \times \left(1 + 12 \times \frac{H}{W}\right)^{-\frac{1}{2}} \quad (2)$$

Due to the fringing effect, the antenna seems larger than its dimensions. The fringing effect of a patch antenna is shown in Fig. 3-2.



(a) Top view

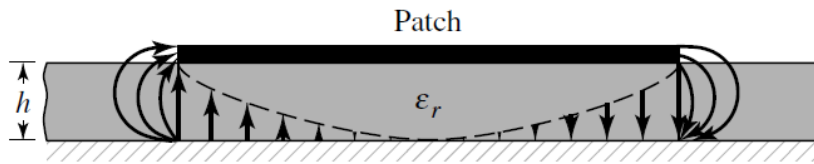


Fig. 3-2: Effective length of patch due to fringing effect [40]

Hence the length which must be added to the antenna ΔL in a practical approach is given by:

$$\Delta L = H \times 0.412 \times \frac{(\epsilon_{reff} + 0.3) \times \left(\frac{W}{H} + 0.264\right)}{(\epsilon_{reff} - 0.258) \times \left(\frac{W}{H} + 0.8\right)} \quad (3)$$

The effective length can be given by:

$$L_{eff} = \frac{c}{2 \times f \times \sqrt{\epsilon_{reff}}} \quad (4)$$

Where c is the speed of light given by:

$$c = 299792498 \text{ m/s}$$

The effective length of the antenna can also be expressed as

$$L_{eff} = L + 2 \times \Delta L \quad (5)$$

Rearranging equation (5), L can be calculated as:

$$L = L_{eff} - 2 \times \Delta L \quad (6)$$

Calculations were done based on the above equations to calculate the patch size of a microstrip patch antenna. The dimensions of the patch is 69 x 91mm which is considerably large considering the fact that the size of the dielectric layer and ground plane which should be a minimum of 120 mm. An antenna of this size is not feasible to be mounted on a doorframe.

Using the speed of light c of 299792458 m/s, resonant frequency f of 870 MHz.

Dielectric constant of the substrate $\epsilon_r=6.15$ and height of substrate $H=3.175$ mm.

The wavelength λ and quarter wavelength $\lambda/4$ for 870 MHz transmission line can be calculated as:

$$\lambda = \frac{c}{f} \quad (7)$$

Hence
$$\lambda = \frac{299792458}{870 \times 10^6} = 344.589 \text{ mm}$$

Quarter wavelength is defined as

$$\text{Quarter wavelength} = \frac{\lambda}{4} \quad (8)$$

And is calculated for 870 MHz as

$$\frac{\lambda}{4} = 86.147 \text{ mm}$$

The width of the microstrip patch can be calculated as:

$$W = \frac{c}{2 \times f \times \sqrt{\frac{\epsilon_r + 1}{2}}} \quad (9)$$

Using (9) this could be calculated as

$$W = \frac{c}{2 \times f \times \sqrt{\frac{\epsilon_r + 1}{2}}} = 91 \text{ mm}$$

The type of antenna can be found by ratio W/H which can be calculated as

$$\frac{W}{H} = \frac{91}{3.175} = 28.6$$

Since $\frac{W}{H} \geq 1$, the antenna falls into the thin microstrip antennae. The length of the microstrip patch can be calculated as

Using equation (2) ϵ_{reff} can be calculated as

$$\epsilon_{reff} = \frac{6.15 + 1}{2} + \frac{6.15 - 1}{2} \times \left(1 + 12 \times \frac{3.175}{91}\right)^{-\frac{1}{2}} = 5.737$$

And by using equation (4) the effective length can be calculated as

$$L_{eff} = \frac{299792458}{2 \times 870 \times 10^6 \times \sqrt{5.737}} = 72 \text{ mm}$$

Using equation (3) ΔL could be calculated as

$$\Delta L = 3.175 \times 0.412 \times \frac{(6.15 + 0.3) \times \left(\frac{91}{3.175} + 0.264\right)}{(6.15 - 0.258) \times \left(\frac{91}{3.175} + 0.8\right)} = 1.415 \text{ mm}$$

The length could be calculated by using equation (5)

$$L = 72 - 2 \times 1.415 = 69.1 \text{ mm}$$

The shift of resonant frequency of the design with a 1 mm patch increment can be calculated in terms of length as:

$$Shift = \frac{|f_L - f_L^+| + |f_L - f_L^-|}{2} \quad (10)$$

Substituting (4) in terms of length the equation could be rewritten as

Shift

$$= \frac{\left| \frac{c}{2 \times L \times \sqrt{\epsilon_r}} - \frac{c}{2 \times (L + 0.001) \times \sqrt{\epsilon_r}} \right| + \left| \frac{c}{2 \times L \times \sqrt{\epsilon_r}} - \frac{c}{2 \times (L - 0.001) \times \sqrt{\epsilon_r}} \right|}{2}$$

And can be calculated as

$$\frac{\left| \frac{299792458}{2 \times 69.1 \times \sqrt{6.15}} - \frac{299792458}{2 \times (69.1 + 0.001) \times \sqrt{6.15}} \right| + \left| \frac{299792458}{2 \times L \times \sqrt{6.15}} - \frac{299792458}{2 \times (69.1 - 0.001) \times \sqrt{6.15}} \right|}{2}$$

$$= 12.661 \text{ MHz}$$

The shift of resonant frequency of the design with a 1 mm patch increment can be calculated in terms of length as:

$$Shift = \frac{|f_W - f_W^+| + |f_W - f_W^-|}{2} \text{ MHz} \quad (11)$$

Substituting (9) in terms of width, equation (10) could be rewritten as

$$\frac{\left| \frac{299492458}{2 \times 91 \times \sqrt{\frac{6.15 + 1}{2}}} - \frac{299792458}{2 \times (91 + 0.001) \times \sqrt{\frac{6.15 + 1}{2}}} \right| + \left| \frac{299792458}{2 \times 91 \times \sqrt{\frac{6.15 + 1}{2}}} - \frac{299792458}{2 \times (91 - 0.001) \times \sqrt{\frac{6.15 + 1}{2}}} \right|}{2}$$

$$= 9.549 \text{ MHz}$$

There is a 9 MHz and 12 MHz shift for every increment in the microstrip patch width and length thus demonstrating the precision of the microstrip which is needed for accuracy in simulations and manufacturing.

Another important aspect in an RFID antenna is the polarisation producing a 'fan beam' that it may read tags irrespective of their orientation. If the tags were aligned with the antenna's polarisation linear antennae will read further with an higher efficiency than a circularly polarised antenna [16]. If tags are not aligned with the antenna's polarisation circular polarised antennae will have the advantage. For the purpose of designing an antenna for a doorway reader system which will be able to read tags moving via the door passage either by a person carrying vertically or horizontally, a circularly polarised antenna will have the advantage and is preferred. A circularly polarised beam is as spiral beam rotating with time, emitting (tornado like) from the antenna giving the beam advantage to read tags in any orientation. Fundamentally a circularly polarised beam is achievable if two orthogonal modes are excited with a 90 time-phase difference between them. When a 90-degree time-phase difference is given to the two feeds of the antenna when the horizontal current flow is maximum, the

vertical current flow will be zero and vice versa in the other quarter cycle. A beam emitting from a circular patch is not necessarily circularly polarised [16].

There are four common methods in achieving a circularly polarised beam:

1. Using two feeds, one with a 90-degree time phase difference.
2. Using a single feed but with asymmetric feature or slot to the radiating patch so that the surface currents will flow in a circular manner
3. Using a single feed on a nearly square patch at a corner if the length were a bit less than resonant length and a bit more than the height.
4. By truncating the diagonal edges of a square patch so that the surface currents will flow in a circular manner.

Circular polarising techniques discussed above are shown in Fig. 3-3.

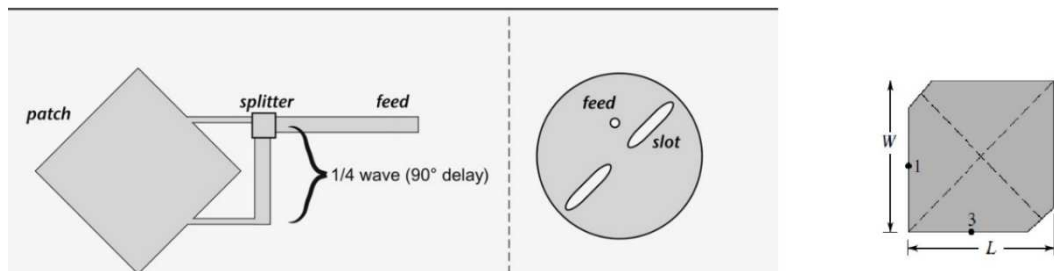


Fig. 3-3: Antenna Circular-polarising techniques [16], [40]

The power divider for the first technique of polarisation can be achieved by using a Wilkinson power divider [45]. A Wilkinson divider circuit is shown in Fig. 3-4.

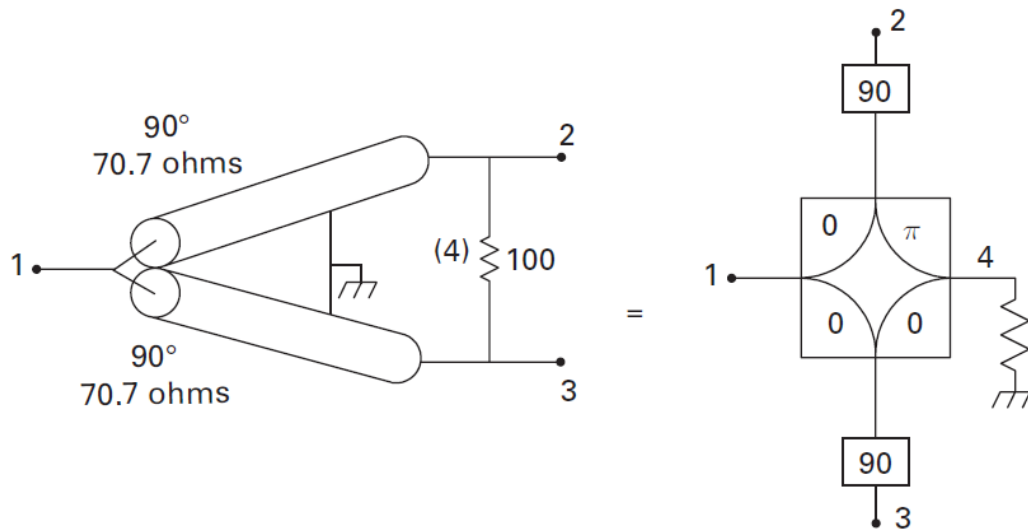


Fig. 3-4: Wilkinson Power Divider [45]

The Wilkinson power divider comprises of two quarter wave pieces of 70.7Ω transmission line having three external ports. When power is applied to port 1 will divide it between port 2 and port 3. The 50Ω load (which is the characteristic impedance of the antenna) is transformed by the 90-degree cables to 100Ω . The shunt connection of port 2 and port 3 with a 100Ω provides the desired 50Ω impedance.

To feed an antenna that is circularly polarised, another quarter wavelength cable should be added to one end so that it would provide the 90-degree time-phase delay.

3.3 Antenna miniaturising techniques

There are many techniques used to miniaturise a microstrip patch antenna. Some of them are by using lumped elements, high dielectric material, conductors on the surface, perforating external slots on the radiating patch and reinforcing the radiator by shielding. The externally perforating method and using high dielectric substrates are two common methods the researchers have looked upon in the last few decades. Since a high electric field could be trapped in a high dielectric substrate, the thickness of the

substrate could be made smaller. Most of these techniques are used in this research to miniaturise the proposed designs.

According to [46], the length of the patch of a microstrip antenna can be estimated as

$$L \approx \frac{c}{2 \times L \times \sqrt{\epsilon_r}} \quad (12)$$

The length of the antenna is inversely proportional to the square root of the dielectric constant of the antenna. Hence the material used for the dielectric substrate directly contribute to miniaturising the antenna. A comparative study was done using 5 dielectric materials in finding the performance with reference to a microstrip antenna [47], [48]. The results are shown in the Table 3-1.

Table 3-1: Various dielectric materials and their performance in a standard patch antenna as in [48]

Resonant Frequency at 10GHz	Bakelite	FR-4	RO4003	Taconic TLC	RT Duroid
Dielectric Constant (ϵ_r)	4.78	4.36	3.4	3.2	2.2
Dissipation factor (Tan δ)	0.03045	0.013	0.002	0.002	0.0004
Side length	9.15 mm	9.575 mm	10.85 mm	11.175 mm	13.475 mm
Antenna Gain	3 dBi	4 dBi	5 dBi	5.5 dBi	6.5 dBi
Antenna efficiency	42-45%	50%	67.5%	70%	80%
Radiating efficiency	42-45%	50%	70%	67.5%	80%

According to results, even though RT Duroid board antenna has the highest gain due to its low dielectric constant, the patch size is quite large. The second best is the Taconic boards giving an antenna gain of 70%. In addition, Taconic board, also provide a narrow beam width when radiation patterns are considered [48].

Other research has been done to evaluate the performance of a radome effect on an antenna with the dielectric substrates. Embedding a dipole antenna [49] and

embedding a microstrip antenna for civil engineering applications in a concrete wall and analysing the radiation pattern [50].

3.4 Fractals and its applications to antennae

A fractal according to discoverer Benoit Mandelbrot is basically a shape where its fragmentation and contrast remains the same when zoomed without fading off or changing, whilst the structure of a piece in a particular zoom is always the basic element of the whole [51]. Fractals have no characteristic size yet possesses a self-affine or recursive geometric nature. The term fractal means broken or irregular fragments. Due to its peculiar nature of self-similarity these patterns were used in electromagnetics thus giving birth to a new field called Fractal Antenna Engineering. During the last two decades the application of fractal patterns became much popular due to the increase in computer-based simulations as researchers were able to experiment with novel and improved designs without adhering to analytical techniques of solving Maxwell's equations. As the iteration of the fractal increases the electrical length of each element of the antenna is also increased and hence the resonant frequency is reduced. In order to increase the resonant frequency, which was lowered to the required frequency, the whole antenna needs to be scaled down which results in miniaturisation of the antenna. The art of miniaturisation is said to be an art of compromise of its volume, bandwidth and efficiency.

Fractals are used in antenna design majorly for miniaturisation purposes and to increase directivity because of the importance of the electrical length to an antenna. Since fractals have a self-similar structure they tend to resonate at different frequencies and hence result in multiband behaviour. There are various techniques to apply fractal patterns to a microstrip antenna. The radiating patch could be externally perforated with a slot pattern, the radiating patch sides could be tapered into a fractal

boundary, the dielectric material could be constructed with metamaterials and arranged in a fractal pattern or multi-layer substrates could be set to a fractal pattern. Slots are used to increase the surface current path lengths compared to a square antenna and thereby reduce the resonant frequency and miniaturise. An extensive study on slot patterns was done in [52]. When a slot pattern is applied to a radiator to miniaturise an antenna, a high concentration of surface currents is manifested resulting in an increased ohmic loss. When using a fractal pattern on an antenna, the fractal dimension and its lacunarity should be taken into account [53]. Fractal patterns having space filling properties are the only ones which increase directivity and effectively miniaturise the antenna [17].

The first known fractal antenna published was done by bending a wire to a fractal shape. The overall length remains the same whilst the size is reduced with the iteration [17], [18]. In [54], [55], [56] a multiband antenna, by applying the Sierpinski Gasket on to the antenna. An extensive study was done about this fractal pattern, the variation of its properties with the flare angle, obtaining multiband with the variation of the scale factor and input impedance. A design of the Koch curve or the snowflake antenna was published in [63]. Its radiating surface of the patch is almost one third of the original design but with better performance. It was also observed that with the increase in the iteration of the fractal, the resonant frequency decreases as the perimeter of the patch decreases. The antenna was operated in the C band at 4-6 GHz. Later Minkowski loops and Minkowski dipoles were invented and studied. Ali and Jalal introduced a Minkowski-Like Pre-Fractal geometry on a relatively high dielectric substrate for GPS L1 applications which had an overall effective size reduction of 64% along with a narrow bandwidth [57]. The co-polar and cross-polar cut radiation patterns showed wide beam widths and wide bandwidths. The antenna was simulated with different slot widths of the fractal and it was observed that the resonant frequency increases

with the slot widths. However, it showed high losses due to surface wave excitations. Even though using high dielectric constant substrates is the simplest solution, they result in narrow bandwidths, high losses and low efficiency because of the surface waves. The losses on Microstrips were studied in [58]. A study carried out later discovered that this kind of slot pattern has a natural meandering effect on the antenna and hence it can be used for polarisation purposes by simply adding an additional stub at the end of the slot [59]. The Minkowski-Like Pre-Fractal pattern has multiband characteristics which was shown by designing a dual band antenna for GPS and GSM frequencies [60]. A stacked antennae for GPS L1/L2 bands with a small air gap between the substrates which produced a dual band and resulted with 78% size reduction compared to a standard patch [61]. An interesting investigation was performed of an inverted Koch square fractal [62]. The simulation was done with 3 variable indentation angles and 3 iterations. It was found that as the indentation angle increased, the resonant frequency was reduced and as the fractal iteration increased the frequency dropped, both resulting in miniaturisation. The patch size of the antenna was 31.3 mm x 31.32 mm. Even though their results show that the resonant frequencies drop with iterations, they claim that it is not fully clear like the case when changing the angle. A novel fractal geometry was introduced again by using L-system algorithms [63]. The final patch size was the same as the previous antenna but resulted with a 60% size reduction. This antenna was simulated both cavity model as well as full wave analysis, where the resonant frequencies differed by 10%. Another famous fractal pattern is the Koch curve or the snowflake fractal.

A fractal patch antenna having a Koch fractal boundary at 1.26GHz was designed in [39] which resulted with high directivity and matched 50Ω at fundamental frequency. The patch is said to have broadside directive patterns.

A GPS patch antenna on a high impedance surface was introduced [64]. Rogers TMM10 material which has a dielectric constant of 10.2 and a thickness of 1.905 mm was used. In general, due to the surface waves, the gain of the conventional patch antenna on a high dielectric surface is low and the bandwidth is narrow. However, in this design an electromagnetic bandgap structure (EBG) was used and hence the gain was increased, and the bandwidth was made wider. This occurred as a reduction of the surface waves due to the electromagnetic bandgap structure. In [55] a similar patch was designed but used substrate perforation exterior to the patch in order to reduce the effective dielectric constant without sacrificing the area of the radiator. This helped to mitigate unwanted interference.

During the last few years novel fractal patterns are being used in order to overcome the challenges in miniaturisation. A Spidron fractal shaped antenna excited by a small microstrip was implemented in order to produce a gain of 4.3 dBi. This design was a circularly polarised with a wide bandwidth [65]. The total size of the patch was 40 x 40 x 1.52 mm. Even though the Spidron fractal is not space filling, the results were positive. A novel self-affine multiband antenna design was done with a 3 mm air gap operating at 2.5GHz [66]. A circularly polarised antennae are usually produced by meandering the patch corners or by cutting the edges off of a square patch [40]. An Hexagonal fractal pattern was studied in [67] which multiband applications were observed similar to the Sierpinski gasket. Miniaturisation was not considered in this design. Again an inverted hexagonal patch was discussed where a hexagonal shape was removed from the patch iteratively [68].

Even though there is some work in fractal antenna design, there has been no work published yet in the investigation of complex/spherical based fractal patterns except for the apollonian gasket recently published or higher order iterations of fractals [69]. In [47] and [48], the work was not conclusive in optimising the antenna model. Neither

is there any work published for using a dual or multi-port feeding system in order to obtain a circular polarisation. No feeding optimisation has been focused on the feeding techniques either. This research aims to produce a novel design of a fractal pattern which has never been generated and/or used before.

When designing a standard microstrip patch antenna for a required frequency f_1 , the width of the patch is given by [70] as:

$$W = \frac{c}{2 \times f_1} \times \sqrt{\frac{2}{\epsilon_{r1} + 1}} \quad (13)$$

Where c is the speed of light in free space and ϵ_r is the relative permittivity of the substrate. Should ϵ_r be increased (i.e. $\epsilon_{r2} > \epsilon_{r1}$) the resonant frequency f_2 will drastically drop.

$$(f_2 < f_1)$$

$$f_2 = \frac{c}{2 \times W_1} \times \sqrt{\frac{2}{\epsilon_{r2} + 1}} \quad (14)$$

And in order to bring back the frequency to f_1 for the new substrate ϵ_{r2} , the width of the patch should be reduced which results in miniaturisation.

$$w_2 = \frac{c}{2 \times f_1} \times \sqrt{\frac{2}{\epsilon_{r2} + 1}} \quad (15)$$

Here w_2 is less than w_1 thus contributing to antenna miniaturisation.

By using specialised printed circuit boards of high dielectric constants, the antennae could be miniaturised due to the above reason.

Useful fractal patterns could be generated by using a method called Iterated Function Systems (IFS) which uses a series of linear affine transformations [71], w is defined as

$$w \begin{bmatrix} x \\ y \end{bmatrix} = \begin{bmatrix} a & b \\ c & d \end{bmatrix} \times \begin{bmatrix} x \\ y \end{bmatrix} + \begin{bmatrix} e \\ f \end{bmatrix} \quad (16)$$

$$w(x, y) = (ax + by + e, cx + dy + f) \quad (17)$$

Where (a,b,c,d,e and f) are real coefficients which control the fractal movement in space. Parameters a and d control the scaling whilst b and c control the rotation by angles ψ_1 and ψ_2 . Parameters e and f are linear transformations. By these the original pattern could be rotated, sheered, translated and scaled. These parameters could also be written as

$$a = \delta_1 \cos \psi_1 \quad (18)$$

$$d = \delta_2 \cos \psi_2 \quad (19)$$

$$b = \delta_2 \sin \psi_2 \quad (20)$$

$$c = \delta_1 \sin \psi_1 \quad (21)$$

If $w_1, w_2, w_3, \dots, w_N$ be considered to be a set of affine transformations of an initial geometry 'A', then the term,

$$w_1(A), w_2(A), w_3(A), \dots, w_4(A)$$

could be written as

$$w(A) = \bigcup_{n=1}^N w_n(A) \quad (22)$$

Where,

$$\bigcup_{n=1}^N w_n(A)$$

is known as the Hutchinson operator. To obtain a required fractal geometry, W is repeatedly applied to the previous geometry since a self-similarity is required. If A_0 be the initial geometry then

$$A_1 = w(A_0) \quad (23)$$

$$A_2 = w(A_1) \quad (24)$$

$$A_3 = w(A_2) \quad (25)$$

Similarly, a general expression could be written as:

$$A_{K+1} = w(A_K) \quad (26)$$

The above iterated function systems could be computed by using IFS, MATLAB tool for most of the fractal patterns or by using a special software called Fern [71].

A study shows how rich the structure of diffractals is even in their simplest form [66] Diffractals are waves which have encountered fractals. Berry suggests that fractals might have caused waves to adopt unfamiliar forms. Here in fractal antennae instead of backscattering, the very radiator from which the waves propagate is a fractal which might imply that the beam which is formed is a beam consisting of different harmonics or operating as a fractal antenna array contrary to Berry whose observations were monochromatic. If it were so this might increase the performance of an RFID near field antenna by increasing the read/write rate.

3.5 Fractal Antenna used in RFID reader antennae

Department of Innovation and Engineering at University of Salanto presents an RFID tag antenna design a short circuited patch, with a Koch curve tapered on two opposite sides of the antenna [72]. Good values for S11 parameters have been obtained in this design. (S11=-24.38 dB) This is done by increasing the ground plane size. The realised antenna has a ground plane of 67x76 mm, however, the bandwidth of the antenna is almost 1 MHz and is not suitable for RFID applications as RFID requires a bandwidth of 5 MHz. The radiation patterns show a spherical radiation pattern as opposed to desired pencil beam for narrow beam width as shown in Fig. 3-5 and Fig. 3-6. [72].

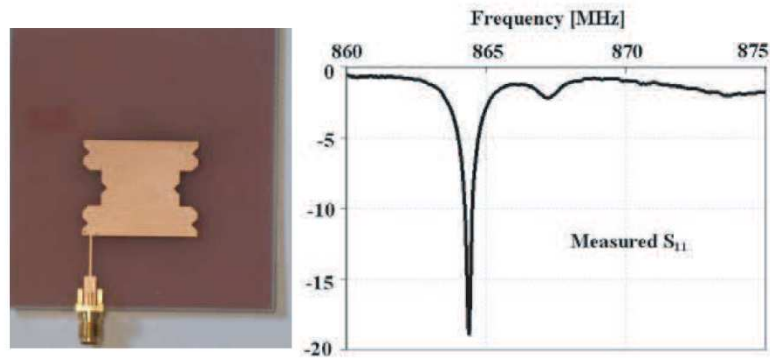


Fig. 3-5: Patch and measured S_{11} in design [72]

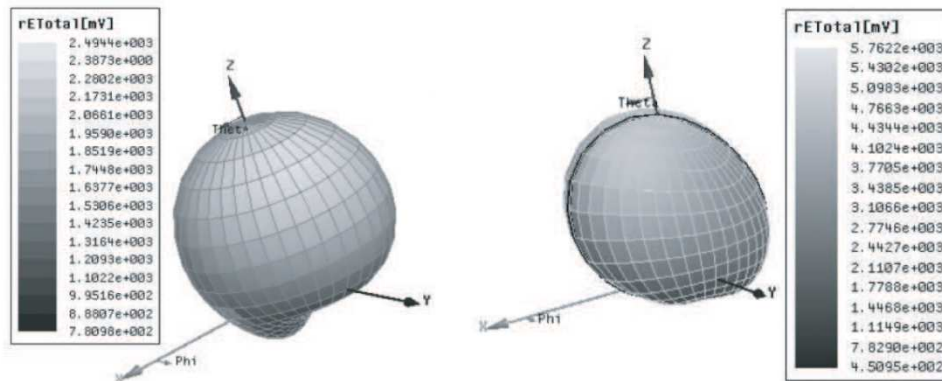


Fig. 3-6: 3D radiation patterns of [72]

A read range comparison of a fractal patch antenna as applied to a handheld RFID reader is compared in [73] where a rectangular patch, H-shaped patch, Fractal patch, a balanced dipole and a circularly polarised patch are compared. However, since this is an industrial comparison unlike in [48], difference heights of dielectric substrates and material have been used. The best S_{11} value was obtained from the circular polarised patch at 869 MHz showing a directed considerably narrow beam. Considering the read ranges for a handheld device, the best (shortest) distance was recorded from the circular polarised fractal antenna with a range from 0.13 to 0.4m. While the balanced dipole and regular patch achieved relatively consistent read ranges, the read ranges for H shaped antenna are relatively poor. According to research, the shortest ranges are

achieved with circularly polarised designs. The radiation patterns for rectangular patch and circularly polarised antenna are shown in Fig. 3-7 and Fig. 3-8.

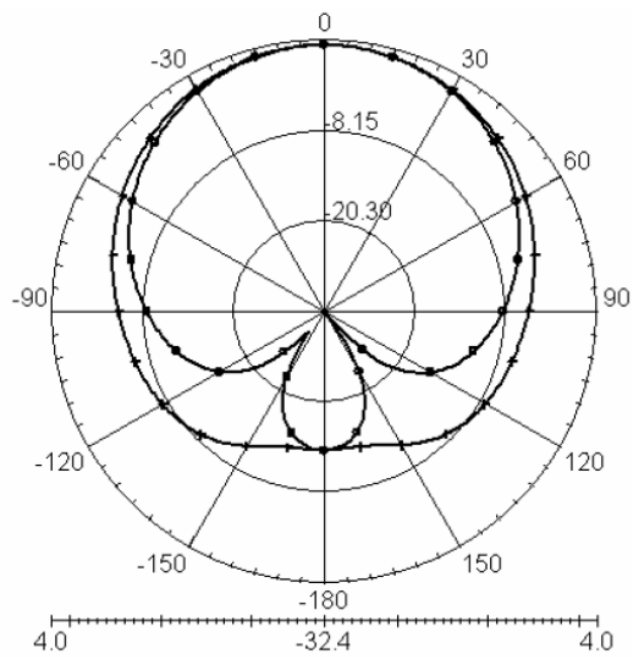


Fig. 3-7: Radiation pattern for Rectangular patch in [73]

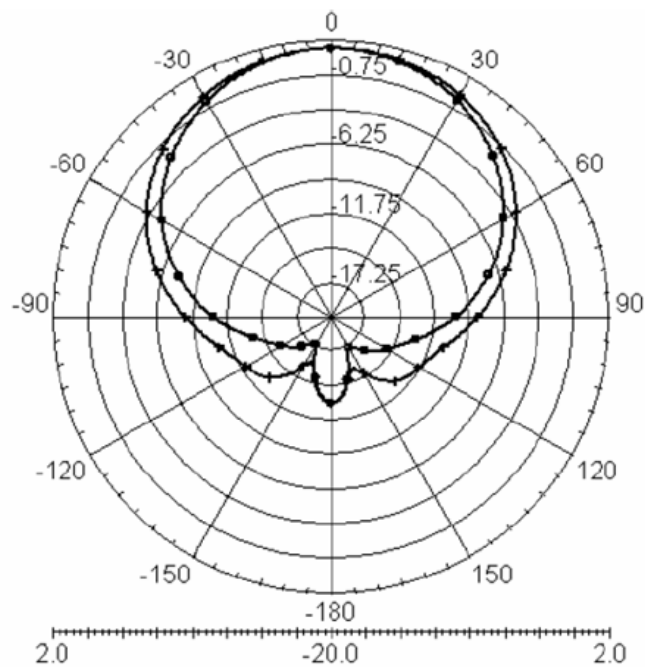


Fig. 3-8: Radiation pattern for Rectangular patch in [73]

Design [74] proposes a design comprised of 4 helical elements fed at each port with 0, 90, 180- and 270-degree phases respectively. The variation in axial length, radius and the number of turns are variables in this design to optimise performance, tune to a required frequency and obtain required radiation patterns. This design helps an RFID antenna to operate in a wider space. Unlike a typical RFID antenna's radiation pattern, this design has its unique radiation pattern. It is not necessary for an antenna to have its peak gain at boresight in some applications. With this radiation pattern two peaks which are not at boresight occurs. This might be used as an antenna where two doors might be covered using a single antenna. The radiation pattern in [74] is shown below in Fig. 3-9.

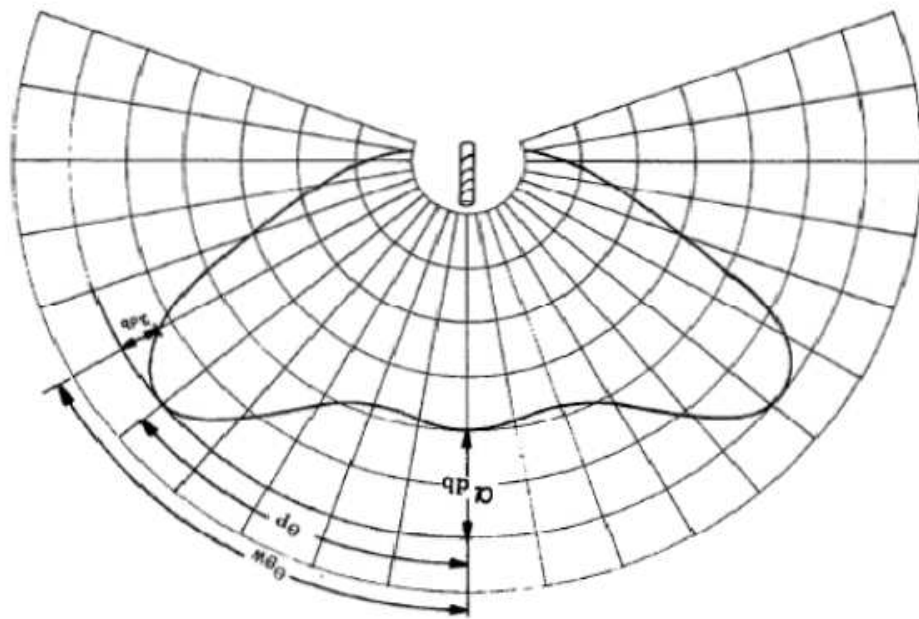


Fig. 3-9: Radiation pattern for [74]

In [75] Koch Fractal has been applied to miniaturise an RFID antenna also to obtain a circularly polarised design operating at 902-928 MHz UHF USA band. The antenna was fabricated on FR4 material with a size of 54x54x1.6 mm. The fractal applied to the antenna, feeding, surface currents and radiation pattern are shown below in Fig. 3-10, Fig. 3-11, Fig. 3-12 and Fig. 3-13.

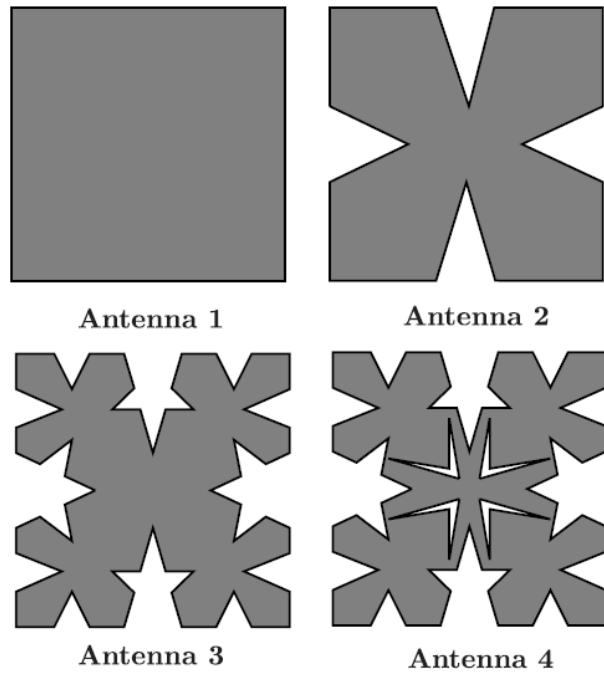


Fig. 3-10: Antennae with different fractal iterations in [75]

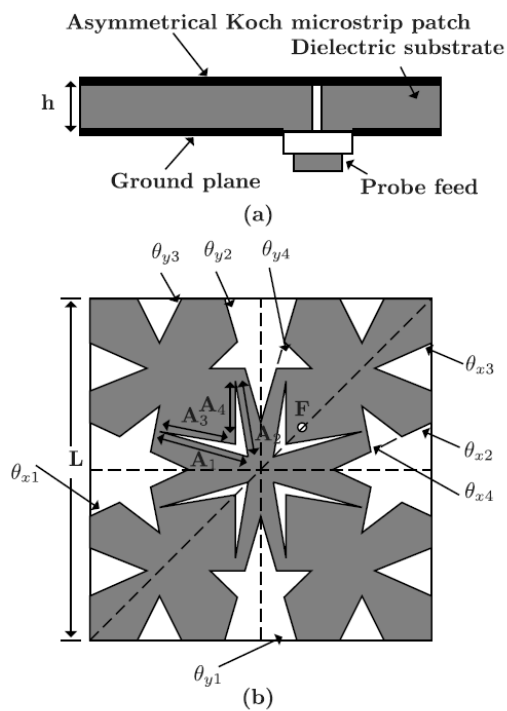


Fig. 3-11: Final design of [75]

Surface current patterns on the patch are shown below both right hand circular polarised (RHCP) and left hand circular polarised (LHCP).

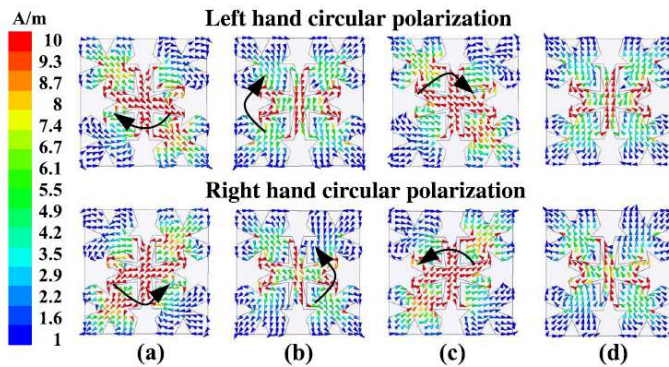


Fig. 3-12: Circular polarised radiation observed by surface currents in [75]

The radiation pattern for both simulated and measured is shown below:

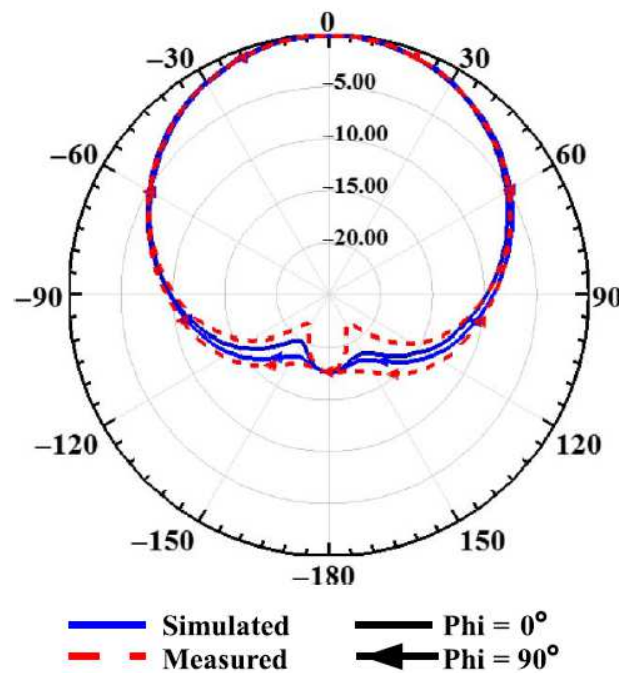


Fig. 3-13: Simulated and measured radiation pattern for [75]

Multiple repeater antenna is considered in [76] where a loop antenna is fabricated and then 4 repeaters are added to it as shown below. These rings are located over the reader antenna. It is noted that the reading area and reading performance of the

antenna is increased in the terms of arbitrary tag orientation. The E field radiation pattern for multiple repeaters are shown in Fig. 3-14.

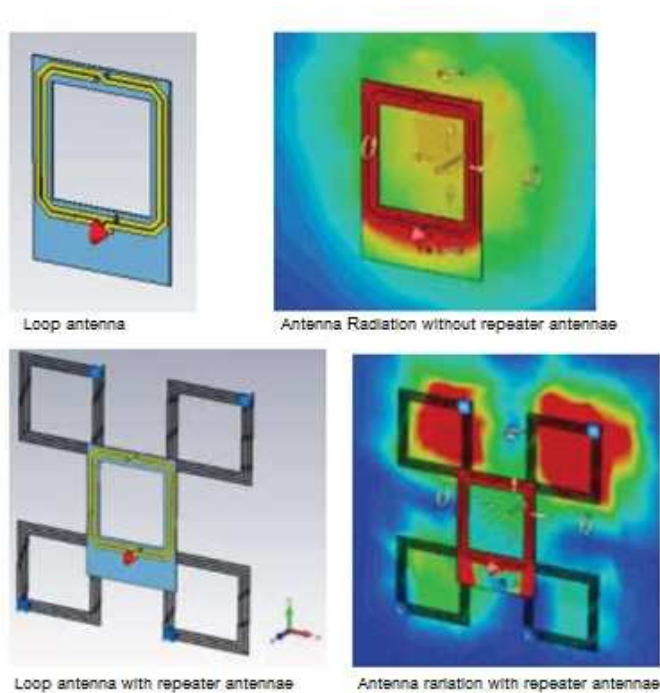


Fig. 3-14: E field radiation patterns of repeater antenna in [76]

Though operating at 13.56 MHz at HF range, this technique is like having a parasitic patch antenna or a fractal pattern.

When detecting tags in an enclosure, it is proposed that by coupling the reader antenna to another, the read performance is increased [77]. Block diagram of enclosure and antenna is shown in Fig. 3-15.

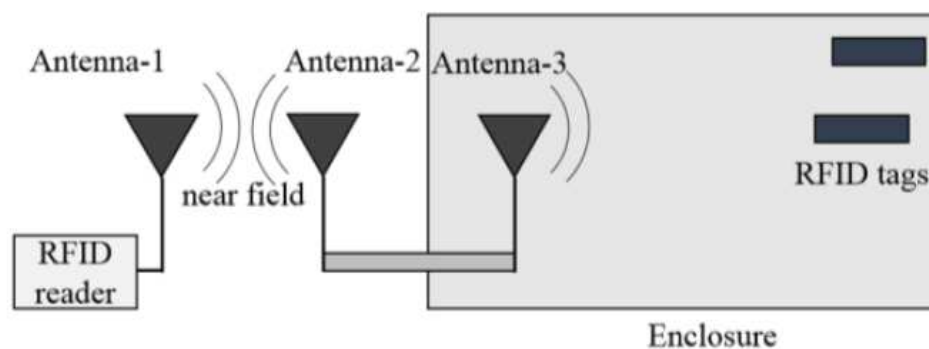


Fig. 3-15: Proposed antenna for enclosure [77]

A loop antenna is proposed in the design to couple nearfield energy. This antenna type might be a possible solution to implementing a doorway reader to an enclosed room. For example, EMC chamber, MRI scan chamber, etc.

A dual band pre fractal antenna is discussed in [78] where CST microwave studio was used to simulate the design and optimise its parametrised dimensions. This antenna operates at 2.42GHz range and 3.5GHz.

A novel method is suggested in [79] by adding a new element known as the 'folded ground element' FGE. Slot patterns are also integrated into the radiating patch of the antenna. Then an RFID right-handed circular polarised feeding network is used to feed and obtain a RHCP. The antenna is shown in Fig. 3-16.

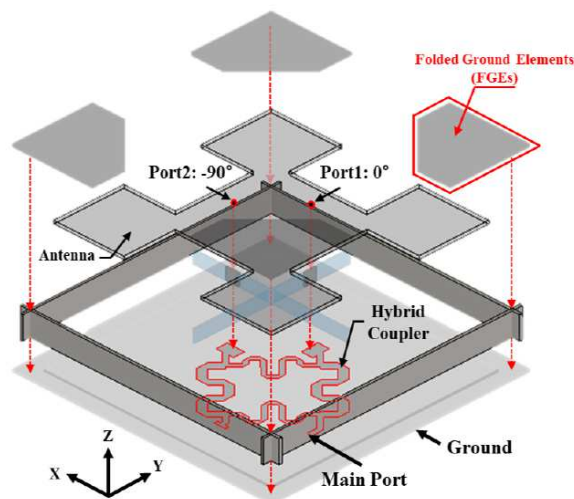


Fig. 3-16: Folded ground plane antenna with 90-degree phase feeding [79]

The RHCP can be seen by observing the E field of the antenna and is shown in Fig. 3-17.

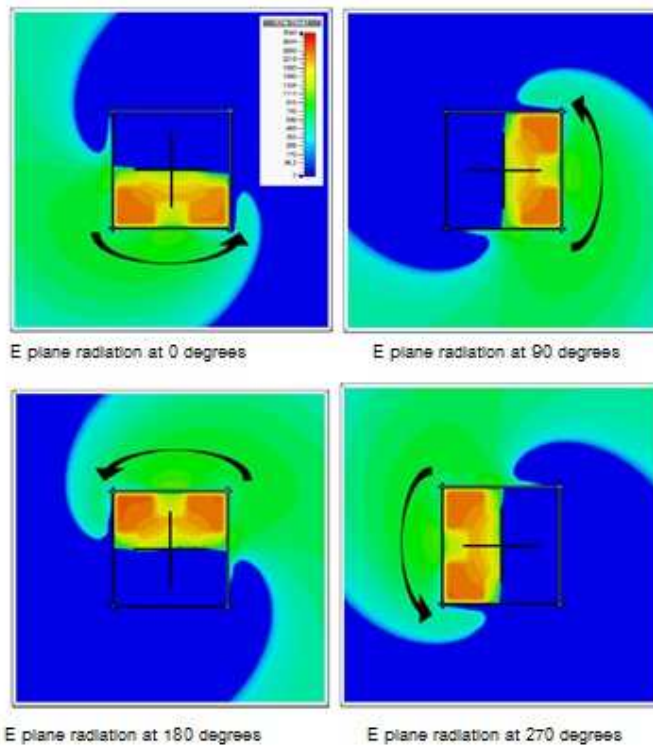


Fig. 3-17: Circular polarised behaviour seen by E plane at 90 degree intervals [79]

The feeding network comprises of a Wilkinson power divider and an extra quarter wavelength element to obtain the 90-degree time phase shift.

3.6 Potential commercially available designs for a doorway reader antenna

Some of the commercially available designs specifically fit for RFID doorway reader application are presented in the Table 3-2.

Table 3-2: Dimensions and antenna parameters of commercially available RFID antenna for Doorway reader application

Antenna	Dimensions (LxWxH mm)	Frequency (MHz)	Gain	Polarisation	Beamwidth (degrees)
MOBILE MARK PN6- 915 [80]	146x146x18	865-870 & 902-928	6 dBi	LHCP	80, 80
iDTRONIC [81]	650x86x8	864-869 & 902-928	5 dBi	Linear	110, 30
T7 – A4030C [82]	280x280x12	864-869 & 902-928	6.5 dBi	circular	60, 60
Abracon [83]	70x70x5.9	902-928	4 dBi	RHCP	
Abracon [84]	40x40x6.5	902-928	1.5 dBi	RHCP	
Abracon [85]	50x50x6.2	902-928	3 dBi	RHCP	

3.7 Summary

This chapter explored the fundamentals of microstrip antenna, its design parameters and governing equations, fractal antennae and its application to the purpose of miniaturisation, as well as overcoming RFID challenges. A fractal having a self-similar pattern radiates a diffractal wave, thus with the aid of frequency hopping provided by the RFID reader could compensate for the detuning of tags due to clusters. The chapter

revealed that a microstrip antenna could be miniaturised by using a high dielectric constant material, as the antenna substrate and a comparative study of antennae with different dielectric substrates were studied. The chapter focuses on the importance of accuracy of a microstrip antenna's dimensions as a 1 mm error could give a 12 MHz deviation in resonant frequency. Hence, fractals when used should be engineered with great precision. The chapter also does a comparative analysis of various geometry techniques used in industry and other published literature. One of the main RFID challenges is to read tags in different orientations as if the tag were in line with the RF beam not crossing, there would be no current and hence the tag would not be activated thus a blind or weak spot in the operational region. To overcome this challenge a circular polarised beam is proposed in the literature. By focusing a tornado like beam radiating out of the patch antenna tags in any orientation would cross the spiral beam. Various circular polarising techniques have been studied in detail in this chapter along with antenna feeding techniques. This knowledge is used in designing a commercially viable antenna design in Chapter four.

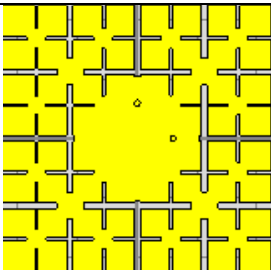
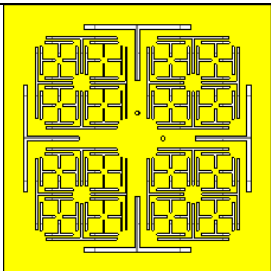
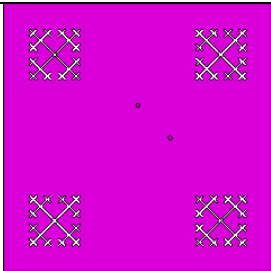
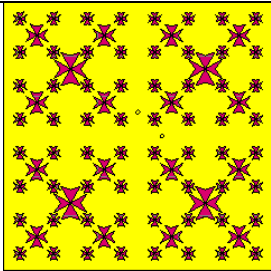
4 Development of a doorway reader antenna: proposed designs and simulation results

4.1 Introduction

In this chapter a development of a doorway reader antenna is presented. Four novel antenna designs are proposed using four fractal patterns.

These are shown in Table 4-1.

Table 4-1: MLPF, Tau, SFT and Maltese cross fractals

Antenna	Fractal pattern
Minkowski-Like Pre-Fractal (MLPF)	
Tau Fractal (Tau)	
Space Filling Tree (SFT)	
Maltese Cross (Maltese Cross)	

These four designs were handpicked since they comprise of unique geometric characteristics which contributes to the electromagnetic behaviour of the antenna. MLPF, having the meandering effect, increases the antenna's electrical length in increments as fractal iteration increases. Tau fractal converges with fractal iteration thus creating smaller parasitic patches. SFT increases slot lengths with iteration whilst keeping the electrical length of the antenna constant. Since surface currents are intense at sharp edges, Maltese cross was considered. The vertical and horizontal flare of the Maltese cross angle could be altered and hence has a potential to contribute to a symmetric circular polarised beam.

This chapter describes the design process using simulation software, CST Microwave Studio Suite to obtain a commercially viable antenna design for an effective RFID doorway reader system. Techniques discussed in Chapter Two and Chapter Three are considered in the design process with other mathematical and geometrical techniques.

4.1.1 Antenna requirement for doorway reader application

An antenna operating at UK UHF RFID frequency (870 MHz) capable of reading multiple passive RFID tags passing in any orientation through a door passage, can be easily mounted on a standard doorframe with a mechanical bracket with a simple installation procedure. The operation of the antenna should be limited to a reasonable distance (of around 100 cm) from the doorway that RFID tags in the vicinity may not have an effect on the count (ideally to be installed for document tracking at a busy hospital building). The antenna should further have the potential to read tags which are clustered together when passing at a reasonable human speed through the doorway.

4.1.2 Available designs and their performance

The most common type of antennae used for this application are RFID gates operating on both HF and UHF ranges usually installed in libraries [36], [37]. These gates are typically bulky weighing around 25kg and requires a complex process in installing on the floor of the building. Approaches to miniaturise antenna with the same performance have been an interesting industrial research for some time. However, most of these designs have blind and/or weak spots through which RFID tags can easily pass without detection. For this reason, most commercial designs require 2 or even 4 antennae mounted on either side of the doorframe instead of one from above [38].

4.1.3 Proposed solution

The proposed solution in this study is to design a Near Field UHF RFID antenna which is miniaturised using fractals and other geometrical techniques radiating a beamwidth not more than 100 degrees. RFID UHF UK operates between 865 – 868 MHz and hence a bandwidth of 4-6 MHz is suitable for this application. The antenna is to be circularly polarised (radiating a spiral beam) to overcome the orientation barrier and read tags passing in any orientation. The antenna is designed to be compact enough to be easily mounted on a standard doorframe with a help of a mechanical bracket, etc., requiring no special installation. A diagram of proposed structure is shown in Fig. 4-1.

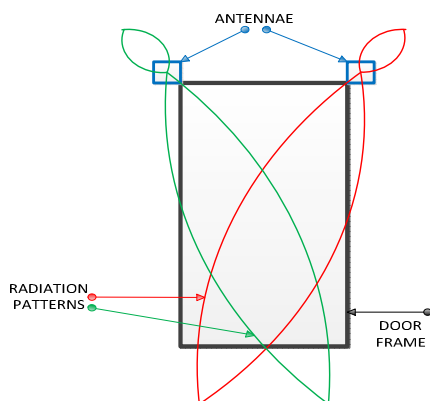


Fig. 4-1: Proposed antennae mounted on a doorframe

The following design criteria is set for an antenna suitable for an RFID doorway reader application. Simulations are performed to obtain the objectives detailed in Table 4-2.

Table 4-2: Design criteria for an RFID doorway reader antenna

Resonant Frequency (MHz)	Return loss S11 (dB)	Directivity (dBi)	VSWR	3dB beam width (degrees)	Antenna input impedance (Z) ohms	Bandwidth (MHz)
870	<-10.0	4.5	<1.8	<100	50+j0	3<BW<6

Note: VSWR is aimed to be <1.8 which will be lowered to <1.2 in prototype tuning.

4.2 Minkowski-Like Pre-Fractal (MLPF)-based antenna

4.2.1 Introduction to the fractal and its construction

Minkowski-Like pre-fractal in its simplest form, is where a square based patch is divided into four from their sides in the first iteration. The squares formed by the previous division, is then considered as the whole structure to be divided into four in the next iteration. Minkowski-like pre-fractals have been used to miniaturise antennae for GPS applications with dual and multiband behaviour in the literature [58], [59], [60], [61], [62]. MLPF fractals are shown in Fig. 4-2 with increasing iteration and curved slot to obtain circular polarisation as shown in Fig. 4-3.

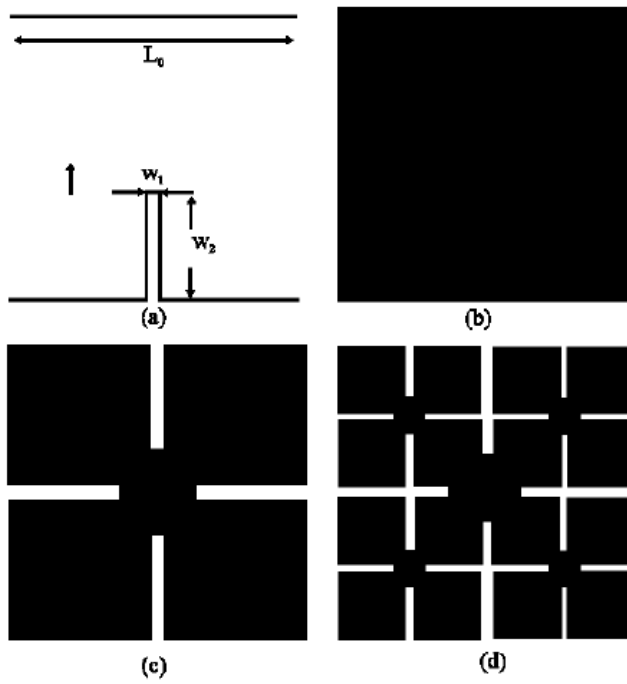


Fig. 4-2: Iterations of a Minkowski like pre fractals [58]

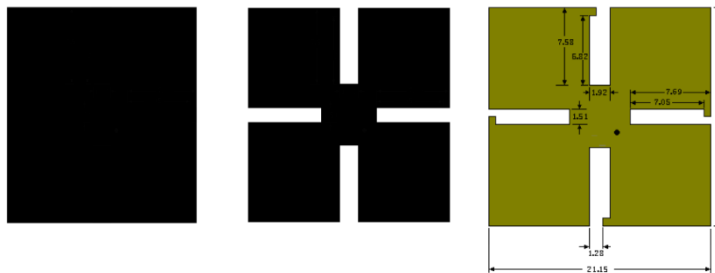


Fig. 4-3: MLPF fractal used to miniaturise antenna with irregular slots curved for circular polarisation [59]

In [59] Right-Handed circular polarisation is obtained by curving the slits of the fractal in one direction. The application of MLPF miniaturises the antenna by 40% [59]

The proposed design is to set a square shaped patch on a dielectric with a ground plane as shown in Fig. 4-4. The dimensions of the patch, its length in y direction P_y measured in millimetres and width in x direction P_x measured in millimetres. The patch is to be perforated with slots horizontally and vertically as depicted below. The lengths and

widths of perforated slots are named $MajorL$ measured in millimetres and $MajorW$ measured in millimetres respectively.

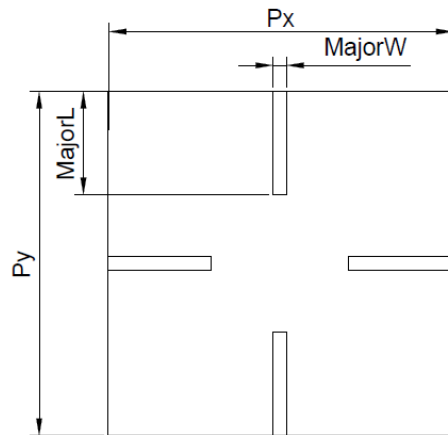


Fig. 4-4: Proposed 1st iteration of MLPF antenna

The second iteration is constructed by considering one squared patch out of the four resulting squares due to the slots perforated in the previous iteration, and then subdividing them again as performed in the previous iteration, this is shown in Fig. 4-5. A self-similar pattern is achieved and hence a fractal can be constructed likewise. The lengths and widths of the perforated slots in the 2nd iteration are named $MinorL$ measured in millimetres and $MinorW$ measured in millimetres respectively.

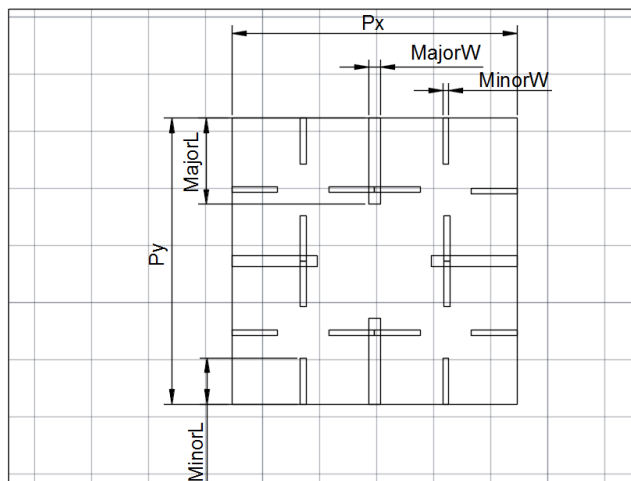


Fig. 4-5: Proposed 2nd iteration of MLPF antenna

The 3rd iteration of the fractal can be constructed again in the same manner by considering the squares resulting from the 2nd iteration as a whole and applying the same pattern to it. The lengths and widths of the slots in the 3rd iteration are named mL measured in millimetres and mW measured in millimetres respectively, as shown in Fig. 4-6.

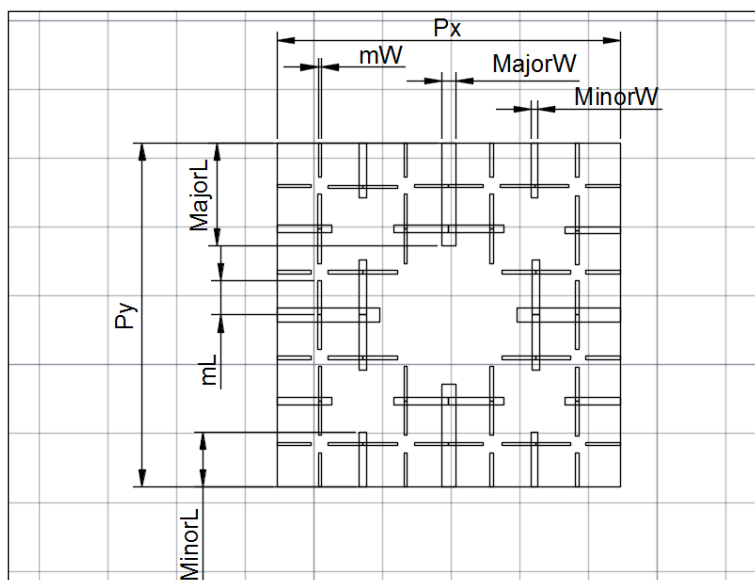


Fig. 4-6: Proposed 3rd iteration of MLPF antenna

4.2.2 Proposed Design and Simulation Results

The proposed design was modelled in CST Microwave Studio and was simulated. The design proposed for simulation is perforating slots on a square patch antenna for the purpose of miniaturisation. The dielectric ground plane and patch are all set to be of square shapes.

The patch size is initially set to 50 mm. Four slots perforated in the first iteration having a length of 15 mm (*MajorL*) and width of 1 mm (*MajorW*) are simulated for -60.0 dB accuracy. The coaxial feed was set at the centre of the patch. The simulated patch and 1D results are shown in Fig. 4-7, Fig. 4-8 and Fig. 4-9.

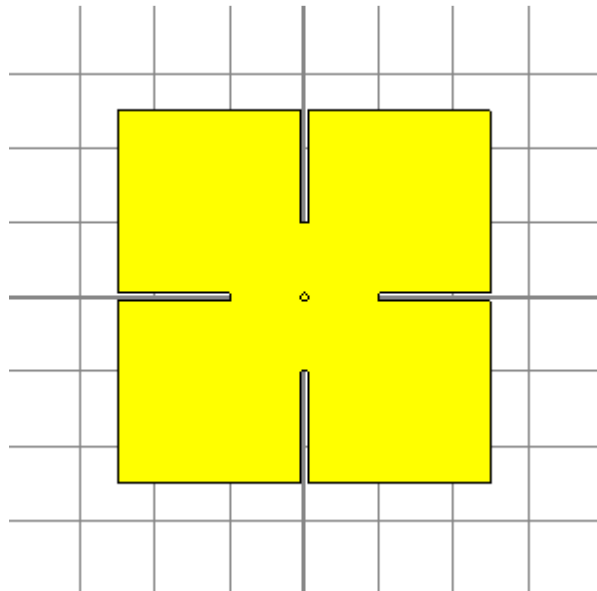


Fig. 4-7: 1st iteration of MLPF antenna in CST

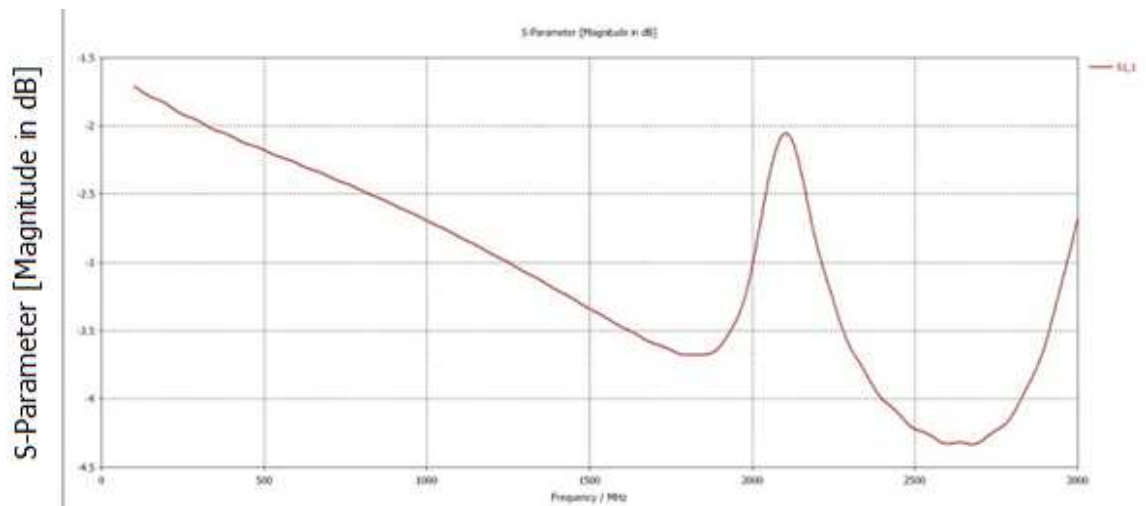


Fig. 4-8: S11 against frequency for the simulated 1st iteration of MLPF antenna

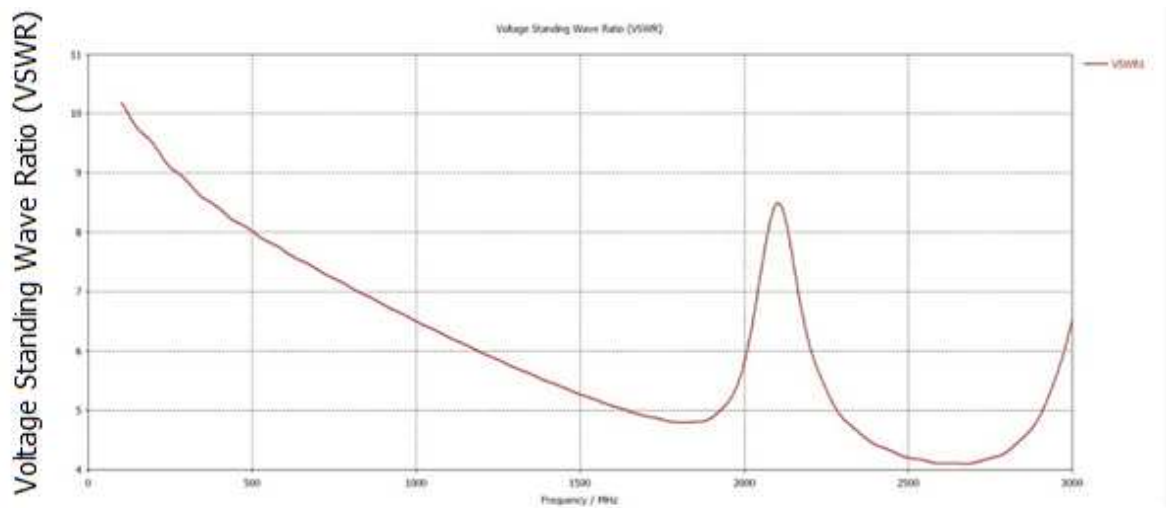


Fig. 4-9: VSWR against frequency for the simulated 1st iteration of MLPF antenna

Since there was no harmonic near to required frequency 870 MHz the location of the coaxial feed was shifted 10 mm horizontally. Harmonics of 1022.2 MHz, 2141.6 MHz and 2741.9 MHz were observed. Radiation patterns for said frequencies are shown in Fig. 4-12, Fig. 4-13 and Fig. 4-14. 1D results are shown below in Fig. 4-10 and Fig. 4-11.

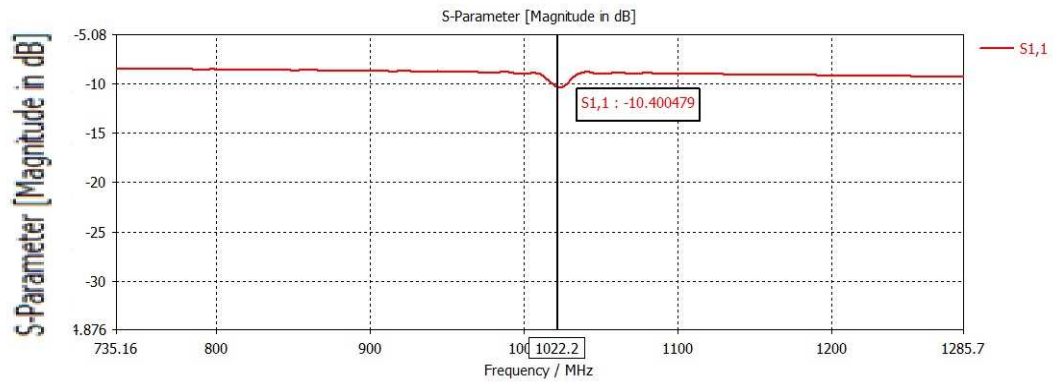


Fig. 4-10: Coaxial port was shifted to get a blip near to 870 MHz, resonating at 1022.2 MHz with $S_{11} = -10.4$ dB

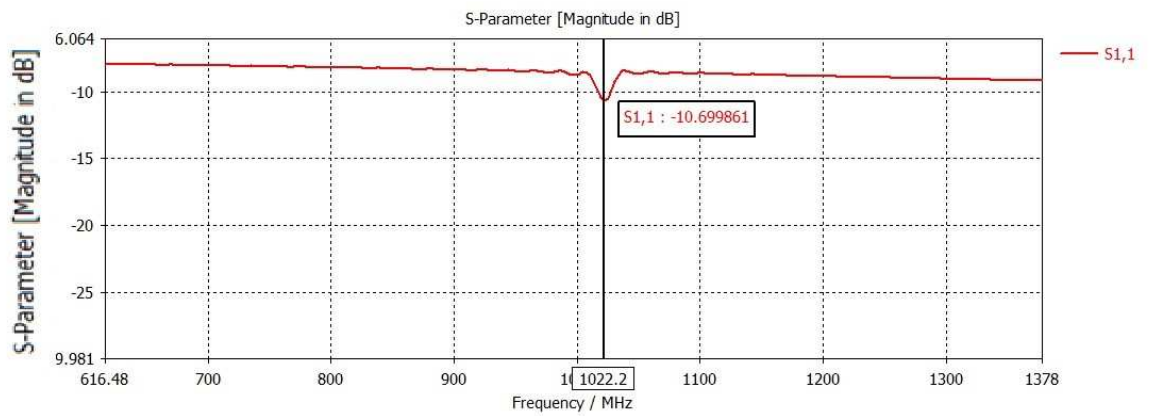


Fig. 4-11: Coaxial port was shifted to get a blip near to 870 MHz, resonating at 1022.2 MHz with $VSWR = 1.8652$

Farfield radiation patterns for frequencies $f=1022.2$ MHz, 2141.6 MHz and 2741.9MHz are shown below in Fig 4-12, Fig 4-13 and Fig 4-14 respectively

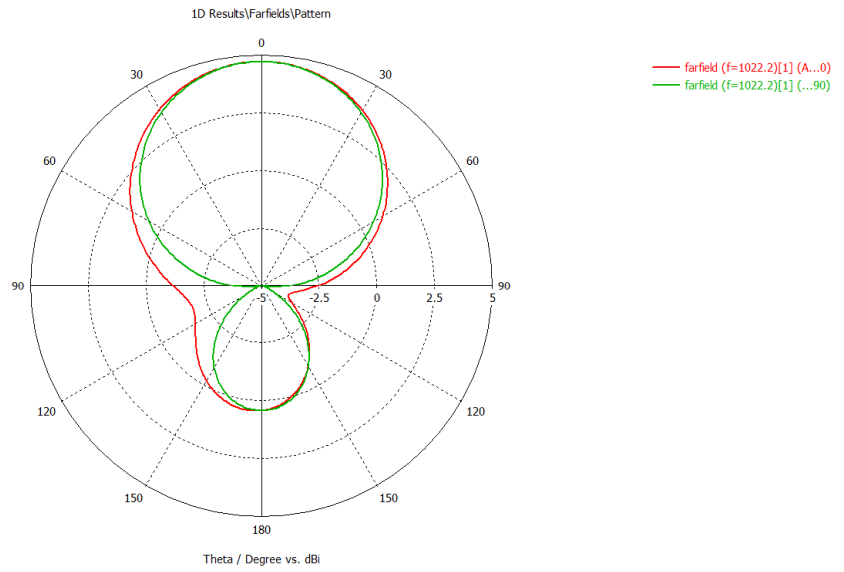


Fig. 4-12: E (Absolute) Farfield radiation pattern for frequency $f=1022.2$ MHz

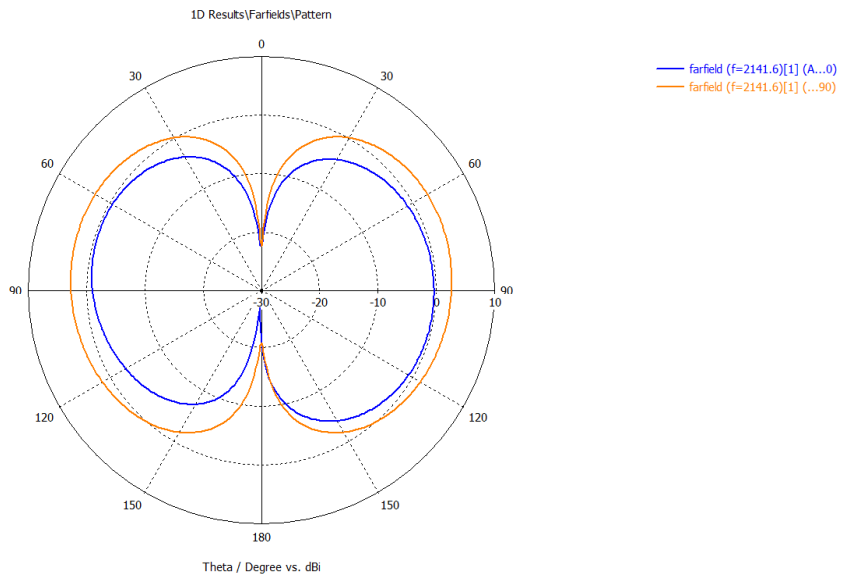


Fig. 4-13: E (Absolute) Farfield radiation pattern for frequency $f= 2141.6$ MHz

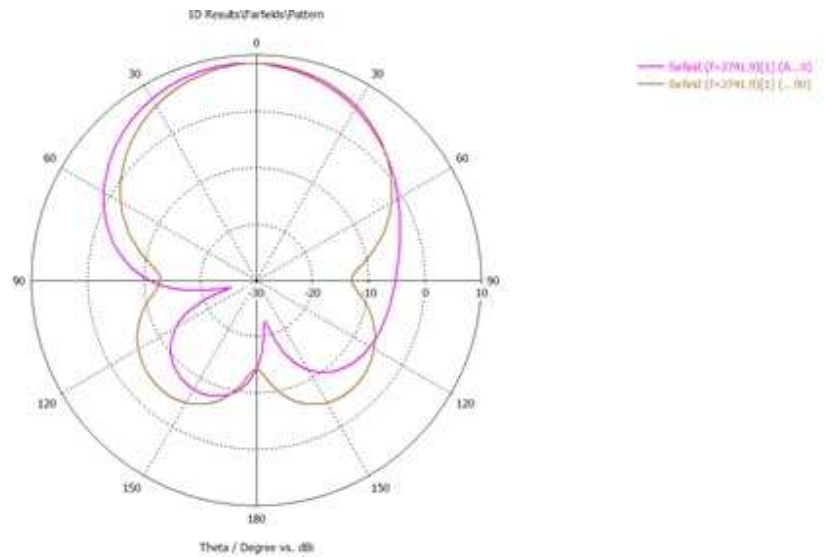


Fig. 4-14: E (Absolute) Farfield radiation pattern for frequency $f= 2741.9$ MHz

Since radiation pattern at $f=1022.2$ MHz promises a pencil beam radiation pattern said harmonic is picked for further tuning. The reflection coefficient S_{11} at $f=1022.2$ MHz is -10.4 dB.

The coaxial port was shifted horizontally to the following values, as shown in Table 4-3.

Table 4-3: Variation in Resonant Frequency, S_{11} and VSWR with Coaxial port coordinate

Coaxial coordinate	Resonant Frequency	S_{11} (dB)	VSWR
(12,0)	1022.2 MHz	-10.7	1.82
(8,0)	1025.1 MHz	-9.67	1.97
(15,0)	1019.3 MHz	-12.03	1.66

The patch was rescaled using the following ratio formula

Since resonant frequency (f) is inversely proportional to the length (l) of the patch

$$f = \frac{k}{L}; \text{ where } k \text{ is a constant} \quad (27)$$

$$f_1 \times L_1 = f_2 \times L_2 \quad (28)$$

$$L2 = \frac{f1 \times L1}{f2} \quad (29)$$

$$L2 = \frac{1019.3 \times 50}{870} = 58.58 \text{ mm}$$

The coaxial port was shifted back to (12,0) since it intersects with the slot on the right. The patch was set to 59 mm and the resonant frequency resulted in 906 MHz closing up to 870 MHz. The results for 906 MHz are listed in Table 4-4.

Table 4-4: S11, VSWR and Directivity at 906 MHz

Frequency (MHz)	S11(dB)	VSWR	Directivity (dBi)
906	-9.7657	1.96	3.847

The radiation patterns for 906 MHz at phi=0 and phi=90 degrees are shown below in Fig. 4-15.

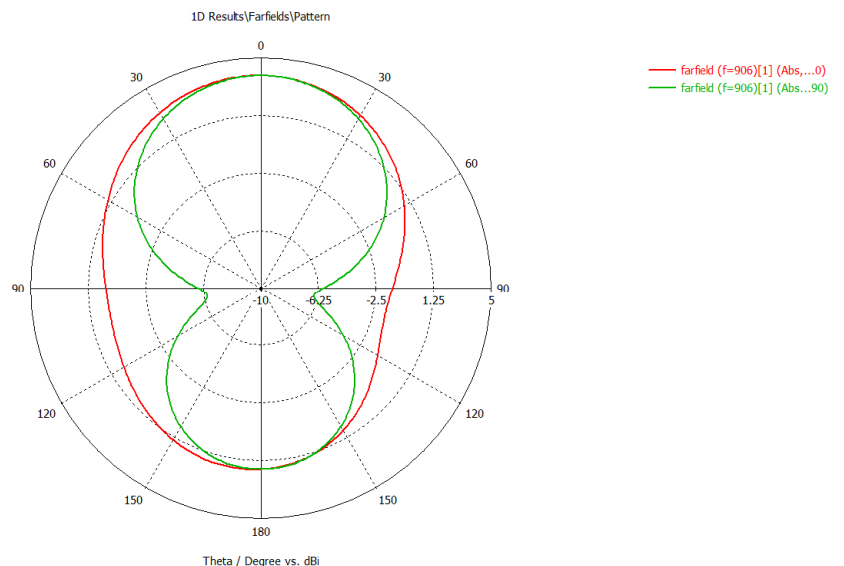


Fig. 4-15: E (Absolute) Farfield radiation pattern for 906 MHz at phi=0 and phi=90 degree cut

Surface currents for the simulated antenna are shown below in Fig. 4-16.

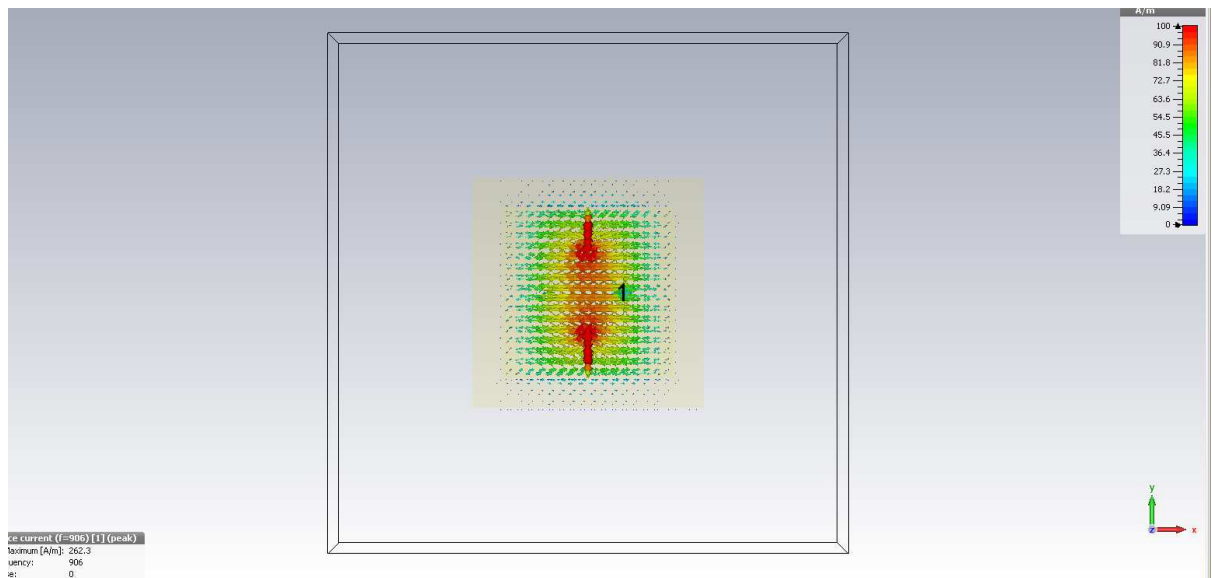


Fig. 4-16: Surface currents of the design showing linearly polarised antenna

Since MLPF fractal is connected to the edges, the total electrical length increases as the iteration goes higher. When electrical length is increased the resonant frequency is decreased. In order to increase the resonant frequency back to its desired value, the length should be increased hence resulting in miniaturisation. Therefore, in this particular fractal, as the iteration increases the antenna is supposed to be miniaturised. A 2nd iteration of the MLPF is considered and shown below with minor slots added with a length of 8 mm (MinorL) and the same width of 1 mm (MinorW). 2nd iteration is shown in Fig. 4-17 below.

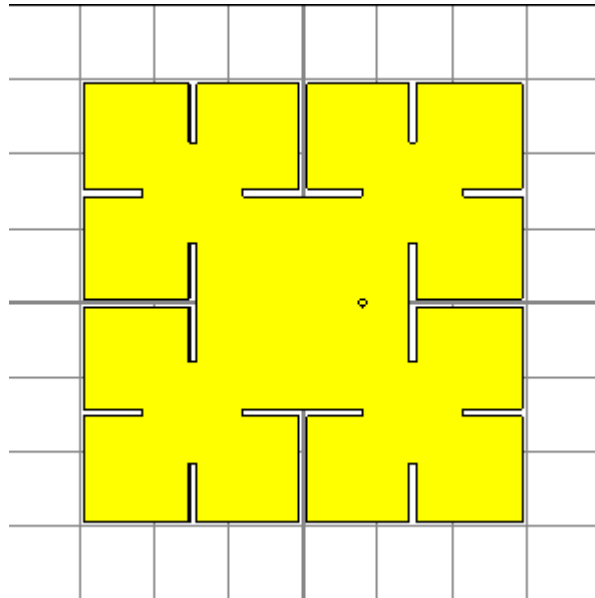


Fig. 4-17: 2nd iteration of MLPF antenna in CST

The coaxial port is shifted to 8 mm horizontally and with a patch size of 59 mm the antenna is simulated. The results are shown in Table 4-5.

Table 4-5: S11 and VSWR at 786 MHz in 2nd iteration of MLPF fractal antenna

Resonant Frequency (MHz)	S11 (dB)	VSWR
786.64	-9.56	2.01

The antenna had to be rescaled up twice using the ratio formula (28) and (29)

$$f1 \times L1 = f2 \times L2$$

$$L2 = \frac{f1 \times L1}{f2}$$

$$L2 = \frac{786.64 \times 59}{870} = 53.34 \text{ mm}$$

And since the frequency was 848.2 MHz, it had to be rescaled again using (29)

$$L2 = \frac{848.2 \times 53}{870} = 50 \text{ mm}$$

The simulation results are shown in Table 4-6.

Table 4-6: Antenna parameter with scaling of the patch size

Patch size	Resonant Frequency (MHz)	S11 (dB)	VSWR	Directivity (dBi)	Angular width(3dB) phi=0 degrees (degrees)	Angular width(3dB) phi=90 degrees (degrees)
53.3	848.2	-10.687	1.8256	4.525	133.4	94.5
50	885.9	-10.116	1.907	3.610	273	95.7

The farfield radiation patterns for both 848 MHz and 885.9 MHz are shown below in Fig. 4-18 and Fig. 4-19.

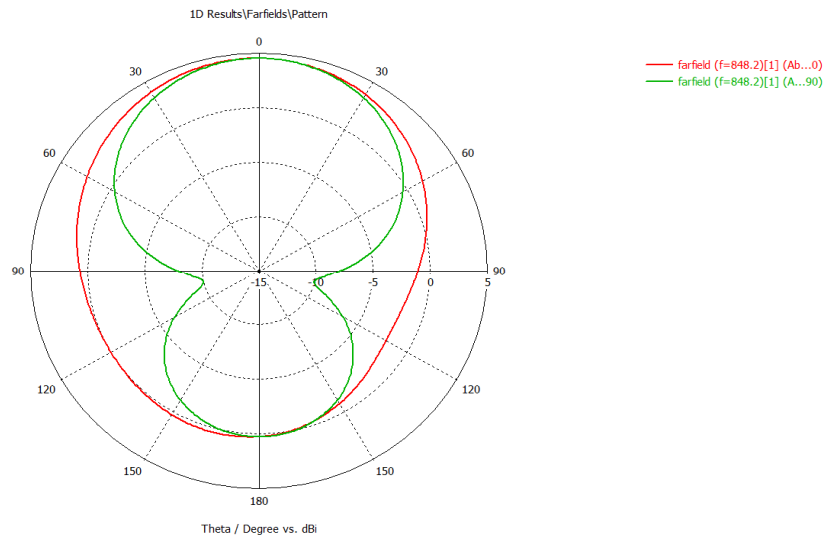


Fig. 4-18: E (Absolute) Farfield radiation pattern at 848.2 MHz both phi=0 and phi=90 degree cuts

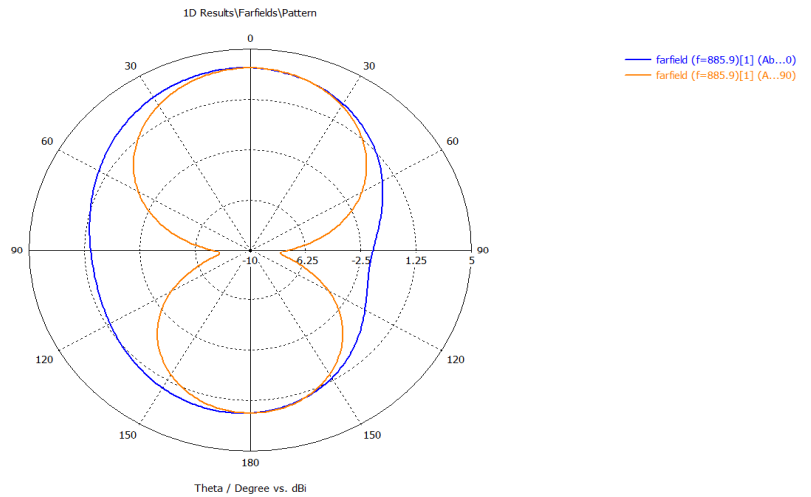


Fig. 4-19: E (Absolute) Farfield radiation pattern at 885.9 MHz both $\phi=0$ and $\phi=90$ degree cuts

The next iteration of the fractal is considered: here another length is introduced dividing the squares again into four, ($m_l=5$ and $m_w=0.5$). The modelled patch is shown in Fig. 4-20.

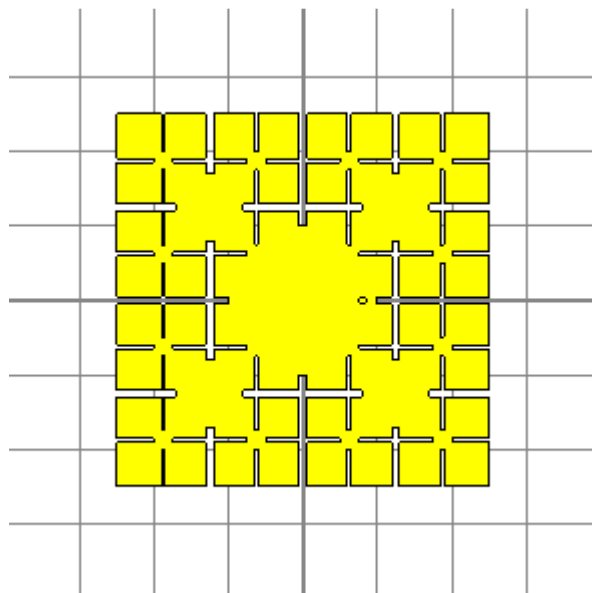


Fig. 4-20: 3rd iteration of MLPF antenna in CST

A drop in resonant frequency is observed as the electrical length of the antenna is increased. Resonant frequency = 807.6 MHz, thus giving the advantage to miniaturise the antenna.

The design is rescaled to tune the antenna back to 870 MHz by using equation (29)

$$L2 = \frac{807.6 \times 50}{870} = 46.4 \text{ mm}$$

Following is a manual tuning (done by trial and error) of the antenna by varying the patch size shown in Table 4-7.

Table 4-7: Resonant frequencies with patch size being scaled to obtain the required frequency

Square patch size	Resonant Frequency
50.0 mm	807.6 MHz
46.4 mm	851.1 MHz
45.0 mm	868.5 MHz

At 45 mm, the results are shown in Table 4-8.

Table 4-8: Antenna parameters when patch size = 46 mm

Patch size	Resonant Frequency (MHz)	S11(dB)	VSWR	Directivity (dBi)	Angular width(3dB) phi=0 degrees (degrees)	Angular width(3dB) phi=90 degrees (degrees)
45.0	868.5	-9.0502	2.09	3.534	264.7	96.5

Since the target of 868.5 MHz is achieved, the 2nd port for the antenna with a 90-degree time-phase shift is added.

The two coaxial port feeding is shown below in Fig. 4-21.

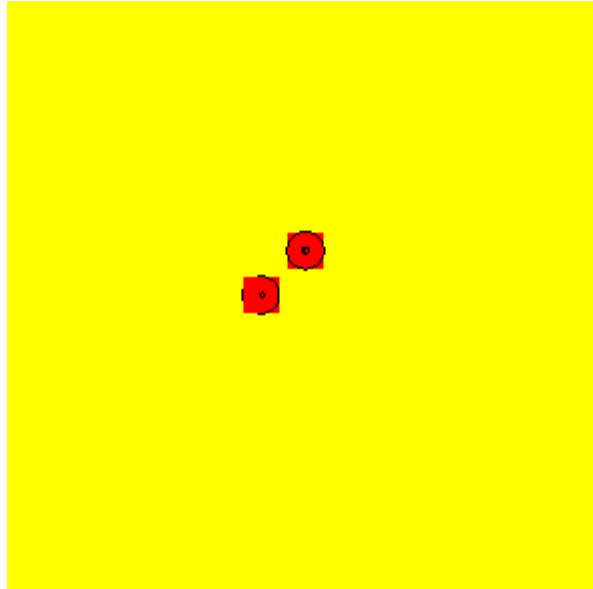


Fig. 4-21: Two coaxial feeding ports on the patch coming via ground plane and dielectric layer

The results are shown in Table 4-9.

Table 4-9: Antenna parameters for 868.5 MHz

Resonant Frequency (MHz)	S11(dB)	VSWR	Angular width(3dB) phi=0 degrees (degrees)	Angular width(3dB) phi=90 degrees (degrees)
868.5	-4.0806	4.3351	95.6	147.0

Radiation pattern at 868.5 MHz is shown in Fig. 4-22. The surface currents on the radiating patch are shown in Fig. 4-23 and the 3D beam of the antenna pattern is shown in Fig. 4-24.

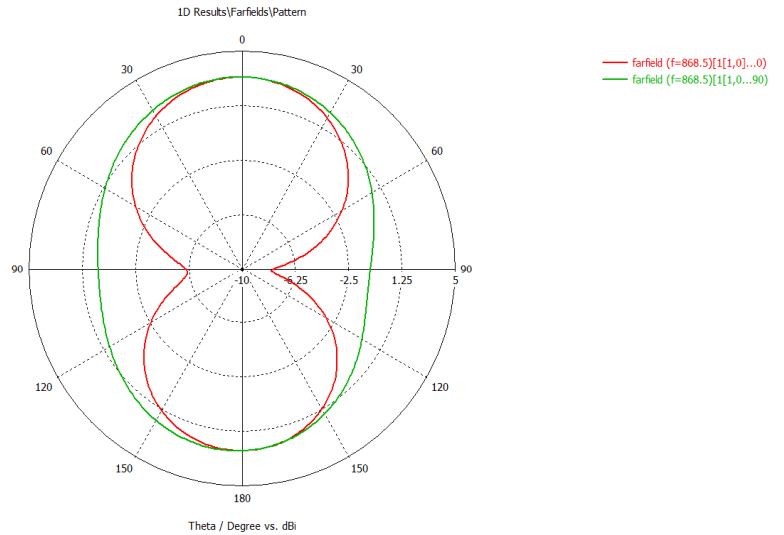


Fig. 4-22: E (Absolute) Farfield radiation pattern at 868.5 MHz both $\phi=0$ and $\phi=90$ degree cuts

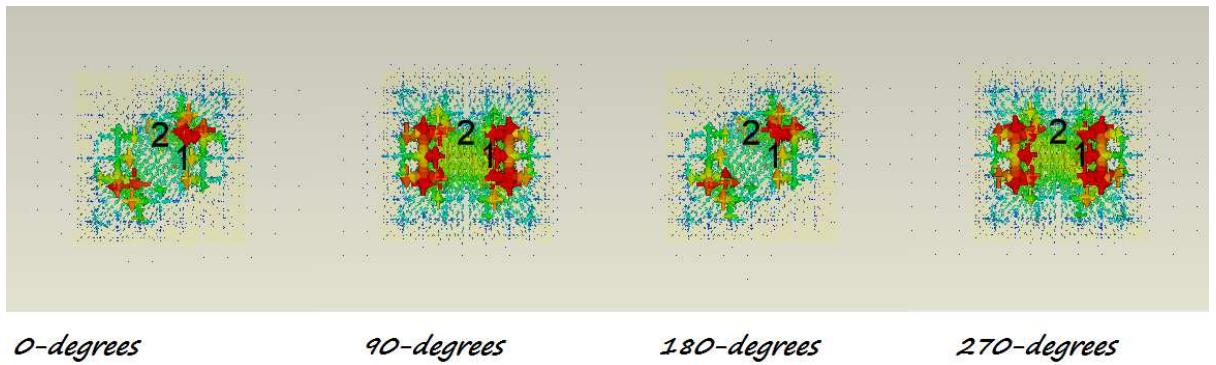


Fig. 4-23: Surface currents on the radiating patch showing circular polarised behaviour

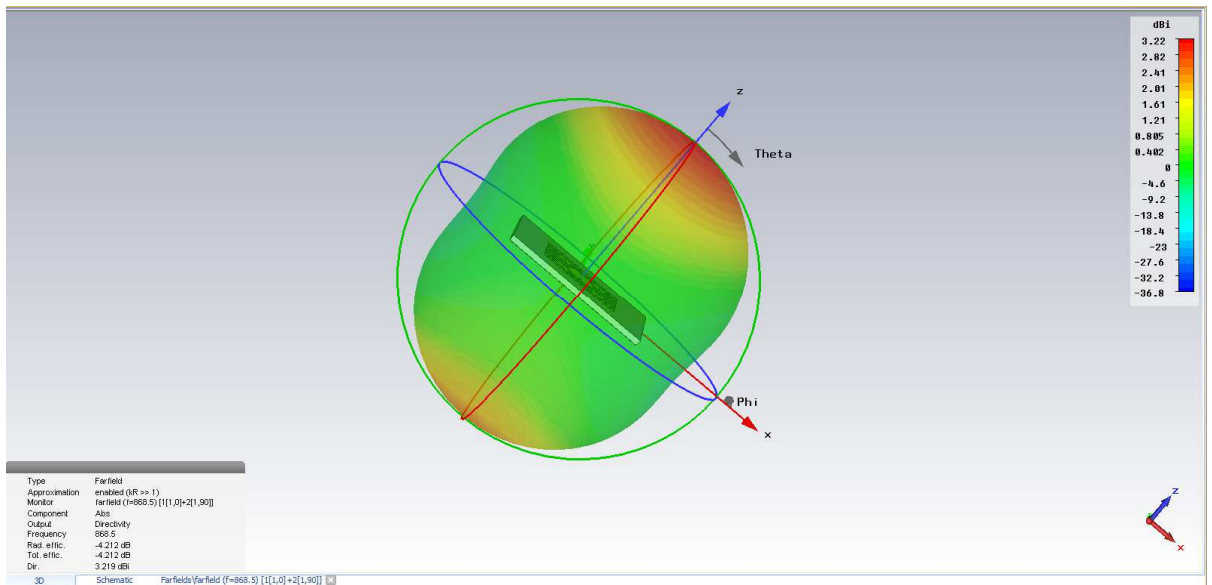


Fig. 4-24: Farfield 3D radiation pattern at 868.5 MHz

Looking at the radiation pattern on antenna, it can be noted that the antenna lacks directivity where there is power even in the back lobe. In order to rectify this, a copper wall is built around the antenna (5 mm tall, 1 mm thick) so that it will act as a reflector. This model is simulated with a two-port feeder, one arm having a delay of a quarter time cycle. The model with constructed copper wall is shown in Fig. 4-25.

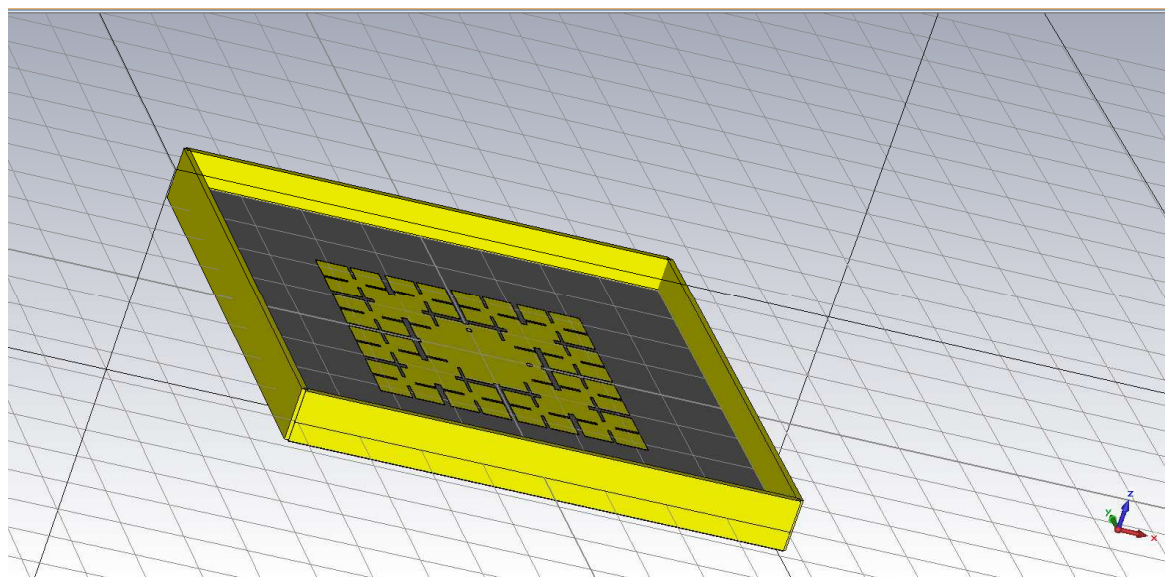


Fig. 4-25: Wall construction around the antenna

Crucial steps of tuning process are indicated below in Table 4-10. (the patch size, some lengths of slot in the iterations are varied)

Table 4-10: Variation of patch size, slot lengths, widths and coaxial coordinates with antenna parameters

Square patch size (mm)	Major L (mm)	Minor L (mm)	mL (mm)	COAX coordinate s (mm)	Resonant Frequency (MHz)	S11 (dB)	VSWR
45	15	8	5	6,0	848.2	-3.81	4.6302
43	12	8	5	8,0	917.0	Not read	Not read
44	12	7	4	8,0	926.5	-4.79	3.7150
44	12	8	4	6,0	903.3	-3.65	4.8250
45	12	8	4	6,0	891.7	-3.63	4.8513
46	12	9	4	6,0	859.8	-3.97	4.4549

The radiation pattern promises a smooth curved pencil beam radiation pattern circularly polarised with a directivity of 4.375 dBi. The beam width is nearly 100 degrees as required for application and is shown in Fig. 44. The 3D beam is shown in Fig. 4-26.

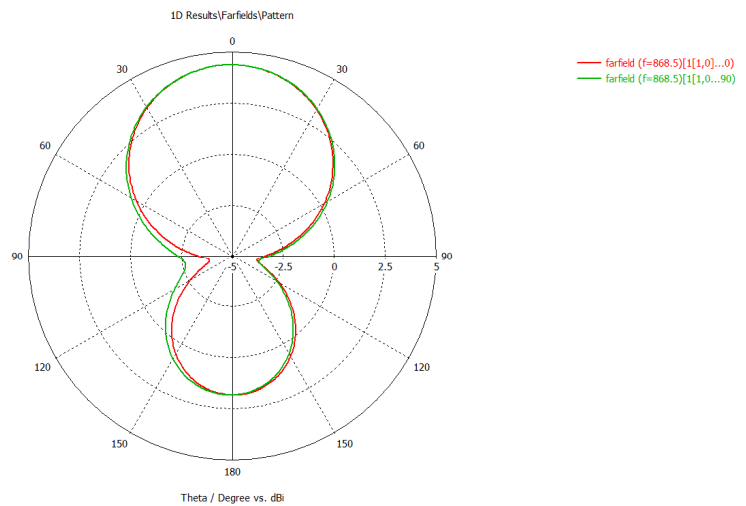


Fig. 4-26: E (Absolute) Farfield radiation pattern at 859 MHz both $\phi=0$ and $\phi=90$ degree cuts. The beam widths are shown in Table 4-11.

Table 4-11: 3dB beamwidths at 859 MHz both $\phi=0$ and $\phi=90$ degree cuts

3db angle at $\phi=0$	3db angle at $\phi=90$
102.4 degrees	105.4 degrees

3D radiation pattern is shown in Fig.4-27 below.

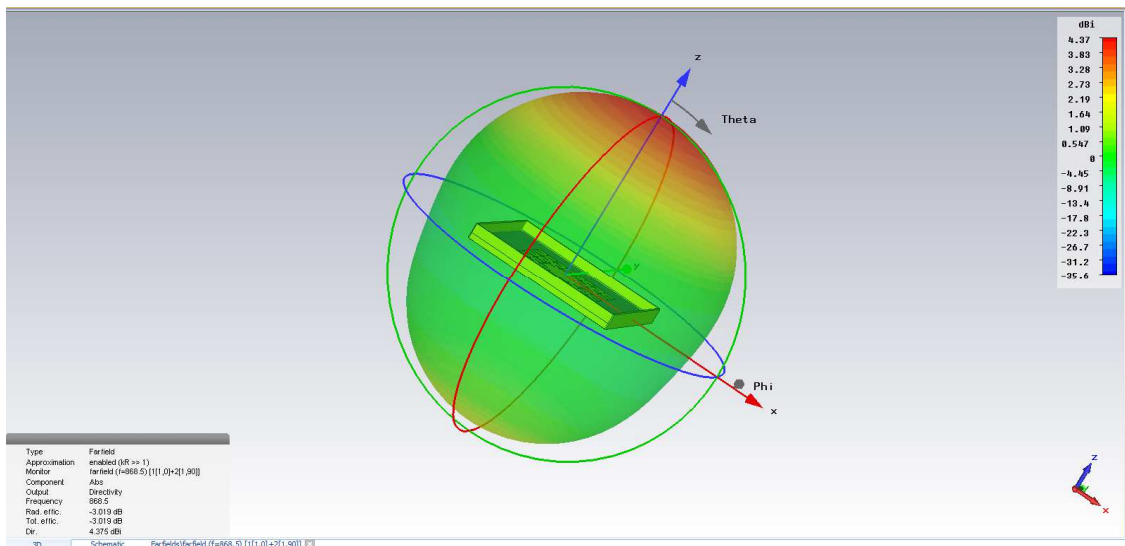


Fig. 4-27: 3D radiation pattern of antenna demonstrating a circularly polarised narrow directed beam

Though the antenna is tuned to 870 MHz with 100-degree beam width, there seems to be an apparent loss in the feeding ports of the antenna since an antenna should have a return loss (S11) of less than -10 dB. [32]

To rectify this, the coaxial ports with which the antenna is being fed needs to be re-designed for precision. The coaxial sheath has an outer core wire mesh which is not modelled in the design since CST is made to consider this as a waveguide port. This skin effect of the wire mech would increase the efficiency of the antenna feeds and hence will result in a better return loss of the antenna. A parameter *coaxthick* representing the outer wire mesh in the coaxial is added to CST environment with which it is simulated for different values. This is depicted in Fig. 4-28 below.

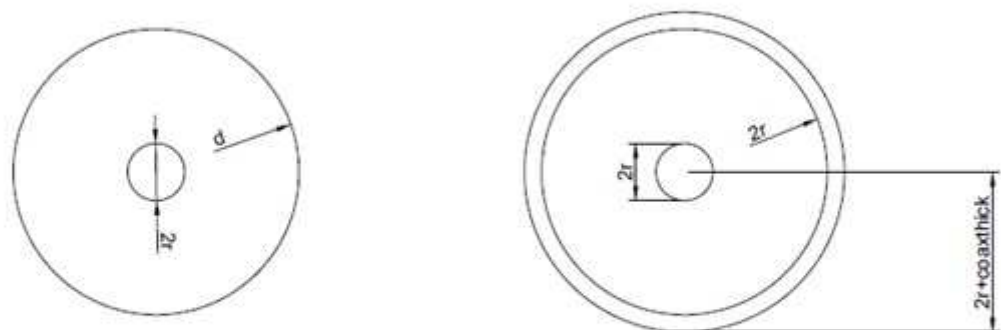


Fig. 4-28: Coaxial outer core added to coaxial ports

Some parameters were changed for optimisation of antenna. Variations and results are tabled below in Table 4-12.

Table 4-12: Changes in Coaxial wire mesh, copper wall height and thickness

Coaxthick (mm)	Copper wall height (mm)	Copper wall thickness (mm)	Patch size (mm)	S11(dB)	Resonant Frequency (MHz)
0.3	5	1	46	-11.4295	865.6
0.25	5	1	46	-11.4385	865.6
0.25	5	0.45	46	-13.0253	862.7
0.25	5	0.45	45	-13.0800	871.4
0.25	8	0.45	46	-12.3645	885.9
0.25	8	0.45	47	-10.98	880.1

When simulating in CST using the time domain solver, to obtain broadband results, the energy in the computational domain needs to be sufficiently decayed. Therefore to termination criterion of the transient (or time-domain) solver is based on the energy remaining in the computational domain. If the energy is not decayed sufficiently the accuracy of the simulation results suffer from truncation error. The CST training manual recommends for accurate S-parameters an accuracy of -40 dB or better. Therefore, the results are re-simulated for better accuracy with -30 dB and are tabled in Table 4-13.

Table 4-13: Re-simulating with high accuracy -30.0 dB

Coaxthick mm	Copper wall height mm	Copper wall thickness mm	Patch size mm	S11 dB	Resonant Frequency (MHz)	Angular width(3dB) phi=0 degrees	Angular width(3dB) phi=90 degrees
0.25	5	0.45	45	-11.9	874.3	104.6	104.8

The directivity of antenna is 4.444 dBi whilst VSWR is 1.5702 having a bandwidth of 5 MHz. The antenna efficiency for Maltese Cross fractal is 87%.

The fractional percentage bandwidth (FBW) of the antenna can be calculated as:

$$FBW = \frac{|f_H - f_L|}{f_c} \times 100 \quad (30)$$

$$FBW = \frac{875.25 - 870.91}{874.3} \times 100 = 0.496\%$$

The antenna is circularly polarised as the 3dB beam width differs only by 0.2 degrees (12 minutes). 1D results, farfield radiation patterns at resonant frequency and surface currents shown in Fig. 4-29, Fig. 4-30, Fig. 4-31, Fig. 4-32, Fig. 4-33 and Fig. 4-34.

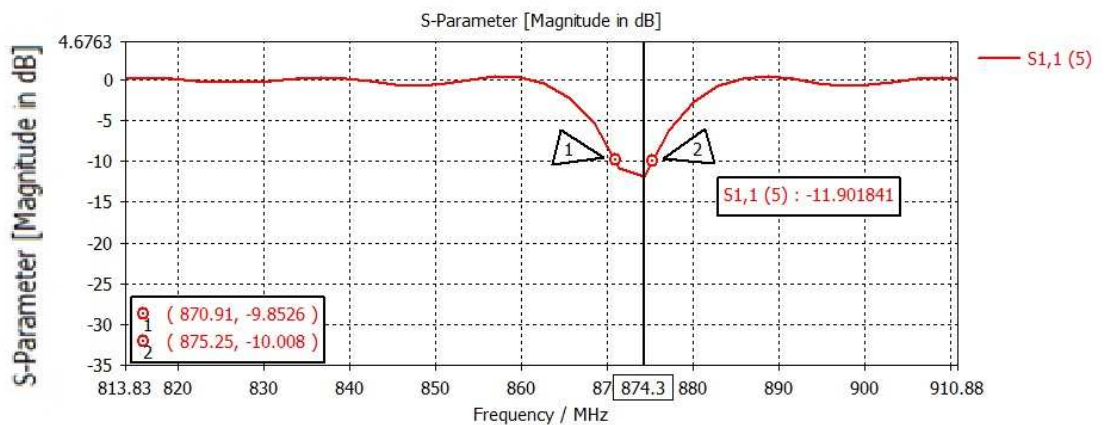


Fig. 4-29: S11 against frequency resonating at 874.3 MHz with bandwidth of 5 MHz

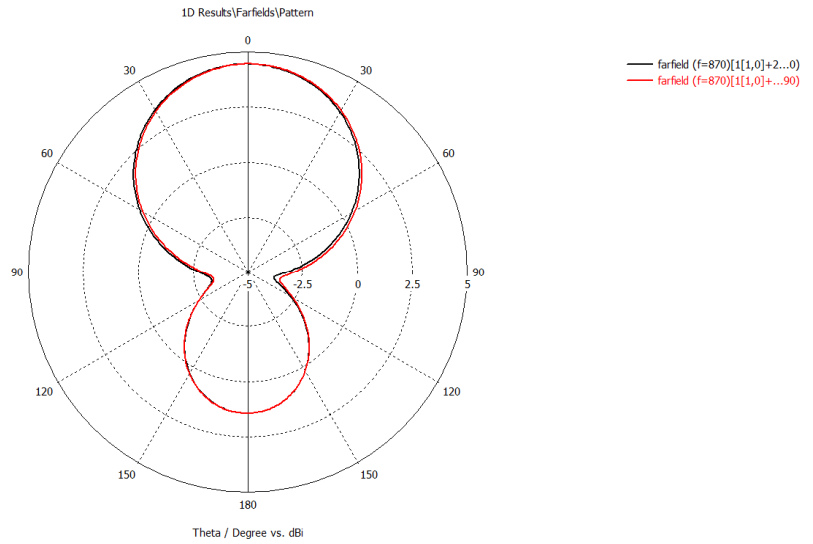


Fig. 4-30: E (Absolute) Farfield radiation pattern for 874.3 MHz at phi=0 and phi=90-degree cuts

E plane vertical (Co-polar cut) and horizontal (cross-polar) cut is shown in Fig. 4-31

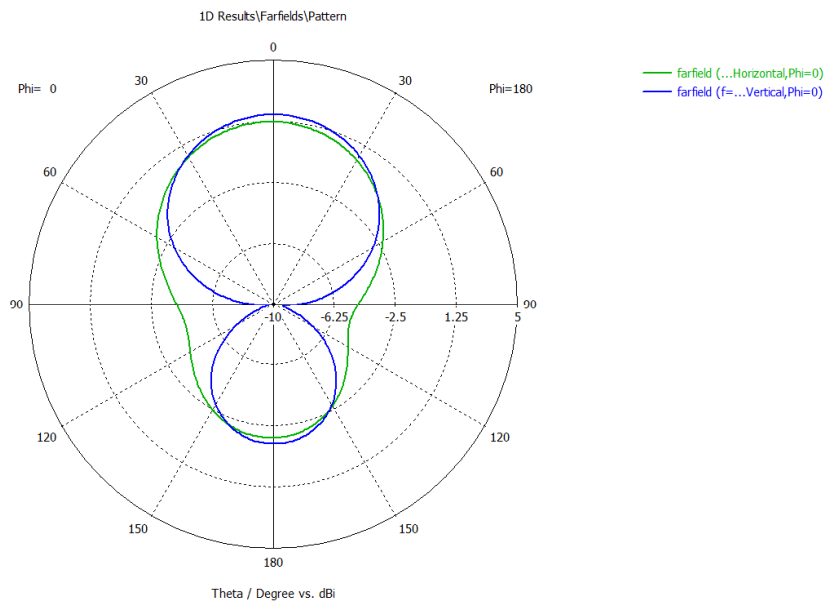


Fig. 4-31: E plane co polar and cross polar cuts on radiation pattern

H plane vertical (co-polar) and horizontal (cross-polar) cut is shown in Fig. 4-32

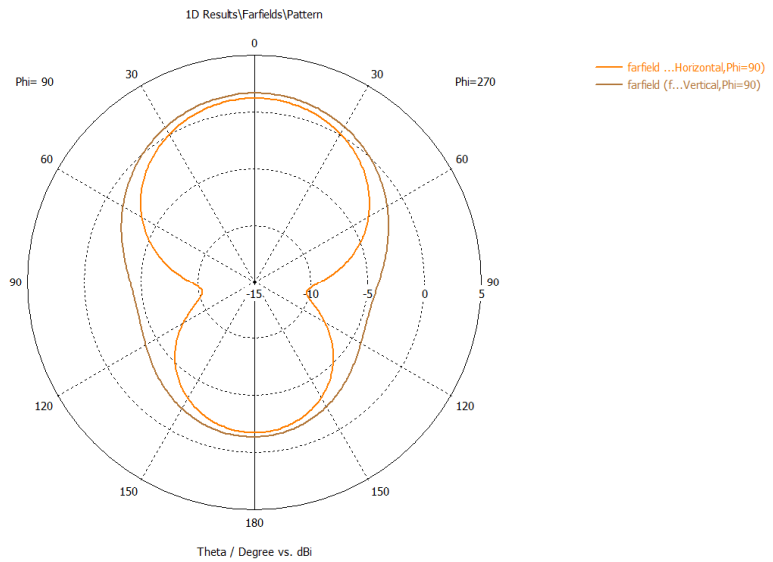


Fig. 4-32: H plane co polar and cross-polar cuts on radiation pattern

The 3D radiation pattern is shown in Fig. 4-33

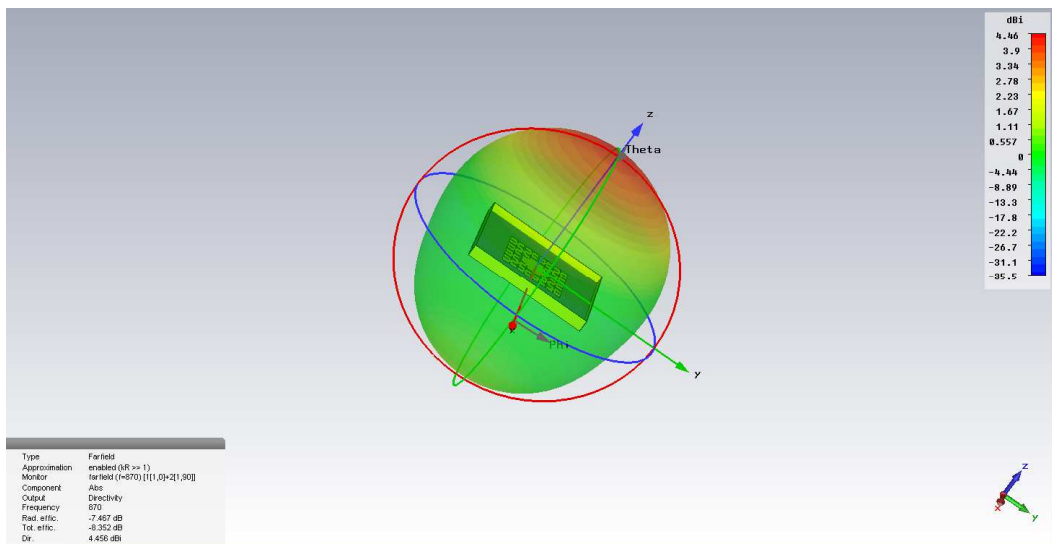


Fig. 4-33: 3D radiation pattern of final MLPF antenna

Surface currents of the patch are shown in Fig. 4-34.

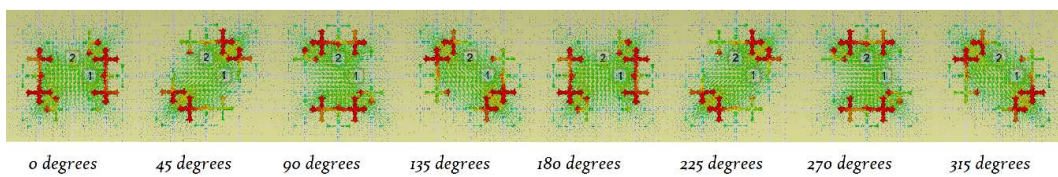


Fig. 4-34: Surface currents on patch

4.3 Tau Fractal based antenna

4.3.1 Introduction to the fractal and its construction

Tau fractal antenna comprises of T-shaped slots which are set in a manner that their bottoms meet perpendicular to each other. The squares which are formed within are then considered as the whole structure to apply the next iteration.

The Tau fractal can be constructed by first defining 4 T-shaped slots (where all 3 elements of the letter T have equal lengths) placed as shown in Fig. 4-35 below. The dimensions of the patch, its length in y direction P_y measured in millimetres and width in x direction P_x measured in millimetres. The length of an element of the T is named Fl measured in millimetres having a width of $2b$ measured in millimetres. The resulting gap due to the T bar perforated slots and the side of the patch is named Gap measured in millimetres. The proposed design for 1st iteration of the Tau fractal is shown in Fig. 4-35.

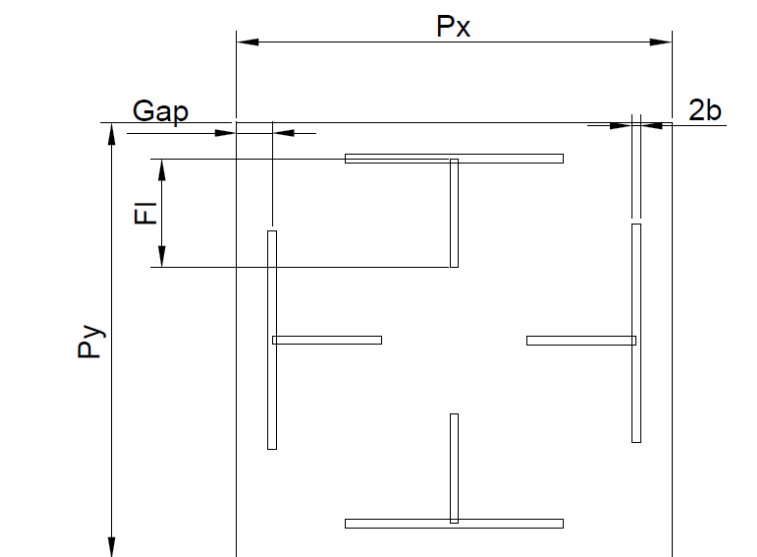


Fig. 4-35: Proposed 1st iteration of TAU fractal antenna

The 2nd iteration of the fractal can be constructed by considering the square formed by the T cross bar and the vertical and horizontal lines as shown in Fig. 4-36 below in 4

green squares. Said square is then considered to be the patch and the same pattern can be applied resulting in self-similar pattern and hence a fractal. This is shown in Fig. 4-36.

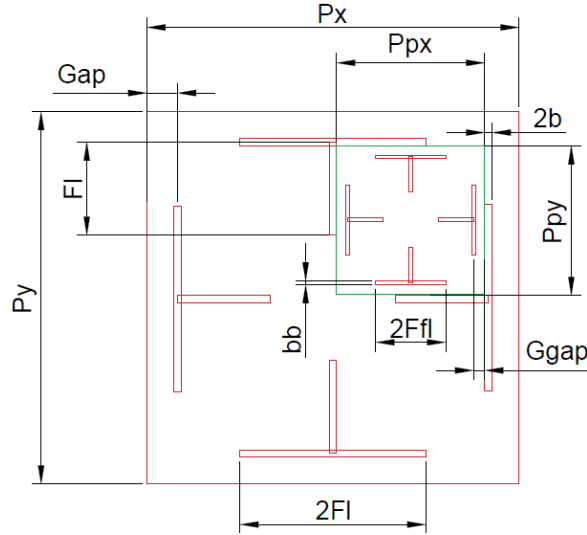


Fig. 4-36: Proposed 2nd iteration of TAU fractal antenna

The length and width being the same for the square formed by the 2nd iteration is named P_{px} measured in millimetres and can be given as

$$P_{px} = \frac{P_x}{2} - Gap_x - 2b \quad (31)$$

Where the gap is initially set to be a 1/12th of the full patch size.

$$Gap = \frac{P_x}{12} \quad (32)$$

The length of an element of the T bar is 1/4th of the patch size having a width of 1 mm.

$$Fl = \frac{P_x}{4} \quad (33)$$

The gap formed in the 3rd iteration is named G_{gap} measured in millimetres which is set to 1/12th of the squares resulting in the 2nd fractal

$$G_{gap} = \frac{P_{px}}{12} \quad (34)$$

The lengths of the T bars in the 2nd iteration F_{fl} measured in millimetres is set initially to 1/4th of the squares resulting in the 2nd fractal.

$$Ffl = \frac{Ppx}{4} \quad (35)$$

The widths of the T bars in the 2nd iteration are set to 0.5 mm.

The third iteration can be constructed by performing the same operation to the 16 blue resulting squares. This is shown in Fig. 4-37.

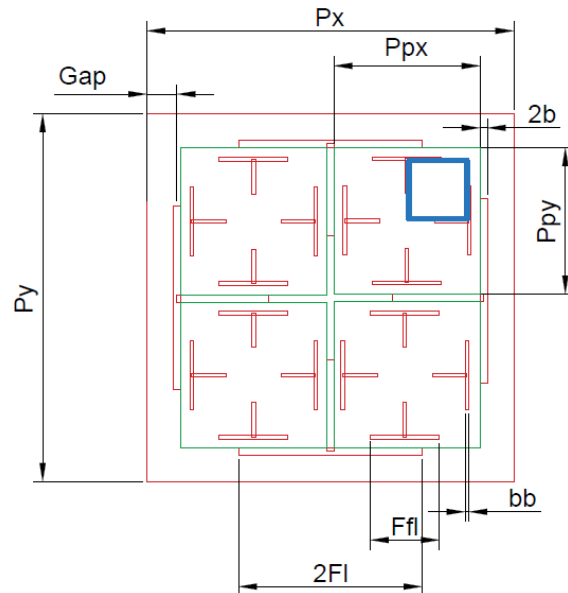


Fig. 4-37: Proposed 3rd iteration of TAU fractal antenna

4.3.2 Proposed Design and Simulation Results

Using the know how obtained in designing and simulation results from simulating MLPF antenna in 4.3.1, the Tau fractal antenna in its 3rd iteration was designed. The size of the square patch was set to 50 mm with coaxial ports set at (10 mm,0 mm). It has been noted that Tau fractal pattern's 2nd iteration slots acts as an obstacle for surface currents when the coaxial port is set to 10 mm. The modelled design on CST Microwave studio is shown in Fig. 4-38.

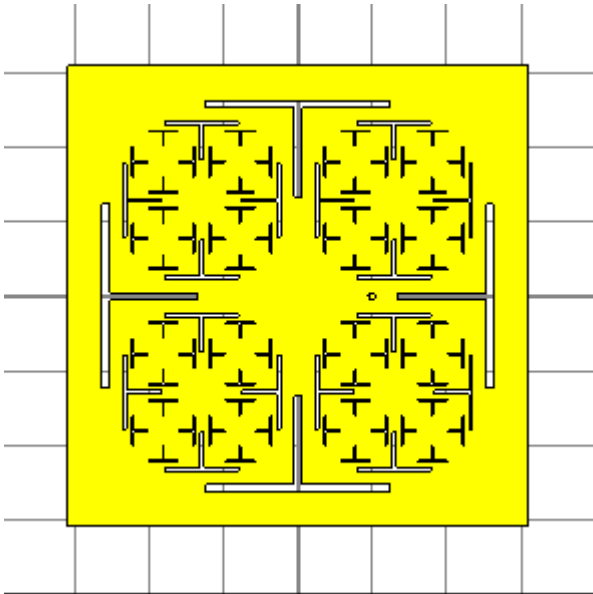


Fig. 4-38: 3rd iteration of TAU fractal antenna in CST

The resonant frequency occurred at 1090 MHz with an VSWR at 1.9662. Therefore, antenna fractal scaling ratio was used to enlarge the antenna to tune into 870 MHz. Also, the 2nd iteration of Tau fractal is considered with the coaxial port set at (5,0) mm. This is shown in Fig. 4-32. 1D results on VSWR against frequency is shown in Fig. 4-39.

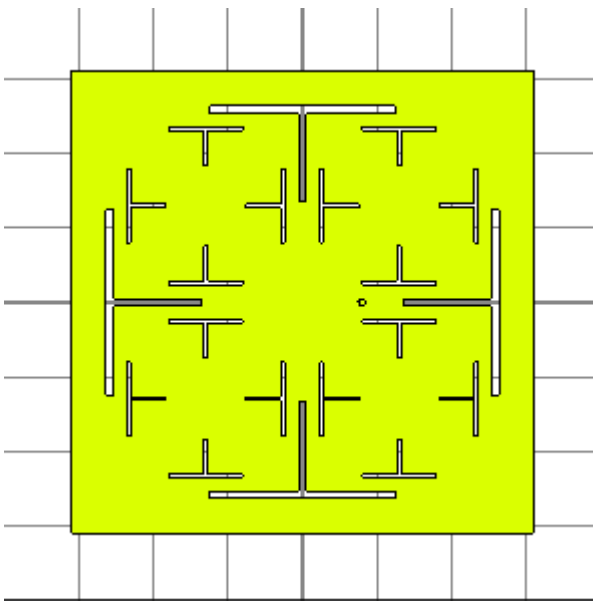


Fig. 4-39: 2nd iteration of TAU fractal antenna in CST

The following simulation results were obtained in the tuning process shown in Table 4-14. VSWR against frequency is shown in Fig. 4-40.

The following parameters are set for the table below:

A= Size of element as a factor of the patch

B= Size of elements of 2nd and 3rd iteration as a factor of the patch in 1st iteration

C= Gap of parasitic square from previous iteration as a factor of the patch in 1st iteration

P=Patch size

Fr=Resonant frequency

Table 4-14: Antenna parameters with varying dimension parameters to obtain a frequency close to 870 MHz

Fractal Iteration	Coaxial position (mm)	A	B	C	P (mm)	Fr (MHz)	S11 (dB)	VSWR
3 rd	(5,0)	¼	¼	1/12	50	1090.3	-9.74	1.9662
3 rd	(5,0)	¼	¼	1/12	62	906.2	-11.52	1.7217
2 nd	(0,0)	¼	¼	1/12	50	1990.8	Not read	Not read
2 nd	(5,0)	¼	¼	1/12	50	1097.6	-10.54	1.846
2 nd iteration	(5,0)	¼	¼	1/12	55	999.0	-9.15	2.06
2 nd	(10,0)	1/5	¼	1/12	55	1015.4	Not read	Not read
2 nd	(5,0)	1/5	¼	1/12	62	906.2	-10.31	1.878
3 rd	(8,0)	1/5	1/5	1/12	62	906.2	-11.08	1.773
3 rd	(10,0)	1/5	1/5	1/12	62	906.2	-11.53	1.722
3 rd	(10,0)	1/5	1/5	1/10	62	906.2	-11.22	1.758
3 rd	(10,0)	1/5	1/3	1/10	62	880.1	-10.86	1.8026

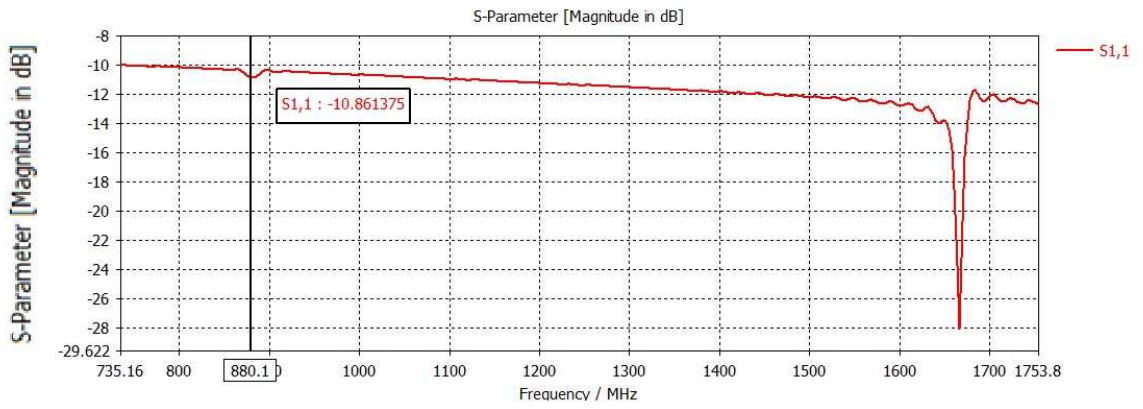


Fig. 4-40: S_{11} against frequency resonating at 880.1 MHz

The last result of the 3rd iteration fractal fed by a single port at (10,0) is as follows with the enlarged slots in the 2nd and 3rd iteration, is shown in Fig. 4-41.

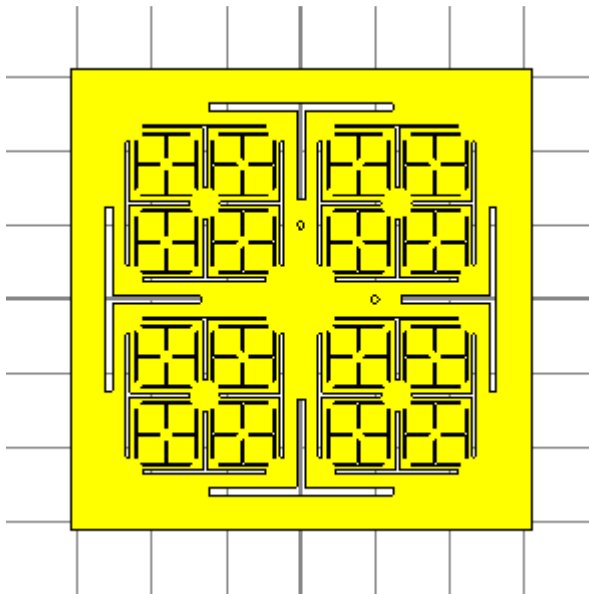


Fig. 4-41: 3rd iteration of TAU fractal antenna in CST

The antenna resulting parameters are shown in Table 4-15.

Table 4-15: Antenna parameters at 880.1 MHz

Resonant Frequency	S11	VSWR	Directivity	3dB Beamwidth at phi=0 degrees	3dB Beamwidth at phi=90 degrees
880.1 MHz	-10.86 dB	1.8026	3.730 dBi	97.6 degrees	136.5 degrees

A two-port feeder is used with a 90-degree time phase delay to simulate the third iteration of the antenna. The results are shown in Table 4-16.

Table 4-16: Antenna parameters when a two port 90 degree phase feeder is applied.

Resonant Frequency	S11	VSWR	Directivity	3dB Beamwidth at phi=0 degrees	3dB Beamwidth at phi=90 degrees
874.3 MHz	-4.0769	4.3300	3.6570 dBi	98.8 degrees	126.7 degrees

The resulting radiation patterns are shown below with surface currents on the circularly polarised patch. The low directivity of the antenna is noted. The radiation pattern is shown in Fig. 4-42.

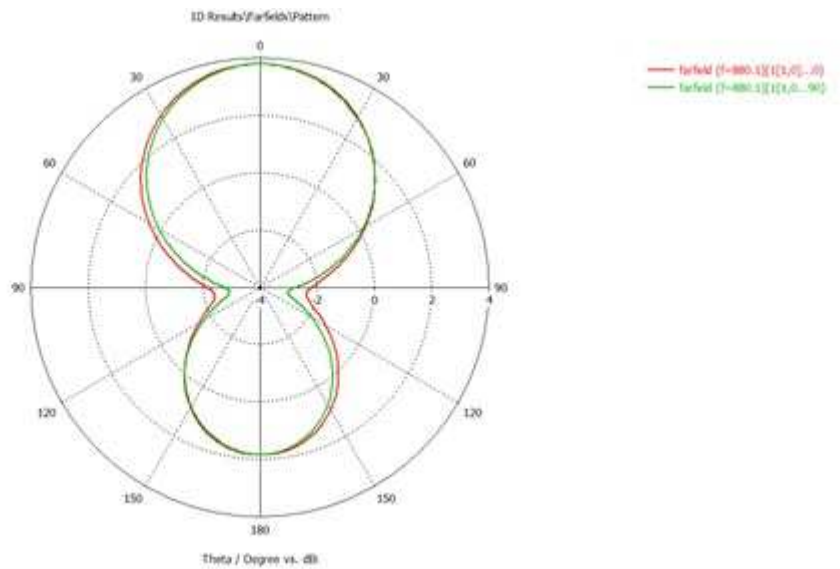


Fig. 4-42: E (Absolute) Farfield radiation pattern at 874.3 MHz both at $\phi=0$ and $\phi=90$ degree cuts

Since there is a drop in directivity of the antenna as performed in MLPF, a wall of 5 mm height and 1 mm of thickness is built around the antenna to improve its directivity by reflecting the back lobe towards the propagating direction. This is shown in Fig. 4-43 and Fig. 4-44.

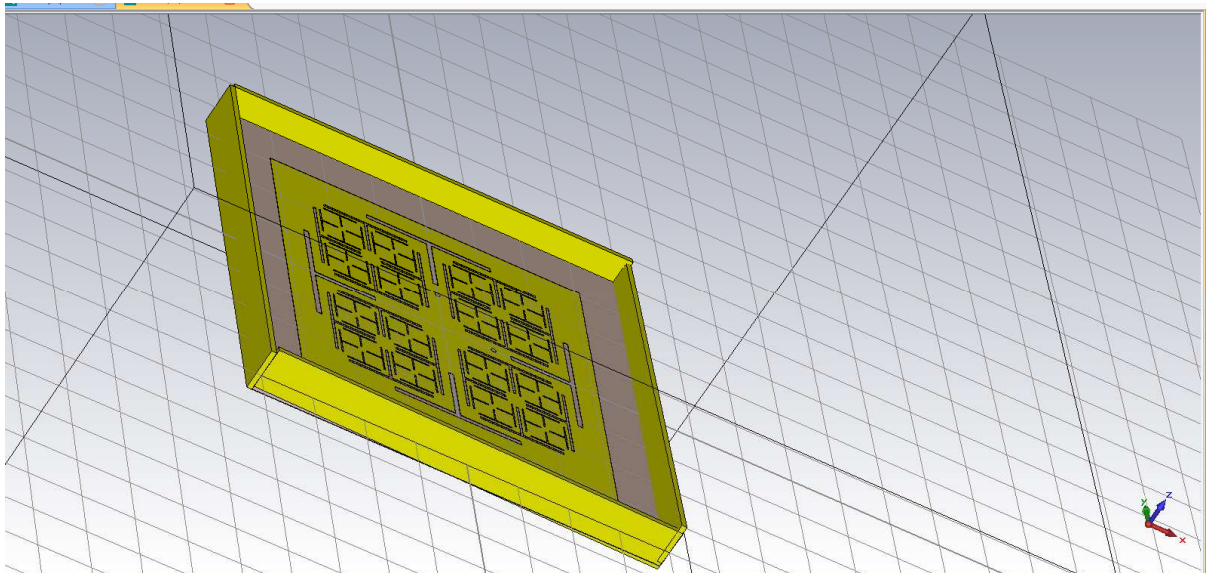


Fig. 4-43: Wall construction around the antenna

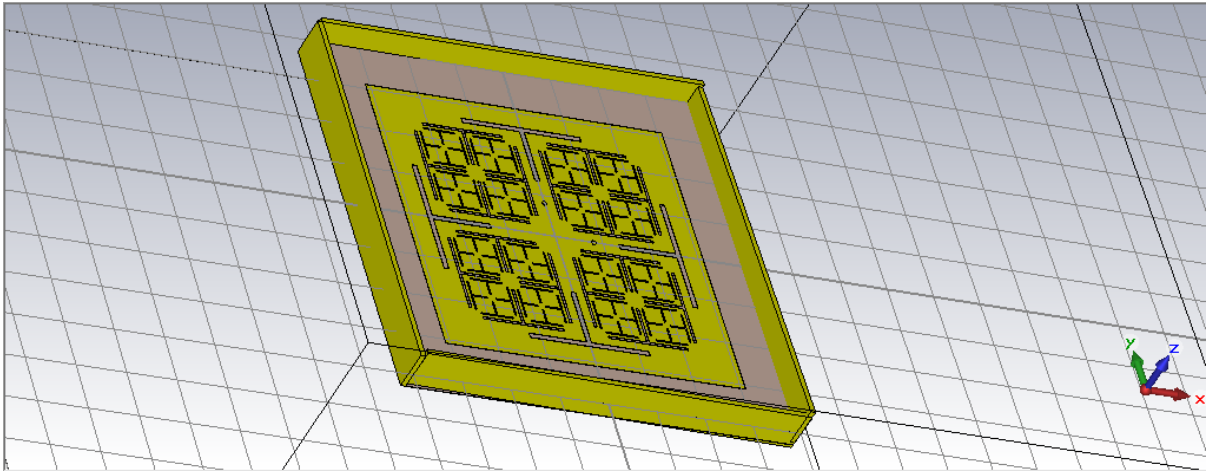


Fig. 4-44: Wall construction of Tau fractal antenna

The results for the model with wall construction are shown in Table 4-17.

Table 4-17: Results for the model with wall construction.

Resonant Frequency	S11	VSWR	Directivity	3dB Beam width at phi=0 degrees	3dB Beam width at phi=90 degrees
877 MHz	-9.7227	1.9695	4.836 dBi	108.5 deg	104.2 deg

The radiation patterns for design are shown below with surface currents providing a circularly polarised beam. The directivity has improved from 3.6570 dBi to 4.836 dBi due to the copper wall surrounding the antenna structure. The radiation pattern and -3dB beam are shown in Fig. 4-45 and Fig. 4-46. The surface currents on the radiating patch is shown in Fig. 4-47.

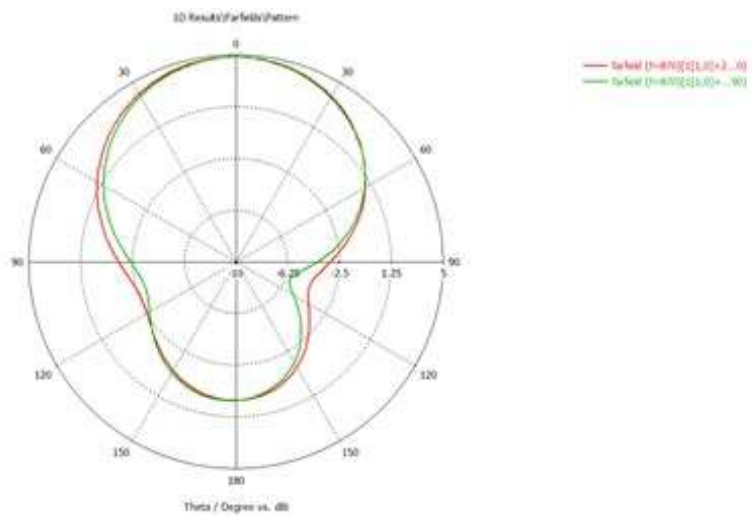


Fig. 4-45: E (Absolute) Farfield radiation pattern at 877 MHz with copper wall

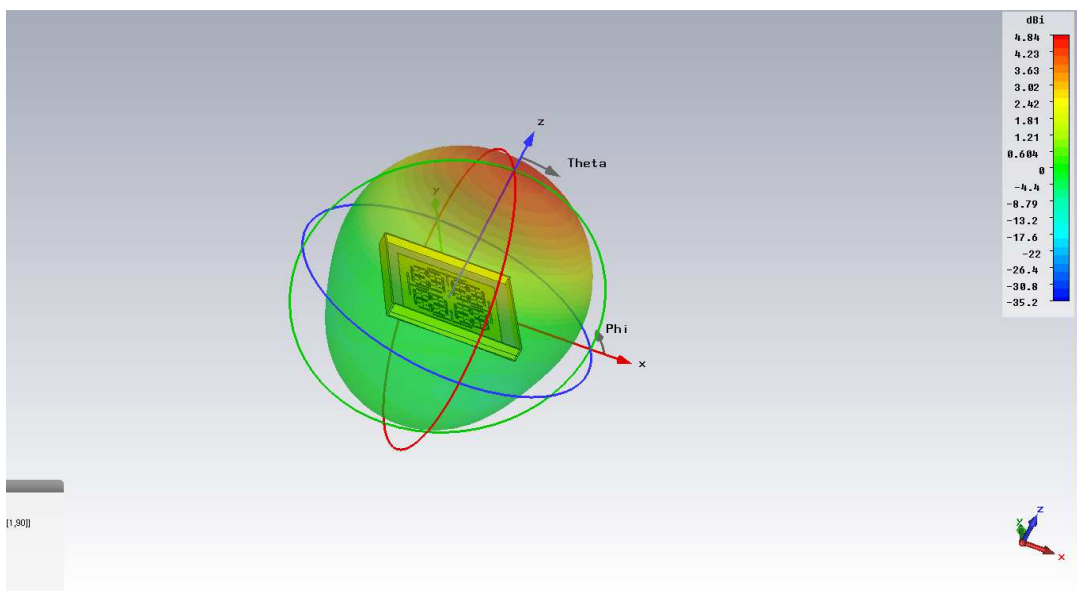


Fig. 4-46: 3D radiation pattern at 877 MHz with copper wall

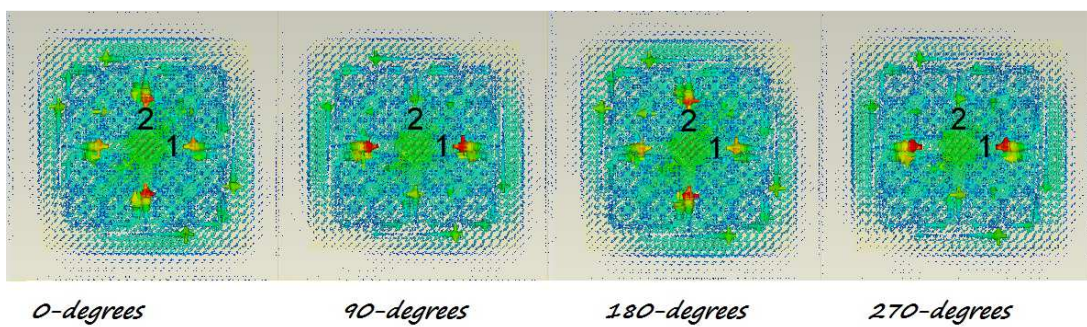


Fig. 4-47: surface currents at 877 MHz demonstrating circular polarisation

With the same patch size of 62 mm, in order to increase the antenna efficiency, it necessitates to get the return loss (S11) below -10 dB. The coaxial port is re-designed with a coaxial mesh around as performed in MLPF design. Since the Tau fractal's vertical bar in T acts as a buffer to the coaxial ports, it needs to be deviated away from them. This resulted in drastic improvement of return loss. However, this has created an elliptically polarised radiation pattern thus making the difference of two 90-degree cuts over 9 degrees. The results are tabled below in Table 4-18.

Table 4-18: Variation of coaxial port location

Copper wall height	Copper wall thickness (mm)	Coax port coordinate	Resonant Frequency (MHz)	Return loss S11 (dB)	3dB Beam width at phi=0 degrees	3dB Beam width at phi=90 degrees
5	0.45	(8,8)	871.4	-8.5798	113	102.2
5	0.45	(6,6)	877.2	-16.766	112.3	103

Since ports are too close to 1st and 2nd iterations of Tau fractal bars, changes in surface currents should be done by altering dimensions of the 3rd iteration. Increasing cross T bars of the 3rd iteration by a multiple of 1/5 from 1/3 in tau fractal increases resonant frequency of the patch antenna thus making miniaturisation more demanding. The width of the cross bar of the T in 3rd iteration apparently contributes very little to resonant frequency. The simulations are tabled below in Table 4-19.

Table 4-19: Variation of 3rd iteration dimensions and ground plane

Patch size (mm)	Ground plane size(mm)	F3l iteration fractal alteration factor	3 rd slot width (mm)	B3 iteration fractal slot width (mm)	Return loss S11 (dB)	Resonant frequency (MHz)
62	80	1/5	0.125	-18.4202	888.8	
62	80	1/5	0.25	-18.16535	891.7	
63	80	1/3	0.25	-15.00471	859.8	
63	85	1/3	0.25	-14.1817	865.6	

With high accuracy for -30 dB dissipated Gaussian pulse time, the following results were achieved as tabled in Table 4-20.

Table 4-20: Tau fractal antenna results

Resonant Frequency (MHz)	Return loss S11 (dB)	Directivity (dBi)	VSWR	3dB Beam width at phi=0 degrees	3dB Beam width at phi=90 degrees
865.6	-14.1817	4.400	1.4856	106.0	105.1

The antenna is circularly polarised with a 0.9 degree 54 minute difference from E and H plane. Return loss is -14.18 dB with a bandwidth of 5 MHz is resulted in simulations. The antenna efficiency for Tau fractal is 86%. The fractional percentage bandwidth (FBW) of the antenna can be calculated using (30) as

$$FBW = \frac{|f_H - f_L|}{f_C} \times 100 = \frac{868.72 - 863.72}{865.6} \times 100 = 0.577\%$$

Return loss S11, farfield radiation patterns are shown below in Fig. 4-48 and Fig. 4-49 to Fig. 4-52.

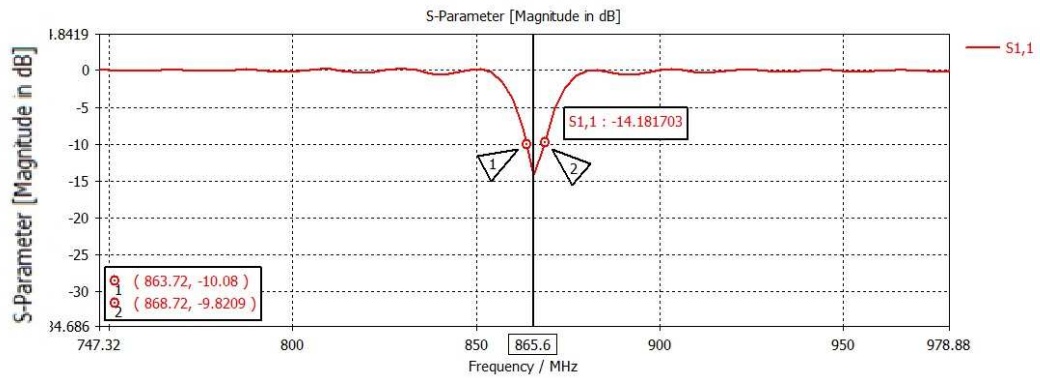


Fig. 4-48: S11 against frequency defining bandwidth of 5 MHz

E plane radiation pattern both co polar and cross polar cuts are shown in Fig. 4-49

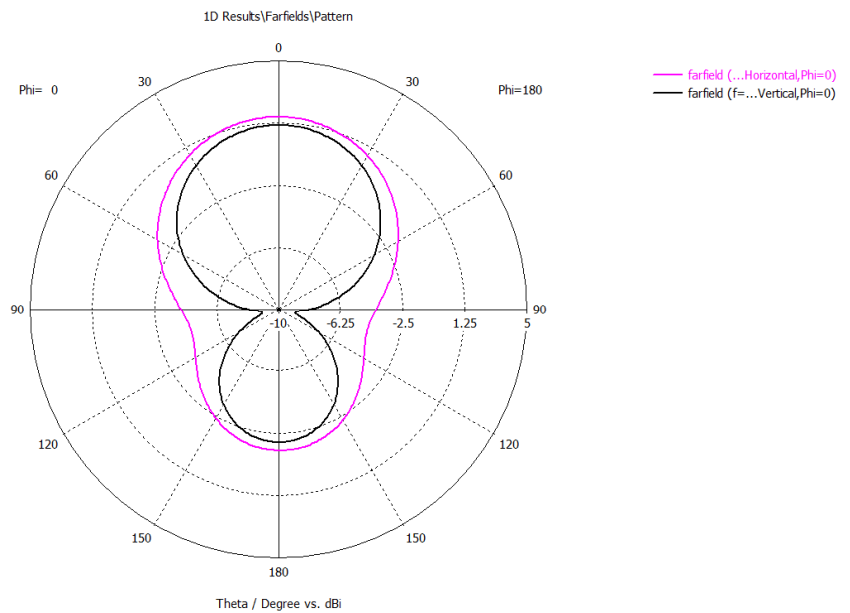


Fig. 4-49: E plane co-polar and cross-polar cuts

H plane radiation pattern both co and cross polar cuts are shown below in Fig.4-50

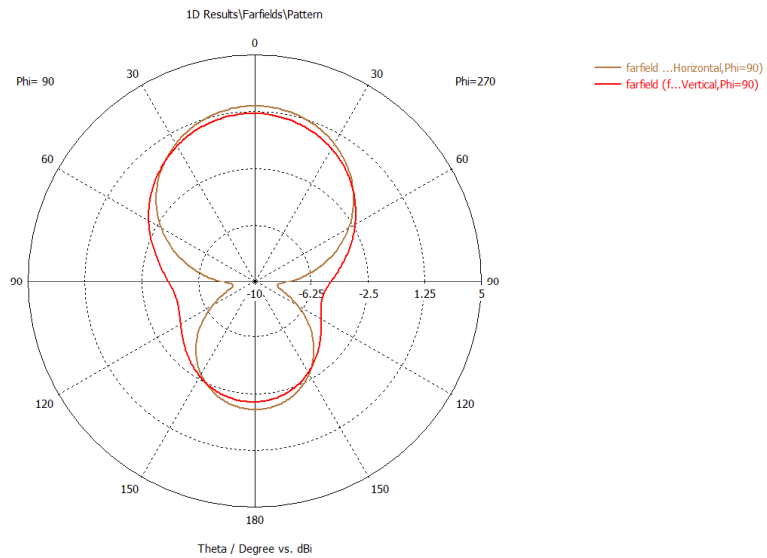


Fig. 4-50: H plane co and cross polar cuts

3D radiation pattern is shown in Fig. 4-51

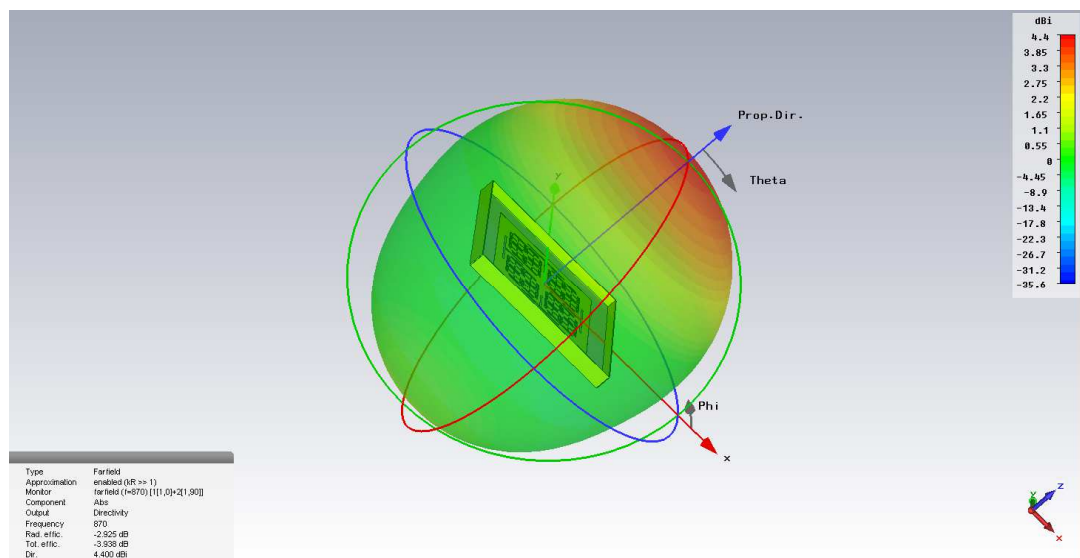


Fig. 4-51: 3D radiation pattern of TAU fractal antenna

Surface currents for Tau fractal antenna is shown in Fig. 4-52

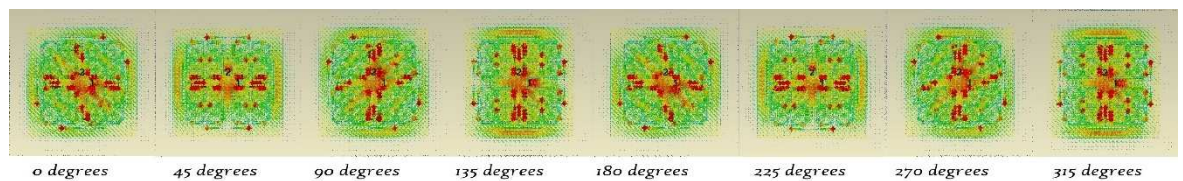


Fig. 4-52: Surface currents on Tau fractal antenna

4.4 Space Filling Tree (SFT) Fractal Antenna

4.4.1 Introduction to the fractal and its construction

Space filling tree also known as the cross-bar fractal is a diagonal length with branching tree-like structure. This is defined by the incremental lengths added to each iteration at each ends. This is much commonly used in Frequency Selective Surface (FSS) applications but also used as the radiating element.

The Space Filling Tree [SFT] or cross bar fractal extends itself from its extremities as shown in Fig. 4-53.

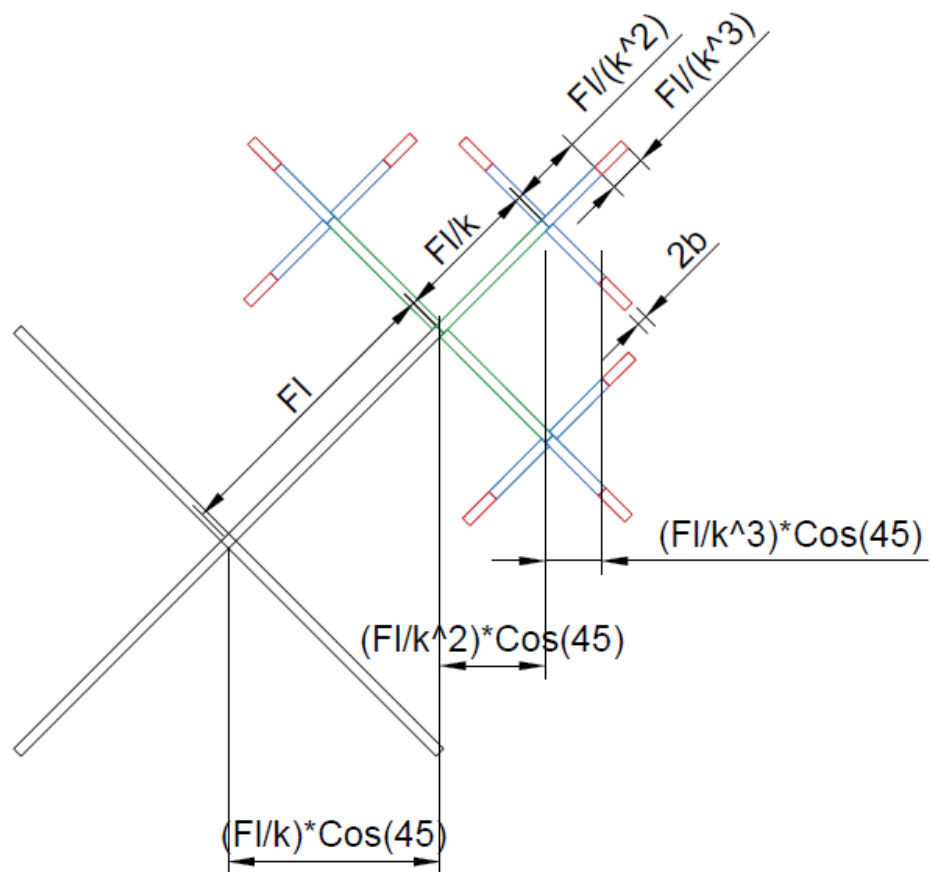


Fig. 4-53: Proposed fractal arm slot with dimensions

The dimensions of the patch, its length in y direction P_y measured in millimetres and width in x direction P_x measured in millimetres. The slot lengths are set to $2b$ measured in millimetres. The section of a length of a bar is set to length FI measured in millimetres

and it's incremented by adding an element which is of a fraction $(1/k)$ of its previous length. Hence the increments will be

$$Fl, \frac{Fl}{k}, \frac{Fl}{k^2}, \frac{Fl}{k^3}, \dots, \frac{Fl}{k^{n-1}} \quad (36)$$

Since the nature of the fractal Space Filling Tree (SFT) or cross bar fractal the two bars cross the two coaxial ports, thus blocking the surface currents and hence effective radiation from the antenna. This is shown in Fig. 4-54.

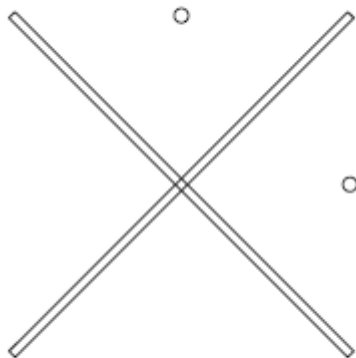


Fig. 4-54: Cross bar fractal places at the centre of the patch

Therefore 4 crossbars are created at four quadrants and then fractal is added as shown in Fig. 4-55.

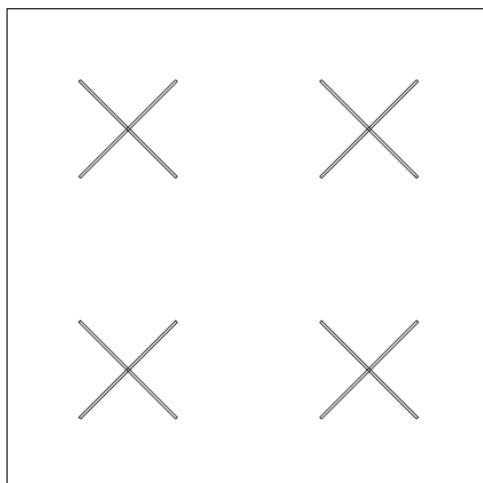


Fig. 4-55: Four cross bars placed at the four quadrants of the patch

The full diagonal length of the crossbar needs to be calculated so that by extending the lengths through fractal iterations, the slot length would not increase beyond the patch.

The full diagonal length on nth fractal can be calculated as follows:

$$FDL1 = 2 \times Fl \quad (37)$$

$$FDL2 = 2 \times \left(Fl + \frac{Fl}{k} \right) \quad (38)$$

$$FDL3 = 2 \times \left(Fl + \frac{Fl}{k} + \frac{Fl}{k^2} \right) \quad (39)$$

.....

$$FDLn = 2 \times \left(Fl + \frac{Fl}{k} + \frac{Fl}{k^2} + \dots + \frac{Fl}{k^{n-1}} \right) \quad (40)$$

$$FDLn = 2 \times Fl \times \left(1 + \frac{1}{k} + \frac{1}{k^2} + \dots + \frac{1}{k^{n-1}} \right) \quad (41)$$

$$FDLn = 2 \times Fl \times \sum_{i=0}^{n-1} \frac{1}{k^i} \quad (42)$$

The framework for SFT fractal is considered as the effective space left after the area which is affected from the coaxial ports is removed, as shown in Fig. 4-56 below: Let coaxial ports be at coordinates $(x1,y1)$ and $(x2,y2)$ from the centre of the patch measured in millimetres. This is shown in Fig. 4-56.

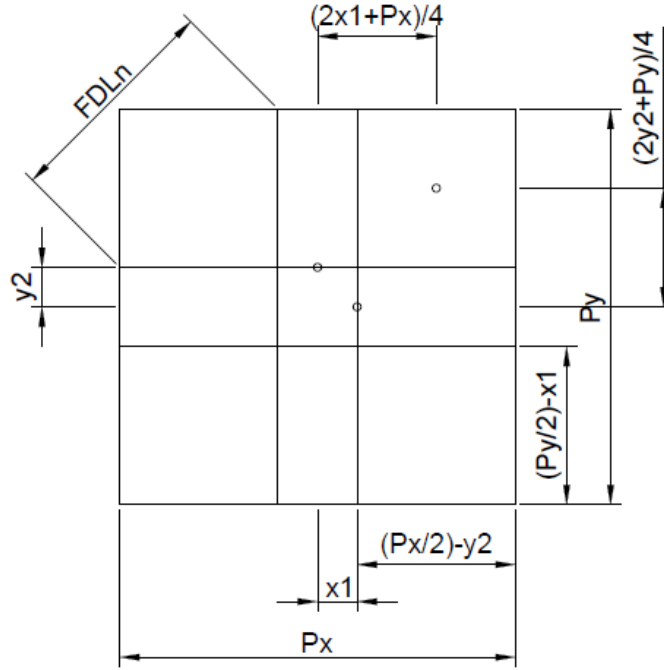


Fig. 4-56: Effective patch area which can be used after the four cross bars are placed

Then the full diagonal length FDL_n from the patch can be calculated as

$$FDL_n = \sqrt{\left(\frac{Px}{2} - x1\right)^2 + \left(\frac{Py}{2} - y2\right)^2} \quad (43)$$

Therefore, a constraint can be obtained using the equations

$$2 \times Fl \times \sum_{i=0}^{n-1} \frac{1}{k^i} \leq \sqrt{\left(\frac{Px}{2} - x1\right)^2 + \left(\frac{Py}{2} - y2\right)^2} \quad (44)$$

Which gives a maximum length for slot length Fl as,

$$Fl \leq \frac{\sqrt{\left(\frac{Px}{2} - x1\right)^2 + \left(\frac{Py}{2} - y2\right)^2}}{2 \times \sum_{i=0}^{n-1} \frac{1}{k^i}} \quad (45)$$

The 1st and 2nd iteration of SFT fractal can be constructed as shown in Fig. 4-57 and Fig. 4-58.

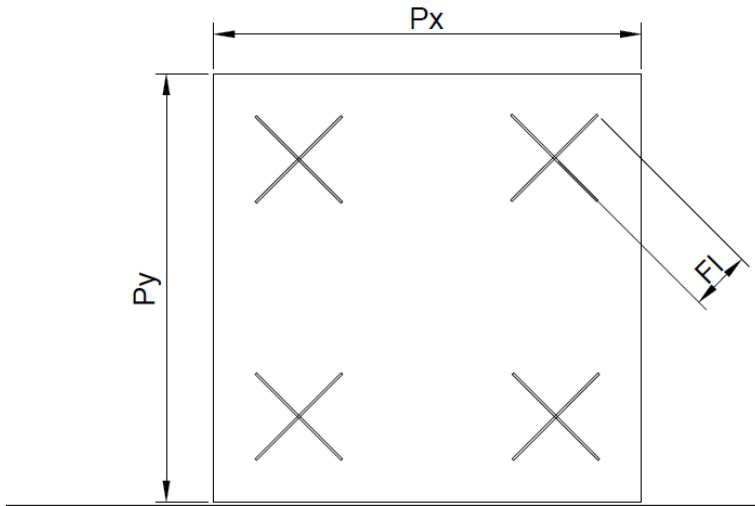


Fig. 4-57: Proposed 1st iteration of the SFT fractal antenna

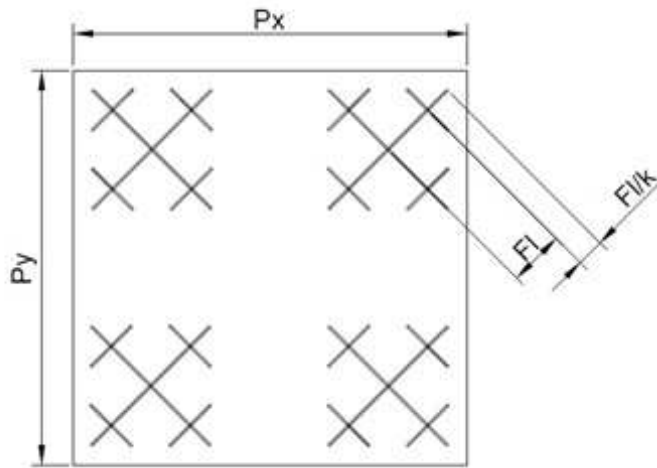


Fig. 4-58: Proposed 2nd iteration of the SFT fractal antenna

4.4.2 Proposed Design and Simulations

The proposed design is to perforate diagonal slots on a square patch antenna and work on the fractal iterations. The length added in each iteration is set by a factor of $\left(\frac{1}{k^n}\right)$ where n is the iteration. The 'Full Diagonal Length' for a rectangular patch antenna where coaxial ports are located at (x_1, y_1) and (x_2, y_2) coordinates with a slot arm of F_l is given by:

$$FDLn = \sqrt{\left(\frac{Px}{2} - x1\right)^2 + \left(\frac{Py}{2} - y2\right)^2} \quad (46)$$

And by considering the length added to each fractal, the full diagonal length of the slot at the nth iteration can be written as

$$FDLn = 2 \times Fl \times \sum_{i=1}^n \frac{1}{k^{i-1}} \quad (47)$$

By equating the equation, a maximum length for the diagonal length for the fractal arm can be written as

$$Fl \leq \frac{\sqrt{\left(\frac{Px}{2} - x1\right)^2 + \left(\frac{Py}{2} - y2\right)^2}}{2 \times \sum_{i=1}^n \frac{1}{k^{i-1}}} \quad (48)$$

The proposed length of the fractal slot Fl and the factor which determined the increment length k can be used to design a reasonable fractal to be implemented on an antenna. Mathcad was used to calculate the results.

The following parameters are defined:

Patch length in x direction Px , patch length in y direction Py , first coaxial port coordinate $(x1, y1)$ and second coaxial port coordinate $(x2, y2)$. The slot length is increased by adding an extra $1/k$ factored length of its length in its previous iteration.

$$Px \text{ and } Py = 50 \text{ mm}$$

$$x1 \text{ and } y2 = 10 \text{ mm}$$

$$k = 3$$

The Maximum/Full Diagonal Length at nth iteration $FDLn$ is given by:

$$FDLn = \sqrt{\left(\frac{Py}{2} - y2\right)^2 + \left(\frac{Px}{2} - x1\right)^2} = \sqrt{\left(\frac{50}{2} - 10\right)^2 + \left(\frac{50}{2} - 10\right)^2}$$

$$FDLn = 15\sqrt{2}$$

$$FDLn = 21.213 \text{ mm}$$

The length of the slot fractal can be calculated as (at 500th iteration)

$$Fl = \frac{\sqrt{\left(\frac{Py}{2} - y2\right)^2 + \left(\frac{Px}{2} - x1\right)^2}}{2 \times \sum_{i=1}^n \frac{1}{k^{i-1}}}$$

$$Fl = \frac{\sqrt{\left(\frac{50}{2} - 10\right)^2 + \left(\frac{50}{2} - 10\right)^2}}{2 \times \sum_{i=1}^{500} \frac{1}{3^{i-1}}}$$

$$Fl = 7.071 \text{ mm}$$

In order to prevent the diagonal slot lengths increasing and expanding beyond the patch, the mid point is shifted each time an iteration is performed. The coordinates for the midpoint can be calculated using

$$Coordinates = \left[x1 + \frac{\frac{Px}{2} - x1}{2}, y2 + \frac{\frac{Py}{2} - y2}{2} \right] \quad (49)$$

Which equates to

$$Coordinates = \frac{2 * x1 + Px}{4}, \frac{2 * y2 + Py}{4} \quad (50)$$

A square patch of a size of 50 mm is proposed to simulate initially. The coaxial position coordinate is set to (10,0). The length of the slot is found to be

$$Fl = \frac{1215\sqrt{2}}{242}$$

which is approximately 7.1 mm and the slot width is set to a thin value at 0.25 mm. This is shown in Fig. 4-59.

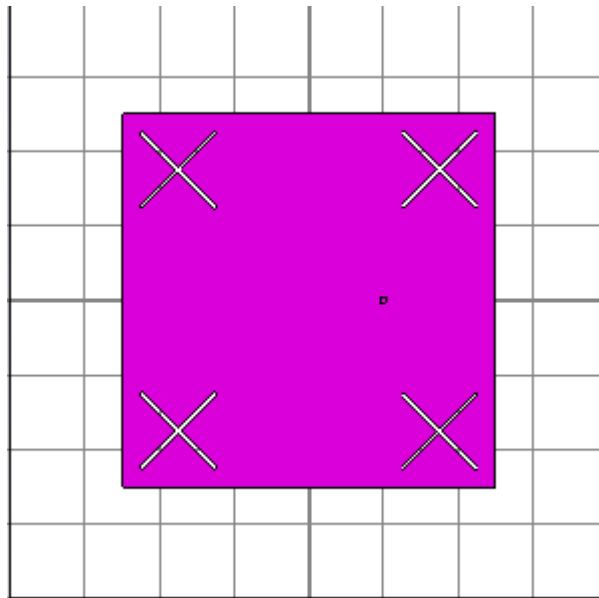


Fig. 4-59: 1st iteration of SFT fractal antenna in CST

The resonant frequency was 1132.4 MHz with harmonics at 2156.1 and 2533 MHz. The results are listed below in Table 4-21. The S11 against frequency is shown in Fig. 4-60.

Table 4-21: S11 and VSWR for 1132.4 MHz on SFT 1st iteration antenna design

Resonant Frequency	S11	VSWR
1132.4 MHz	-10.86 dB	1.802

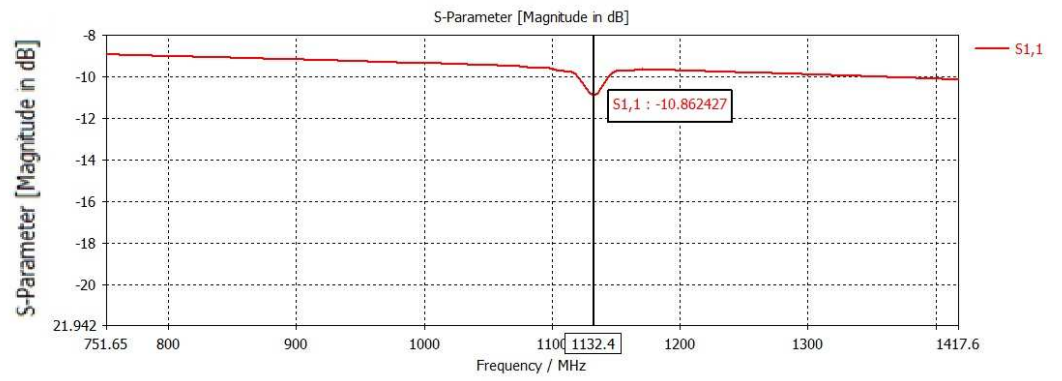


Fig. 4-60: S11 against frequency showing 1132.4 MHz as resonant frequency having an S11 of -10.86 dB

The 2nd iteration of the fractal was simulated which resulted in a slight drop of the resonant frequency. This is shown in Fig. 4-61.

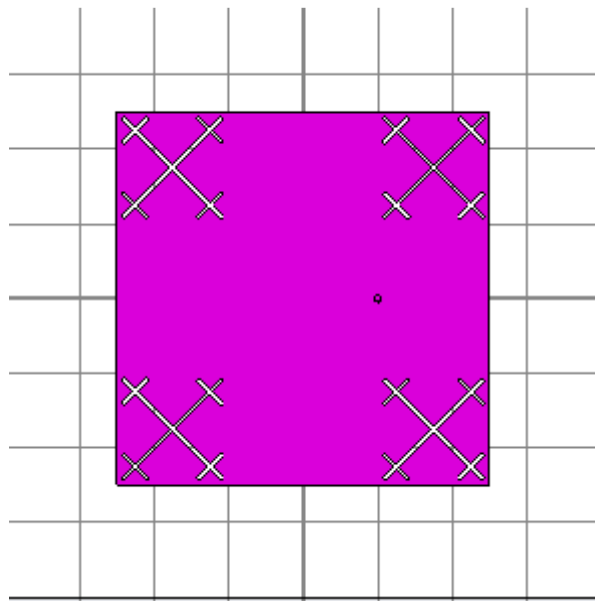


Fig. 4-61: 2nd iteration of SFT fractal antenna in CST

The results are tabled below in Table 4-22 and the radiation pattern is shown in Fig. 4-62.

Table 4-22: Antenna parameters for 1126.6 MHz on SFT 2nd iteration fractal antenna

Resonant Frequency	S11	VSWR	Directivity	3dB Beam width at phi=0 degrees	3dB Beam width at phi=90 degrees
1126.6 MHz	-10.7165	1.8216	5.256 dBi	103.9 deg	105.2 deg

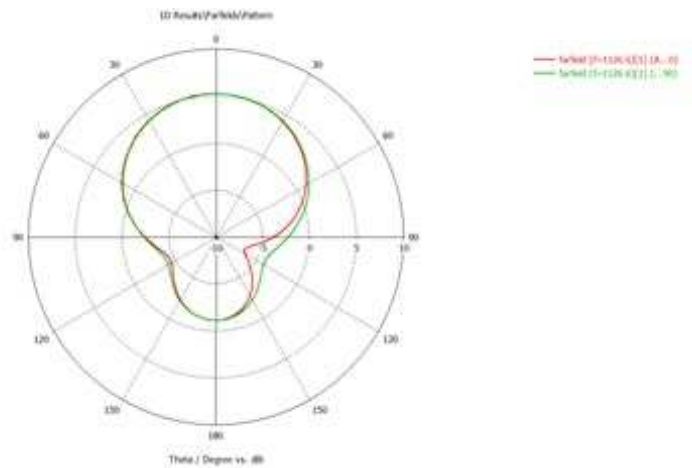


Fig. 4-62: E (Absolute) Farfield radiation patterns at 1126.6 MHz both phi=0 and phi=90 degree cuts

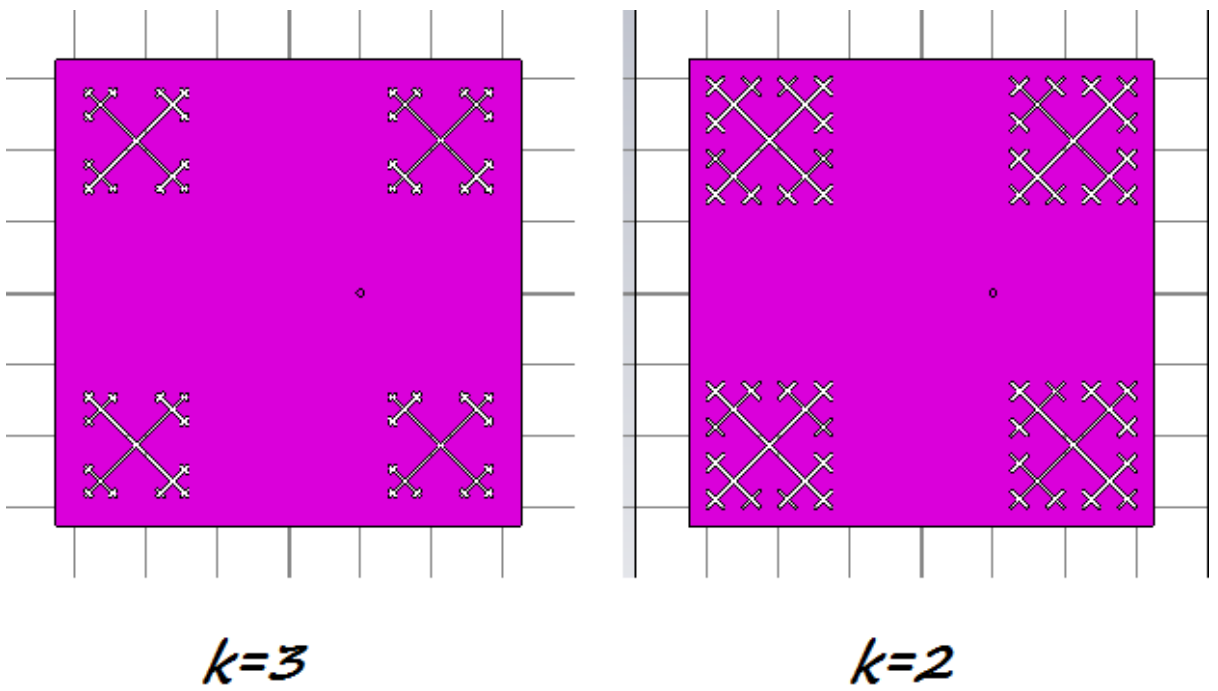
The following simulations were done to reduce the resonant frequency as shown in Table 4-23.

Table 4-23: Antenna parameters with varying patch size

Patch size (mm)	Resonant Frequency (MHz)	S11(dB)	VSWR	3dB angular width at phi=0 deg	3dB angular width at phi=90 deg
60	961.3	-10.2883	1.881	Not read	Not read
65	885.0	-9.6400	1.9823	127.9 deg	97.3 deg

The next iteration of the fractal is simulated: k varied over two values.

The value of k is altered to change the impedance on the surface of the patch and therefore increase the surface currents, since the fractal is in diagonal position to the intended vertical and horizontal polarisation performed by coaxial ports with time phase delay. During design process it was estimated that this will contribute to multiband behaviour as well as the electromagnetic beam radiating from the patch due to fringing effects. This is shown in Fig. 4-63.



*Fig. 4-63: variation of k , which changes factor of which the next iteration's length is added
(3rd iteration of SFT fractal antenna in CST)*

The results for $k=3$ and $k=2$ are shown in Table 4-24 for a patch size of 65 mm.

Table 4-24: Antenna parameters with varying k and coaxial port coordinate

Coax coordinate (mm)	k	Resonant Frequency (MHz)	S11 (dB)	VSWR	Directivity (dBi)	3dB angular width at $\phi=0$ deg	3dB angular width at $\phi=90$ deg
10,0	3	888.8	-9.94	1.9345	4.600	125.1 deg	118.7
10,0	2	885.9	-9.95	1.9322	4.689	97.4	98.7
12,0	2	880.1	-9.73	1.9673	4.482	127.0	97.0

Note: The lower value of $k=2$ provides a narrower beam width for the antenna.

A two-port feeder is attached to feed the antenna with 90-degree time phase shift. The length of the diagonal slot arm previously calculated at 7.1 mm is then varied. These are in Table 4-25.

Table 4-25: Antenna parameters with varying SFT slot length Fl.

Fl (mm)	Resonant Frequency	S11	VSWR	Directivity	3dB Beam width at phi=0 degrees	3dB Beam width at phi=90 degrees
7.1	880.1 MHz	-9.72 dB	1.9703	4.30 dBi	106.6	106.5
8	885 MHz	-9.86 dB	1.9553	Not read	Not read	Not read
5	871.4 MHz	-10.06 dB	1.9161	4.405 dBi	128.7	96.6

A copper wall was constructed to improve directivity and narrow the beam width. This is shown in Fig. 4-64.

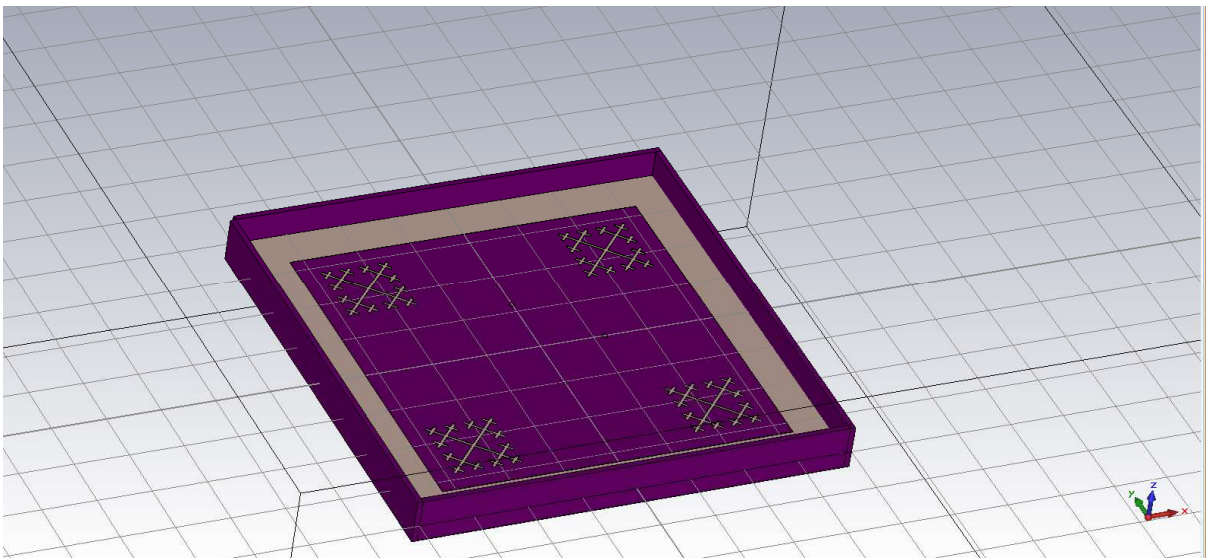


Fig. 4-64: Wall construction around the SFT fractal antenna

The results and radiation patterns are shown in Table 4-26 and the radiation pattern and 3D beam are shown in Fig. 4-65 and Fig. 4-66. Surface currents of the patch when circular polarised is shown in Fig. 4-67

Table 4-26: Antenna parameter results at 880 MHz with wall constructed around it.

Resonant Frequency	S11	VSWR	Directivity	3dB Beamwidth at phi=0 degrees	3dB Beamwidth at phi=90 degrees
880 MHz	-9.986 dB	1.9272	4.615 dBi	104.1	104.3

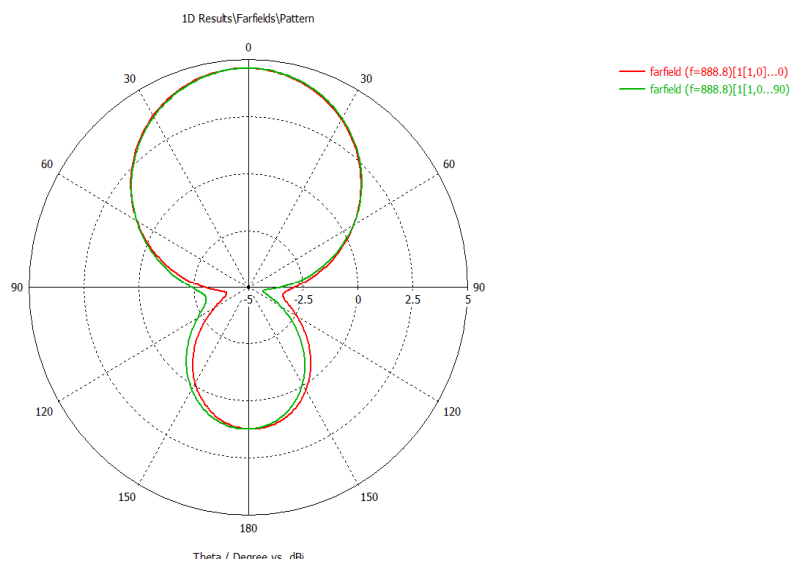


Fig. 4-65: E (Absolute) Farfield results of the SFT fractal antenna with wall at 880 MHz both phi=0 and phi=90 degree cuts

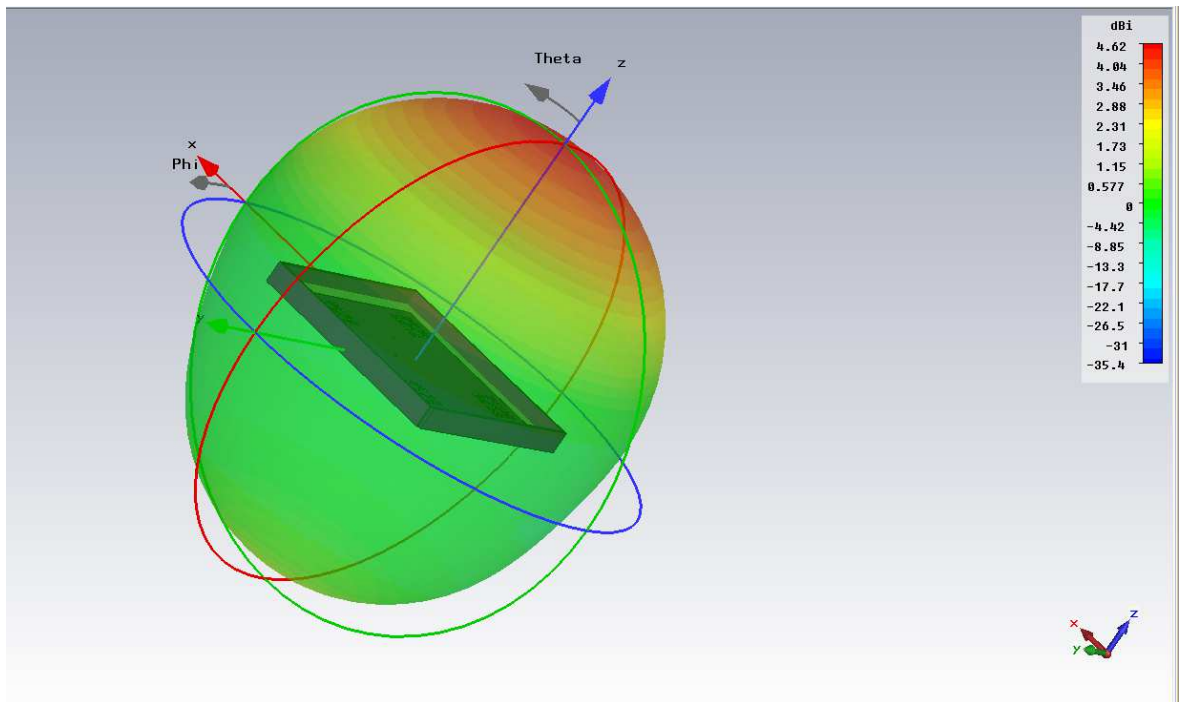


Fig. 4-66: 3D radiation pattern

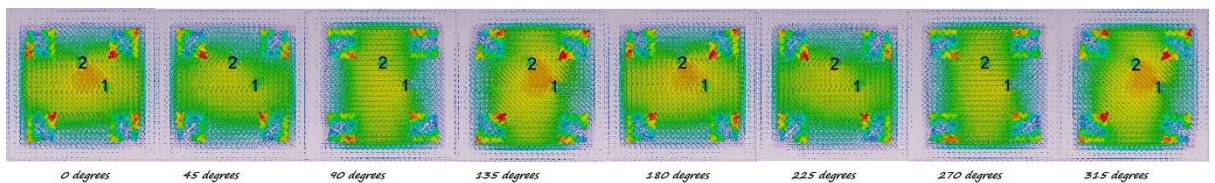


Fig. 4-67: Surface currents on SFT 3rd iteration antenna demonstrating circular polarisation

With the same patch size of 65 mm in order to increase the return loss S11 below -10 dB, the coaxial port is re-designed with a coaxial mesh around as performed in both MLPF and TAU design. The thickness of copper wall was changed from 1 mm to 0.45 mm. The reflector size is increased to 85 mm from 80 mm. The increase of length contributes to reducing return loss magnitude. The coaxial ports were spaced at (8,8) instead of previous (12,12) as shown in Fig. 4-68.

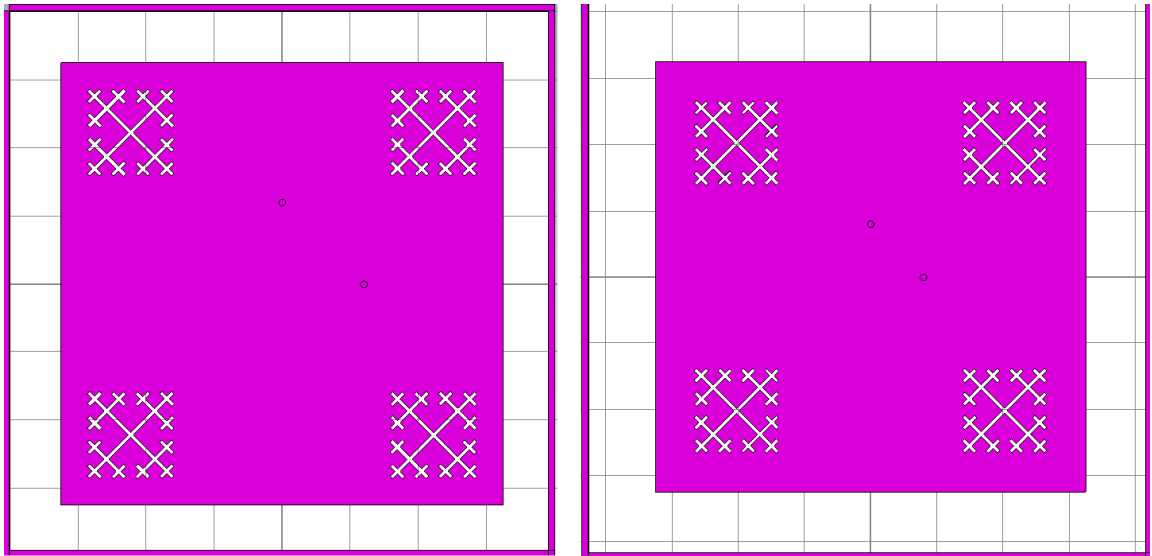


Fig. 4-68: Coaxial ports moved closer to centre from (12,12) to (8,8)

The results are tabled below in Table 4-27.

Table 4-27: variation of coax ports and retuning of SFT fractal antenna

Patch size (mm)	Ground plane size (mm)	Coax port coordinates in mm	Return loss S11 (dB)	Resonant Frequency (MHz)	3dB Beam width at phi=0 degrees	3dB Beam width at phi=90 degrees
65	85	8,8	-17.43	883	105.1	104.9
66	85	8,8	-18.93	871.4	105.9	105.7

Antenna directivity is 4.371 dBi where VSWR is 1.2551 having a bandwidth of 6 MHz which is 1 MHz wider than the expected however, the antenna is applicable for the application. The antenna efficiency is 89%. The fractional percentage bandwidth (FBW) of the antenna can be calculated using (30) as:

$$FBW = \frac{|f_H - f_L|}{f_c} \times 100 = \frac{874.14 - 868.15}{871.4} \times 100 = 0.687\%$$

The return loss and bandwidth are defined in Fig. 4-69.

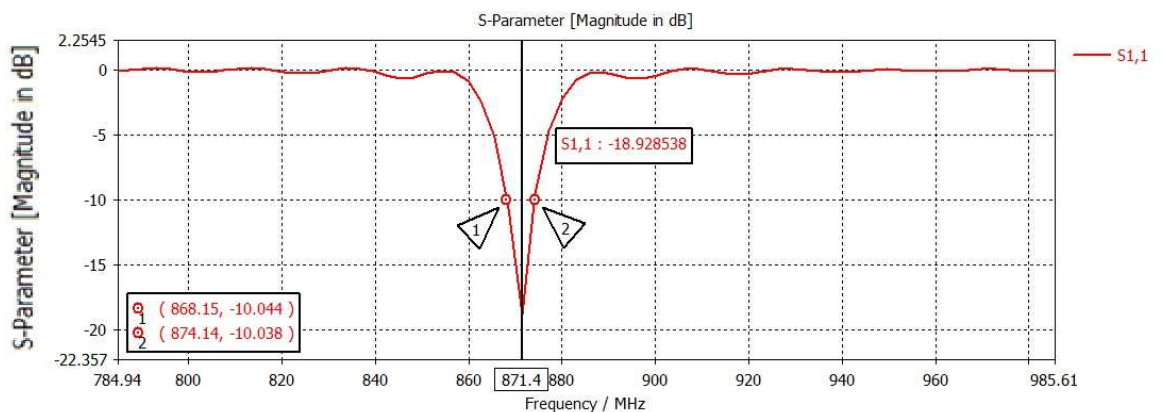


Fig. 4-69: Return loss S11 at 871.4 MHz with a bandwidth of 6 MHz

The antenna is circularly polarised as the angle difference is 0.8 degrees (48 minutes).

Farfield radiation patterns are shown in Fig. 4-70 to Fig. 4-72 and surface currents in Fig. 4-73.

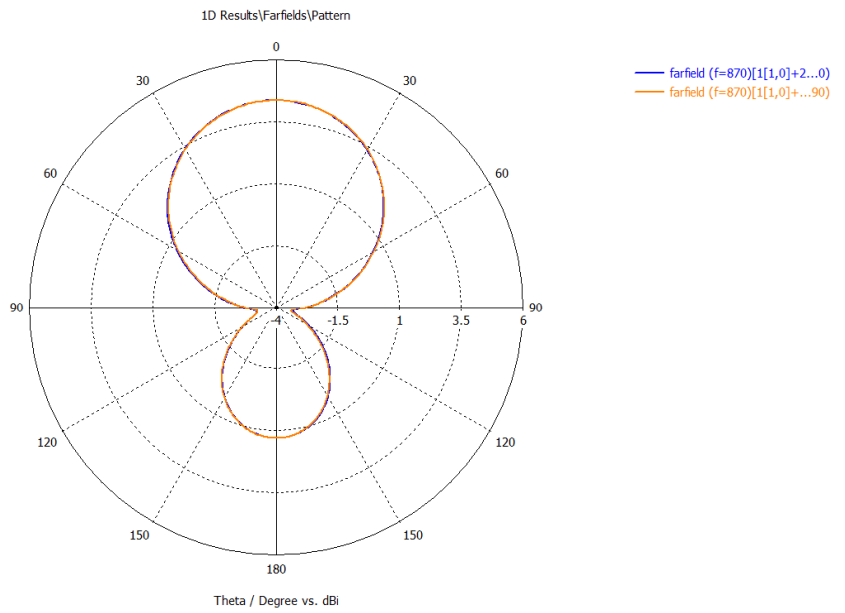


Fig. 4-70: E (Absolute) Farfield radiation patterns for $\phi=0$ and $\phi=90$ -degree cuts

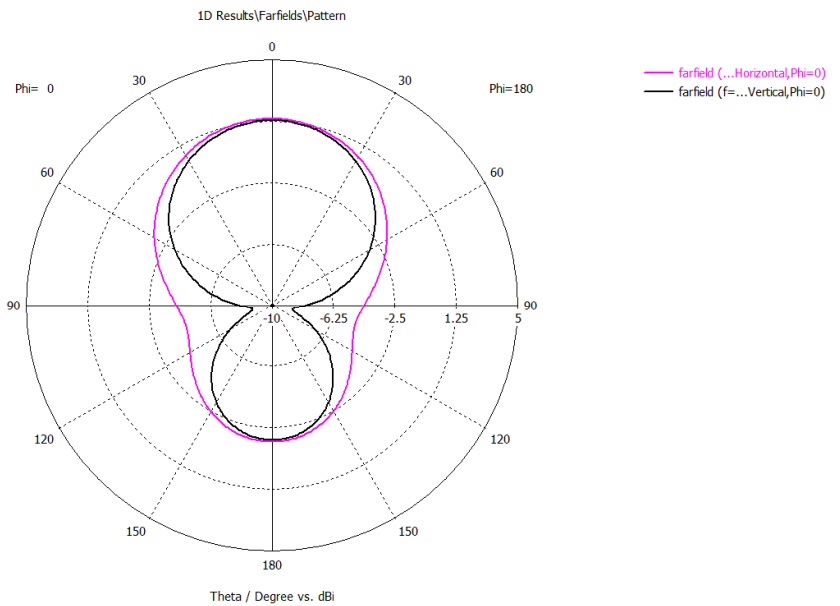


Fig. 4-71: E plane co-polar and cross-polar cuts

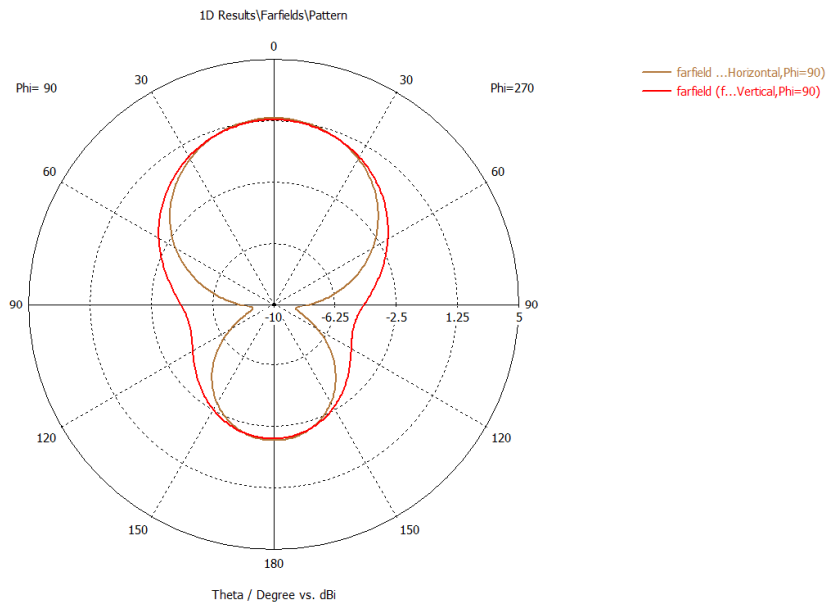


Fig. 4-72: H plane co-polar and cross-polar cuts

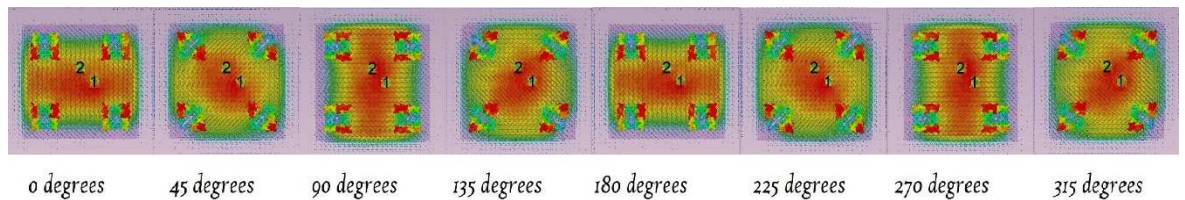


Fig. 4-73: Surface current patterns on SFT antenna

4.5 Maltese Cross Fractal Antenna

4.5.1 Introduction to the fractal and its construction

A Maltese cross based fractal antenna is proposed in this section to miniaturise and help improve surface currents on the radiation element and therefore, radiate a circularly polarised beam, since there is flexibility to change not only the size but also the angle of the diagonal sections of the fractal. By doing so it is expected to optimise and find the best possible design to be manufactured. The dimensions of the patch, its length in y direction P_y measured in millimetres and width in x direction P_x measured in millimetres. Variables lengths a and b , angles α and β are shown in Fig. 4-74.

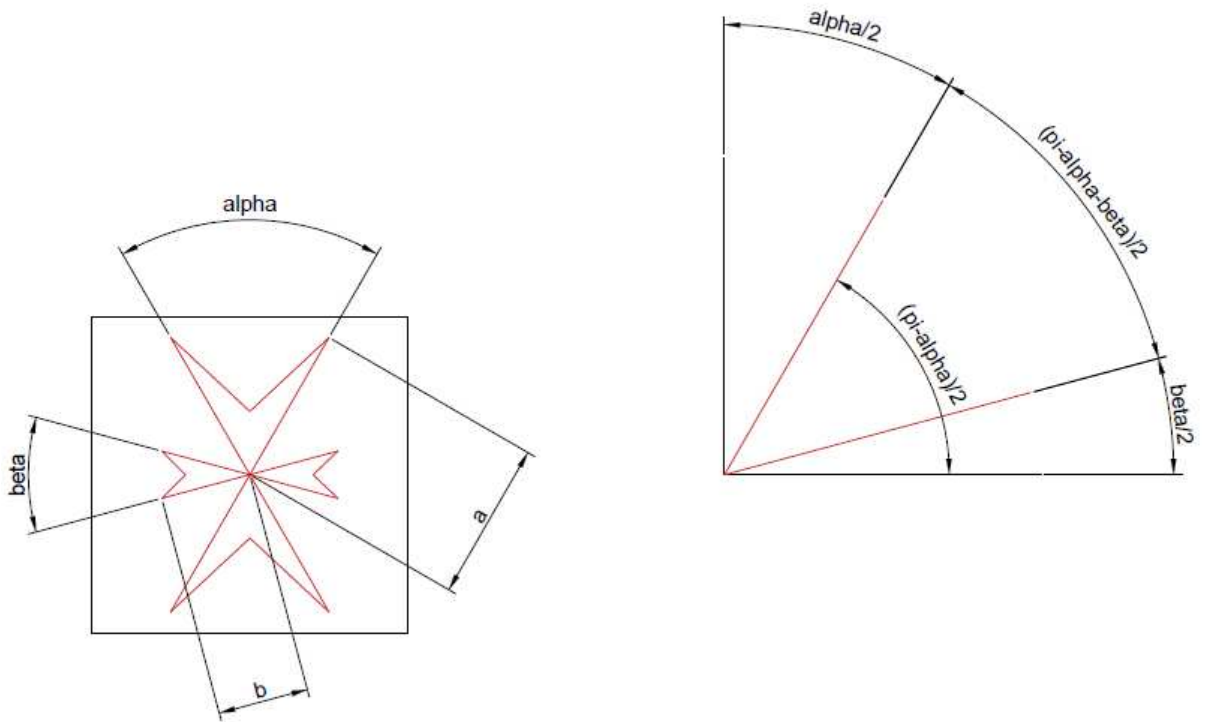


Fig. 4-74: Proposed Maltese Cross depicting lengths and flare angles

In this fractal, both vertical and horizontal angles can be changed for better surface currents. Vertical element angle α and horizontal element β are shown in Fig.4-74.

As electric charge emanates from edges, this element makes it possible even to change the angle of extremities by varying the heights:

$$\text{vertical length in } y \text{ direction: } k \times a \times \cos\left(\frac{\alpha}{2}\right) \quad (51)$$

$$\text{horizontal length in } x \text{ direction: } q \times b \times \cos\left(\frac{\beta}{2}\right) \quad (52)$$

Where k and q are factors initially set to 0.8 as depicted in Fig. 4-75.

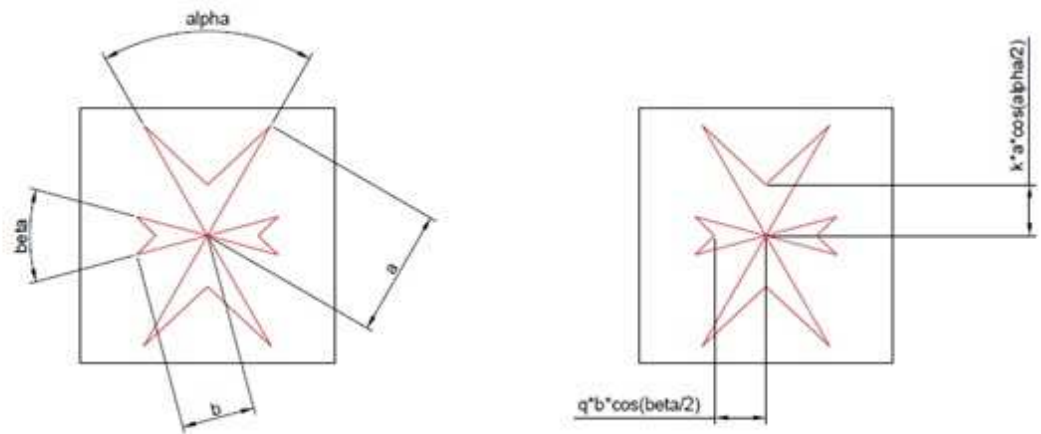


Fig. 4-75: Proposed Maltese cross fractal with vertical and horizontal lengths

Similar to Tau fractal in order not to obstruct the coaxial feeding, four elements were set at 4 quadrants. The 1st and 2nd iterations are shown in Fig. 4-76.

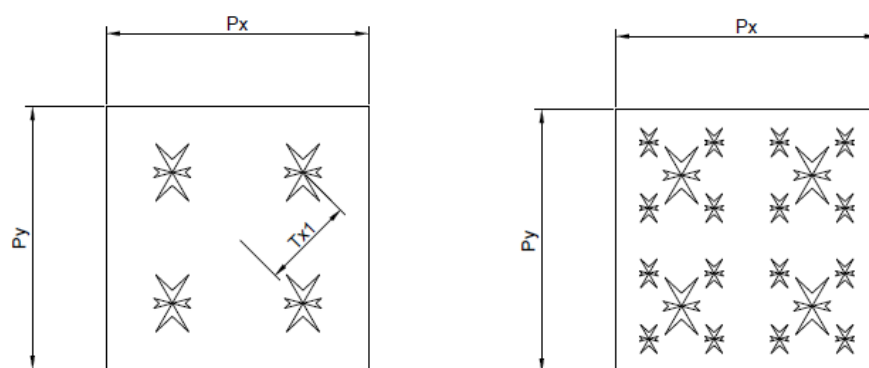


Fig. 4-76: Proposed 1st and 2nd iterations of the Maltese cross fractal antenna

4.5.2 Proposed Design and Simulations

Proposed design was modelled in CST Microwave Studio and the 3 iterations of proposed fractal are shown in Fig. 4-77.

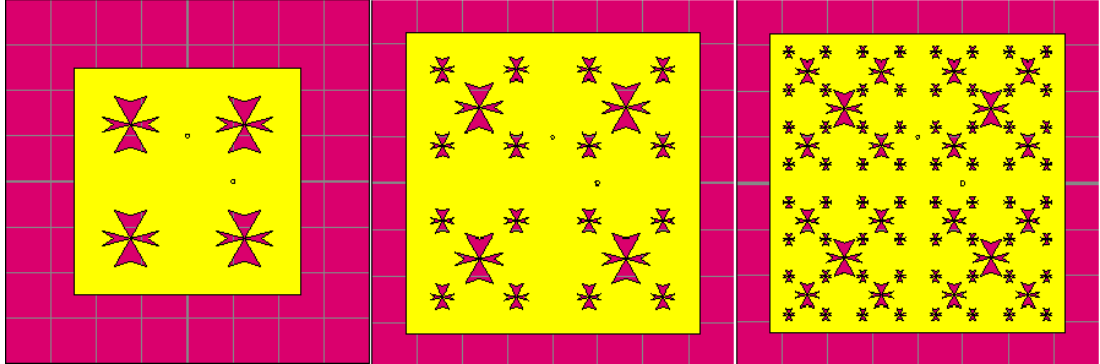


Fig. 4-77: Proposed Maltese Cross antenna in CST (1st, 2nd and 3rd iteration of the fractal)

In the design, an element of Maltese Cross fractal is being translated to the centres of the patch by dividing the patch into four parts. Then the resultant patch is divided into four again and a scaled down (in length) version of the same Maltese Cross fractal is translated having the same angles. NOTE: Simulations were done by using a two-port feeding network.

The first iteration of the Maltese Cross fractal was perforated on a square patch of 50 mm and simulated. Resonant frequency harmonics of 1129.5, 2072, 2190.9 and 2504.1 MHz were found. This is shown in Fig. 4-78.

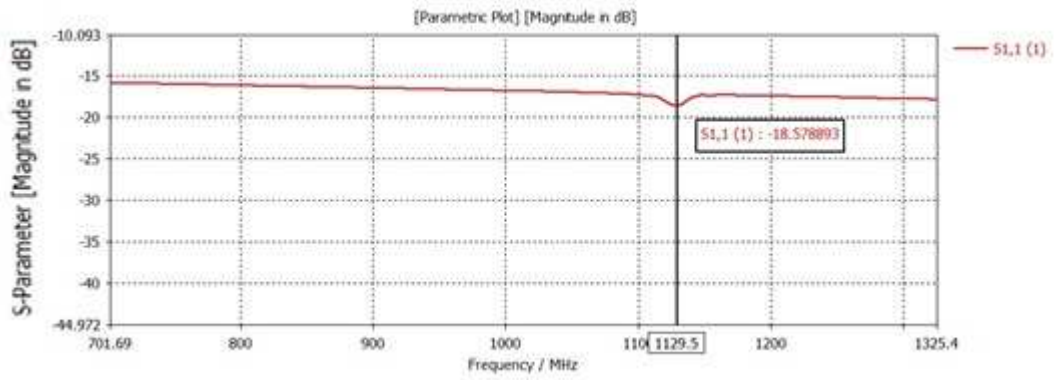


Fig. 4-78: S11 parameter against frequency showing 1129.5 MHz as resonance and S11 as -18.5789 dB on Maltese Cross 1st iteration

The results are shown in Table 4-28.

Table 4-28: S11 and VSWR at 1129.5 MHz on Maltese cross 1st iteration

Resonant Frequency	S11	VSWR
1129.5 MHz	-18.58 dB	1.2669

Scaling ratio was used to scale the design using equation (29)

$$\frac{1129.5 \times 50}{870} = 64.9 \text{ mm}$$

The patch of the antenna was scaled to 65 mm and simulated.

The 2nd and 3rd iteration of the proposed Maltese Cross fractal was simulated.

The results are shown in Table 4-29.

Table 4-29: Antenna parameter variation with 1st, 2nd and 3rd iterations of the Maltese Cross fractal

Fractal Iteration	Resonant Frequency (MHz)	S11 (dB)	VSWR	Directivity (dBi)	3dB Beamwidth at phi=0 degrees	3dB Beamwidth at phi=90 degrees
1 st	883	-8.9	2.11	4.014	114.0	104.8
2 nd	885.9	-10.5	1.86	3.042	276.6	125.6
3 rd	888.8	-10.5	1.85	4.085	108.8	109.8

A wall like in previous designs was created around the antenna to improve directivity and make the beam width narrower. The results are shown in Table 4-30.

Table 4-30: Antenna parameters at 894.6 MHz on Maltese Cross fractal 3rd iteration with wall construction

Resonant Frequency	S11	VSWR	Directivity	3dB Beamwidth at phi=0 degrees	3dB Beamwidth at phi=90 degrees
894.6 MHz	-10.40 dB	1.8651	4.323 dBi	108.8	109.0

The resulting radiation pattern, surface currents are shown in Fig. 4-79 and the 3D beam is shown in Fig. 4-80. The surface currents on radiating surface are shown in Fig. 4-81.

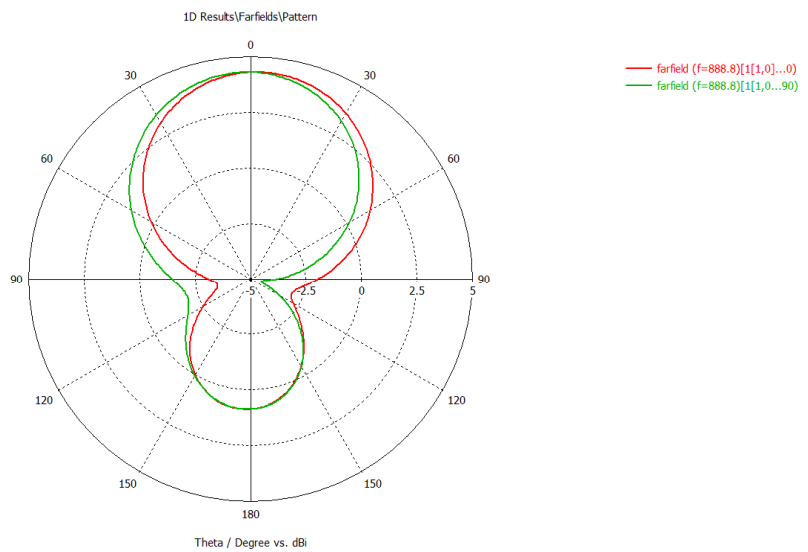


Fig. 4-79: E (Absolute) Farfield radiation pattern of 3rd iteration of Maltese cross fractal with wall constructed around

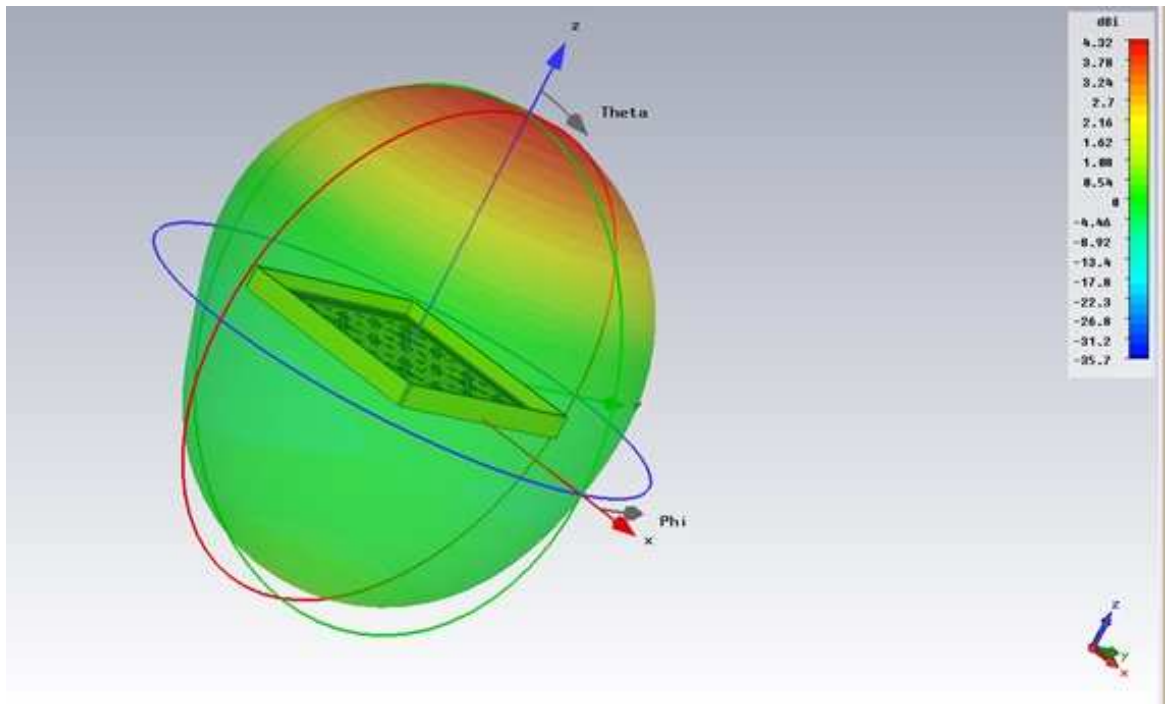


Fig. 4-80: 3D radiation pattern of Maltese cross 3rd iteration fractal antenna with wall contraction

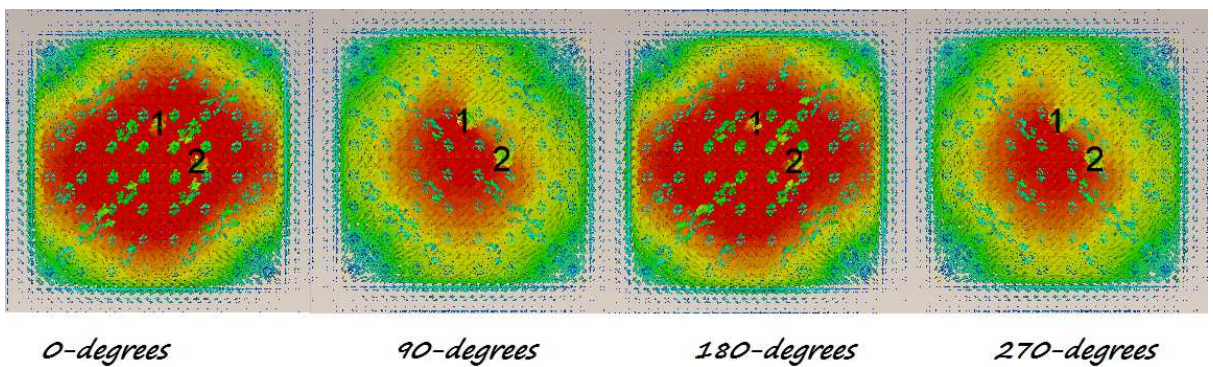


Fig. 4-81: Surface currents on radiating patch of the 3rd iteration of Maltese cross fractal demonstrating circular polarised behaviour

With the same patch size of 65 mm in order to increase the return loss S₁₁ below -10 dB, the coaxial port is re-designed with a coaxial mesh around as performed in previous MLPF, TAU and SFT designs. The thickness of copper wall was changed from 1 mm to 0.45 mm. The reflector size is increased to 85 mm from 80 mm. The coaxial ports were

spaced at a very close range at (6,6) instead of previous (10,10). The ground plane was enlarged to 85 mm square patch.

The arm lengths vertical and horizontal were increased as follows:

Vertical arm parameter 'a' was set as

$$a = \frac{Px}{8 \times u \times \cos\left(\frac{\alpha}{2}\right)} \quad (53)$$

Whist 'b' was set as

$$b = \frac{Py}{8 \times u \times \cos\left(\frac{\beta}{2}\right)} \quad (54)$$

Values for a were changed

$$\text{from } \frac{Px}{6 \times u \times \cos\left(\frac{\alpha}{2}\right)} \text{ to } \frac{Px}{7 \times u \times \cos\left(\frac{\alpha}{2}\right)}$$

Values for b were changed

$$\text{from } \frac{Py}{6 \times u \times \cos\left(\frac{\beta}{2}\right)} \text{ to } \frac{Py}{7 \times u \times \cos\left(\frac{\beta}{2}\right)}$$

Let changing factor be R.

The results are tabled below in Table 4-31.

Table 4-31: Variation of flare lengths

R	Patch size (mm)	Ground plane (mm)	Resonant Frequency (MHz)	Return loss S11 (dB)
8	65	85	897.0	-12.377
6	65	85	897.5	-11.5653
6	67	85	874.3	-10.914
7	67	85	874.3	-11.1697

Since vertical and horizontal angles were set to 60 and 30 degree in the flares, the 3D radiation pattern was elliptically polarised and hence the horizontal flare angles were set to 60 degrees for a geometrically symmetrical patch, therefore an electrically symmetrical radiation pattern. The results for a 67 mm patch antenna are tabled below in Table 4-32.

Table 4-32: Maltese Cross fractal final design

Resonant Frequency (MHz)	Return loss S11 (dB)	Directivity (dBi)	VSWR	3dB Beam width at phi=0 degrees	3dB Beam width at phi=90 degrees
874.3	-11.1697	4.388	1.6677	105.8	105.7

The return loss S11 and bandwidth are defined in Fig 4-82.

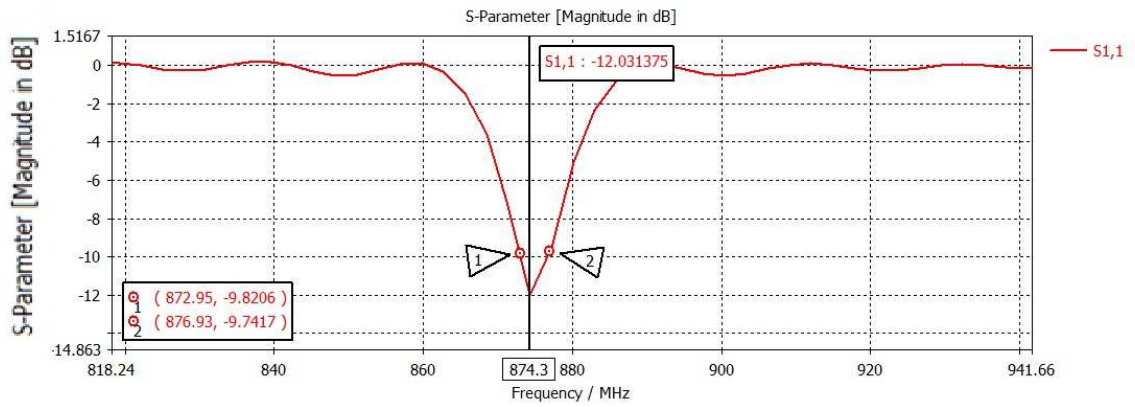


Fig. 4-82: Return loss S11 and Bandwidth 4 MHz

The design is circularly polarised with 3 dB error of 0.1 degrees (6 minutes). The bandwidth on this design is 4 MHz and is suitable for the application. The fractional percentage bandwidth (FBW) of the antenna can be calculated using (30) as:

$$FBW = \frac{|f_H - f_L|}{f_C} \times 100 = \frac{876.93 - 872.95}{874.3} \times 100 = 0.455\%$$

The antenna efficiency for Maltese Cross fractal is 87%.

The respective radiation patterns for Maltese cross antenna is shown in Fig. 4-83 to Fig. 4-85 and surface currents in Fig. 4-86.

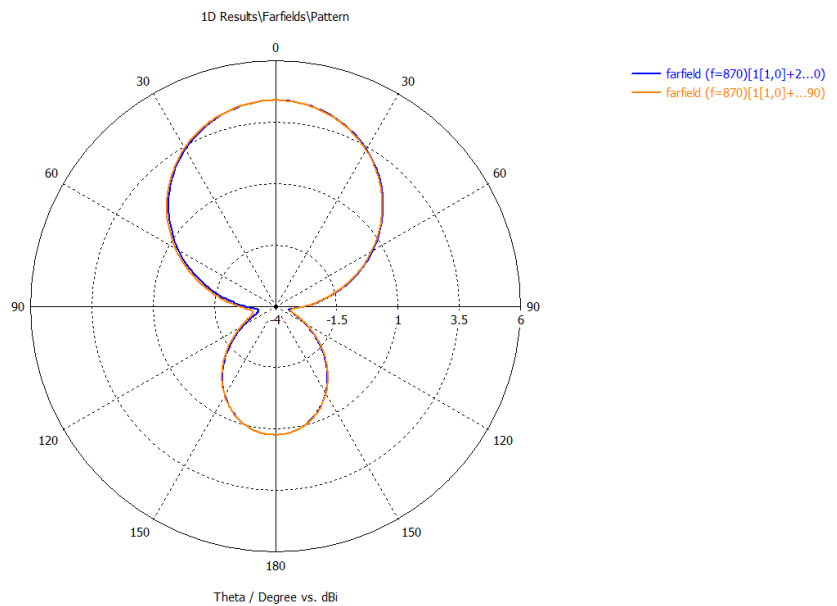


Fig. 4-83: E (Absolute) Farfield radiation pattern phi=0 and phi=90 degree cuts



Fig. 4-84: E plane radiation pattern co-polar and cross-polar cuts

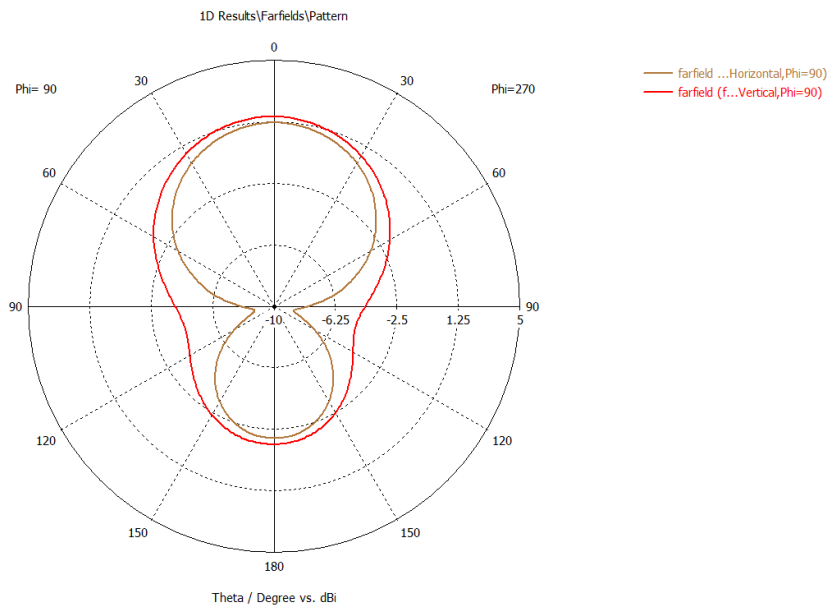


Fig. 4-85: H plane radiation pattern co-polar and cross-polar cuts

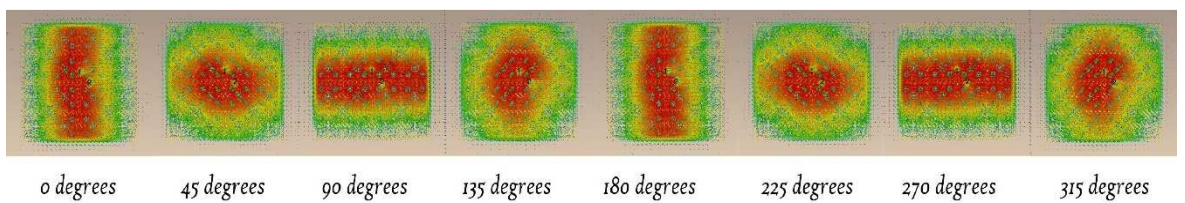
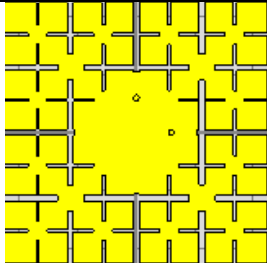
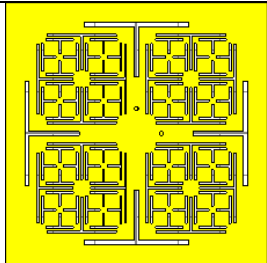
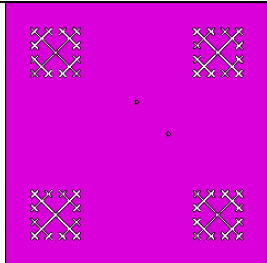
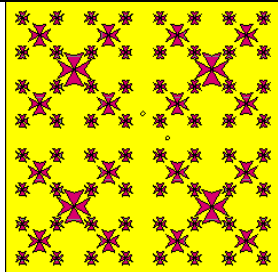


Fig. 4-86: surface currents on Maltese cross fractal antenna

4.6 Summary

In this chapter, four novel antenna models were simulated using CST Microwave Studio. Four fractal patterns namely, Minkowski-Like Pre-Fractal, Tau fractal, Space Filling Tree (SFT) and Maltese Cross fractal were applied to a microstrip patch antennae on a specialist PCB material RF60A, having a dielectric constant of 6.15. The dimensions of final designs are summarised below in Table 4-33.

Table 4-33: Final dimensions of MLPF, Tau, SFT and Maltese Cross antennae

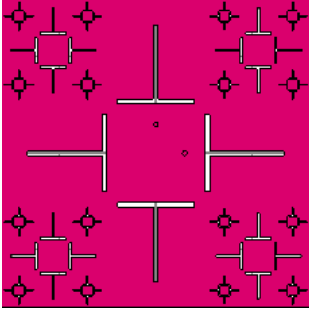
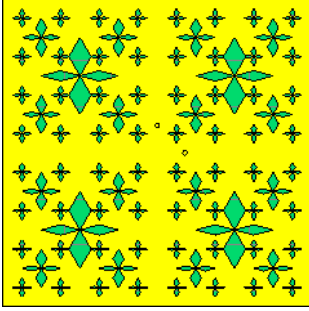
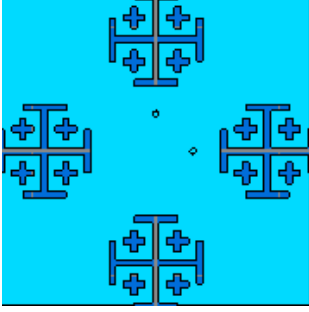
Antenna	Image of patch	Patch size	Ground plane size	Coaxial port coordinate (X,Y) in mm
MLPF		45 mm	86 mm	(6,6)
Tau		63 mm	85 mm	(6,6)
SFT		66 mm	85 mm	(8,8)
Maltese Cross		67 mm	85 mm	(6,6)

5 Development of doorway reader antenna: more proposed designs and simulation results

In this chapter, three further designs were investigated by the simulation knowledge gained in simulations of the first four designs in Chapter four. Design frame remains the same whilst perforating the patch with novel fractals. Inverted Tau (Inv Tau) fractal was proposed to increase performance of the Tau fractal. The Inverted Tau also create parasitic patches as iteration increases; however, it diverges contributing to higher lacunarity whereas in Tau fractal it converges. Stanley fractal was proposed as an alternative to Maltese cross. Maltese cross fractal has an inverted edge which deflected most of surface currents during simulations. Stanley fractal removes the inverted edge. Jerusalem cross fractal was proposed as the fractal element in itself adds a large portion to the antenna's electrical length and hence should not need to go to higher iterations as in MLPF.

These are tabled below in Table 5-1.

Table 5-1: Inv Tau, Stanley and Jerusalem Cross fractal

Antenna	Fractal pattern
Inverted Tau Fractal (Inv Tau)	
Stanley Fractal (Stanley)	
Jerusalem Cross Fractal (Jerusalem Cross)	

5.1 Inverted Tau Fractal Antenna (Inv Tau)

5.1.1 Introduction to the fractal and its construction (Inv Tau)

The inverted Tau fractal contains “T” shaped slots which are set in a matter where the cross bars of “T” meet each other. This can also be seen as the Tau fractal being inverted when perforating on the patch in the objective that lacunarity or the spread factor of the fractal may be affected, i.e., in Tau fractal the surface currents were to travel through the main “T” bar and then spread towards the edges, whereas in the inverted Tau fractal a parasitic patch is created in the middle. However, as the fractal iteration

proceeds higher where Tau fractal converges, the inverted Tau fractal diverges thus increasing lacunarity or spread factor of the fractal. This is shown in Fig. 5-1.

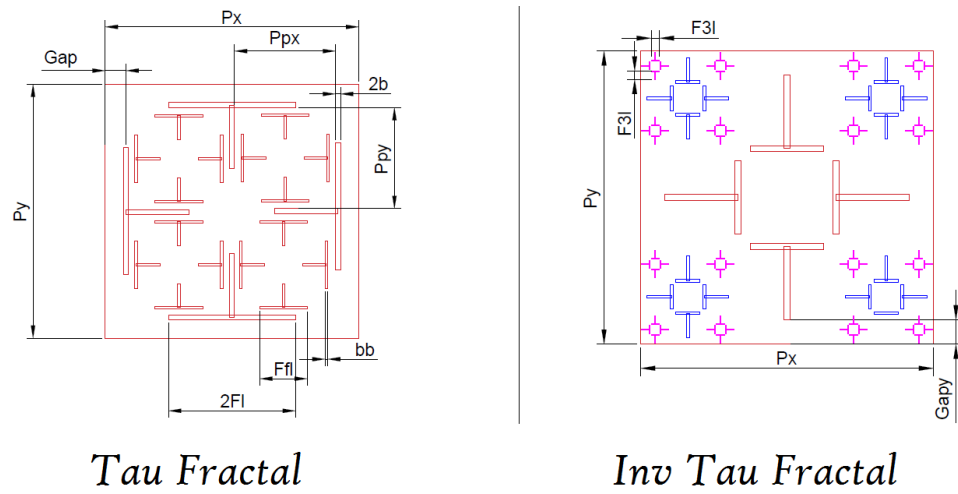


Fig. 5-1: Spread factor or Lacunarity of Tau and Inverted Tau fractal

The inverted Tau fractal can be constructed by first defining four ‘T’-shaped slots (where all 3 elements of letter ‘T’ have equal lengths) places as shown in Fig. 5-2.

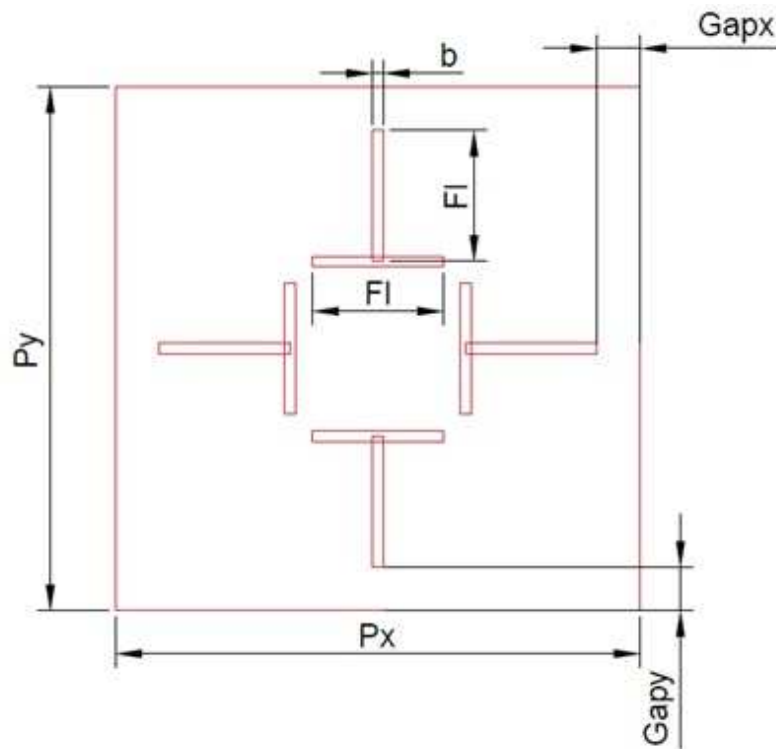


Fig. 5-2: Proposed 1st iteration of Inverted Tau fractal antenna

The dimensions of the patch its length in y direction P_y measured in millimetres and width in x direction P_x measured in millimetres. The length of an element of letter 'T' is named Fl measured in millimetres having a width of $2b$ measured in millimetres. The resulting gap due to cross bars of T and the sides of the patch is named Gap measured in millimetres. This gap is initially set to $1/12^{\text{th}}$ of the patch size whilst Fl is set to $1/4^{\text{th}}$ of the patch size.

The 2nd iteration of the fractal can be constructed by considering the 4 squares which result at four corners by joining the ends of cross bar edges with main patch sides as shown in Fig. 5-3. The size of the new square is:

$$P_{2x} = Gap + Fl \quad \text{measured in mm (75)}$$

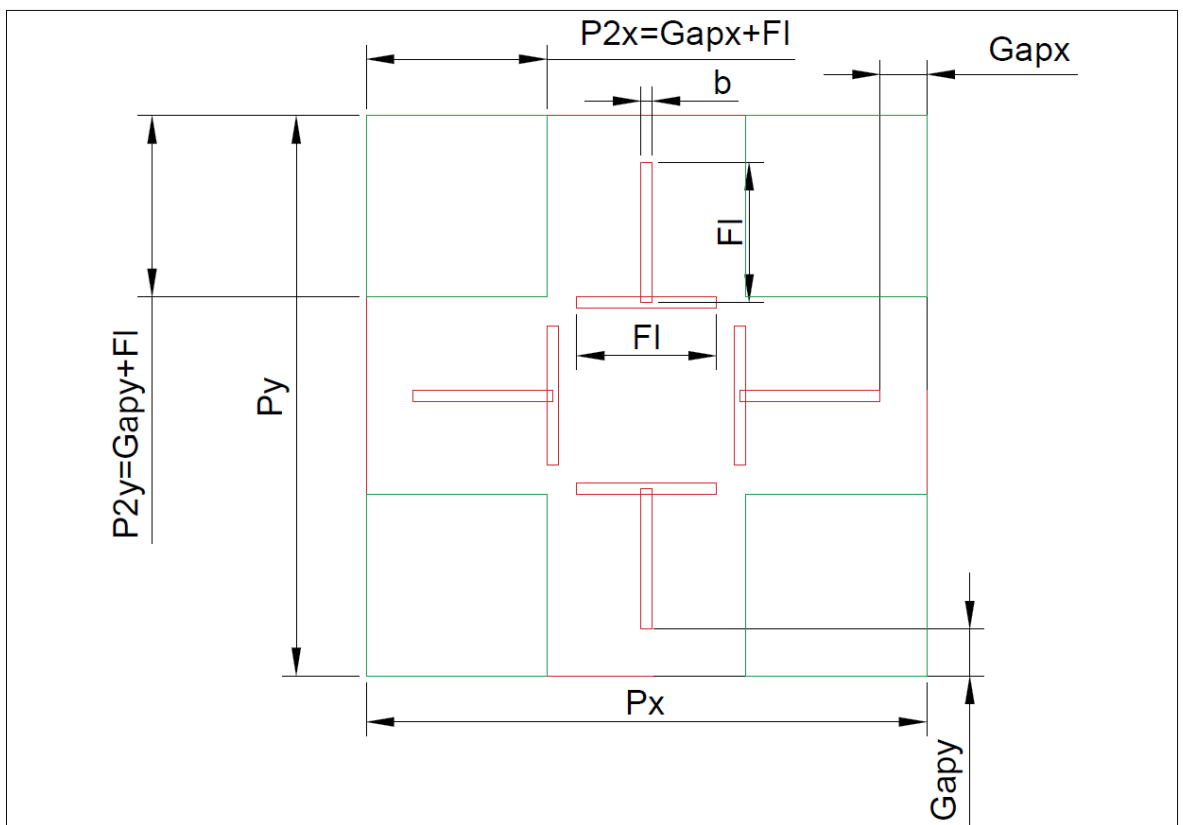


Fig. 5-3: Framework for 2nd iteration of Inverted Tau fractal

These squares are then considered to be the patch and the same pattern can be applied resulting in self-similar patterns and hence a fractal as shown in Fig. 5-4.

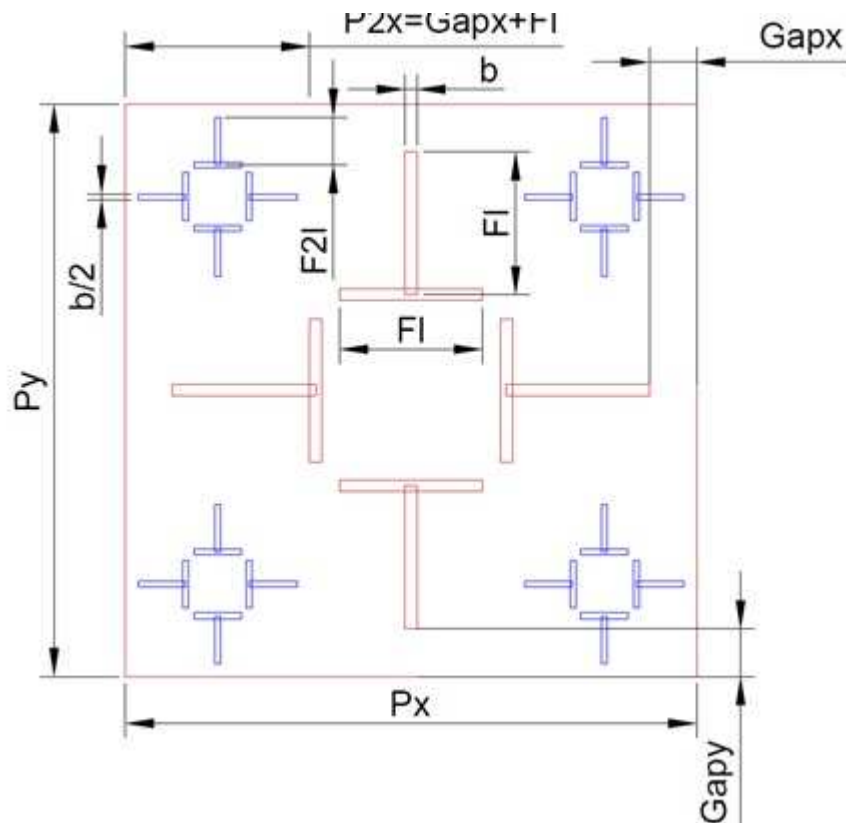


Fig. 5-4: 2nd iteration of the Inverted Tau fractal

The cross lengths of the 2nd iteration are set to 1/4th of the green boxes whilst its width is reduced to half in each iteration. (from $2b$ to b)

$$Fl = \frac{P2x}{4} \quad (55)$$

Moving towards the 3rd iteration, the new gap formed from the 2nd iteration is set to 1/12th of the green box and the new T element lengths are set to 1/4th of the side of the green box, as shown in Fig. 5-5 and Fig. 5-6.

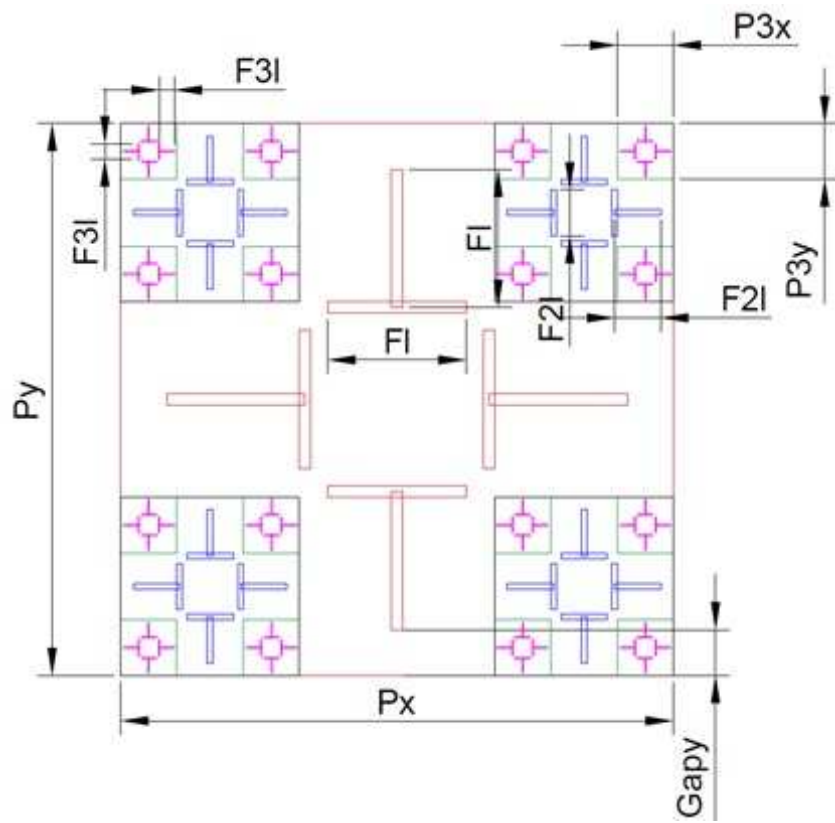


Fig. 5-5: Framework for 3rd iteration of Inverted Tau fractal

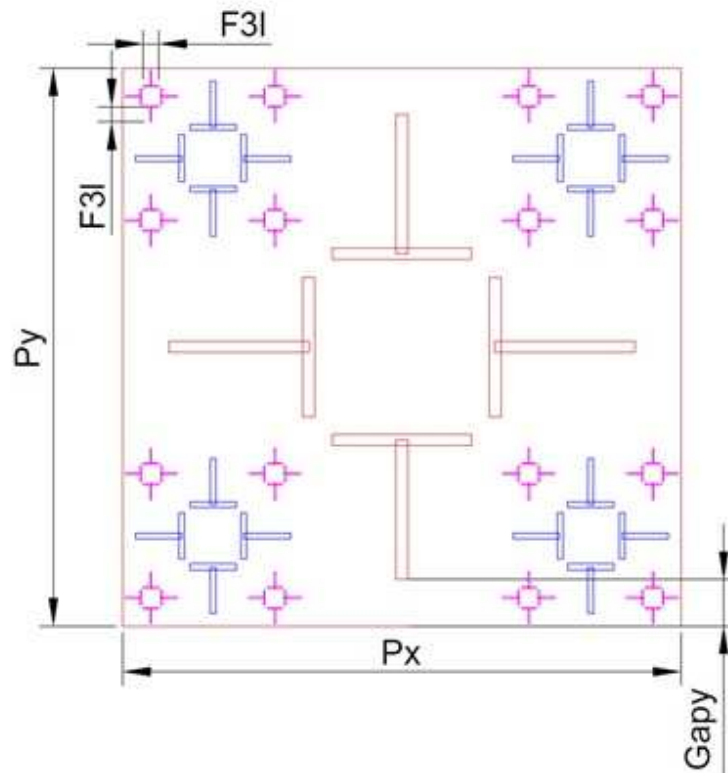


Fig. 5-6: 3rd iteration of Inverted Tau fractal

5.1.2 Proposed design and Simulation results

Using the results obtained in designing previous antennae, the 2nd and 3rd iterations of Inverted Tau fractal were designed. The size of the square patch was initially set to 50 mm with a ground plane of 80 mm fed with two ports placed at (6,6) mm. The constructed models are shown in Fig. 5-7.

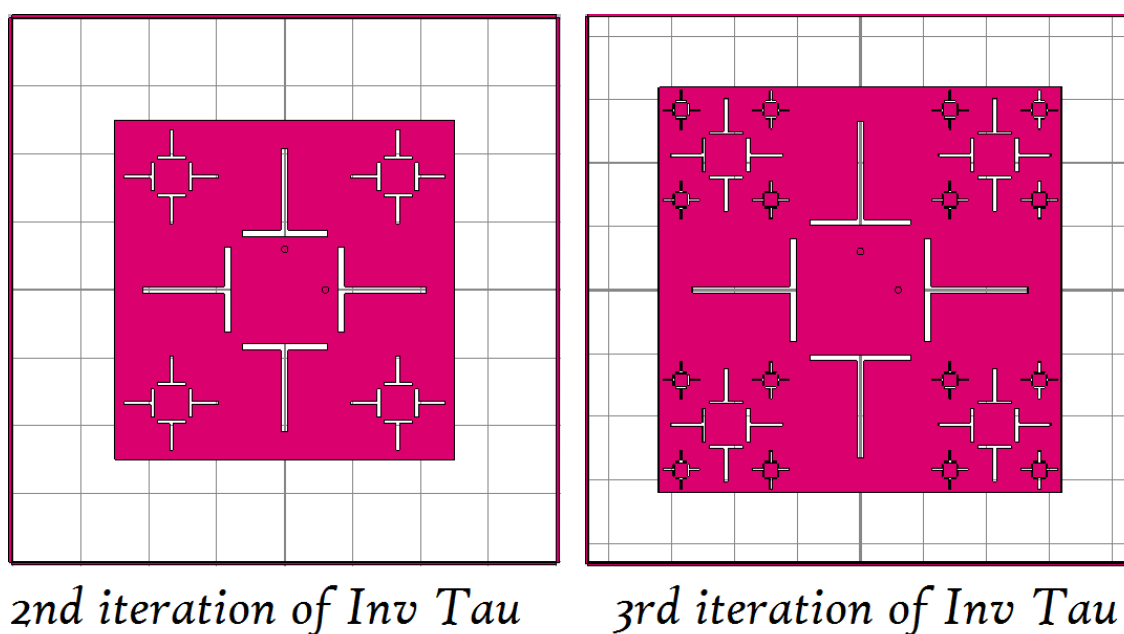


Fig. 5-7: CST models of 2nd and 3rd iteration of Inverted Tau Fractal antennae

A copper wall having a height of 5 mm and a thickness of 0.45 mm was constructed as performed before in previous designs. The outer wire mesh of the coaxial ports was also modelled. The results are tabled below in Table 5-2.

Table 5-2: Inverted Tau simulation results

Antenna	Patch size	Resonant Frequency (MHz)	Directivity (dBi)	Return loss S11(dB)	3dB Beamwidth at phi=0 degrees	3dB Beamwidth at phi=90 degrees
Inv Tau 2 nd iteration	50	1109.2	Not measured	-18.9469	Not measured	Not measured
Inv Tau 2 nd iteration	64	871.4	4.461	-12.4991	104.9	105.7
Inv Tau 3 rd iteration	64	865.6	4.454	-11.7254	104.8	105.8

The antenna is circularly polarised with 1 degree of error. The final design shows a bandwidth of 4 MHz which is suitable for this application. The antenna efficiency for Inv Tau fractal is 79%. The fractional percentage bandwidth (FBW) of the antenna can be calculated using (30) as:

$$FBW = \frac{|f_H - f_L|}{f_C} \times 100 = \frac{868.67 - 864.58}{865.6} \times 100 = 0.472\%$$

The simulation results are shown in Fig. 5-8 to Fig. 4-12 for the 3rd iteration.

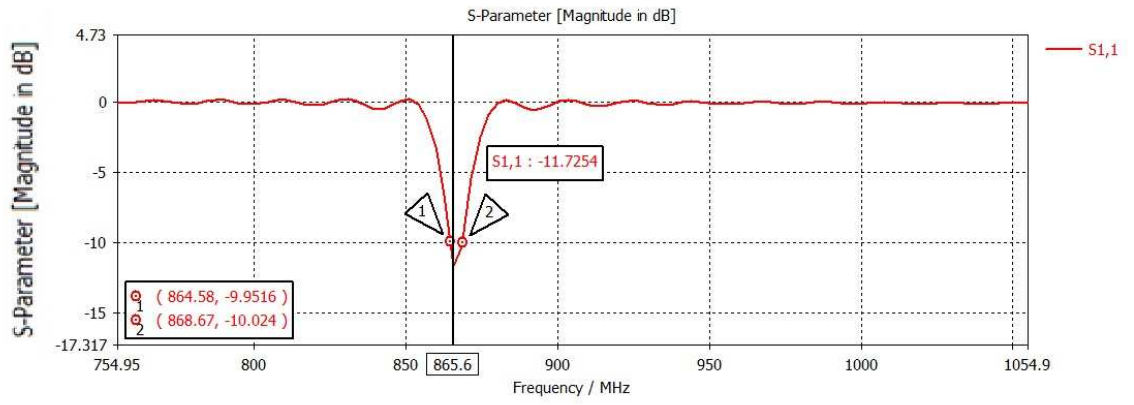


Fig. 5-8: S_{11} against frequency of Inverted Tau fractal antenna having a bandwidth of 4 MHz.

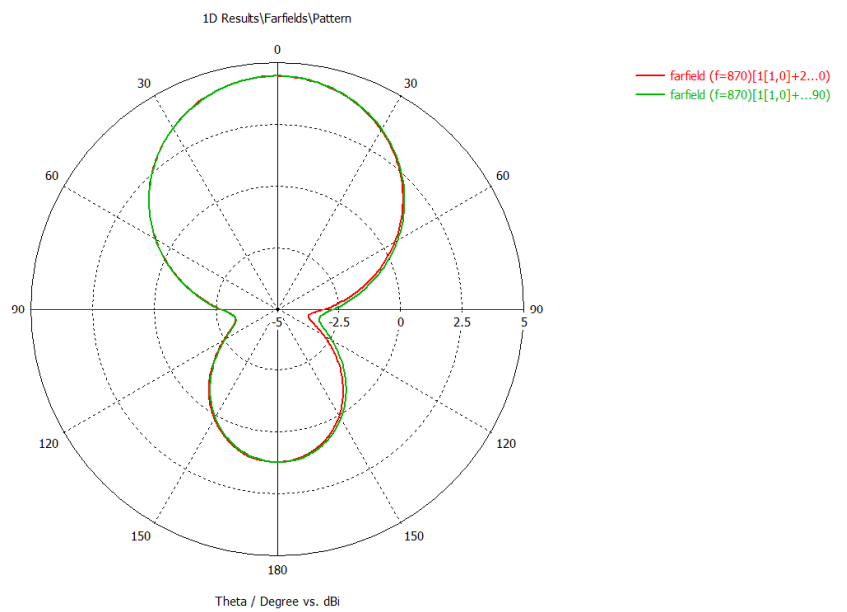


Fig. 5-9: E (Absolute) Farfield radiation patterns at $\phi=0$ and $\phi=90$ degrees

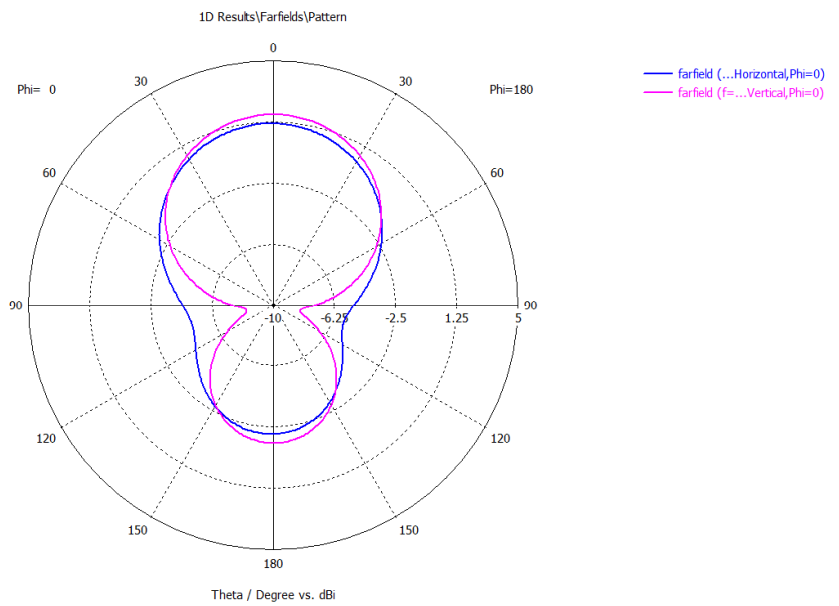


Fig. 5-10: E plane co-polar and cross polar radiation patterns

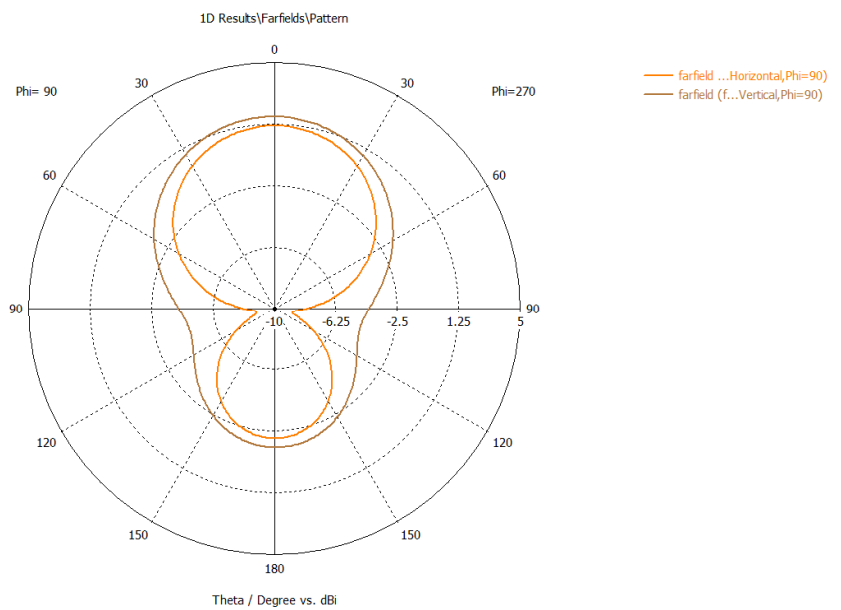


Fig. 5-11: H plane co-polar and cross-polar radiation patterns

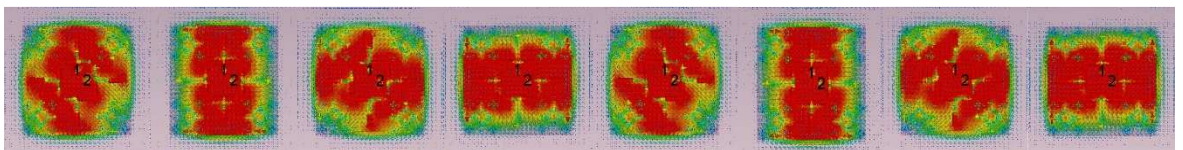


Fig. 5-12: Surface currents of Inverted Tau fractal antenna (3rd iteration) from 0 degrees to 315 degrees in 45-degree intervals

5.2 Stanley Fractal Antenna

5.2.1 Introduction to the fractal and its construction

The flare of Maltese cross fractal antenna had an in-bent arm with a sharp edge which deflects a large portion of surface currents travelling towards the patch edges. The Stanley fractal antenna proposes to rectify this by having a diamond-like shape which would increase the efficiency of the radiator. A comparison of Maltese Cross and Stanley fractal elements are shown in Fig. 5-13.

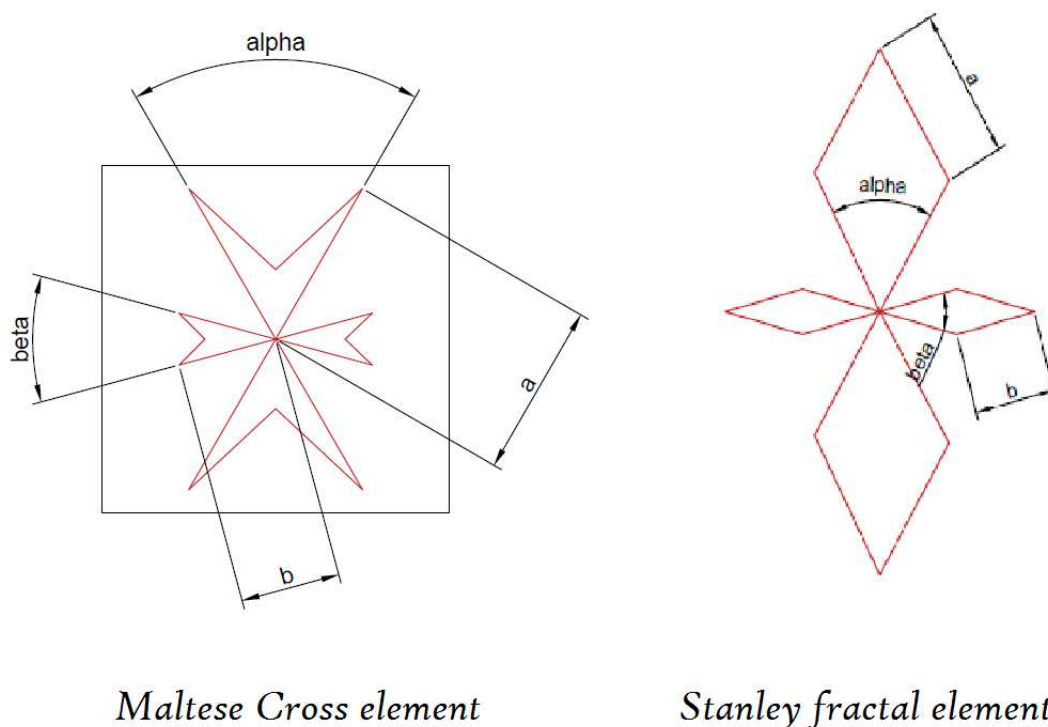


Fig. 5-13: Comparison of Maltese Cross and Stanley fractal elements

Similar to Tau fractal not obstructing the coaxial ports, 4 elements were set at 4 quadrants, this is the 1st iteration. Each quadrant is then subdivided into their 4 quadrants and thus 2nd iteration of the fractal is created. 3rd iteration of the fractal is

created following the same process. The 1st, 2nd and 3rd iterations of Stanley fractal are shown in Fig. 5-14, Fig. 5-15 and Fig. 5-16.

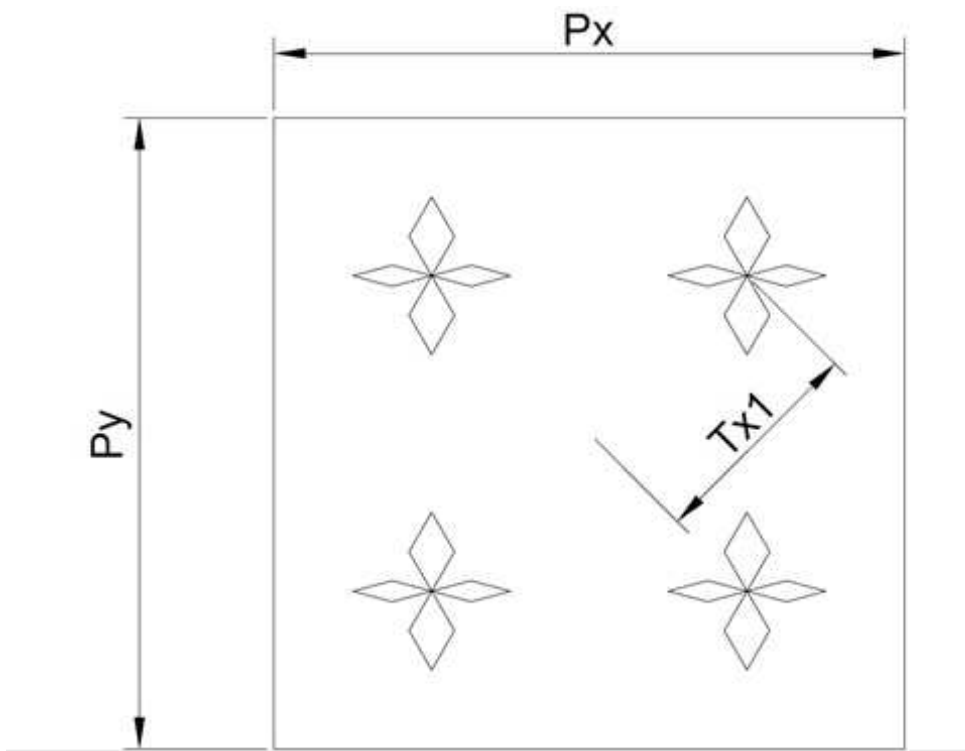


Fig. 5-14: 1st iteration of Stanley fractal antenna

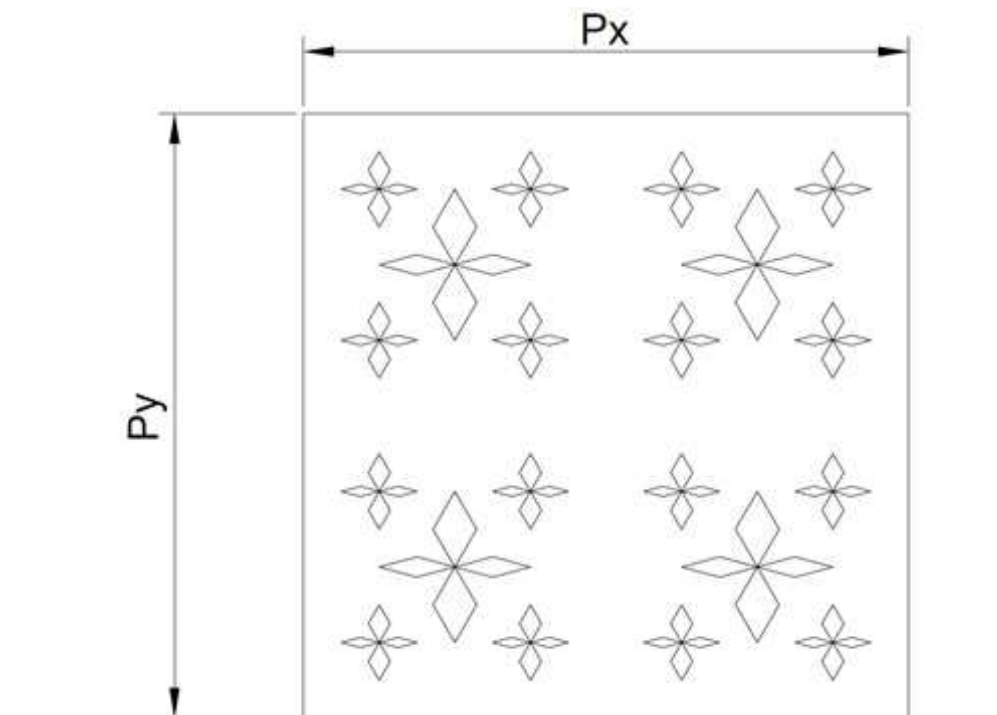


Fig. 5-15: 2nd iteration of Stanley fractal antenna

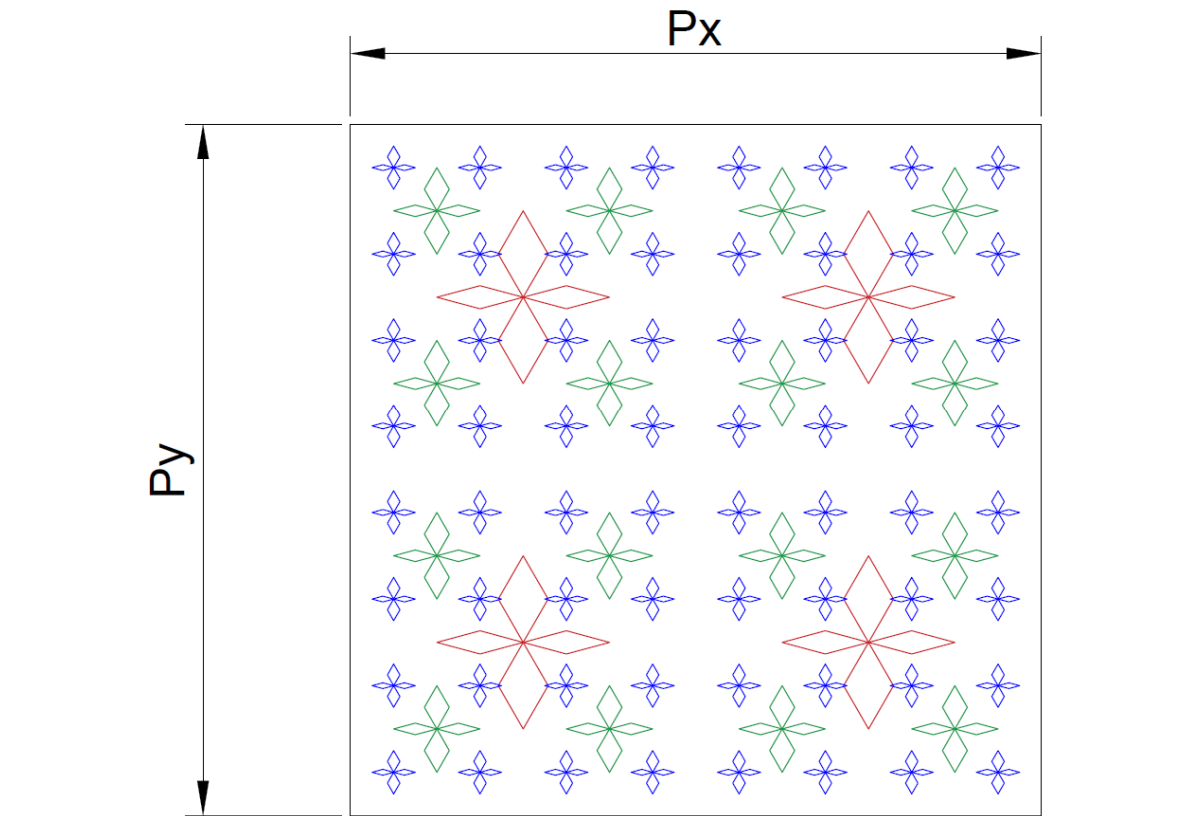


Fig. 5-16: 3rd iteration of Stanley fractal antenna

The dimensions of the patch, its length in y direction P_y measured in millimetres and width in x direction P_x measured in millimetres.

In this fractal, both vertical and horizontal angles could be changed for better surface currents and polarisation if need be. The Stanley element and its algebraic dimensions are shown in Fig. 5-17.

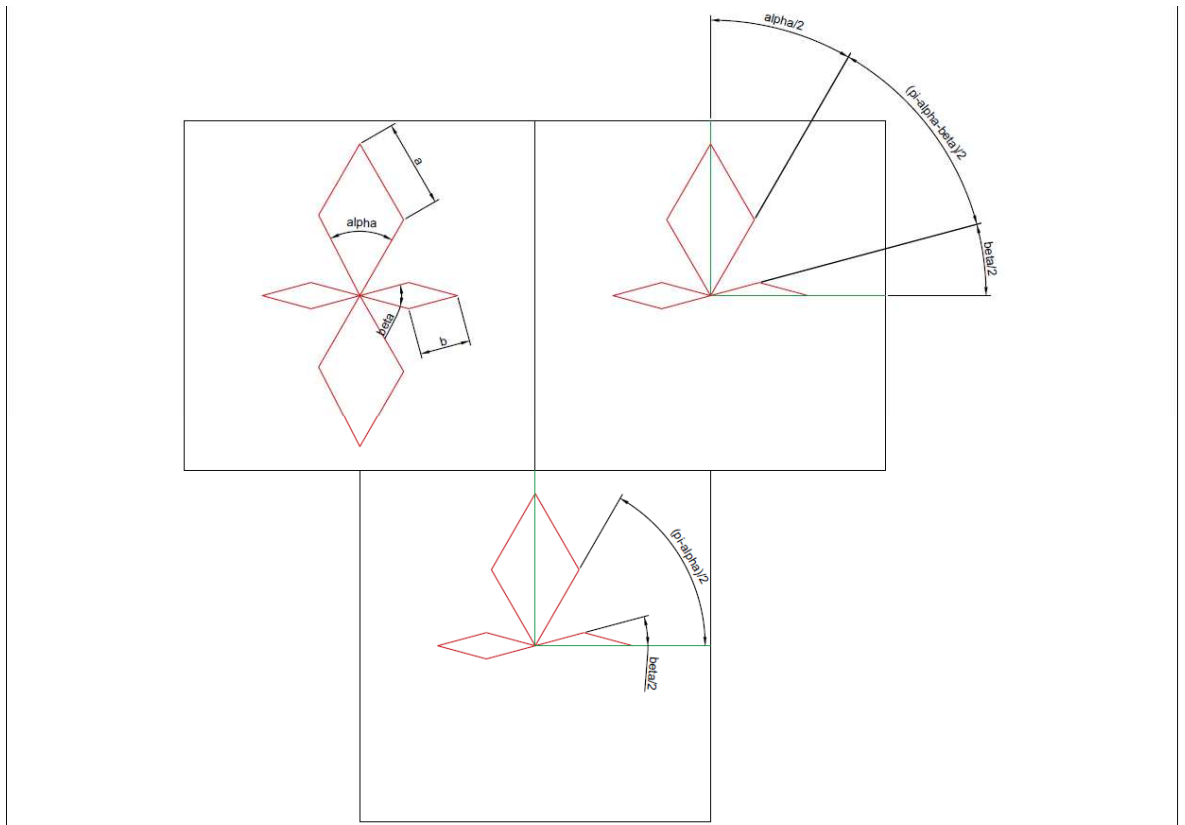


Fig. 5-17: Stanley fractal element and its variable dimensions

Full vertical length of the fractal element can be observed as:

$$2 \times \left(2 \times a \times \cos\left(\frac{\alpha}{2}\right) \right)$$

which is set as 1/4th of the total vertical height of the patch which is set as:

$$2 \times \left\{ 2 \times a \times \cos\left(\frac{\alpha}{2}\right) \right\} = \left\{ \frac{Py}{2} \right\} \times \frac{1}{2} \quad (56)$$

Hence a can be calculated by using the following equation:

$$a = \frac{Py}{16 \times \cos\left(\frac{\alpha}{2}\right)} \quad (57)$$

Where the horizontal length of the fractal element can be observed as:

$$2 \times \left(2 \times b \times \cos\left(\frac{\beta}{2}\right) \right)$$

which is set as 1/4th of the total horizontal width of the patch which is:

$$2 \times \left\{ 2 \times b \times \cos\left(\frac{\beta}{2}\right) \right\} = \left\{ \frac{Px}{2} \right\} \times \frac{1}{2} \quad (58)$$

Hence b can be calculated by using the following equation:

$$b = \frac{Px}{16 \times \cos\left(\frac{\beta}{2}\right)} \quad (59)$$

The side length and width of the element in 2nd iteration aa and bb are set to be $\frac{1}{2}$ of a and b .

5.2.2 Proposed design and simulation results

Proposed Stanley fractal was modelled in CST microwave studio and 3 iterations of proposed fractal are shown in Fig. 5-18.

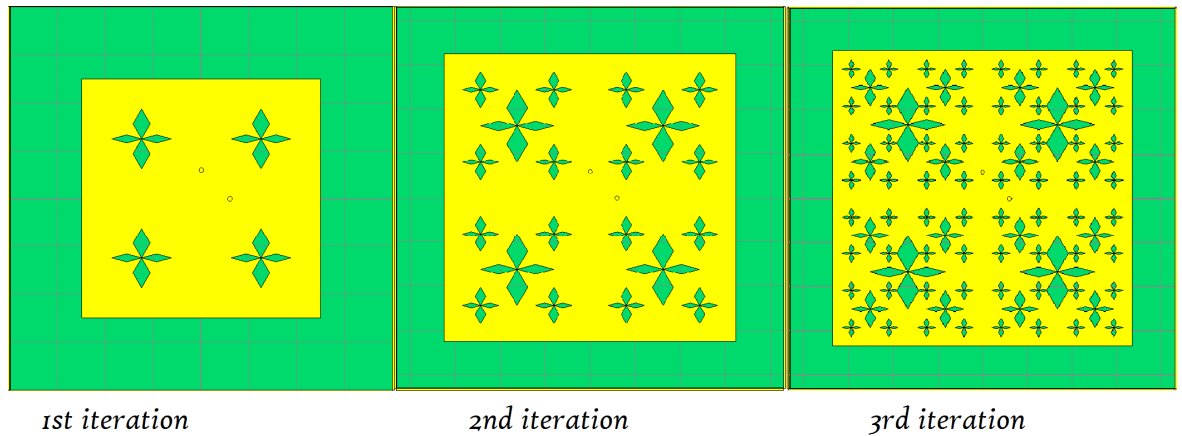


Fig. 5-18: first three iterations of proposed Stanley fractal modelled in CST Microwave Studio

Using the results obtained in designing previous antennae, the 1st, 2nd and 3rd iterations of Stanley fractal were designed. The size of the square patch was initially set to 50 mm with a ground plane of 80 mm fed with two ports placed at (6,6) mm. Angle alpha is set to 60 degrees whilst the angle beta is set to 30 degrees. A copper wall having a height of 5 mm and a thickness of 0.45 mm was constructed as performed before in previous designs. The outer wire mesh of the coaxial ports was also modelled.

The simulation results are tabled below in Table 5-3.

Table 5-3: Simulation results for Stanley fractal antenna

Antenna	Patch size	Ground plane size	Return loss S11 (dB)	Resonant frequency (MHz)	3dB Beam width at phi=0 degrees	3dB Beam width at phi=90 degrees
Stanley 2 nd iteration	50	80	-6.427	1138.2	Not measured	Not measured
Stanley 2 nd iteration	65	86	-11.194	900.4	Not measured	Not measured
Stanley 3 rd iteration	67	86	-9.692	868.5	105.0	105.9

The antenna is circularly polarised with a 0.9-degree error. The antenna directivity is 4.452 dBi in the final design with a bandwidth of 6 MHz which is suitable for this application. The antenna efficiency is 74%. The fractional percentage bandwidth (FBW) of the antenna can be calculated using (30) as:

$$FBW = \frac{|f_H - f_L|}{f_C} \times 100 = \frac{876.91 - 870.23}{874.3} \times 100 = 0.764\%$$

The simulation results are shown in Fig. 5-19 to Fig. 5-23.

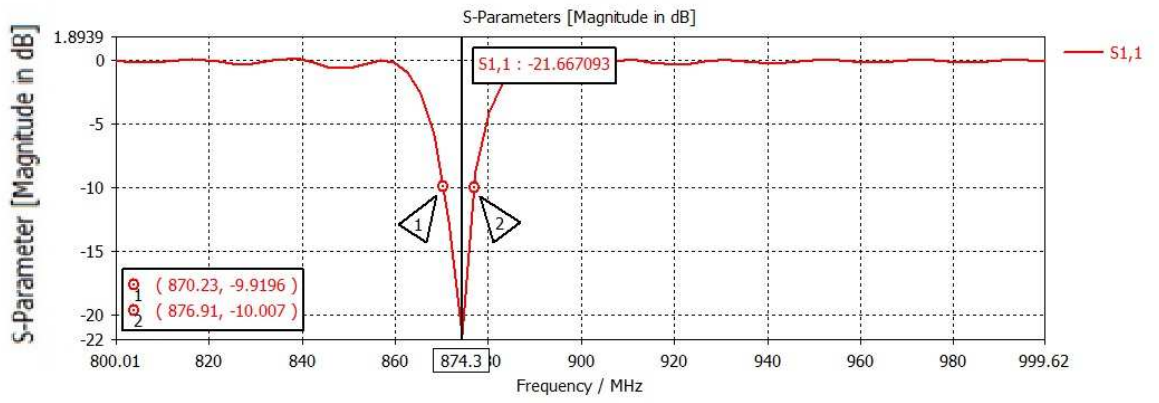


Fig. 5-19: Return loss S_{11} against frequency with a bandwidth of 6 MHz

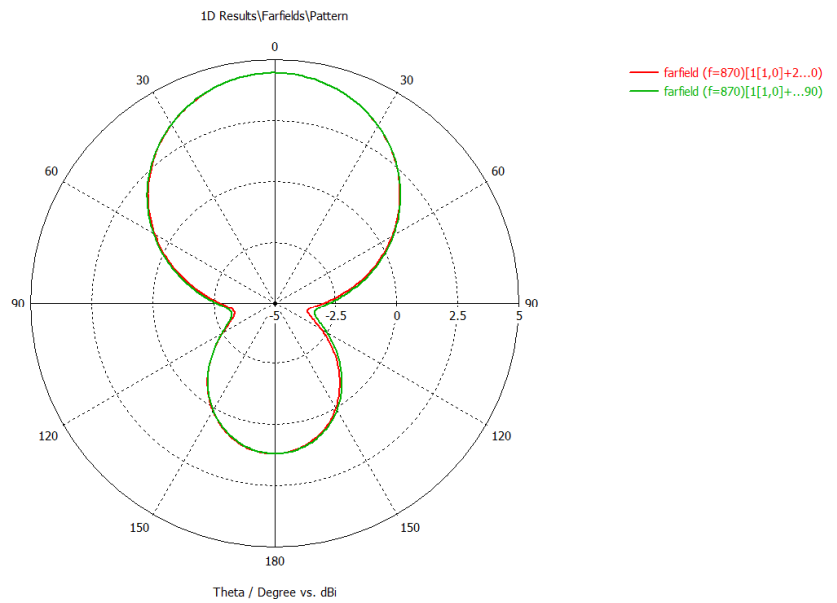


Fig. 5-20: E (Absolute) Farfield radiation patterns at $\phi=0$ and $\phi=90$ degree cuts

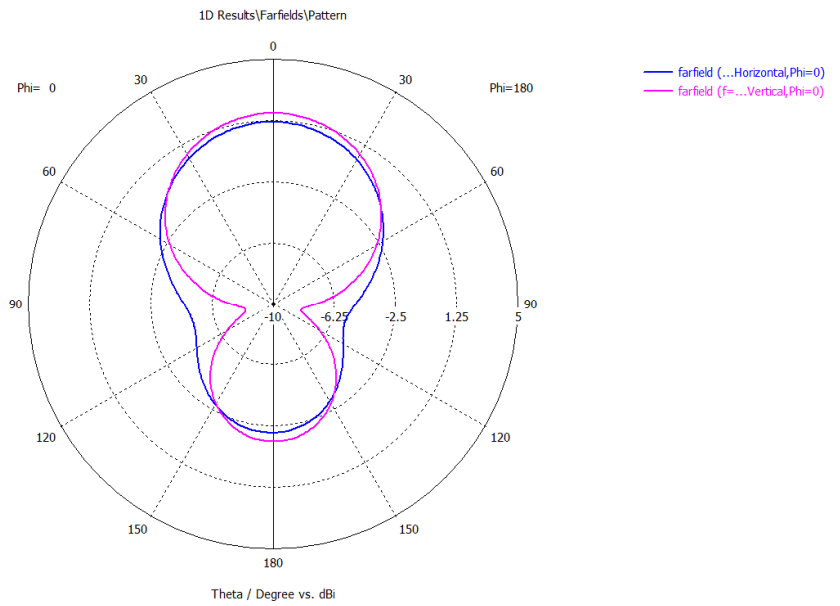


Fig. 5-21: E plane radiation pattern Co-polar and Cross-polar cuts

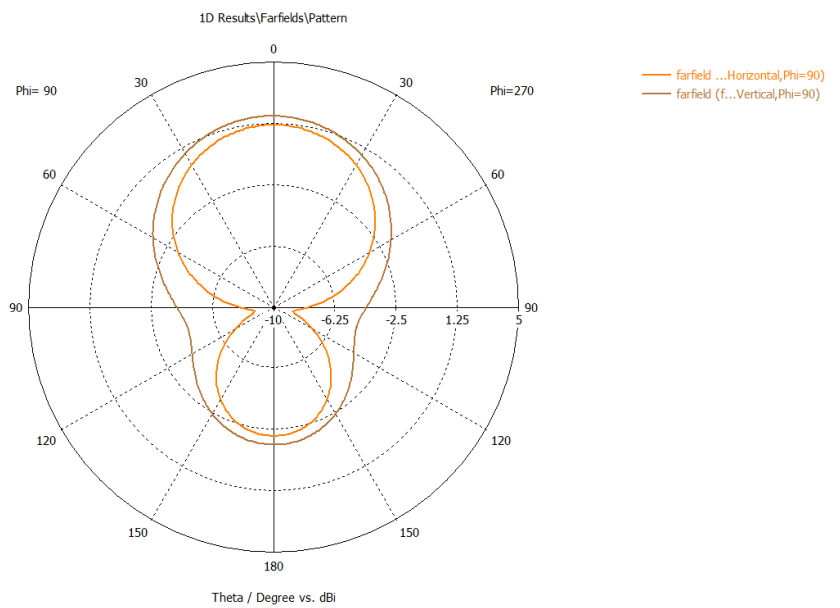


Fig. 5-22: H plane radiation pattern co-polar and cross-polar cuts

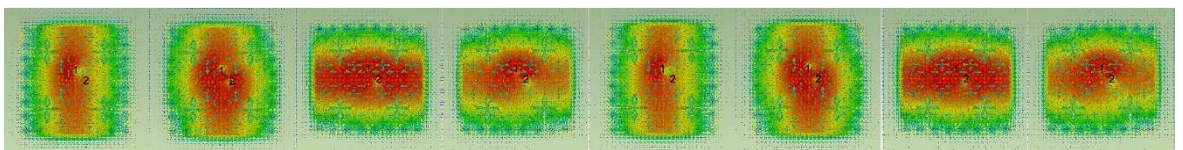


Fig. 5-23: Surface currents of Stanley fractal antenna from 0 degrees to 315 degrees in 45-degree intervals

5.3 Jerusalem Cross fractal antenna

5.3.1 Introduction to the fractal and its construction

The Jerusalem cross fractal was proposed to miniaturise the antenna size with fractal iteration. As fractal iteration increases, it contributes to the total electrical length of the antenna also known as the meandering effect as observed in the MLPF design. The Tau, Inverted Tau, Stanley, Maltese cross or the SFT did not contribute to meandering effect of the antenna, as such fractals were perforated such that the patch edge wasn't affected. The proposed design is to perforate a Jerusalem cross on the four sides of the patch and optimise its length so that it may be miniaturised.

Proposed Jerusalem cross element and proposed antenna are shown in Fig. 5-24 and Fig. 5-25.

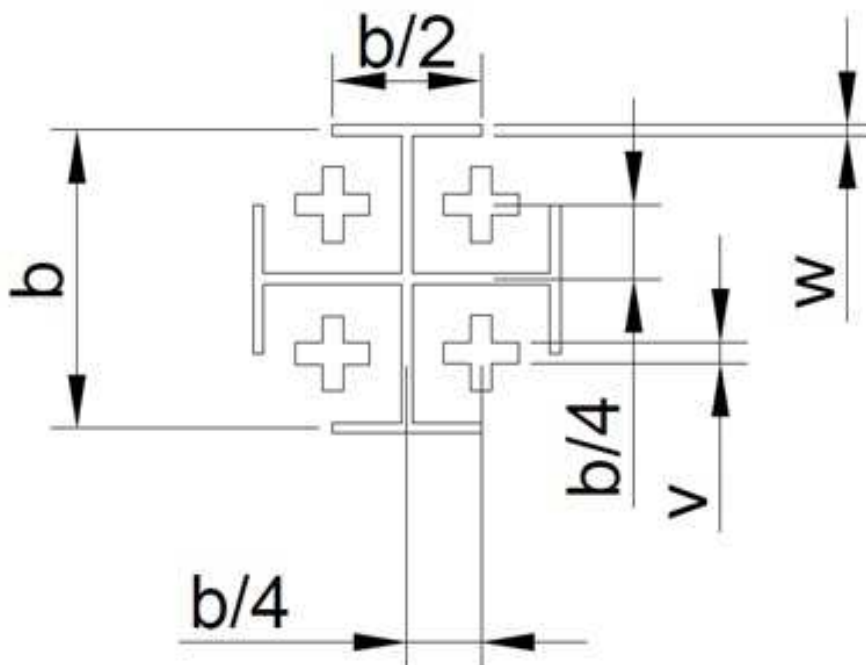


Fig. 5-24: Jerusalem cross element

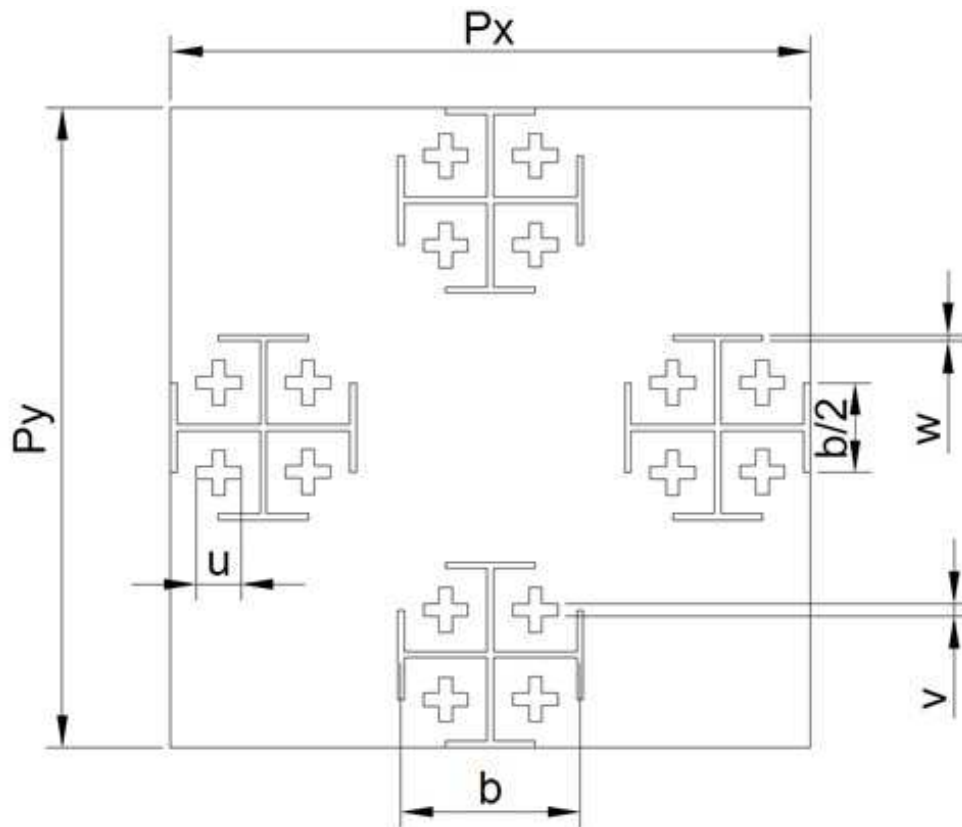


Fig. 5-25: Proposed fractal antenna

The dimensions of the patch, its length in y direction P_y measured in millimetres and width in x direction P_x measured in millimetres. The Jerusalem cross perforation element is translated vertically and horizontally to all four sides of the patch that it contributes to the total length of the radiating patch. As the length increases the frequency drops and in order to increase the frequency from the drop, the whole radiator needs to be scaled down and hence miniaturisation.

The arm lengths of the element are set to variable b whilst the lengths of small crosses within the element are set to variable u . The cross bar of the Jerusalem cross is set to half the value of b . Widths of large and small crossed elements are set to variables w and v respectively.

5.3.2 Proposed design and simulation results

Using the results obtained in designing previous antennae, the Jerusalem cross antenna was designed. A copper wall having a height of 5 mm and a thickness of 0.45 mm was constructed as performed before in previous designs. The outer wire mesh of the coaxial ports was also modelled. The CST model of Jerusalem cross is shown in Fig. 5-26.

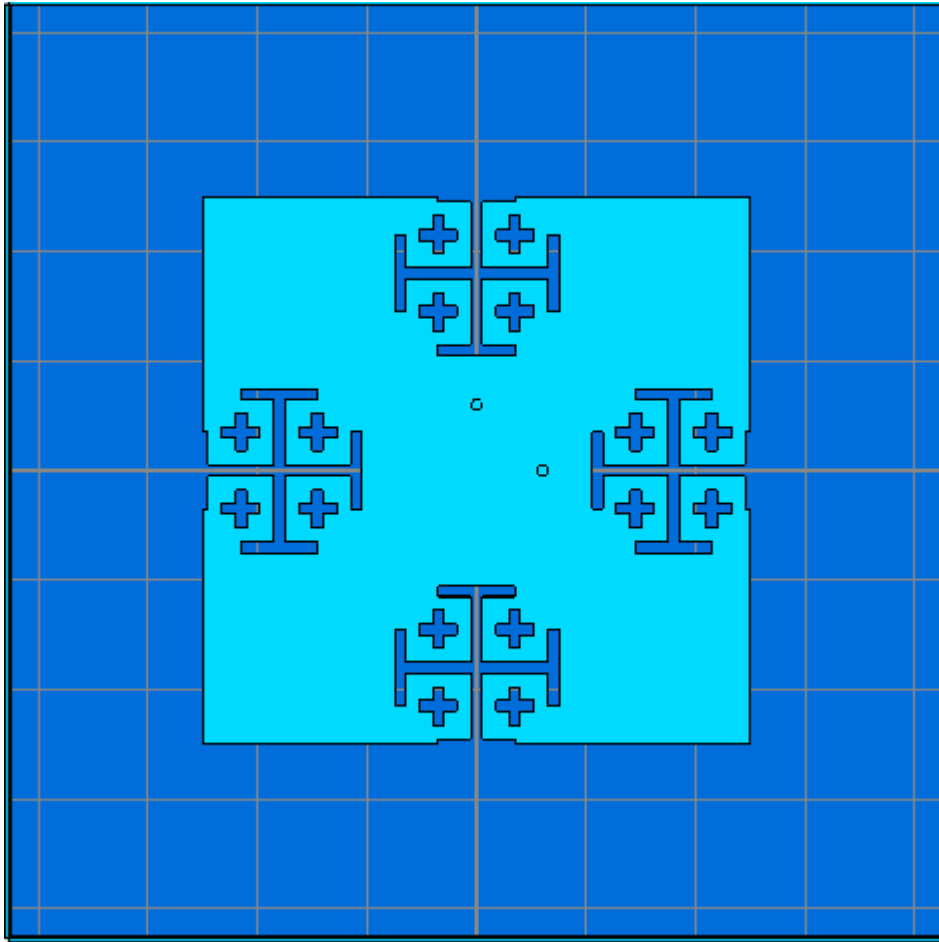


Fig. 5-26: CST model of Jerusalem cross fractal antenna

The following simulations were done in order to obtain the desired performance of the antenna.

The patch was initially set to 50 mm with a ground plane of 80 mm. Widths parameters w and v (of cross bar and small crosses) were both set to 1 mm. Results are tabled in Table 5-4.

Table 5-4: Simulation results for Jerusalem cross fractal antenna

Patch size (mm)	Parameter 'b' (total length Jerusalem cross element)	Coaxial port location coordinate (x,y) in mm	Resonant Frequency (MHz)	Return loss S11 (dB)
50	16	(6,6)	790.0	-15.951
45.4	16	(5,5)	801.8	-14.98
42	12	(6,6)	1013.5	-6.788
50	12	(6,6)	935	-12.117
50	14	(6,6)	865.6	-15.257

Directivity of final design was 4.427 dBi and the 3dB beam widths at phi=0 and phi=90 were 104.9 and 105.1 degrees. The antenna is circularly polarised with an error of 0.2 degrees. The return loss S11 against frequency with a bandwidth of 5 MHz is shown in Fig. 5-27. The antenna efficiency is 80%. The fractional percentage bandwidth (FBW) of the antenna can be calculated using (30) as:

$$FBW = \frac{|f_H - f_L|}{f_C} \times 100 = \frac{868.23 - 863.44}{865.6} \times 100 = 0.553\%$$

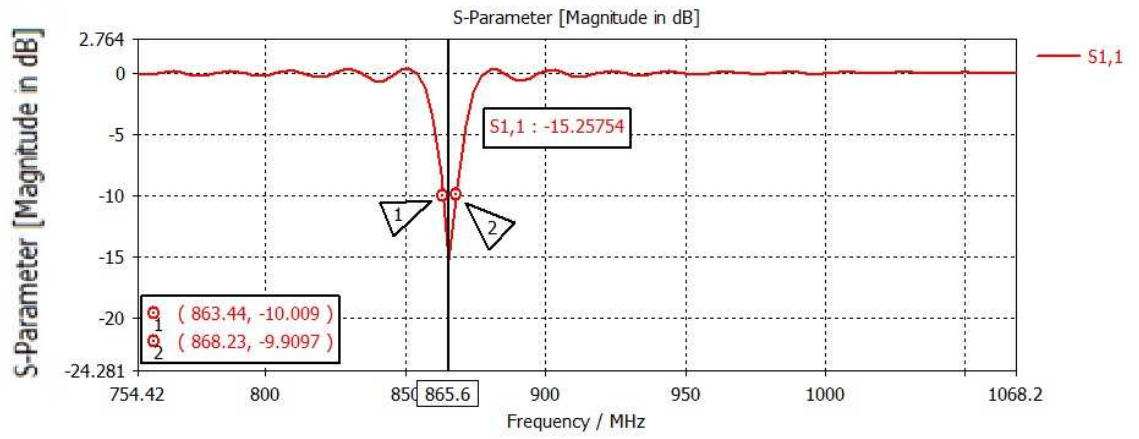


Fig. 5-27: S_{11} against frequency with a bandwidth of 5 MHz

The farfield radiation patterns are shown in Fig. 5-28 to Fig. 5-31.

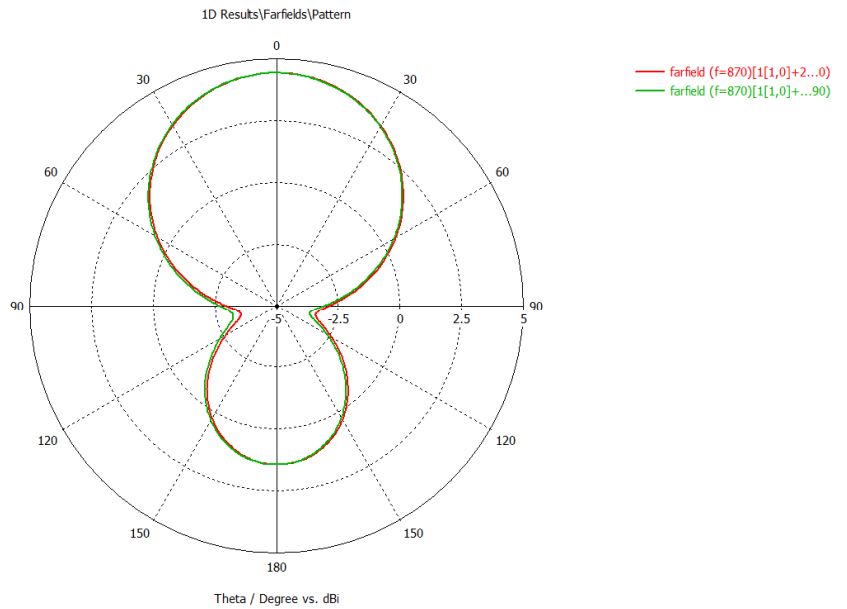


Fig. 5-28: E (Absolute) Farfield radiation patterns for $\phi=0$ and $\phi=90$ degree cuts

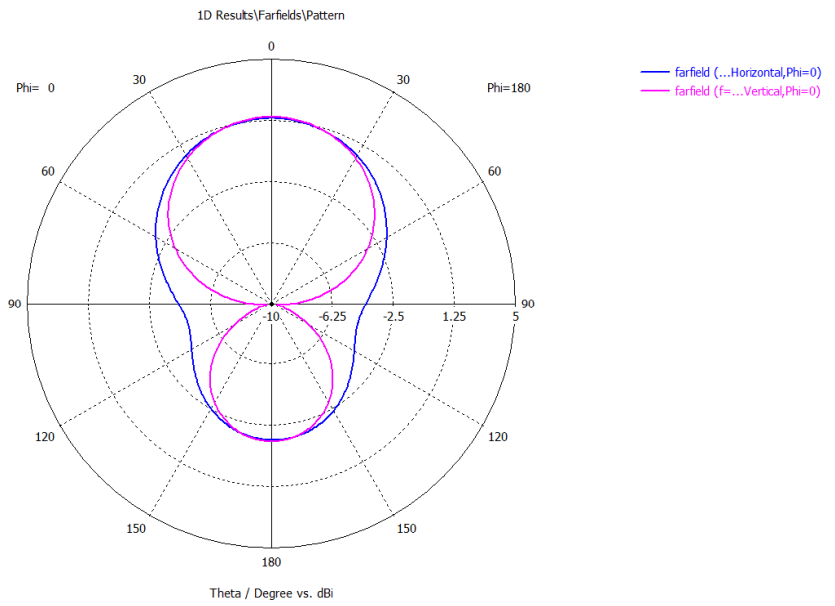


Fig. 5-29: E plane radiation pattern co-polar and cross-polar cuts

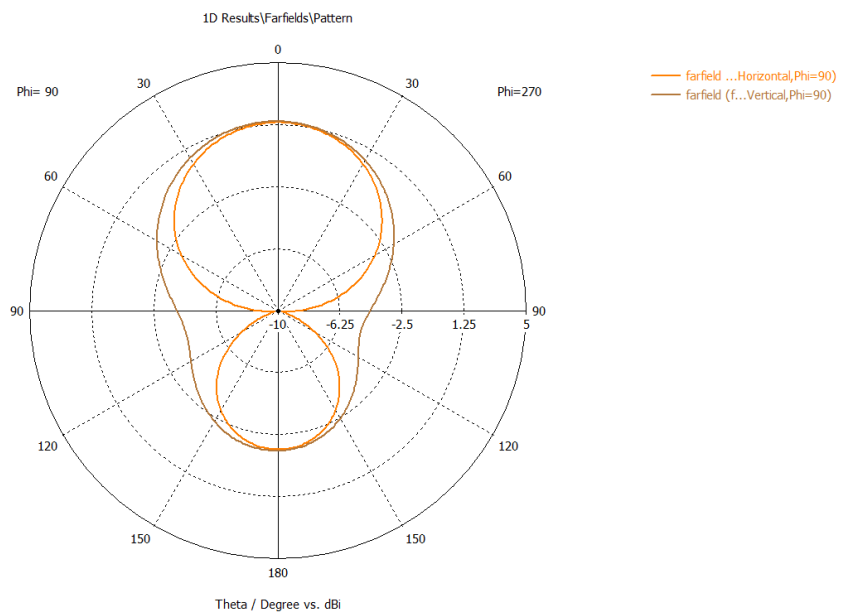


Fig. 5-30: H plane radiation pattern co-polar and cross-polar cuts

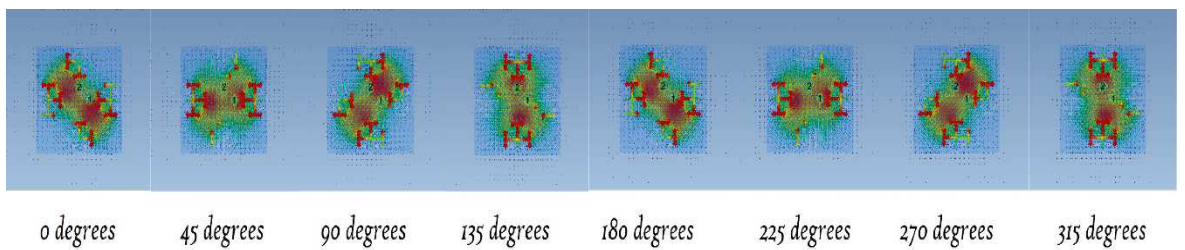
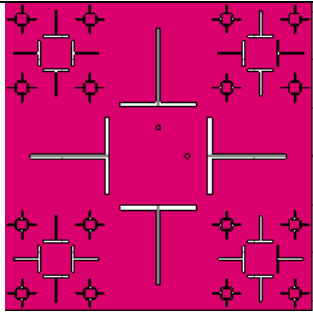
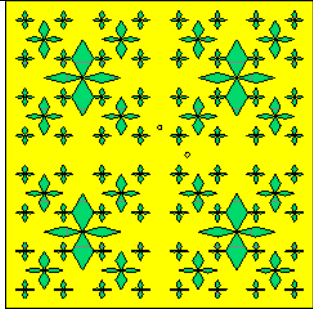
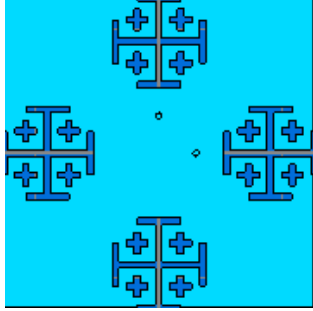


Fig. 5-31: Surface currents on Jerusalem cross fractal antenna

5.4 Summary of simulated results of proposed models

In this chapter, 3 novel antenna models were designed and simulated using CST Microwave Studio. 3 fractal patterns were applied to a microstrip patch antennae on a specialist PCB material RF60A, having a dielectric constant of 6.15. The dimensions of final designs are summarised below in Table 5-5.

Table 5-5: Final dimensions of Inv Tau, Stanley and Jerusalem Cross

Antenna	Image of patch	Patch size	Ground plane size	Coaxial port coordinate (X,Y) in mm
Inv Tau		64 mm	86 mm	(6,6)
Stanley		67 mm	86 mm	(6,6)
Jerusalem Cross		50 mm	85 mm	(6,6)

Antenna performances of designs are tabled below in Table 5-6 showing design criteria for an RFID doorway reader are met by these 7 novel designs. Both results of Chapters 4 and 5 are presented together for comparison.

Table 5-6: Antenna performances of final designs

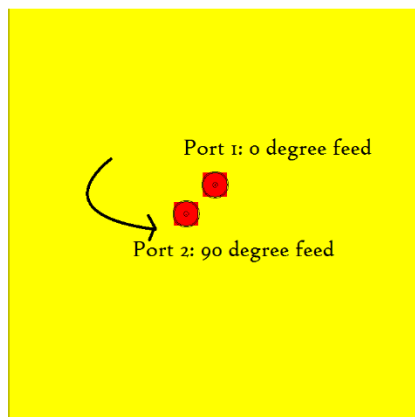
Design	Resonant Frequency (MHz)	S11 (dB)	Directivity (dBi)	VSWR	3dB Beamwidth at phi=0 degrees	3dB Beamwidth at phi=90 degrees	Bandwidth (MHz)
MLPF	874	-11.9	4.444	1.57	104.6	104.8	5
TAU	865.6	-14.2	4.400	1.49	106.0	105.1	5
SFT	871.4	-18.9	4.371	1.26	105.9	105.7	6
Maltese	874.3	-12.0	4.388	1.67	105.8	105.7	4
Inv Tau	865.6	-11.7	4.454	1.69	104.8	105.8	4
Stanley	868.5	-9.7	4.452	1.97	105.0	105.9	6
Jerusalem	865.6	-15.3	4.427	1.42	104.9	105.1	5

The port impedances port 1 (Z11) and port 2 (Z22) are tabled below in Table 5-7.

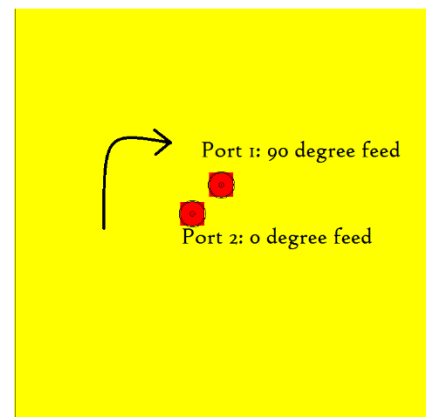
Table 5-7: Z11 port impedances of antenna designs

Antenna Design	Z11 port impedance (Ohms)	Z22 port impedance (Ohms)
MLPF	$(79.2565 - j36.0463)$	$(78.1479 - j36.2719)$
TAU	$(47.8851 + j12.7168)$	$(47.8852 + j12.7166)$
SFT	$(78.1868 - j11.3627)$	$(77.7477 - j11.0969)$
Maltese Cross	$(36.4486 + j2.2301)$	$(36.1745 + j1.8915)$
Inverted Tau	$(43.8118 + j18.1446)$	$(43.8256 + j17.7395)$
Stanley	$(36.6916 + j17.7324)$	$(35.1054 + j11.0916)$
Jerusalem Cross	$(93.1971 - j5.1619)$	$(93.2011 - j5.1622)$

Polarisation of the antenna Left hand circular polarised (LHCP) or Right hand circular polarised (RHCP) for all designs may be obtained by changing the 90-degree feed of the antenna, i.e., by changing the direction of lagging port excitation branch as shown in Fig. 5-32. Note: view from ground plane.



LHCP Left Hand circular polarisation



RHCP Right Hand Circular polarisation

Fig. 5-32: Change of polarisation from LHCP to RHCP by changing 90-degree feed

In Table 4-39, it can be observed that design criteria set in Table 4-3 have been achieved for all proposed designs and are suitable for prototype build and performance

test, as simulation results have achieved requirements for an RFID doorway reader antenna.

The patch size for a standard 870 MHz antenna theoretically calculated in Chapter three gives a length of 91.1 mm and a width of 69.1 mm for RF60A PCBs having a dielectric constant of 6.15. For FR4 which is standard PCB material having a dielectric constant of 4.3, these values are 105.8 mm and 82.5 mm. These are tabled in Table 5-8.

Table 5-8: Miniaturisation due to high dielectric substrate

For an 870 MHz patch	FR4 ($\epsilon_r = 4.3$)	RF60A ($\epsilon_r = 6.15$)
Length	105.8 mm	91.1 mm
Width	82.5 mm	69.1 mm

This is a 27.9% size reduction in surface area of the patch.

By applying fractal patterns, this was further reduced from a lowest of 45 mm x 45 mm and a highest of 67 mm x 67 mm. This is a further 67.8% to a 28.7% size reduction. Thus, resulting in a 76.8% and a 48.5% of total size reduction in surface area of the patch.

The dimensions of the antenna including the dielectric and ground plane are 86 mm x 86 mm x 3.2 mm which is compact enough to be mounted on a standard doorframe.

The Minkowski-Like Pre-Fractal was suggested due to its meandering effect which adds to the electrical length of the antenna. For each iteration, the electric length of the antenna increases and hence miniaturisation is possible. The MLPF design resulted with the smallest patch size of 45 mm x 45 mm. Jerusalem cross has a meandering effect much larger than the Minkowski-Like Pre-Fractal as in one iteration it adds a considerable length to the patch. Where MLPF took 3 iterations to achieve 45 mm patch

length resonating at 870 MHz, Jerusalem Cross was able to perform in one iteration resonating at 870 MHz with a length of 50 mm. Both designs resulted in similar antenna gain. However, the Jerusalem cross had the second-best return loss S_{11} of -15 dB out of all designs.

The Tau fractal antenna (Tau) and Inverted Tau fractal antenna (Inv Tau) were designed considering their lacunarity which is the spread factor of the fractal. This means, when fractal iteration increases the Tau fractal having a low lacunarity converges whilst Inverted Tau fractal with a higher lacunarity diverges. This has an effect on the electromagnetic beam emanating from the fractal. Both creating parasitic patch like squares radiate beams of higher frequencies off the patch. In Tau, said beams converge whereas in Inverted Tau the beams diverge. This has an effect in reading detuned tags in an RFID reader where tags are clustered. These multibeam resonating slightly higher than the frequency with frequency hopping provided by the RFID reader should be able to detect the undetectable tags in a field. Inverted Tau fractal however, like Stanley fractal antenna, had a poor return loss S_{11} closing enough to -10 dB whereas Tau fractal performed in a high return loss proving the transmission line.

Maltese Cross and Stanley fractal were considered in simulations for their unique ability to change the flare angle with which the surface currents could be controlled. Both comprising of sharp edges help to move surface currents fed from the ports towards the edges of the patch. Unlike in Tau and Inverted Tau where the vertical and horizontal bars block the surface currents and buffer the antenna efficiency. By changing the flare angles the antenna could be made electrically symmetrical to obtain a circularly polarised beam radiating from the patch of the antenna on top of the 2-port feeding mechanism implemented.

The space filling tree fractal antenna (SFT) though not contributing to meandering effect, has a unique feature. The Space filling tree fractal increases the slot length with

fractal iteration. It should be noted that in SFT it is the same slot which increases and not different slots as in Tau and Inv Tau fractals. This design has the best return loss of -18 dB and the lowest VSWR of 1.2, however with a large patch size. This is an interesting fractal to be tested on the RFID doorway reader.

Antennae are said to be circularly polarised if the two vertical planes are equally matched. This is measured by axial ratio. When axial ratio is greater than 1, antenna is said to be elliptically polarised. When axial ratio is infinite, then the antenna is linearly polarised. Circularly polarised antennae ideally have an axial ratio of 1 i.e. when two vertical planes are identical. These are tabled in Table 5-9. Showing all antennae are circularly polarised as they are close to 1.

Considering all designs, it can be noted that fractal patterns which do not contribute to meandering effect could not be miniaturised below 60 mm and where meandering effect contributed directly, they could easily be miniaturised to 50 mm or below having the same antenna gain.

Table 5-9: Axial Ratios of simulated antenna design

Antenna design	Axial Ratio
MLPF	1.20
Tau	1.30
SFT	1.24
Maltese	1.09
Inv Tau	1.28
Stanley	1.09
Jerusalem Cross	1.10

6 Prototype build and test

6.1 Introduction

This chapter demonstrates the prototype build and test of simulated antenna models in Chapter four. Based on simulations of 7 proposed designs in Chapter 4, 4 designs were chosen to be prototyped and tested for performance, as a proof of concept of its suitability for an RFID doorway reader system. Mits PCB milling machine was used to build these prototypes on specialised RF friendly boards 'RF60A' (Appendix A) having a high dielectric constant of 6.15. Two designs namely Maltese Cross and Stanley fractal antenna were not compatible for Mits PCB machine, as these designs require precise manufacturing since they comprise sharp angles which a 60-degree milling bit cannot accurately mill. Instead the machine would rub out the sides and edges and leave out copper bits remaining. These could be manufactured by industrial board manufacturer however; this is not within the scope of this research.

Considering simulation performances Inverted Tau fractal was left out due to wide beamwidth and large patch size. The following designs were chosen to be prototyped and tested:

1. MLPF antenna
2. Tau fractal antenna
3. SFT antenna
4. Jerusalem cross fractal antenna

A standard commercially available patch antenna is tested for performance with same methodology as a control for this research. This chapter discusses calculation of electrical lengths and impedances required for both prototype building and experimental work, design of a Wilkinson power divider, Test methodology and sample size estimation and test results.

6.2 Calculations and design of power divider with extra 90-degree feeder at one port

Antennae designed for this project requires a power splitter with one end comprising of an extra 90-degree time phase shift for antennae to be circular polarised. A microstrip Wilkinson power splitter is designed to split power received from RFID reader via SMA connectors, where the extra quarter wavelength is added to one by crimping RG58 coaxial cable with the extra length, as shown in Fig. 6-1.

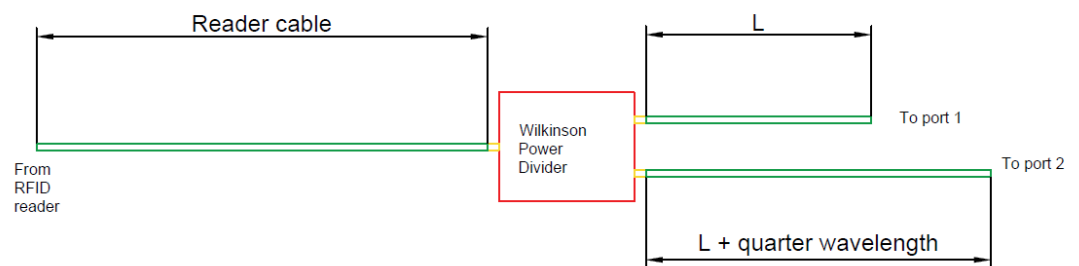


Fig. 6-1: Power splitter set up

The Wilkinson power divider is built on a normal FR4 PCB substrate with RG58 coaxial cables for reader and antenna port connections. A sketch of Wilkinson power splitter is shown in Fig. 6-2.

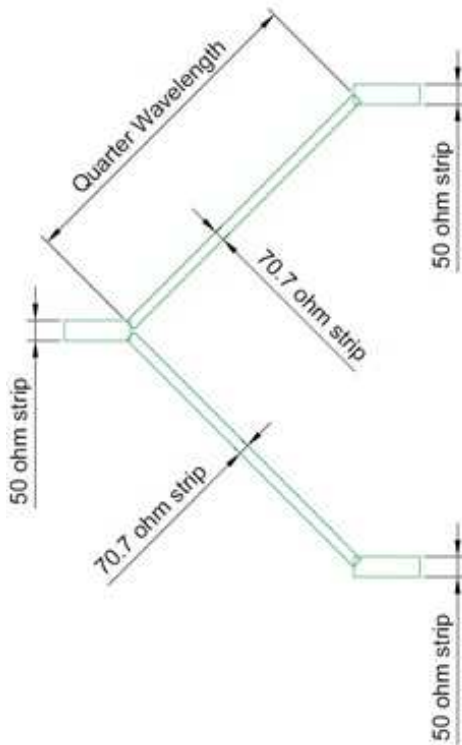


Fig. 6-2: Stripline wilkinson power divider

The following calculations are needed for the design of a power divider:

- a. Stripline width for 70.7-ohm characteristic impedance line
- b. Stripline width for 50-ohm characteristic impedance line
- c. Stripline length of a quarter wavelength element
- d. Coaxial cable length of a quarter wavelength element

6.2.1 Calculations of stripline widths and quarter wavelengths

6.2.1.1 Stripline width for 70.7 ohm and 50-ohm arms of the Wilkinson power divider

The characteristic impedance of a microstrip line is based on the width W of the stripline. This can be calculated by two methods. Since the calculation is analytically complex to solve, a numerical solver embedded in Mathcad Prime is used. This was later verified by an industrial software Microwave Impedance calculator MWI-2019 developed by the Rogers Corporation.

6.2.1.1.1 Method 1: Using microstrip fundamentals

As stated in equation (2), when Microstrip width and substrate height ratio W/H is equal or greater than 1, the microstrip is classified as a thin microstrip and hence equation (2) could be used to compute effective dielectric constant and characteristic impedance.

$$\epsilon_{reff} = \frac{\epsilon_r + 1}{2} + \frac{\epsilon_r - 1}{2} \times \left(1 + 12 \times \frac{H}{W}\right)^{-\frac{1}{2}}$$

$$\epsilon_{reff} = \frac{4.3 + 1}{2} + \frac{4.3 - 1}{2} \times \frac{1}{\sqrt{1 + \frac{12 \times 1.6}{1.6}}}$$

$$\epsilon_{reff} = 3.107628$$

The characteristic impedance of the stripline is given by

$$Z_0 = \frac{120 \times \pi}{\sqrt{\epsilon_{reff}} \times \left(\frac{W}{H} + 1.393 + \frac{2}{3} \times \ln\left(\frac{W}{H} + 1.444\right)\right)} \quad (60)$$

The board thickness of FR4 PCB is $H=1.6$ mm.

By calculation as well as Mathcad numerical solver, the following values for 70.7 ohm and 50-ohm lines were obtained. Results are tabled in Table 6-1.

Table 6-1: Stripline widths for 70.7-ohm and 50-ohm lines by Method 1

Characteristic Impedance (Z_0)	Stripline width (W)
70.7 ohms	1.6 mm
50 ohms	3.1 mm

6.2.1.1.2 Method 2: Using Wheeler's Equation

Wheeler's Equation published in 1978 revised for accuracy with additional variable of copper thickness t [86] can be used to calculate stripline width for a certain characteristic impedance. Instead of an effective dielectric constant, Wheeler's theory

is based on calculating an effective stripline width. The effective stripline width W_{eff} is given by

$$W_{eff} = W + \left(\frac{t}{\pi}\right) \times \ln\left(\frac{(4 \times e^1)}{\sqrt{\left(\frac{t}{H}\right)^2 + \left(\frac{t}{W \times \pi + 1.1 \times t \times \pi}\right)^2}}\right) \times \left(\frac{\epsilon_r + 1}{2 \times \epsilon_r}\right) \quad (61)$$

Value for t is set as 30 micro metres as FR4 boards are 1 oz copper cladded.

Two further parameters are defined thus

$$X1 = 4 \times \left(\frac{14 \times \epsilon_r + 8}{11 \times \epsilon_r}\right) \times \left(\frac{H}{W_{eff}}\right) \quad (62)$$

$$X2 = \sqrt{16 \times \left(\frac{H}{W_{eff}}\right)^2 \times \left(\frac{14 \times \epsilon_r + 8}{11 \times \epsilon_r}\right)^2 \times \left(\frac{\epsilon_r + 1}{2 \times \epsilon_r}\right) \times \pi^2} \quad (63)$$

Then characteristic impedance $Z0$ is given by the following equation and are tabled in Table 6-2.

$$Z0 = \frac{\left(\frac{1}{c \times \epsilon_0}\right)}{2 \times \pi \times \sqrt{2 \times (\epsilon_r + 1)}} \times \ln\left(1 + 4 \times \left(\frac{H}{W_{eff}}\right) \times (X1 + X2)\right) \quad (64)$$

Table 6-2: Stripline widths for 70.7 ohm and 50-ohm lines by Method 2

Characteristic Impedance (Z0)	Stripline width (W)
70.7 ohms	1.6 mm
50 ohms	3.1 mm

6.2.1.1.3 Method 3: Rogers Impedance calculator

Rogers impedance calculator in [87] gave the same results as by equations and are shown in Fig. 6-3 and Fig. 6-4.

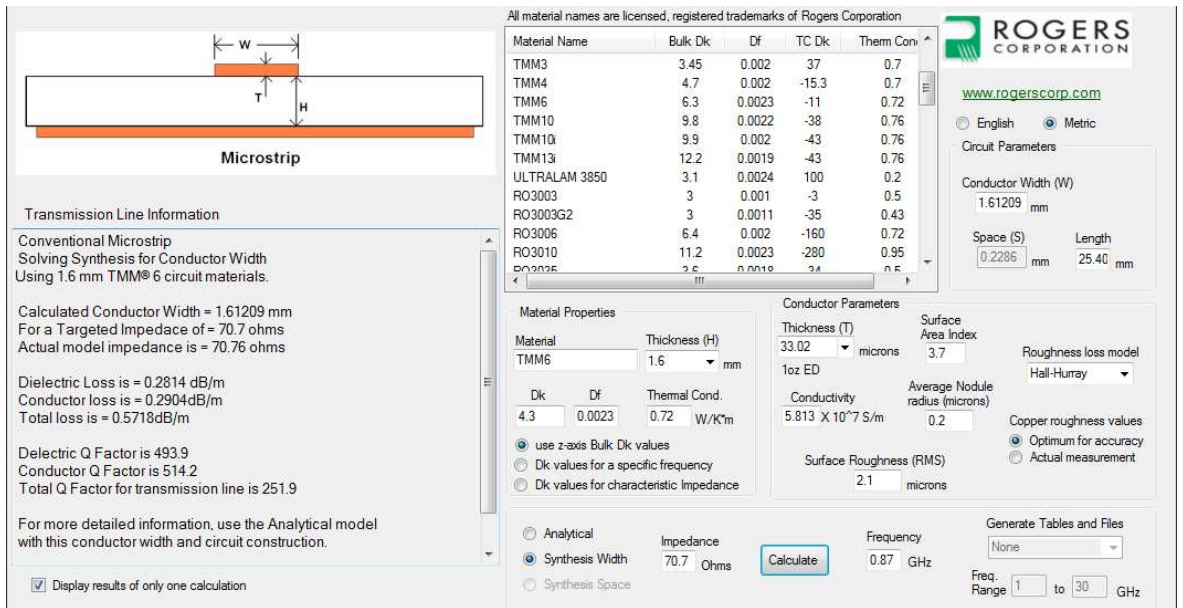


Fig. 6-3: Rogers Impedance calculator computing 70.7 ohm stripline width

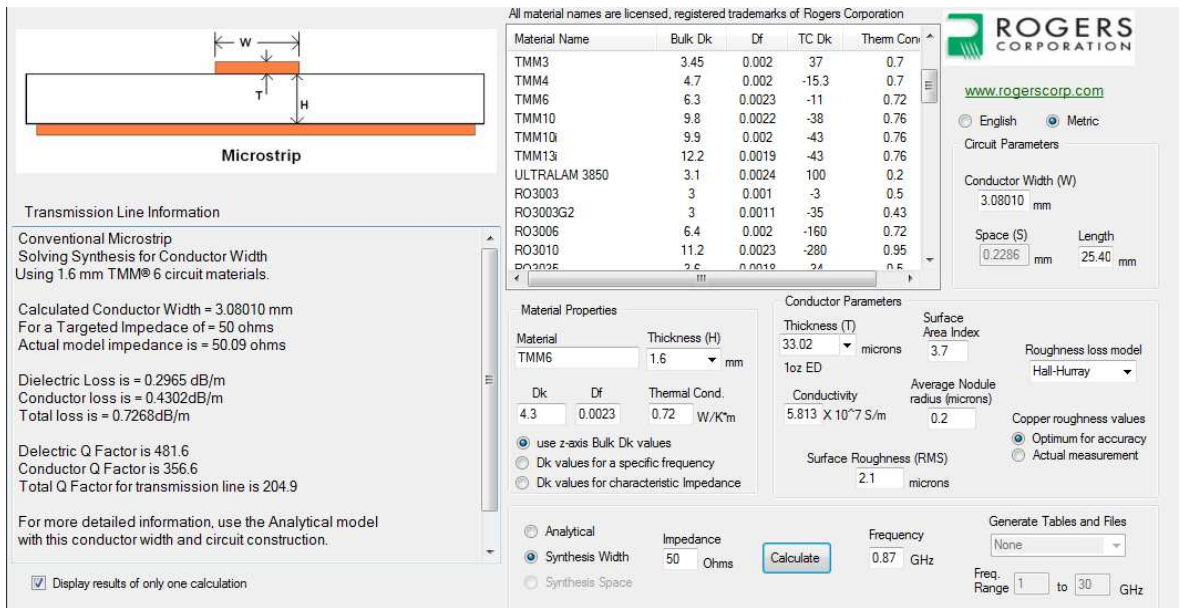


Fig. 6-4: Rogers Impedance calculator computing 50-ohm stripline width

6.2.1.2 Quarter wavelength calculations

In this section, quarter wavelengths for both coaxial cable and microstrip line are calculated which are needed to build the power splitter.

6.2.1.2.1 Quarter wavelength of a coaxial cable

The wavelength in free space at 870 MHz can be calculated using equation (7) as

$$wavelength = \frac{299792458}{870 \times 10^6} = 0.344589 \text{ mm}$$

And a quarter wavelength in free space at 870 MHz is calculated by using equation (8)

$$\frac{\lambda}{4} = 86.1 \text{ mm}$$

The coaxial cable has a velocity factor κ

$$\kappa = \frac{1}{\sqrt{\epsilon_r}} \quad (65)$$

where ϵ_r is the relative permittivity of Teflon sheath between inner and outer conductor. In a standard RG58/58 coaxial cable $\epsilon_r = 2.25$ thus $\kappa = 0.66$. Hence the effective wavelength of a wave travelling via a coaxial cable can be given as

$$\lambda_{eff} = \frac{(c \times \kappa)}{f} \quad (66)$$

$$\lambda_{eff} = \frac{c}{f \times \sqrt{\epsilon_r}} \quad (67)$$

$$\lambda_{eff} = \frac{299792458}{870 \times 10^6 \times \sqrt{2.25}}$$

$$\lambda_{eff} = 229.72 \text{ mm}$$

A quarter wavelength of a coaxial cable by equation (8) is

$$\frac{\lambda_{eff}}{4} = 57.432 \text{ mm}$$

6.2.1.2.2 Quarter wavelength of a microstrip for 70.7-ohm arm

Quarter wavelength of a microstrip line is required for 70.7-ohm arm of the Wilkinson power splitter. with a width of 1.6 mm on a standard FR4 substrate having a dielectric constant $\epsilon_r = 4.3$ and a board thickness of 1.6 mm can be calculated as follows:

Since $\frac{\text{stripline width } (W)}{\text{board height } (H)} = 1$, equation (2) can be used to calculate the effective dielectric

constant and thereby wavelength as shown below:

$$\epsilon_{reff} = \frac{4.3 + 1}{2} + \frac{4.3 - 1}{2} \cdot \frac{1}{\sqrt{1 + \frac{12 * 1.6}{1.6}}}$$

$$\epsilon_{reff} = 3.107628$$

Wavelength of a stripline can be calculated as shown below:

$$\lambda = \frac{c}{f \times \sqrt{\epsilon_{eff}}} \quad (62)$$

$$\lambda = \frac{299792458}{870 \times 10^6 \times \sqrt{3.107628}}$$

$$\lambda = 195.473 \text{ mm}$$

Using equation (8) a quarter wavelength can be calculated as below:

$$\frac{\lambda}{4} = 48.868$$

6.2.2 Wilkinson Power divider on PCB

Based on calculated results, a Wilkinson power divider needs to be designed with dimensions as shown in Fig. 6-5.

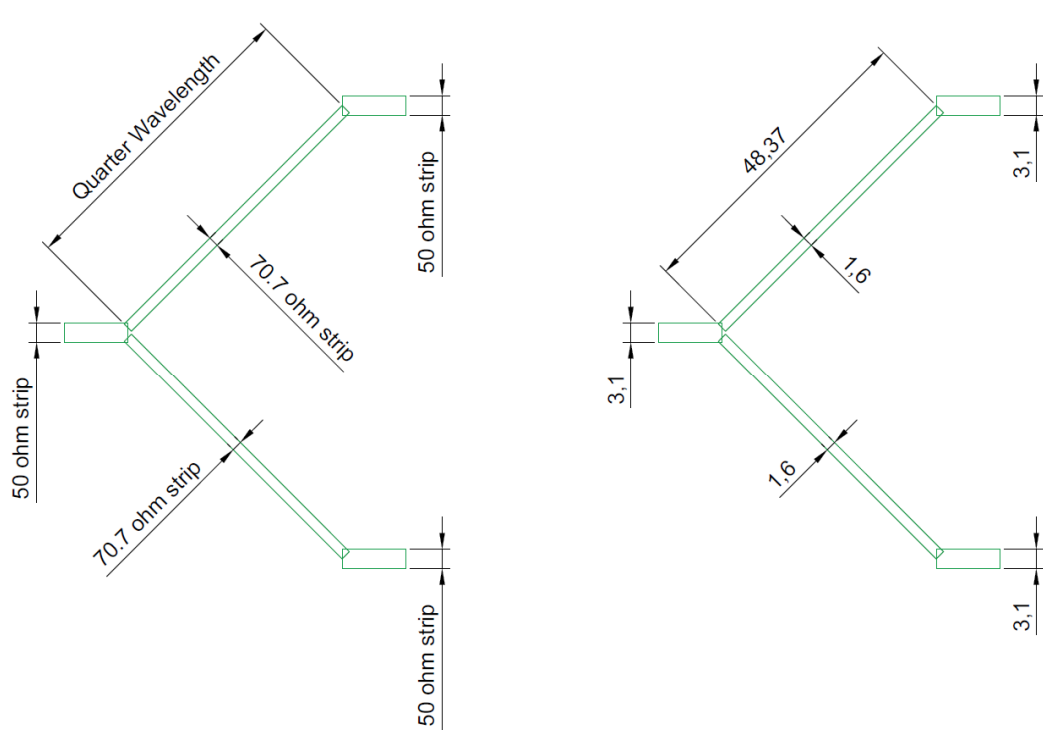


Fig. 6-5: Stripline dimensions for Wilkinson Power Divider

However, the Wilkinson Divider circuit comprises of a shunt connected to 100-ohm resistor between the ends of port 1 to port 2 as shown in Fig. 6-6.

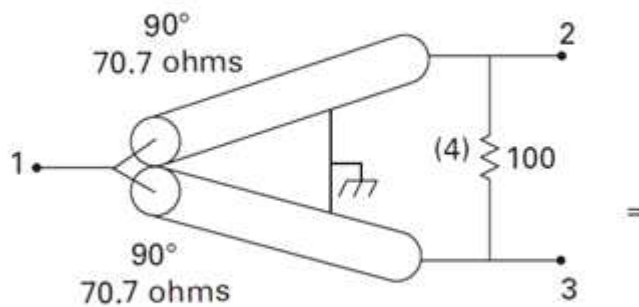


Fig. 6-6: Wilkinson Power divider circuit

Connecting a wire resistor or a long stripline adds an inductive element to the circuit thus resulting in impedance mismatch.

To rectify this issue, the 70.7-ohm arms are designed in a circular form that they may leave the gap between two ports to a feasible minimum that a surface mount resistor may be soldered straight to the two 70.7-ohm copper strips. A conceptual drawing for Wilkinson ring splitter is shown in Fig. 6-7.

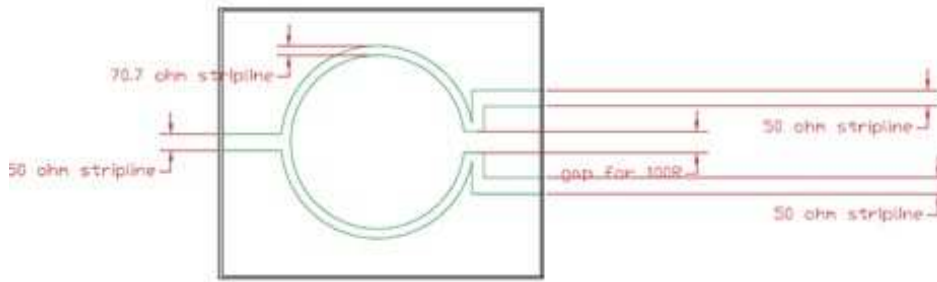


Fig. 6-7: Wilkinson ring splitter circuit

The 70.7-ohm arc lengths should be set to quarter wavelengths calculated above, i.e., 48.8 mm whilst thicknesses of 1.6 mm.

The gap left out is for the 100-ohm resistor and hence it is the remaining arc length which needs to be a quarter wavelength of 48.8 mm.

To complete the design, the radius of 70.7-ohm arm and its full angle should be computed as depicted in Fig. 6-8.

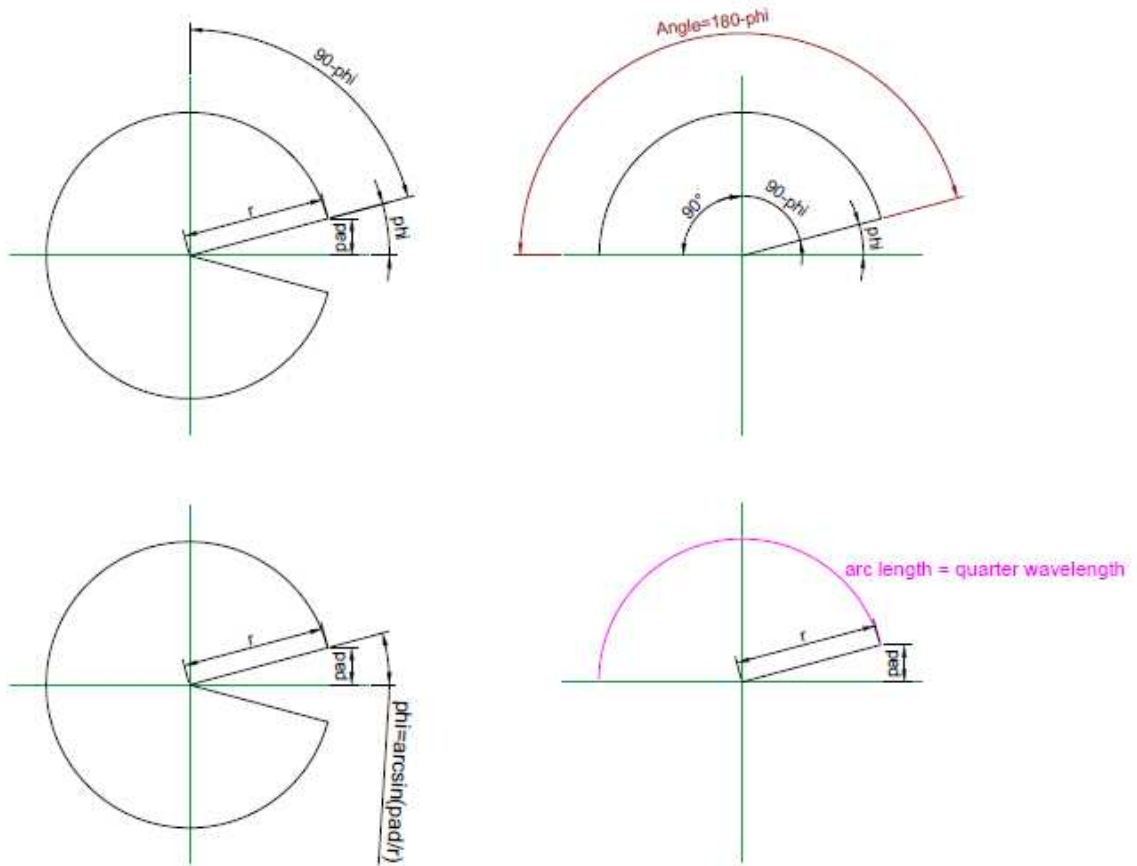


Fig. 6-8: Relationship between angle and radius

The angle between x axis and the top of 100-ohm resistor is ϕ whilst the total length set for 100 ohm resistor pads is pad . The Angle can be seen as

$$Angle = 180 - \phi \quad (68)$$

Where

$$\phi = \sin^{-1}\left(\frac{pad}{r}\right) \quad (69)$$

Where r is the mean radius of the 70.7-ohm line.

Therefore

$$Angle = 180 - \sin^{-1}\left(\frac{pad}{r}\right) \quad (70)$$

The arclength could be calculated by

$$arc\ length = \frac{Angle}{180} \times \pi \times r \quad (71)$$

Substituting equation (70) in equation (71) the arc length can be given as

$$arc\ length = \frac{180 - \sin^{-1}\left(\frac{pad}{r}\right)}{180} \times \pi \times r \quad (72)$$

The pad size is set to 2 mm. ($pad = 2\text{ mm}$)

The radius can be calculated when arc length is equal to a quarter wavelength.

Since Mathcad failed to compute results in this format, the equation is rearranged in radians

$$Angle = \pi - phi \quad (73)$$

$$Angle = \pi - \sin^{-1}\left(\frac{pad}{r}\right) \quad (74)$$

Substituting equation 180 with π in equation (71), the arc length could be obtained as

$$arc\ length = \frac{Angle}{\pi} \times \pi \times r \quad (75)$$

Is simplified to

$$arc\ length = Angle \times r \quad (76)$$

Substituting equation (74) in equation (76)

$$arc\ length = \left(\pi - \sin^{-1}\left(\frac{pad}{r}\right)\right) \times r \quad (77)$$

The pad size is set to 2 mm. ($pad = 2\text{ mm}$)

The radius can be calculated when arc length is equal to a quarter wavelength.

$$48.8 = \left(\pi - \sin^{-1}\left(\frac{2}{r}\right)\right) \times r \quad (78)$$

Using a numerical method this is computed to be 16.19 mm as shown in Fig. 6-9.

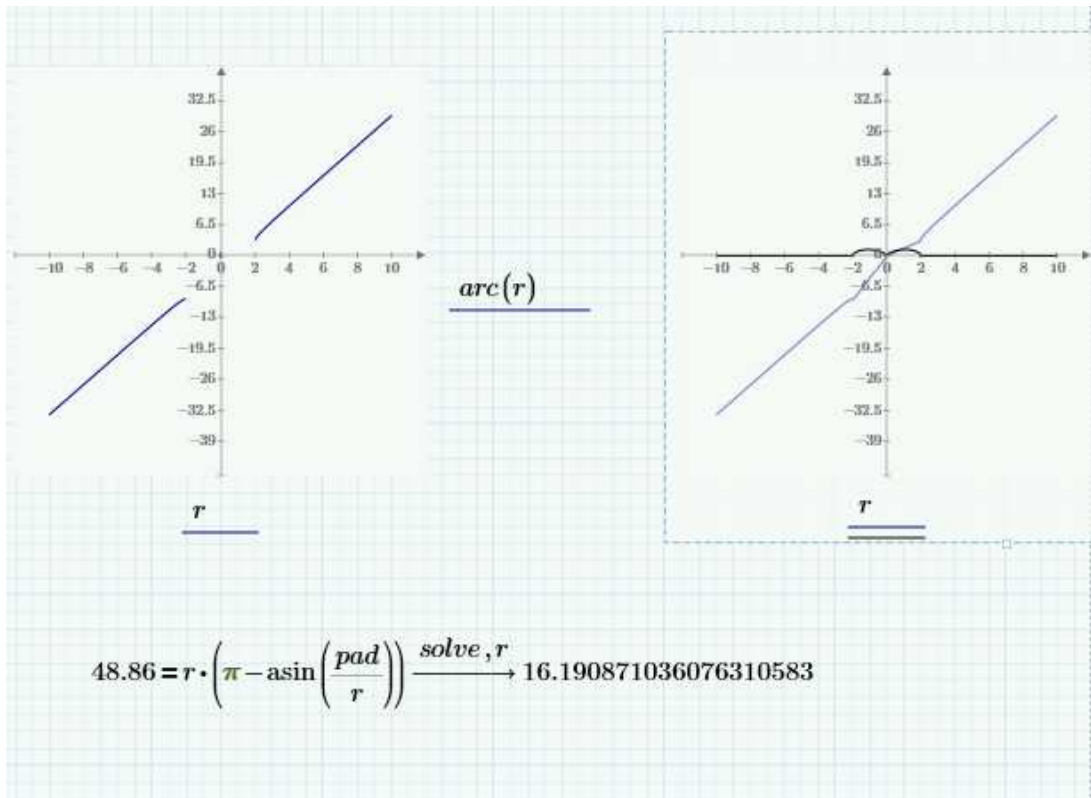


Fig. 6-9: Numerical solution obtained by Mathcad for radius $r=16.19$ mm

Final Wilkinson ring splitter dimensions are shown in Fig. 6-10.

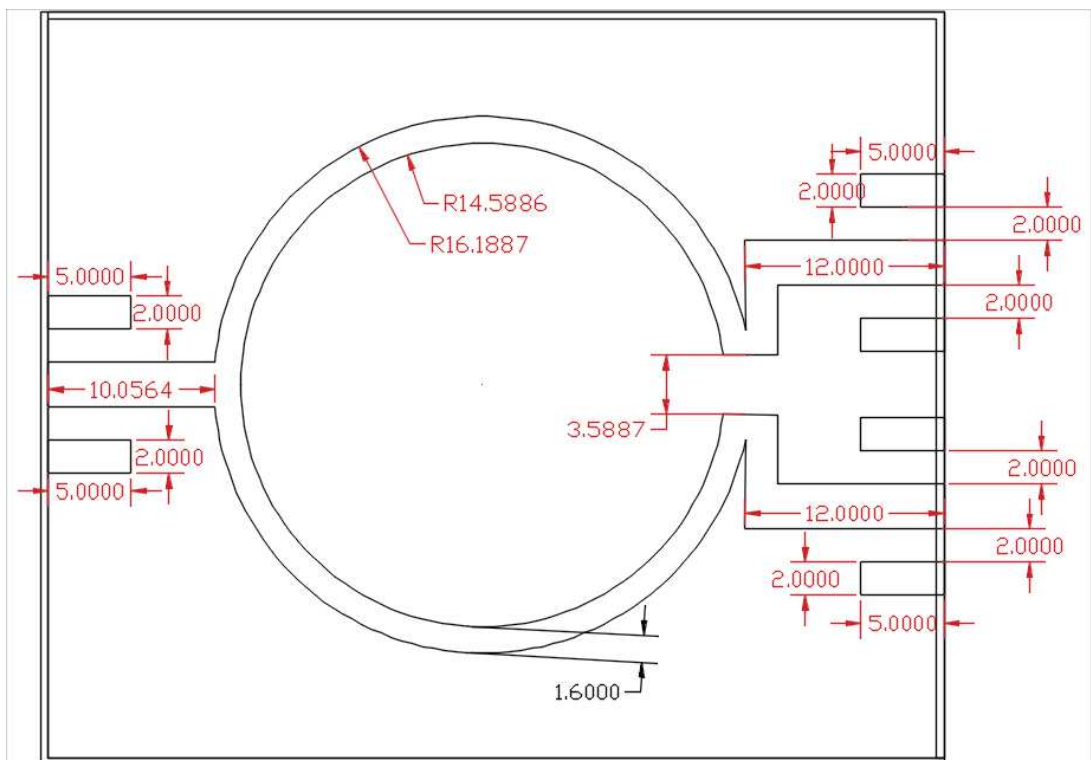


Fig. 6-10: Final dimensions of Wilkinson power divider

Here the 50-ohm pads having a width of 3.1 mm had to be reduced to 2 mm in order to connect SMA end launch connectors. This variation had to be compromised by stub tuning of the antenna. And SMA end launch connector sitting on PCB is shown in Fig. 6-11.

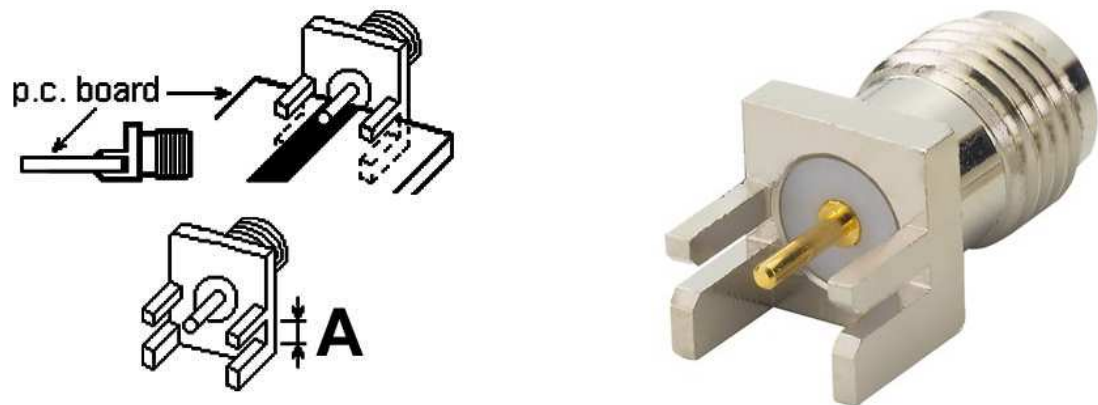


Fig. 6-11: SMA end launch connector

Generated Gerber file for designed Wilkinson power divider is shown in Fig. 6-12.

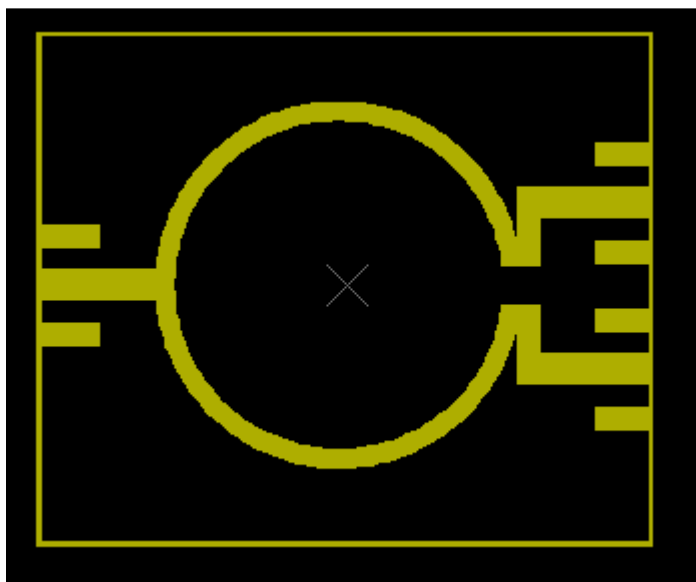


Fig. 6-12: Gerber for Wilkinson power divider circuit

The design was simulated using CST Microwave Studio software for S11, S12 and S13 responses at 859.8 MHz. This is since 100-ohm resistor is not modelled in the CST. The results are shown in Fig. 6-13.

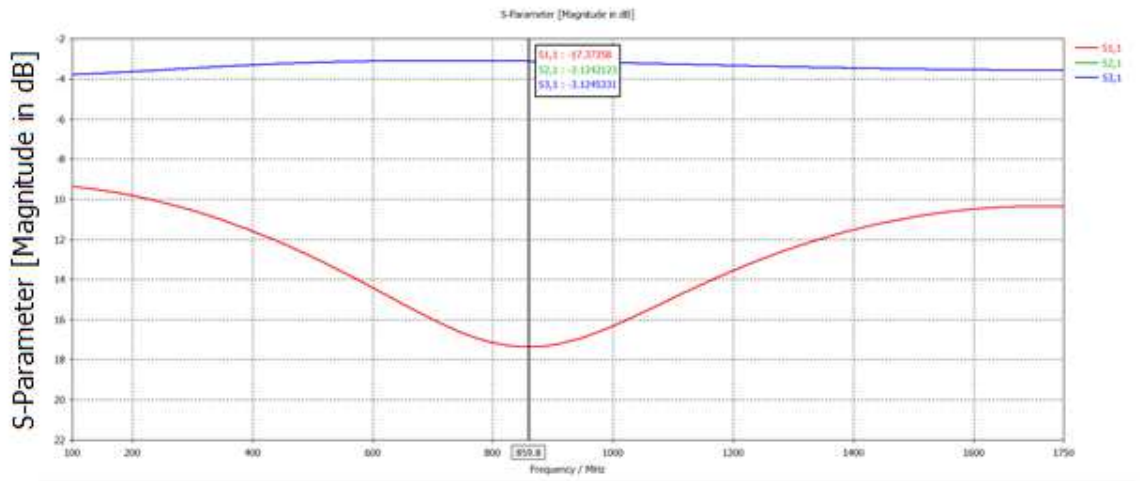


Fig. 6-13: S11 S12 and S13 response for proposed ring splitter

The design was then fabricated using Mits PCB milling machine. SMA connectors and 100-ohm resistor were soldered to the PCB as shown in Fig. 6-14.

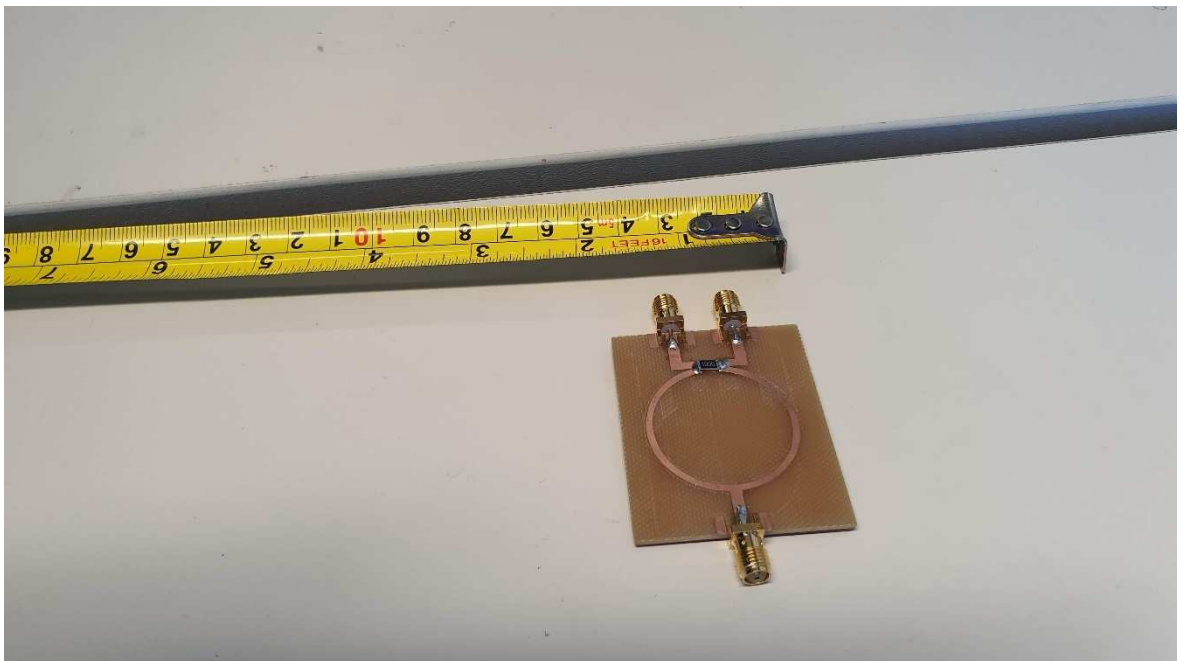


Fig. 6-14: Manufactured Wilkinson power divider with 100-ohm resistor

Wilkinson power divider with extra quarter wavelength set up is shown in Fig. 6-15.



Fig. 6-15: Full Wilkinson set up with extra quarter wavelength

6.3 Antenna prototype build

Gerber files for MLPF, TAU, SFT and Jerusalem cross antennae are shown in Fig. 6-16.

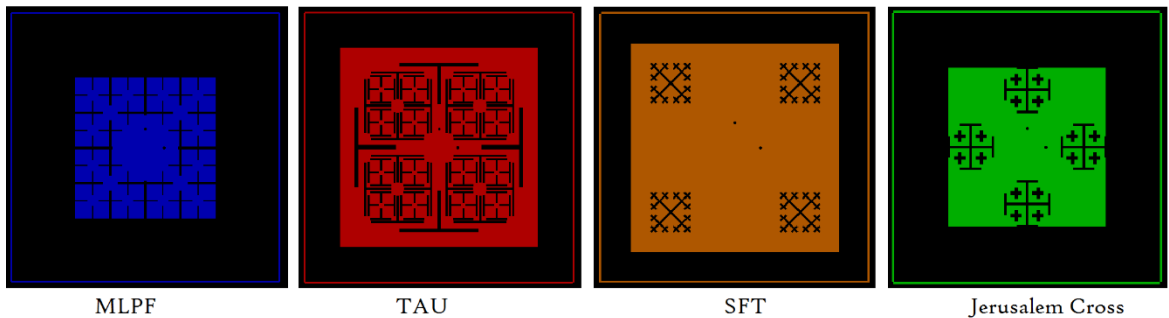


Fig. 6-16: Gerber files for MLPF, TAU, SFT and Jerusalem Cross fractal antennae

Gerber files were imported to Mits PCB milling machine, the outer square was set as the routing file with holes as the drill file. Specialist PCB RF60A boards were used to design these models.

PCB milling machine and PCB outputs are shown in Fig. 6-17 and Fig. 6-18.



Fig. 6-17: Mits PCB milling machine

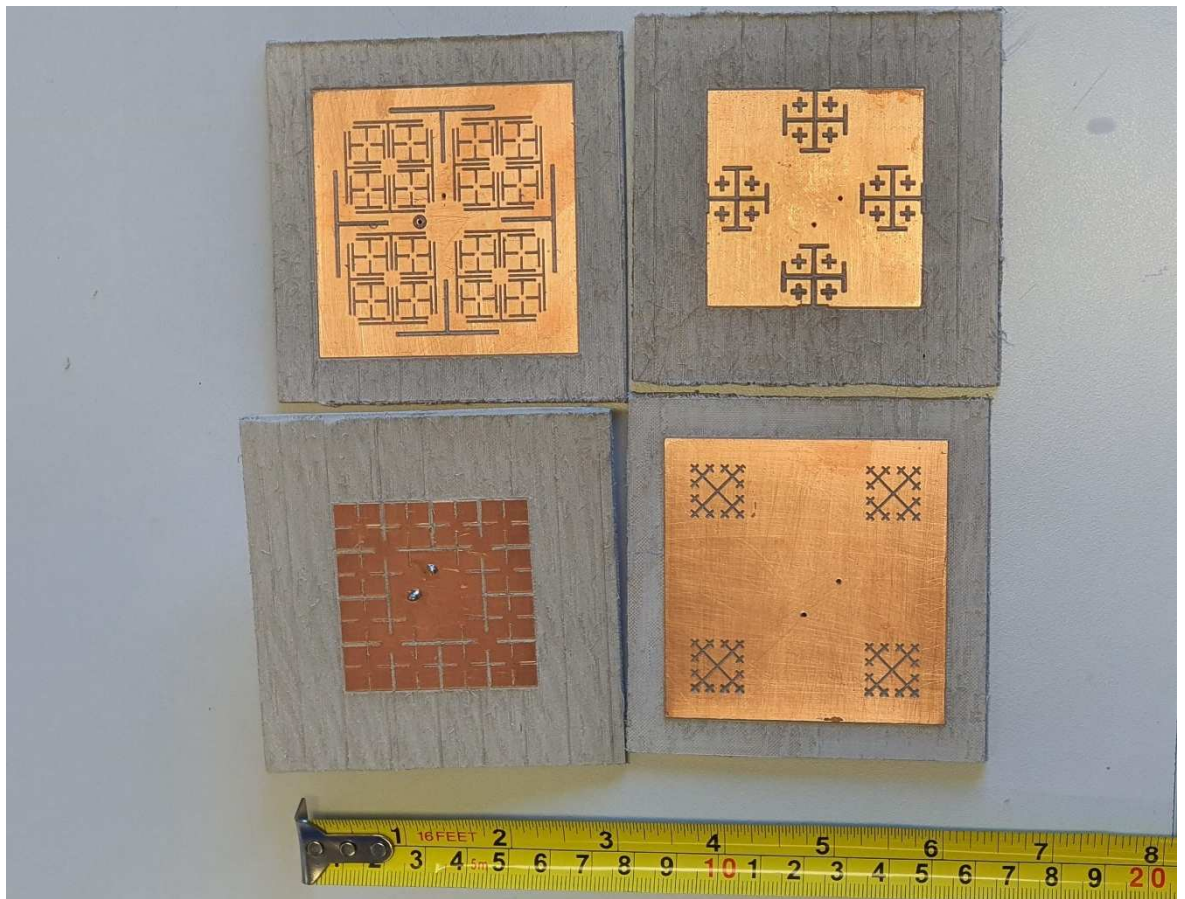


Fig. 6-18: Milled PCB antenna TAU, Jerusalem cross, MLPF and SFT

SMA connectors were soldered to the antenna. Using 0.45 mm thick 5 mm height copper strips, copper walls were built around all 4 antenna designs as shown in Fig. 6-19. These walls were attached to the PCB side with superglue since RF60A has a thickness of 3.2 mm.



Fig. 6-19: Copper wall built around the antenna

Using a Fieldfox Network Analyser, the following S11, Z11 and VSWR were measured at 870 MHz which is the intended resonant frequency to measure the deviation from simulations.

Z11 and Z22 of the port impedances were measured individually as shown in Fig. 6-20.



Port 1

Port 2

Fig. 6-20: Individual port impedances (Z_{11} and Z_{22}) measurement set up

The designed Wilkinson power divider with extra quarter wavelength set up was connected to two ports and impedance (Z), return loss (S_{11}) and VSWR were measured as shown in Fig. 6-21.



Fig. 6-21: Impedance, return loss and VSWR measurements with Wilkinson power divider and quarter wavelength set up

The results are tabled below for 870 MHz in Table 6-3.

Table 6-3: Measured antenna parameters at 870 MHz

Antenna	Z11 (Ohms)	Z22 (Ohms)	Z (Ohms)	S11 (dB)	VSWR
MLPF	281.2+j509.4	247+j290	82.1+j0.9	-12.49	1.627
Tau	67.2+j273	65.8+j272	87.6+j19.9	-10.30	1.881
SFT	57.5+j34.1	65.5-j6.6	82.6+j22.5	-10.442	1.882
Jerusalem Cross	35.6-j44	33.8-j57	57.4+j3.9	-19.11	1.218

To rectify the manufacturing error, a stub tuning method was used. This was done by plastering the radiating patch with small lead tape bits to obtain (50+j0) ohm impedance at 870 MHz as shown in Fig. 6-22.

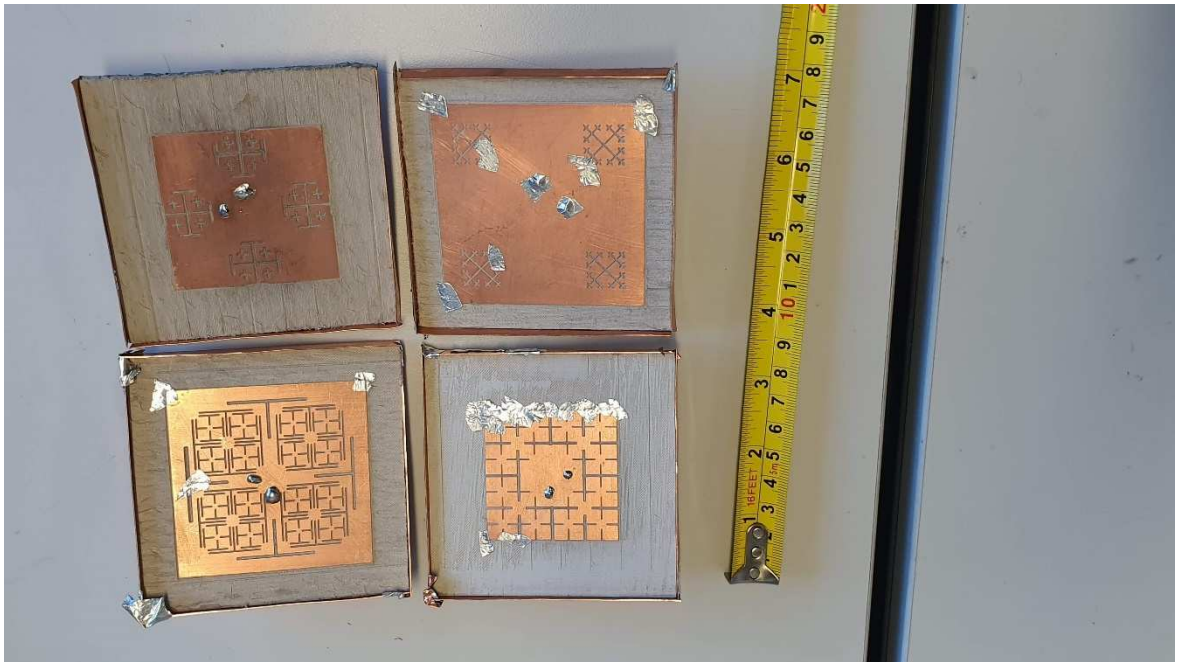


Fig. 6-22: Stub tuned antennae with copper walls ready for testing

6.4 Antenna performance testing

6.4.1 Test variables and methodology

6.4.1.1 Variables

The objective of this experiment is to evaluate RFID performance of 4 antenna designs applicable to a doorway reader system, as well as test commercially available patch antenna as a control for this research. A FEIG LRU 1002 long range reader is used to read paper padded folders which are tagged with RFID tags carried by a person by hand, walking through the doorway.

A free-standing wooden doorframe was constructed for this experiment as shown in Fig. 6-23.



Fig. 6-23: Wooden doorframe used to antenna testing

The test subject is to walk through the wooden doorframe and route back around maintaining the same direction. The walking route for testing is shown in Fig. 6-24.

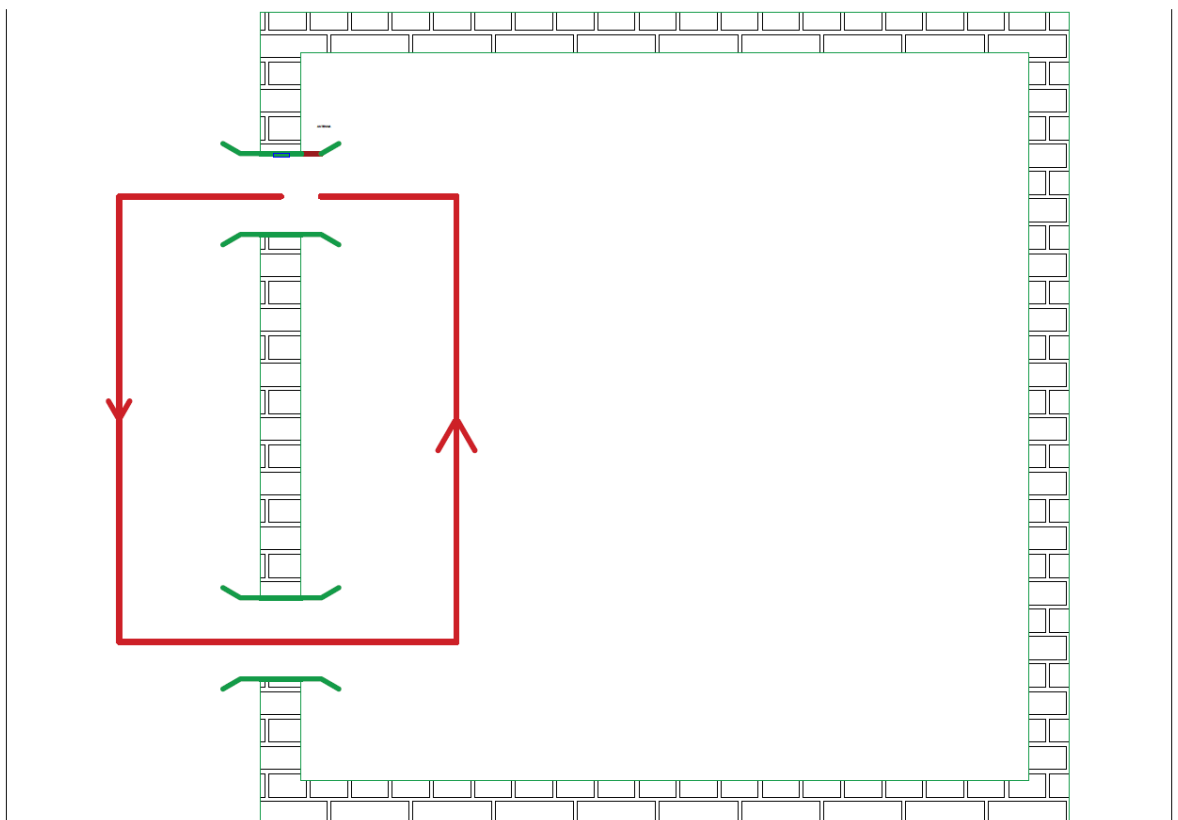


Fig. 6-24: Walking route (marked in red) of the test subject

The following test variables need to be considered for performance testing:

1. Number of antennae that needs testing (MLPF, Tau, SFT, Jerusalem Cross and an industrially available antenna)
2. Location of antennae. The antenna could be mounted on the top or sides of the doorway to cover the crucial region, i.e., the area between human chest and knee which covers most of file carrying positions. Single or two antennae may be used to cover this region effectively in different locations, as shown in Fig. 6-25. It must be noted since this is a doorway reader system and not a security gate, much importance and focus is given to the feasibility of the system design, whereas in security gates comprising high power portal-like large antennae are used to cover each and every inch of the doorway area.

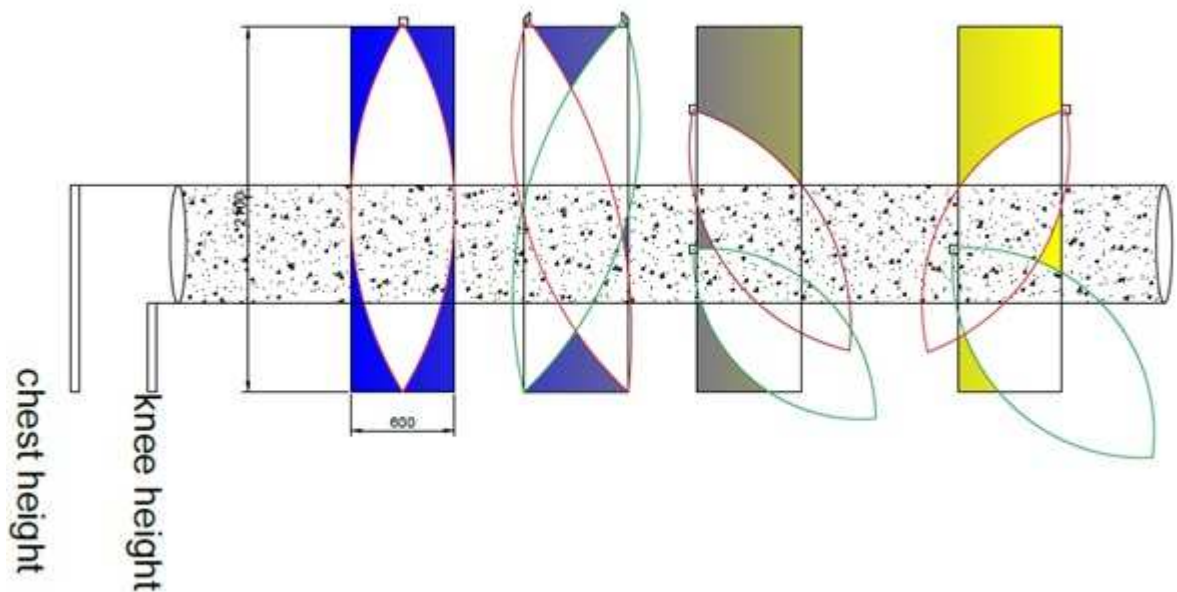


Fig. 6-25: Antenna locations on doorframe and radiation patterns covering chest to knee height

3. Tilt angle must be considered as the antenna beam needs to be steered to cover the chest-knee region. This is done by mounting the antenna by using a mechanical bracket which could be swivelled both vertically and horizontally. A car mobile phone holder was used to hold and mount the antennae to the doorframe as shown in Fig. 6-26. By this method the tilt angle could be varied if and when needed to steer the RF beam.



Fig. 6-26: Car mobile phone holder used as a bracket to hold antenna to the doorframe

4. The orientation of the tag is a major contributing factor to the test. A file carried in different ways could alter this orientation of the tag thus affecting the efficiency of the system. All antenna designs were circularly polarised to overcome this challenge and this needs to be tested for validation. There are three main orientations a file may be carried by a human as shown in Fig. 6-27. below. These orientations are holding the file flat to chest (XZ), holding the file by the side of body (YZ) and holding the file forth (XY)

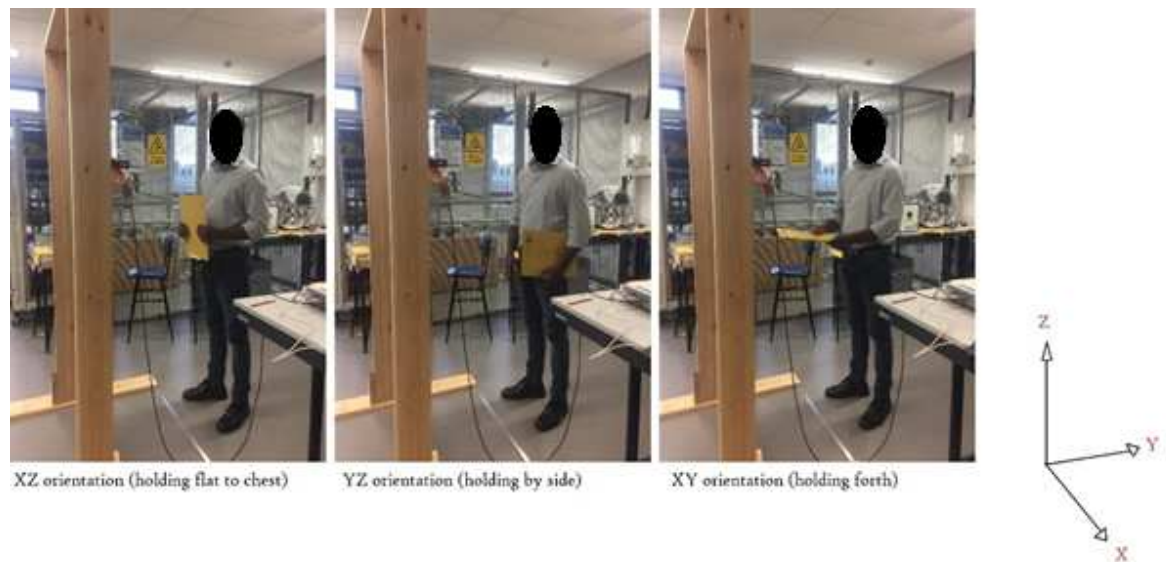


Fig. 6-27: File carrying orientations

- When carrying multiple files through the door passage they may be arranged in three different ways. Face to face, back to back or face to back as shown in Fig. 6-28.

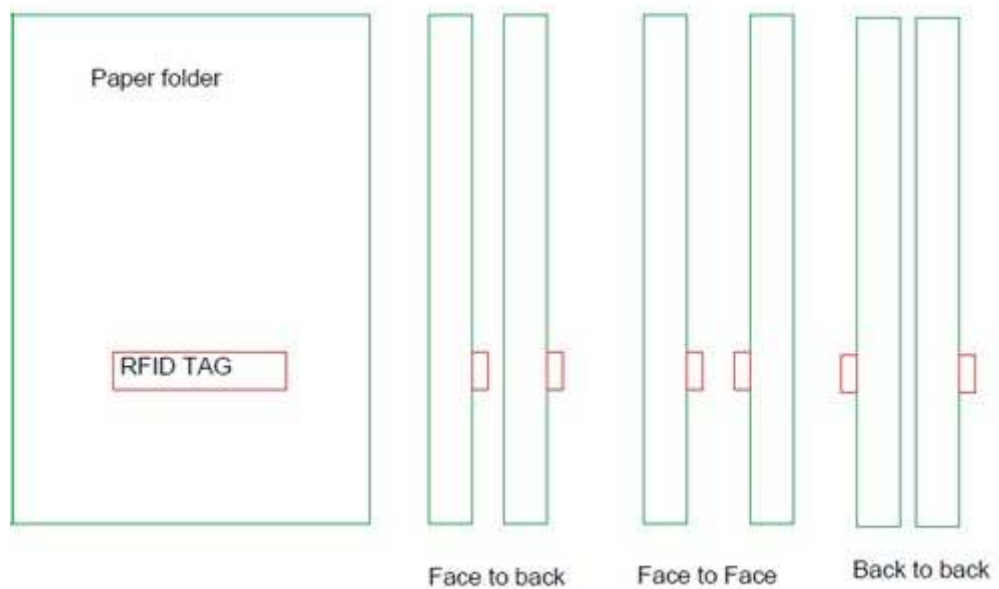


Fig. 6-28: Files may be clustered together in three different ways (Face to face, back to back and face to back)

This affects the efficiency of the doorway reader system, since antenna coils on the RFID tags show a mutual coupling when placed close to each other resulting in shifting their resonant frequencies, thus making it hard to detect. The coupling effect is highest when placed face to face and lowest when back to back. The thickness of the file also contributes to the coupling effect as it constraints the distance from one tag to another.

6. The number of files carried is another variable.
7. The travelling speed of the individuals walking through the door contributes to the efficiency of the doorway reader. Two feasible speeds may be considered, i.e., walking and running through the door passage.

6.4.1.2 Sample size calculation and test runs

Running a simple pilot test for a small sample size of 10, the estimate proportion of tag detection \hat{P} was obtained as 90% where error margin (confidence level) e was set to 10%. Using standard normal table, the sample size can be calculated as explained in [88], as:

$$n = \frac{Z_{\alpha}^2 \times \hat{P} \times (1 - \hat{P})}{e^2} \quad (79)$$

$$\frac{1.96^2 \times 0.9 \times (1 - 0.9)}{0.1^2} = 34.5744$$

This is the sample size.

If the above estimation of sample size (35) was used for variables discussed, the total amount of test runs which needs to be performed could be calculated as below in Table 6-4.

Table 6-4: Sample size estimation for 95% confidence interval

Number of antennae	5 (MLPF, TAU, SFT, Jerusalem & control)
Number of antenna positions	4 (Single on top, two on top, two on the same side, two on either sides)
File carrying orientations	3 (XY, YZ and XZ)
Number of files carried at one time	4 (up to four files)
Speed of travelling	2 speeds (walking and running)
Total combinations	$5 \times 4 \times 3 \times 4 \times 2 = 480$
Test runs for a 95% confidence level	$480 \times 35 = 16,800$

According to the above number, to achieve a 95% confidence interval, the test subject should travel through the doorway reader for 16,800 times with a laboratory footpath of 8 metres, the test subject would have to walk 134.4 km. Considering the antenna being an prototype (not industrially manufactured one) as well as the feasibility of research as a proof of concept, several variables were removed and reduced. The sample size was also reduced to 10 as shown in Table 6-5.

Table 6-5: Feasible sample size estimation

Number of antennae	5 (MLPF, TAU, SFT, Jerusalem & control)
Number of antenna positions	1 (Single on the side of door frame)
File carrying orientations	3 (XY, YZ and XZ)
Number of files carried at one time	4 (up to four files)
Speed of travelling	1 speed (walking only)
Combinations	$5 \times 1 \times 3 \times 4 \times 1 = 60$
Test runs with a sample size of 10	$60 \times 10 = 600$

According to the above table, the test subject would only need to walk through the door passage 600 times which is a sample of 100 files were tagged with RFID tags numbered 1 to 100. A random number generator was used to populate a random number table for selecting files for testing. The random number table is attached in Appendix C. The test subject picks 1, 2, 3, 4 files at a time and walks through the doorframe holding them in three orientations (XY, YX, XZ) for all five antennae. (MLPF, Tau, SFT, Jerusalem cross and control)

6.4.2 Test set up

The doorframe was set up inside a laboratory and re-tuned as detuning occurred by metallic objects in the vicinity. Tuning was performed by pasting lead bits on the patch of the antenna with the network analyser. The antennae were mounted on the side of the doorframe with the car mobile phone holder. The test set up comprising of power divider and FEIG LRU1002 reader connected to a laptop with a USB interface for the doorway reader are shown in Fig. 6-29 and Fig. 6-30.

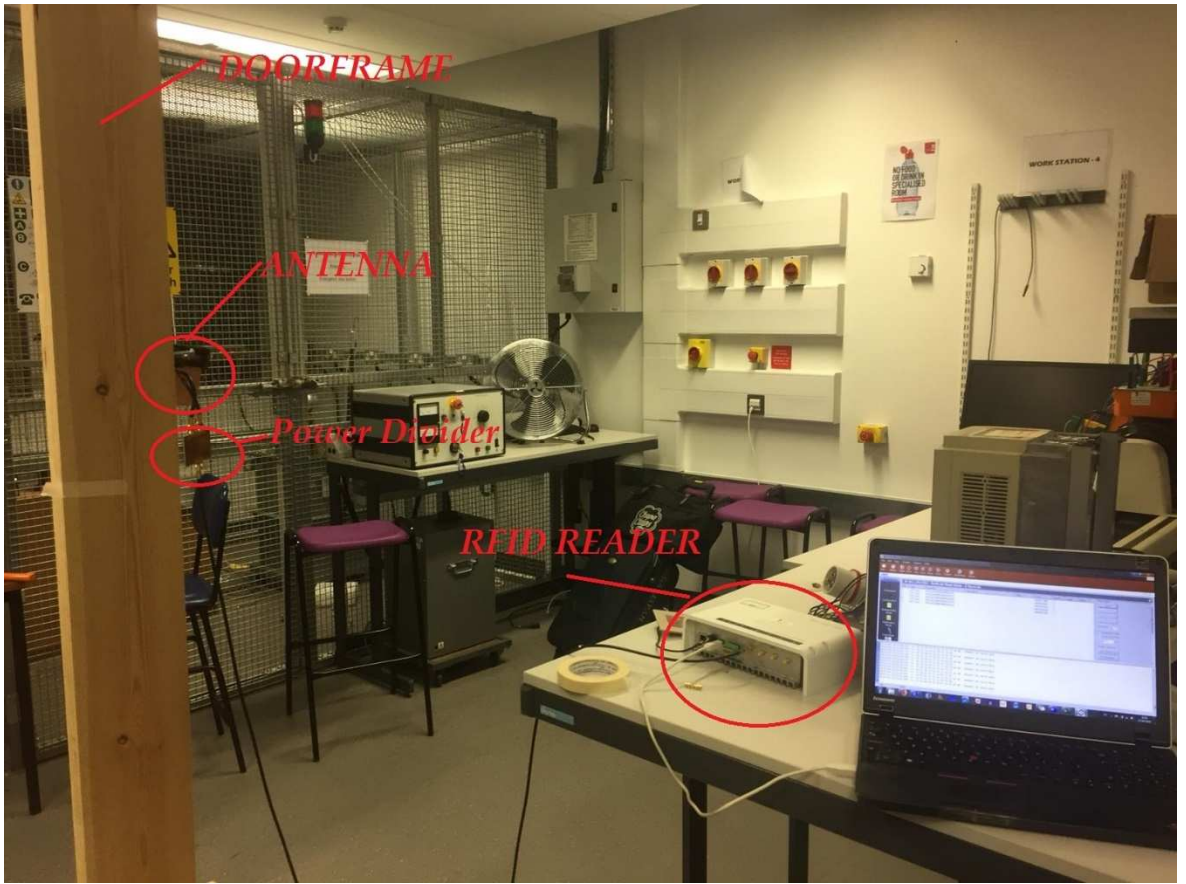


Fig. 6-29: Doorway reader test set up comprising of power divider and FEIG LUR1002 reader



Fig. 6-30: Doorway reader test set up comprising of power divider and FEIG LRU 1002 RFID reader

The length of the cable which connects the RFID reader to the antenna needs to be a multiple of wavelength of the operating frequency. For this test, an extra quarter wavelength was added to act as a quarter wavelength transformer. The multiple is set to 11. This was done as a rough estimate from RFID reader to door frame where the antenna is mounted. The length from RFID reader to antenna can be calculated as:

$$\text{Reader cable length} = 11 \times \lambda_{eff} + \frac{\lambda_{eff}}{4} \quad (80)$$

The effective wavelength can be calculated by using equation

$$\lambda_{eff} = \frac{c}{f \times \sqrt{\epsilon_r}}$$

$$\lambda_{eff} = \frac{299792458}{870 \times 10^6 \times \sqrt{2.25}}$$

$$\lambda_{eff} = 229.726 \text{ mm}$$

Hence the length of reader cable

$$\text{Reader cable length in milimetres} = 11 \times 229.726 + \frac{229.726}{4}$$

$$\text{Reader cable length} = 258 \text{ cm}$$

The RF output power of FEIG LRU 1002 reader was set 2 watts. The LRU1002 long range reader has four modes of operations. Host-mode, buffered read mode, notification mode and the scan mode. In host mode, the commands need to be sent to the reader step by step from the host. There is no automated multiplexing or triggering in this mode. The notification mode needs to define a standard data set for operations and only supports TCP/IP which is an automated read mode. In scan mode, read data is sent without buffering to the host immediately. The scan mode will only allow communication via USB after that the computer has detected the reader via RS232. Since the experiment necessitates only to detect the number of tags, the buffered read having an additional feature of clearing the buffer after each round of tag detection is used. Buffered read mode is shown in Fig. 6-31.

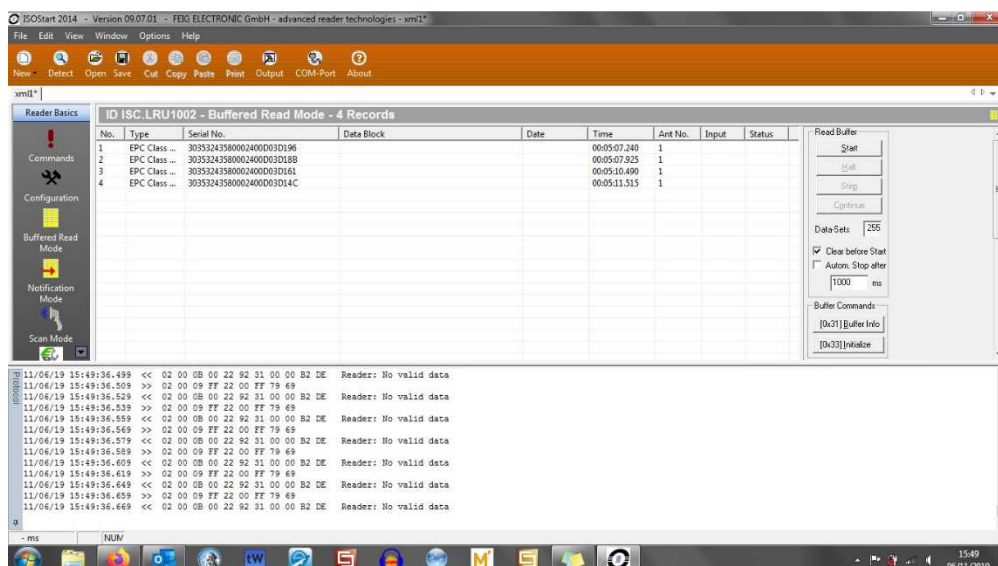


Fig. 6-31: LRU1002 reader operating in buffered read mode detecting tags passing through the doorway.

An UHF near filed patch antenna operating at 870 MHz with a gain of 6 dBi is used as a control for this experiment. The dimensions for this antenna are 23cm x 23cm x 4cm and this is a left-handed circular polarised design. The antenna parameters for Mobilemark PN8-868LCP-1C-WHT-12 are tabled in Table 6-6 and a picture of control antenna is shown in Fig 6-32.

Table 6-6: Antenna parameters for MobileMark PN8-868LCP-1C-WHT-12 antenna

Resonant Frequency (MHz)	Gain (dBi)	VSWR	3dB Beamwidth at phi=0 degrees	3dB Beamwidth at phi=90 degrees
865-870 & 902-928	6	1.5	70	70



Fig. 6-32: Control antenna (Mobilemark)

A sample format of completed risk assessment form, information sheet and consent letter used for this experiment, are attached in appendix B

6.4.3 Results

The results for MLPF, Tau, SFT and Jerusalem cross are tabled below.

Results of MLPF antenna are tabled in Table 6-7.

Table 6-7: MLPF performance table

ML PF	Flat to chest (XZ)				By body side (YZ)				Holding forth (XY)			
	1 Tag	2 Tags	3 Tags	4 Tags	1 Tag	2 Tags	3 Tags	4 Tags	1 Tag	2 Tags	3 Tags	4 Tags
1	1	2	3	4	1	2	3	4	1	2	3	4
2	1	2	3	4	1	1	3	4	1	2	3	4
3	1	2	3	4	1	2	3	4	1	2	3	4
4	1	2	3	4	1	2	3	3	1	2	3	4
5	1	2	3	4	1	2	3	3	1	2	3	4
6	1	2	3	4	1	2	2	2	1	2	3	4
7	1	2	3	4	1	2	3	4	1	2	3	4
8	1	2	3	4	1	2	3	4	1	2	3	4
9	1	2	3	4	1	2	3	3	1	2	3	4
10	1	2	3	4	1	2	3	4	1	2	3	4
	10/ 10	20/ 20	30/ 30	40/ 40	10/ 10	19/ 20	29/ 30	35/ 40	10/ 10	20/ 20	30/ 30	40/ 40
%	100%				93%				100%			

Results for Tau fractal antenna are tabled below in Table 6-8.

Table 6-8: Tau performance table

TA U	Flat to chest (XZ)				By body side (YZ)				Holding forth (XY)			
	1 Tag	2 Tags	3 Tags	4 Tags	1 Tag	2 Tags	3 Tags	4 Tags	1 Tag	2 Tags	3 Tags	4 Tags
1	1	2	3	4	1	2	3	4	1	2	2	4
2	1	2	3	4	1	2	3	4	1	2	3	2
3	1	2	3	4	1	0	3	4	1	2	2	4
4	1	2	3	4	1	1	3	4	1	2	3	4
5	1	2	3	4	0	2	2	3	1	1	3	2
6	1	2	3	4	0	2	2	3	1	1	3	2
7	1	2	3	4	0	2	3	4	0	2	3	4
8	1	2	3	4	1	2	3	4	1	2	3	4
9	1	2	3	4	1	2	3	4	1	2	2	4
10	1	2	3	4	1	1	3	4	1	2	3	2
	10/ 10	20/ 20	30/ 30	40/ 40	7/1 0	16/ 20	28/ 30	38/ 40	9/1 0	18/ 20	27/ 30	36/ 40
E %	100%				89%				90%			

The results for SFT antenna are tabled below in Table 6-9.

Table 6-9: SFT performance table

SF T	Flat to chest (XZ)				By body side (YZ)				Holding forth (XY)			
	1 Tag	2 Tags	3 Tags	4 Tags	1 Tag	2 Tags	3 Tags	4 Tags	1 Tag	2 Tags	3 Tags	4 Tags
1	1	2	3	4	1	2	3	4	1	2	3	4
2	1	2	3	4	1	2	3	4	1	2	3	4
3	1	2	3	4	1	2	3	4	1	2	3	4
4	1	2	3	4	1	2	3	3	1	2	3	4
5	1	1	3	2	1	0	3	3	1	2	3	4
6	1	2	3	4	1	0	3	3	1	2	3	4
7	1	2	3	4	1	2	1	3	1	2	3	4
8	1	2	3	4	1	1	3	3	1	2	3	4
9	1	2	3	4	1	2	3	4	1	1	3	4
10	1	2	3	4	1	2	1	4	1	2	3	4
	10/1 0	19/2 0	30/3 0	38/4 0	10/1 0	15/2 0	26/3 0	35/4 0	10/1 0	19/2 0	30/3 0	40/4 0
E %	97%				86%				99%			

The results for Jerusalem cross fractal antenna are tabled below in Table 6-10.

Table 6-10: Jerusalem cross performance table

Jerusalem cross	Flat to chest (XZ)				By body side (YZ)				Holding forth (XY)			
	1 Tag	2 Tag s	3 Tag s	4 Tag s	1 Tag	2 Tag s	3 Tag s	4 Tag s	1 Tag	2 Tag s	3 Tag s	4 Tag s
1	1	2	3	4	1	2	3	4	1	2	3	4
2	1	2	3	4	1	2	3	4	1	2	3	4
3	1	2	3	4	1	2	3	3	1	2	3	4
4	1	2	3	4	0	1	3	3	1	2	3	4
5	1	2	3	4	1	1	3	3	1	2	3	4
6	1	2	3	4	1	2	3	3	1	2	3	4
7	1	2	3	4	1	2	2	4	1	2	3	4
8	1	2	3	4	1	2	3	4	1	2	3	4
9	1	2	3	4	1	2	3	4	1	2	3	4
10	1	2	3	4	1	2	2	4	1	2	3	4
	10/ 10	20/ 20	30/ 30	40/ 40	9/ 10	18/ 20	28/ 30	36/ 40	10/ 10	20/ 20	30/ 30	40/ 40
E%	100%				91%				100%			

The results for control (Mobilemark) are tabled in Table 6-11.

Table 6-11: Performance table for Control

Control	Flat to chest (XZ)				By body side (YZ)				Holding forth (XY)			
	1 Tag	2 Tags	3 Tags	4 Tags	1 Tag	2 Tags	3 Tags	4 Tags	1 Tag	2 Tags	3 Tags	4 Tags
1	1	2	3	4	1	2	3	4	1	2	3	4
2	1	2	3	4	1	2	3	4	1	2	3	4
3	1	2	3	4	1	2	3	4	1	2	3	4
4	1	2	3	4	1	2	3	4	1	2	3	4
5	1	2	3	4	1	2	3	4	1	2	3	4
6	1	2	3	4	1	2	3	4	1	2	3	4
7	1	2	3	4	1	2	3	4	1	2	3	4
8	1	2	3	4	1	2	3	4	1	2	3	4
9	1	2	3	4	1	2	3	4	1	2	3	4
10	1	2	3	4	1	2	3	4	1	2	3	4
	10/ 10	20/ 20	30/ 30	40/ 40	10/ 10	20/ 20	30/ 30	40/ 40	10/ 10	20/ 20	30/ 30	40/ 40
E%	100%				100%				100%			

6.5 Summary

This chapter discusses in detail prototype building and testing procedure of 4 proposed novel fractal antennae simulated in Chapter four. Stanley fractal antenna and Maltese Cross fractal had to be left out due to manufacturing constraints of the Mits PCB milling machine. The design calculations of a Wilkinson power divider circuit with a quarter

wavelength are discussed in this chapter using various calculation and design methods. The prototypes were built using Mits PCB milling machine with a 60-degree milling bit for precision. The construction of the copper wall as discussed in simulations to improve directivity is done here by hand using super glue and a 0.45 mm thick copper sheets. The port impedances were measured, and the antennae were tuned to 870 MHz at VSWR to be less than 1.2 by using a technique called stub tuning. Lead tapes were pasted on the radiator as well as the copper wall. The antennae were mounted on a wooden doorframe with a mechanical bracket (here a phone holder is used) having the ability to swivel both vertically and horizontally.

The FEIG LRU 1002 long range RFID reader was used in buffered read mode for tag detection. Paper files tagged with UHF dog-bone RFID tags were picked using a random number table for 1 to 4 files combinations. These were carried in three different orientations at a walking speed. The RF power of LRU 1002 was set at 2 watts constant throughout the testing.

A commercially available antenna Mobile mark PN8-868LCP-1C was used in addition to the 4 designs as a control.

The results suggest that with precision manufacturing and tuning, a 100% detection rate could be obtained for MLPF and Jerusalem cross. Both MLPF and Jerusalem cross fractal antenna have 93% and 91% detection rate when files are carried by the body's side. This might be because of the manufacturing error of the copper wall which was hand glued thus having characteristics of elliptically polarised beam which misses the middle part of the YZ orientations.

The control antenna mobile mark having a gain of 6 dBi with a size of 230 mm x 230 mm which is comparatively large to the 4 tested prototypes, gives a 100% detection rate in all orientations. This is a wide beam antenna and detects tags even at a wide angle from the door passage. Considering its size, this is not suitable for an RFID

doorway reader application to be mounted on each door passage of a commercial building contributing to visual pollution and obstructing door passage which is a health hazard.

The test results suggest that with precision manufacturing and tuning an 86 mm x 86 mm x 3.2 mm antenna could be used for an effective tracking of RFID tagged documents implemented in an automated doorway reader system.

7 Applications of RFID doorway readers

In this chapter, applications for proposed RFID doorway reader systems are discussed in detail. This thesis proposes an automated doorway reader system in contrast to a security system in which the antenna acts as a second pass after tagged items have been manually checked out by another reader. A doorway reader system requires to have 100% tag detection efficiency for reliability of the system. RFID antennae in RFID systems can be classified as fixed reader antennae, handheld reader antennae and tag antennae. Unlike handheld reader antennae, which are mostly linear or dual polarised, the fixed doorway reader antenna proposed in the thesis requires circular polarisation to read tags passing through the door passage in any orientation. Such an antenna needs to be compact enough to be fitted on to a door frame easily, able to detect RFID tags in any orientation, read blind spots in a clustered tag environment and have a narrow radiation beamwidth just enough to cover the door passage. Proposed fractal antenna designs have achieved these requirements.

7.1 Doorway reader applications for Healthcare

A research led by the University of York in 2018 analysing 36 major studies estimates seven out of ten potentially harmful errors are being made by GPs and pharmacists with an estimate that could contribute to 22000 deaths [89], [90]. In the United States, this number is said to be between 44000 and 98000 due to medical errors. Adverse drug events and improper transfusions and mistaken patient identities contribute to this [91]. It has been found that junior doctors are responsible for two thirds of hospital prescriptions. It has been said that prescribing errors are a 'common occurrence' affecting 7% of medical orders. The cause of prescribing error is located to complex and highly stressed working environment in hospitals and time constraints and staffing issues [92]. It has been suggested that an effective RFID system could be implemented

for such a situation for people, document and prescription tracking and thereby automating the process. Even though optical-based systems such as QR codes and barcodes have been introduced to the field of medicine, accurate traceability of patients during different stages of medical treatments at a hospital cannot be achieved except with an RFID system for both near field and far field technologies, as it can be implemented for different purposes [93]. An evaluation of a tracking system for patients is discussed in detail in [94].

Hull and East Yorkshire NHS Trust's two main hospital sites, Hull Royal Infirmary and Castle Hill Hospital are now live with an effective patient record tracking system. This has enabled the trust to reduce costs by effectively streamlining processes with coordinated working. Retrieving patient records ahead of appointments within the trust has boosted patient experience drastically. With the RFID infrastructure and smart devices in place the trust has had opportunity to expand its use of GS1 compliant system to track other hospitals' medical equipment, IT, and pharmaceutical supplies [95]. To ensure patient records are at the right place at the right time, a system with efficient protocol is required. Operations include request patient record, transfer record to another location, tracker location maintenance and sublocation facility within a trust. Most trusts operate with both physical and digital records [96]. Restore Records Management offers smart solutions for complete record management for NHS records, both digital and paper-based records. These include secure document storage and archiving, document audition and data destruction, archive scanning with classification and indexing in digital databases as depicted in Fig. 7-1 [97].

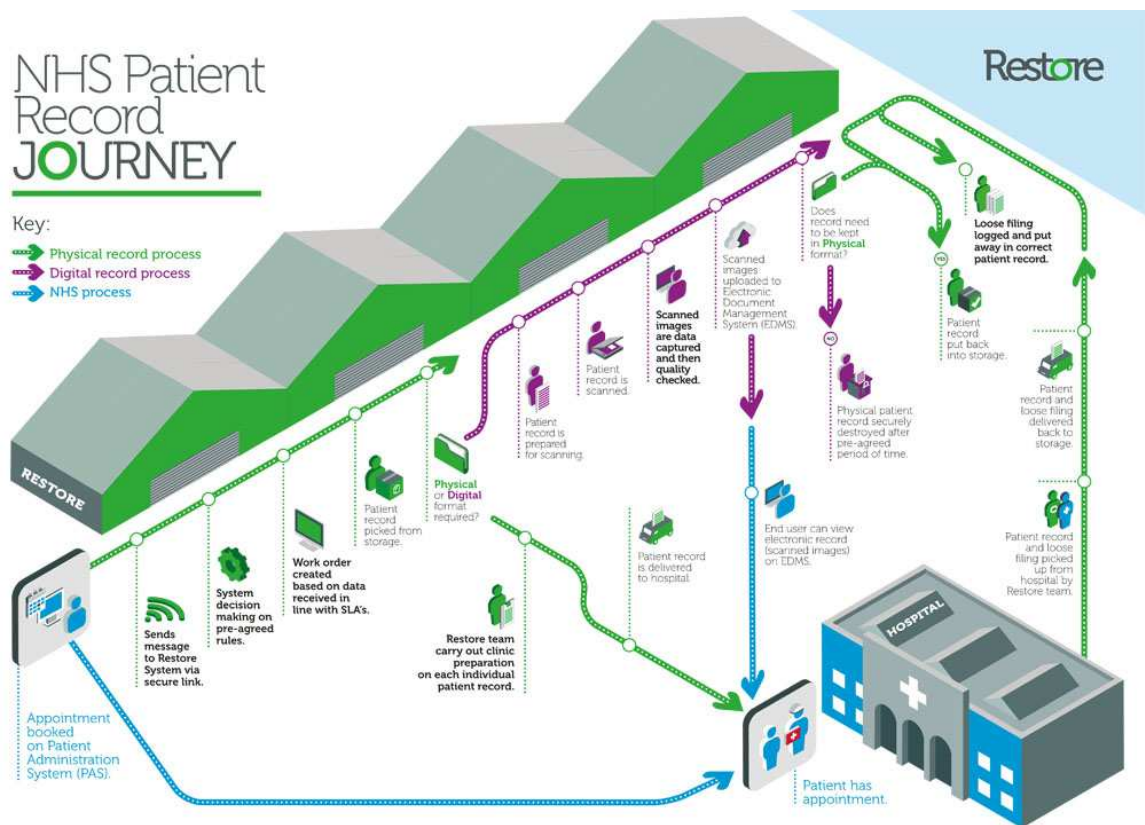


Figure 7-1: NHS Patient Record Journey by Restore Records Management [97]

The UK's largest integrated Health and Social care trust introduced electronic tracking system in 2017 using RFID tags which could be read 13 feet away from the filing cabinet. RFID sensors were located at strategic locations in the hospital to track record movement. The system was implemented by Idox Health in 2017 [98]. NHS Forth Valley Royal Hospital has saved £360,000 through cost avoidance by placing passive RFID tags on 10,000 medical devices. 75 syringe drivers and 12 bladder scanners were accounted to be unused. A further saving of £200,000 is anticipated in the next financial year. According to the Department of Health's piloted six NHS trusts for tracking patients, medical devices could save up to £1 billion in the next seven years [99]. Theatre inventory management is another key factor in healthcare which benefits from RFID technology as it can minimise waste, optimise stock holding with reliable replacement and free up time for clinical staff. Theatre staff in most trusts is tied up preparing kits for operations next day. By centralising and streamlining the

management of theatre supplies, Cambridge University Hospitals NHS Trust (CUH), have freed up their time for clinical staff to invest in patient care [100].

With RFID technology emerging, the concept of “smart hospitals” has been discussed widely in the 21st century. In an RFID enhanced hospital, all medical equipment are embedded with an RFID tag by the manufacturer with a standardised unique identification number. This is done with “smart manufacturing” as defined in Industry 4.0 where automated manufacturing (human-free manufacturing) is possible. Patient wrist bands are embedded with a long-range RFID tag and staff members are given a “smart badge” for tracking their locations. Medical records are tagged with self-adhesive passive RFID tags. Blood bags and drug packs are labelled with RFID labels. Since RFID chips could be re-written, mis-transfusion of blood, over dosage of drugs and patient confusion could be rectified by matching the blood bag or drug with the patient ID or bed number before treatment and performing a RFID tag “kill” command for used labels. Bedside checks are currently done with eye-readable data by hospital staff. Barcodes are not suitable as they require line of sight to read the label which in most theatre environments are not feasible [101].

The doorway reader system proposed in this thesis could be used to automate the entire process by reading patient data, drug labels, bed numbers as well as theatre supplies for a particular operation reducing human errors. Smart hospitals currently operate with RFID handheld readers and kiosks to read and write tags. Further development of the antenna for a higher efficiency and increased reliability of the asset tracking software could automate the entire process. The inter-trust transference of patient records could be done by standardising software used to read RFID tags.

During COVID-19 pandemic, the UK had to ramp up testing as peaks of first and second waves approached. This was challenging due to lack of facilities. An additional 200,000

testing had to be performed per day. As NHS frontline workers and other essential workers rely on receiving results quickly without compromising accuracy. Here a supply-chain like solution was used. RFID has been suggested to overcome these hurdles in avoiding laboratory mix-ups, readability and human errors, logistical errors involved in moving, storing, and analysing samples [102]. An automated test kit transportation system would benefit with the proposed doorway reader antenna to read large samples passing through a door passage instead of scanning them manually with a handheld or kiosk-type RFID reader.

Seasonal flu arrives at a predictable timetable every year. Pathogens that trigger it have been exposed to most people which help them develop resistance to it. Unlike seasonal flu, a pandemic flu like COVID-19's strains are novel and therefore vaccines are not stockpiled to be released. Pandemic waves are not predictable either having high fatalities [103]. "Project Jumpstart" and "RAPID USA" (Rapid Aseptic Packaging of Injectable Drugs) funded by the department of defence aims to provide a solution for this by the end of 2020 by mass distributing vaccines in pre-filled syringes. The prefilled syringes eliminate the need of a glass vial by using blow-fill-seal technology on plastic units developed by Apiject systems. The syringe has an RFID tag under its label enabling healthcare workers to remotely track every injection that takes place as they scan it with their mobile phone's RFID reader via an app [104]. A compact antenna could be of use for mass tracking of vaccines in and out of a warehouse. Another application would be a human implantable chip as discussed in [105], [106], [107], [108] where drugs had been administered wirelessly to patients with a help of a microchip releasing the right amount of dosage. This study proved that it is safer to use the same technology to track people who have been vaccinated. This will make the quarantine process much faster by automation. ID2020 manifesto speaks of giving a

digital identity for each global citizen which is in line with the potentials of RFID [109]. Doorway readers mounted on airports could easily automate this process.

7.2 Doorway reader applications for retail

Near Field Communication (NFC) uses a low power RFID reader and a chip embedded payment card for transactions operating at RFID's High Frequency (HF) band, 13.56 MHz [110]. On April 2020, during the first COVID-19 peak, the United Kingdom raised the contactless payment limit to £45 from £30 [111]. Sainsbury's Supermarkets introduced a "SmartShop app" to pay for in-store shopping where people would use their mobile phone to scan items and pay without contact with a cashier [112]. A similar system has been introduced by Amazon Go's "Just Walk Out" shops where there are no waiting lines or bagging up items. It relies on RFID as well as artificial intelligence to detect picked/purchased items and an exit scanner antenna to check out items when walking out of the shop automatically charging the shopper's account [113], [114]. Further development of the proposed doorway reader antenna system is potentially suitable for such automation applications by some modifications to widen the 3 dB beamwidth and increase efficiency cutting installation costs of large RFID gates when replaced with a mountable compact antenna on a doorframe.

7.3 Doorway reader applications for airports

E-passports contain an RFID chip which also serves as a storage media for transmitting facial images and fingerprints of the passport holder in addition to existing personal data [115], [116]. Together with ID2020's manifesto in giving a digital identity for each global citizen border crossing could be automated by either a tap and go system or a doorway reader.

7.4 Doorway reader applications for Smart Manufacturing

Industry 4.0 requires a digital identification for workpieces in manufacturing. Tools, containers, machinery, and equipment have a unique digital identification. Barcodes are not suitable as they require line of sight from detector to transponder which constraints efficiency of 3D modelling. The objects need to exchange information amongst one another for smart manufacturing. RFID chips are rewritable. Information flows both ways making it possible to update at each stage of manufacturing. A workpiece communicating with the reader both ways. Smart factories control the material to be manufactured as part of the production phase. Detecting multiple workpieces requires an efficient antenna compact enough not to consume much space in the factory [117], [118], [119]. Miniaturised fractal antennae having capability to read clustered and detuned RFID tags in a dynamic environment (tracking items travelling through a conveyor belt by a fixed portal reader antenna) proposed in this thesis are suitable for smart factories in future.

7.5 For smart waste management

One of the main complaints of waste producers is that they are being charged on a flat rate and not according to the waste they produce. With the coming of smart manufacturing in the future, each manufactured item will have a standardised unique identification number which reveals its chemical contents. Information stored in the RFID chip could be used to determine the type of waste and composition and thereby managing waste smartly and charging waste producers in proportion to the hazardousness of their waste instead of a flat rate. Since RFID doesn't require line of sight an efficient antenna could read tagged waste material covered in snow, ice, dust or dirt [120]. One of the major hurdles is detecting tags when metals are in the vicinity. Reading tags in water is another challenge. Low Frequency (LF) and High Frequency (HF) bands are usually recommended in RFID for detecting tags that are in metallic

surroundings and water. However, [121] shows that by insulating the UHF tag with a Electromagnetic Band Gap (EBG) structure, UHF band can be used as well. The UK's environment agency classifies waste into three categories when dumping into landfills. They are hazardous, non-hazardous and inert waste. Each going to dedicated landfills [122]. The waste producers must pay a rate for each. The antenna proposed in the thesis could be used to screen the composition of waste dumped on landfills. This is useful for the UK's Environment Agency to detect misclassification of hazardous waste. Another place where knowing the composition of waste is useful are recycle plants for effective cost management.

7.6 Summary

In this chapter, applications using the proposed antennae are presented. Doorway reader antenna are used mostly in library security systems however, they can be used for healthcare applications widely for patient as well as patient record tracking, medical equipment/supplies inventory management, inter-trust transfer of drugs and administration of drugs as defined in smart hospitals. This chapter discusses the future of retail industry where automated "pick and go" systems are currently being implemented in places such as Amazon Go shops. RFID automated doorway readers are currently used for "touch and go" systems in certain airports. One of the main beneficiaries of RFID automation is smart manufacturing where a two-way communication from item to reader is possible. Line of sight is not required here, and hence automated 3D printing with RFID tagged components and automated assembly are made possible. This chapter also discusses about the use of RFID automated composition screening of waste in smart cities. The antennae proposed in this thesis are suitable for doorway readers which have wide applications in diverse fields.

8 Discussion, Conclusions and further work

8.1 Discussion

This thesis presents 7 novel UHF RFID antenna designs resonating at 870 MHz out of which 4 were prototyped and tested for their performances. Design work comprised of extensive step by step simulations using geometry techniques, fractal patterns, antenna feeding techniques, antennae were designed on specialist PCB material (Taconic RF60A) to obtain an antenna suitable for a fully automated RFID doorway reader system. The aim of this research was to develop a near field microstrip patch antenna when a fractal pattern is applied for the purpose of miniaturisation whilst optimising its gain, directivity and beam width in order to produce a novel microstrip antenna suitable for an RFID doorway reader system.

RFID has been the subject of broad and current interest recently after the rise of fully automated manufacturing and service: Industry 4.0. A literature survey of RFID technology and systems was done in Chapter two. This included a study on RFID standards, classifications and applications revealing that in order to implement an automated doorway reader system for an high-volume document tracking, the most suitable method is by using a low power near field antenna with passive tagged assets, since active and semi-passive tags are battery powered and are not suitable for tracking large volumes of low cost assets at a close range. Passive tags harvest power from the electromagnetic energy field of the RFID reader antenna and activate the chips themselves, therefore, its range is limited. Active tags are used for ocean containers, large military and high valued assets. Whereas semi-passive tags are used for tracking temperature sensitive items, perishable food, chemical and other industrial products having large memory capacities. The choice of tag type is a matter of balance between the value of an individual asset and the price of a tag. For this application though a real-time tracking is not necessary. Therefore, passive tags are used for document tracking

applications. The ultra-high frequency band is preferred for effective detection having a speed twenty times faster and accurate on passive RFID tags than commonly used high frequency RFID. Considering installation costs, passive tags are advisable for a large volume of assets which need to be tracked. A near field antenna could easily detect passive tags at close range with high accuracy. Even in this event, the main challenge remains when detecting clustered tags. When RFID tags are clustered, the resonant frequency of RFID tags shifts resulting in blind or weak spots in the RF region. This is due to the mutual coupling of the transponder antennae of tags which are placed close to each other. Applications of fractals have been studied extensively in farfield antennae where the governing equations differ from near field antennae. However, the same application could be used for near field for the purpose of miniaturising the antenna to a feasible size which could fit into a doorframe. Fractal antennae have been known to increase the rate of tag detection due to diffractal behaviour of the backscattered electromagnetic beam when fractals are encountered. Confining the operational region of the near field antenna to a doorframe is another challenge in this application.

Microstrip antennae have been considered the most suitable and are the most commonly used antennae for RFID applications. This is mainly due to its characteristics of being low profile, low cost as well as its performance. These can be manufactured easily by printed circuit technology. A basic microstrip antenna comprises a radiating patch, ground plane (reflector) and a dielectric layer between them. Advantages and disadvantages of different feeding techniques of microstrip antennae have been discussed in Chapter three as it contributes to gain and bandwidth of the antenna. A coaxial like feed travelling through the dielectric substrate not crossing the radiating beam is found to be the most efficient in literature. Other impedance matching techniques are hard to tune, as the shielding effect contributes to the patch's copper.

The dielectric substrate contributes much to miniaturising this antenna by a factor of $1/\sqrt{\epsilon_r}$. Various dielectric materials used on antennae and their performance have been studied in literature. Since the main objective of this research is to miniaturise the antenna, a specialist PCB material, Taconic RF60A having a dielectric constant of 6.15 has been used instead of building the antenna on traditional FR4 PCB having a dielectric constant of 4.3. This reduces the size of the antenna by 16.3%. Emphasis should be put on precision manufacturing since at 870 MHz, a 1 mm error in the radiating patch contributes to a 12 MHz offset in resonant frequency, this has been discussed in detail. Effective detection of tags irrespective of their orientation is one of the main concerns in an RFID system. If the antenna were linearly polarised, a tag travelling through its operational region in line with the polarisation does not have any perpendicular cuts to the electromagnetic beam and hence, the tag is not activated resulting in blind or weak spots. To overcome this, a circularly polarised antennae have been proposed in literature. A circularly polarised antenna produces a tornado-like electromagnetic beam in spiral form thus making perpendicular cuts on tags places in any orientation. Techniques in obtaining circular polarisation such as truncating the diagonal edges of a square patch, using a single feed on a nearly square patch at a corner if the length were a bit less than the resonant length and bit more than the height, using a single feed but with asymmetric feature or slot and using two feeds with a 90-degree time phase difference are studied in Chapter three. When a two-port feeder is used, it necessitates that both ports should have the 50 ohm impedance as in the feedline. To obtain this, a Wilkinson power divider comprising of two 70.7-ohm quarter wavelength arms splitting the input port and a shunt resistor of 100 ohms between the output ports have been studied. Another technique of miniaturising the antenna is by using a fractal pattern to the antenna. A fractal is a mathematical object in which each fragment, when zoomed has a resembling structure as the whole. These

can be used in miniaturizing antennae since, as the fractal iteration increases, the electrical length of the antenna increases yet maintaining the same size. Since electrical length has increased, the resonant frequency of the antenna is lowered. To bring the resonant frequency back to the original value, the length should be decreased – thus miniaturisation occurs. Fractals also contribute to other factors in an antenna. Studies have been done on fractals applied to antenna to obtain multiband characteristics. A detailed study is presented in Chapter three. This multiband behaviour with the help of frequency hopping provided by the RFID reader could resolve the detuned transponders in a cluster due to mutual coupling. In frequency hopping, a signal is transmitted from the reader with a 1 MHz bandwidth on 75 or more non-overlapping channels within 30 seconds. By doing so, the reader allows itself to read detuned tags which are either clustered or shielded. In a fractal antenna having a multiband behaviour, each fragment of a fractal emanates a higher frequency and with frequency hopping this helps to pick up tags which are detuned over the 1 MHz bandwidth thus reducing blind or weak spots in the RF region.

A simulation-based design process followed in the development of a near field UHF RFID fractal antennae. By using an electromagnetic simulation software CST Microwave Studio Suite, 7 novel antenna models were simulated where 7 fractal patterns were used. The design criteria suitable for a RFID doorway reader antenna were set in Table 4-3. An antenna should have a return loss less than -10.0 dB and a VSWR less than 1.2. For this application, the antenna should resonate at 870 MHz having a directivity around 4.5 dBi. The antennae should be a narrow beam width device to confine its operation to the door frame. The 3dB beam widths were set to 100 degrees. Four fractals were handpicked for their unique geometric nature which could benefit the antenna radiation. Minkowski-Like Pre-Fractal (MLPF) was chosen for its unique characteristic of meandering effect which increases the antenna's electrical

length with fractal iteration, when slots are perforated at the sides of the patch. The Tau fractal creates parasitic patches within the patch by making 4 'T'-shaped elements. This fractal converges as iteration increases. The Space filling tree (SFT) was chosen for its unique nature as it adds to the slot length with fractal iteration. The fractal pattern consists of one slot unlike other slots. Maltese cross was considered for its ability to change the vertical and horizontal flare angles and thereby contribute to circular polarisation. All designs were fabricated on RF60A high dielectric substrate. Since the reflector of these designs were relatively smaller than other patch antenna, a 0.45 mm thick copper wall was constructed around the antennae to increase directivity of the antenna. Designs were fed via two coaxial ports at a 90-degree time phase difference to obtain a circularly polarised beam. Here, the circular polarisation could be interchanged from Left-handed Circular Polarised (LHCP) beam to a Right-handed Circular Polarised (RHCP) beam by simply changing the two coaxial feed cables. If another technique like truncation or port location were used, this circular polarisation is fixed to the antenna. 3 further designs were investigated and simulated using the same substrate, and geometry techniques used in the 4 designs simulated before. Inverted Tau (Inv Tau) was investigated as an alternative to Tau fractal for its lacunarity. The spread factor or lacunarity increases with fractal iteration in Inverted Tau fractal, whereas in Tau fractal it converges. Stanley fractal was proposed as an alternative to Maltese cross fractal to eliminate the inverted edge deflecting surface currents travelling to the sides of the patch. Jerusalem cross like MLPF increases the electrical length of the antenna by a large factor. By iterative simulation-based designing, all proposed antenna models were able to achieve design criteria mentioned in Table 4-3 and therefore are suitable to be prototyped and tested for RFID performance by using a UHF RFID reader.

4 of the 7 simulated designs were chosen to be prototyped and tested as a proof of concept of the viability of simulated antenna for an RFID doorway reader application. A Wilkinson power divider was designed by 3 methods for verification of accuracy and fabricated with an extra quarter wavelength arm to obtain the 90-degree time phase shift. Antenna models MLPF, Tau, SFT and Jerusalem cross were prototyped by using a PCB milling machine. The copper wall was constructed around the wall by hand. The test is proposed to be carried by testing the detection efficiency of the antenna when a person is carrying a number of files walking through a wooden doorframe on which the antenna is mounted with a mechanical bracket powered by an RFID reader. A FEIG LRU1002 reader is used for this testing. Several variables exist for an effective testing of an RFID doorway reader which affects the sample size. The number of antennae which needs to be tested, location of antenna on the doorframe, tilt angle, file carrying orientation, file stacking positions, number of files carried and the speed of travel through the door passage. As discussed in section 5.4.1.2, for a 95% confidence level unbiased test, the test subject would have to walk 16,800 times across the doorframe. Since this is not within the scope of this research, several variables were altered resulting in 600 rounds. Four prototyped antennae will be tested along with an industrially available near field antenna as a control. The test subject will be picking 1-4 files according to a random number table from a population of 100 files with 10 test runs as the sample size for all three file carrying orientations depicted in Fig. 5-27.

Antenna performance tests demonstrated that a 100% detection rate could be obtained with precise manufacturing, tuning and further modifications. In MLPF and Jerusalem Cross antenna designs, 100% was obtained except when files were carried by the side of the body. This is the most common file carrying position. It should be noted that tests were carried out by using a single antenna mounted to the door frame. The experimental work proves that with 2 or more antennae mounted on the

doorframe with the same power from RFID reader, a 100% detection rate is not impossible. This requires further industrial scale testing with large sample sizes for accuracy to determine the location of the antennae on the doorframe and the tilt angle with which it should be positioned. The size type/material of files used in the NHS trust should be considered when tags are placed. The size of the file determines the spacing between two tags which contributed directly to clustering effect. In this experiment, tags were placed on the same location horizontally on the file. If they were placed randomly, it is more logical to assume higher performance of the doorway reader system since then they are unlikely to be clustered.

The common blind spots occurring from tag clustering and orientation were overcome by using a fractal pattern on the antenna. The tags were detected even when 4 files were clustered together. The performance test also proves that a 100-degree beam width was sufficient for effective detection of files confining the operational region only to the door passage.

8.2 Conclusions

The research contributed 7 novel antenna designs suitable for an RFID doorway reader system as per pre-defined requirements in section 4.1. from extensive step by step simulations performed on CST Microwave Studio Suite. 7 fractal patterns were applied to a standard microstrip patch antenna built on specialist material Taconic RF60A. Antenna designs were fed with two port at 90-degree time phase shift delays with each other. This was obtained by splitting the signal with a Wilkinson power divider to obtain matched impedances at both ports and then adding an extra quarter wavelength, to obtain the 90 degree phase shift ($T/4$ delay) to obtain a circularly polarised beam to overcome blind spots occurring due to tag orientation and clusters. A copper wall was built around the antenna to increase its gain as the wall connects

with the ground plane, both act as a reflector and hence a more directed beam. Simulation results suggested that design criteria for an automated doorway reader antenna has been achieved as defined in section 4.1.

Simulated models were prototyped using a PCB milling machine and then tested for performance on a doorframe. A Wilkinson power divider was designed on standard FR4 PCB and was connected to the antennae with coaxial cables. The RFID reader used for testing was a FEIG LRU 1002 Long Range reader. Two designs namely MLPF and Jerusalem cross fractal antennae having the minimum patch size achieved the best performance in reading RFID tags passing through the door passage. The antennae were able to read 100% of tags in 3 different orientations except when carried by body side which were 93% and 91%. The tests infer with extra tuning and precise manufacturing, a 100% detection rate could be obtained. This was observed when port impedances from simulations and measured values didn't match.

Simulations and prototype testing revealed that with high dielectric substrate material and fractal patterns implemented, a microstrip antenna could be miniaturised with its performance optimised. When compared with the control which performed at 100% throughout, it must be noted that all proposed novel antennae have been significantly miniaturised from a standard 91 x 69 mm patch by using fractals and other geometry techniques to a maximum of 67 x 67 mm. The total dimensions of the novel antennae are 86 x 86 x 3.2 mm which is compact enough to be mounted on a doorframe easily with almost the same performance of a 230 x 230 x 40 mm industrially available near field antenna.

8.3 Further work

Since design by nature is a constant iterative process, there is no terminal point where a system could not be developed further even though objectives of the project have

been met. The following solutions are proposed as further development in overcoming issues pertaining to antenna performance.

8.3.1 Mits PCB milling machine's limitations

1 mm change in antenna dimensions contributes to 12 MHz offset, precision manufacturing is required for accuracy and performance of antenna. Antenna produced by Mits PCB milling machine contributes to back scattering of electromagnetic waves as surface of antenna isn't smooth as shown in Fig. 8-1.

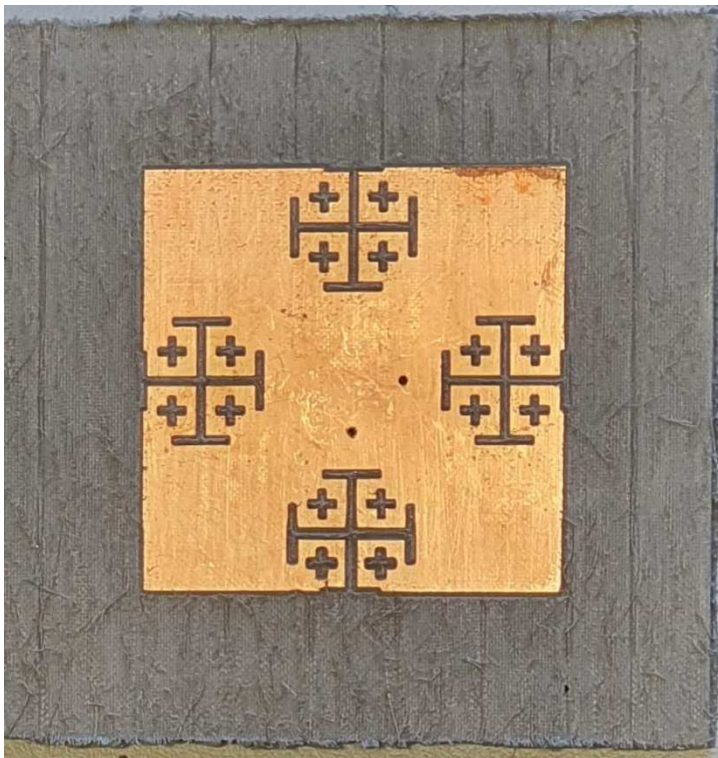


Fig. 8-1: manufactured antenna by Mits PCB milling machine depicting surface roughness

This may be rectified by changing the width of the milling bit. The prototypes produced for this research were built using a 60-degree milling bit. If the angle of drill bit be reduced to 30 degrees with an increased spindle speed, the circuit boards would have a smoother surface as shown in Fig. 8-2, where Wilkinson power dividers were produced using both 60 degree and 30 degree milling bits.

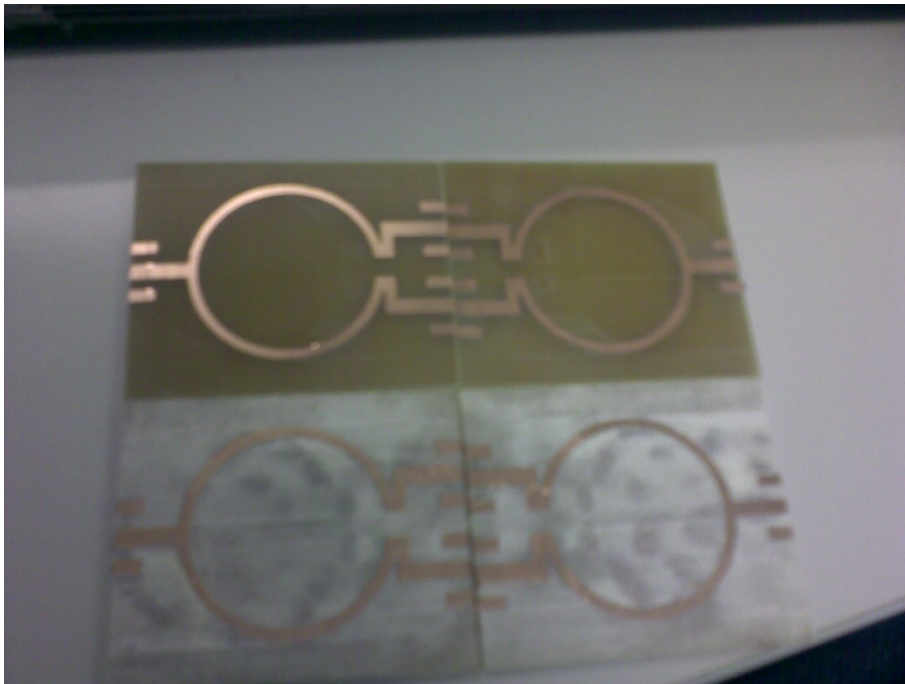


Fig. 8-2: Top 2 board produced with 30 degree milling bits whilst bottom 2 boards where produces of 60-degree bits

Using a milling bit having low milling width with increased spindle speed, improved the accuracy of copper tracks as well as improved the smoothness of design. This technique could be used in construction of antenna on RF60A boards as well.

8.3.2 Accuracy of copper wall constructed around the antennae

The construction of copper wall was done manually by hand using superglue as the adhesive and hence, the contact between copper wall and ground plane was not intact thus contributing mismatch of total antenna impedance in comparison with simulated results. This can be seen in Fig. 8-3.



Fig. 8-3: Gap between copper wall and antenna ground plane

Precision manufacturing will improve the performance of the antenna with a tightly constructed wall to the ground plane.

8.3.3 Issues with feeding mechanism of the radiating patch

One of the major issues of antenna feeding is that the two ports were too close to each other, so that the SMA connectors would contribute to interference when ports are excited with a 90-degree time phase delay as connector legs are too long, this will contribute to inductive coupling between the two ports. This is shown in Fig. 8-4.

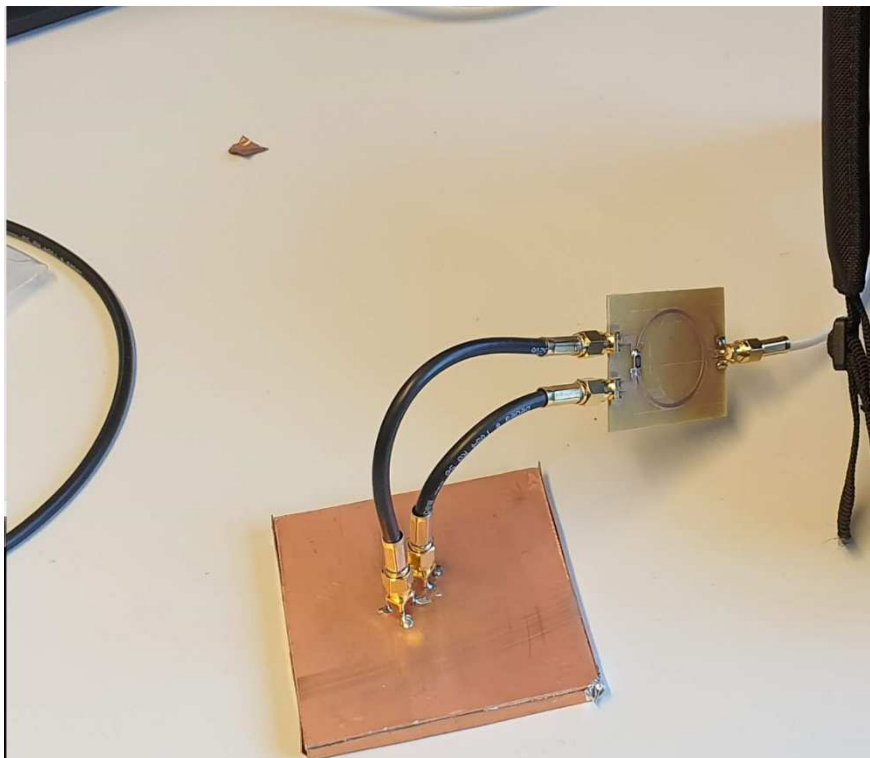


Fig. 8-4: Ports too close to each other

The ports were close as 8 mm where RG58 SMA connectors are comparatively too large. The coaxial ports' outer and inner diameters as per simulations were 2.5 mm and 1 mm. An MMCX straight plug PCB mount would be more suitable for this design connected along with a MMCX to RG58 converter as shown in Fig. 8-5.



MMCX straight plug PCB mount



MMCX to SMA converter cable

Fig. 8-5: MMCX straight plug PCB mount and MMCX to RG58 converter

8.3.4 Errors in Wilkinson power divider's copper pads

As discussed before, due to commercial constraint of RG58 PCB end launch connector's pad size, the copper pads of the Wilkinson divider had to be reduced from 3.1 mm to 2.7 mm as shown in Fig. 8-6.

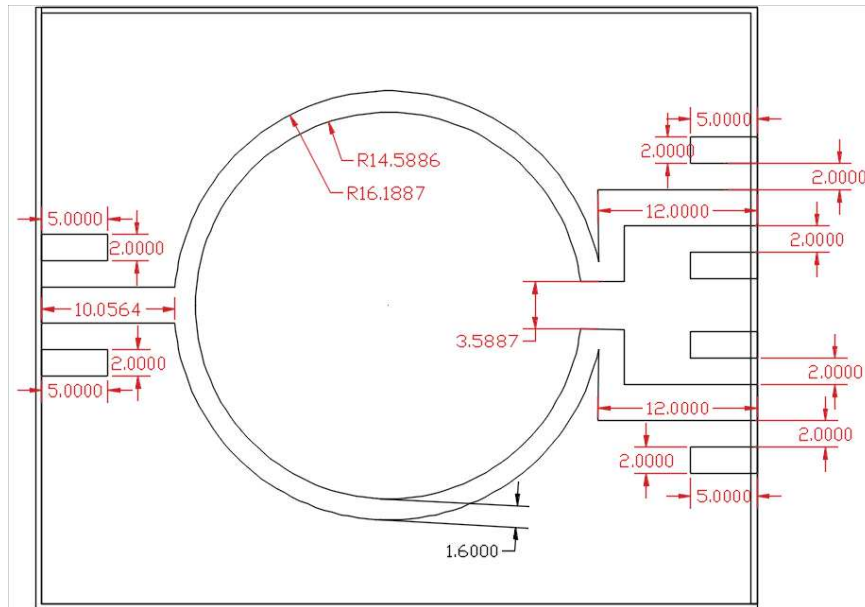


Fig. 8-6: Wilkinson power divider dimensions

Theoretically according to Wheeler's equation, a 2.7 mm copper pad will give a characteristic impedance of 53.8 ohms instead of 50 ohms. This occurs in all 3 ports of the Wilkinson power splitter, thus resulting in small mismatch of the antenna impedances. Whereas for a MMCX end launch PCB mount, a 2.7 track is too large. The solution is to redesign the Wilkinson power divider without coaxial cables, thus stacking them on top from the ground plane feeding them with thin solid wires. The circuit should be designed such that the extra quarter wavelength element is also embedded in the ring splitter. A proposed circuit is shown in Fig. 8-7.

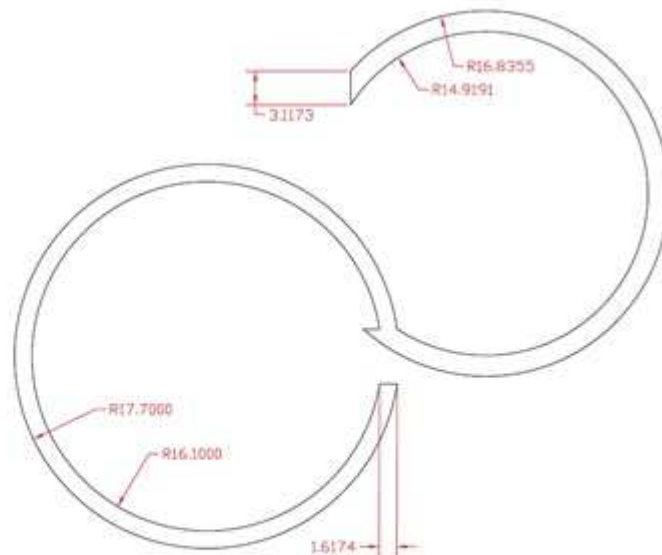


Fig. 8-7: Proposed Wilkinson circuit divider with quarter wavelength element embedded to splitter

8.3.5 Port impedances Z11 and Z22

There were huge differences between simulated port impedances and measured. In as much as this may have been contributed by hand building of the copper wall, the Wilkinson splitter with the extra quarter wavelength element could have been simulated using CST Design Studio as an holistic model. The CST Design Studio enables the two models to be connected. Errors in Wilkinson splitter due to pad size error and effects of RG58 connections could also be simulated and thereby a more accurate S11 parameter grid could have been generated. This will enable to tune the design to 870 MHz at 50 ohms from the main reader cable.

8.3.6 Burden of stub tuning

It should be noted when operating in ultra high frequencies with high Q factors, the antenna becomes unstable even with an error of 1 mm. The antenna was tuned by a

technique called 'stub tuning' using lead tapes pasting to the sides of the radiation patch as shown in Fig. 8-8. Even though this will tune the antenna, it also hugely contributes to the return loss as impedances mismatch with this.

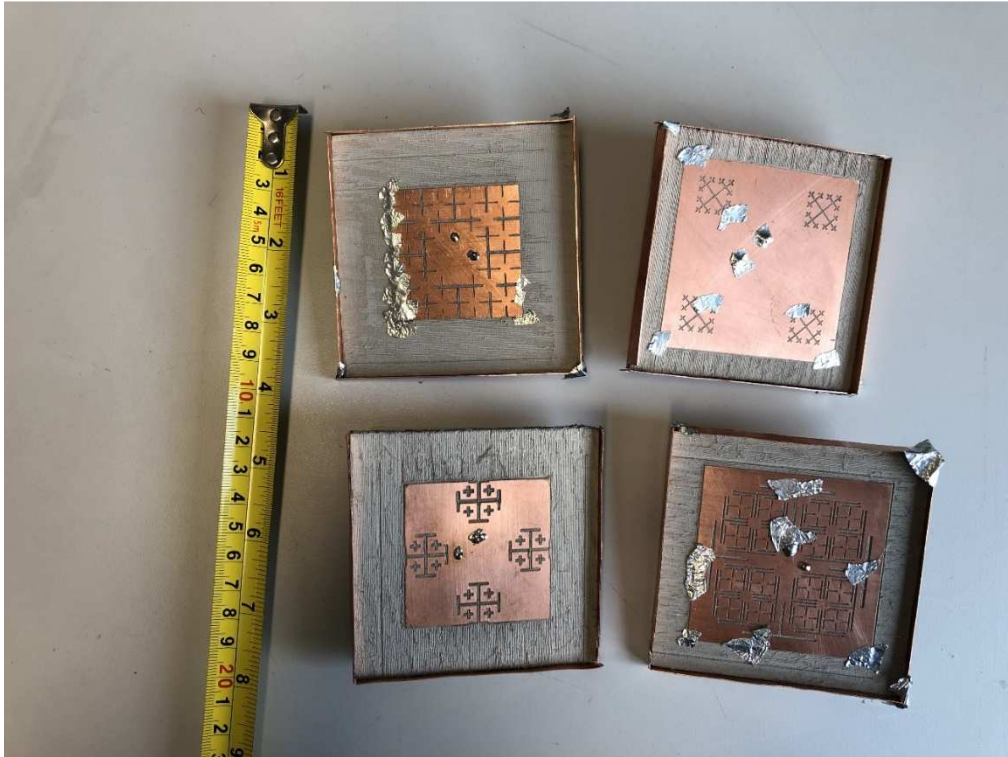


Fig. 8-8: Tuning antennae using copper taped pasted on radiating patch

A better tuning approach could be performed by adding trimmer capacitors of small values as 1pF to 30pF to Wilkinson power splitter's feedline to be connected in shunt with the ground plane of the antenna for effective tuning as suggested in Fig. 8-9.

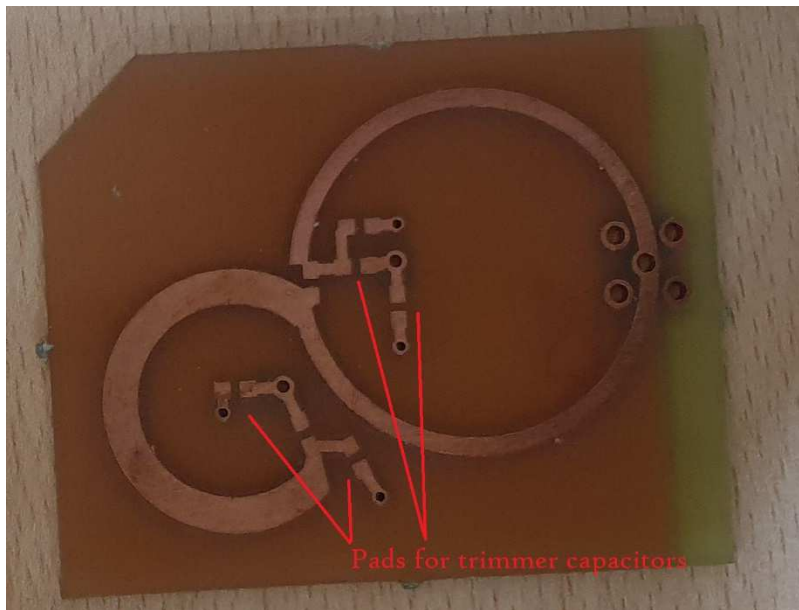


Fig. 8-9: Depicting suggested pads for trimmer capacitors for effective tuning

And hence the antenna could be fed as shown in Fig. 8-10, by placing the Wilkinson feeder on the reverse side (ground plane) with a small airgap and connecting feedlines to the radiator with solid wires.



Fig. 8-10: Wilkinson divider with embedded quarter wavelength arm to feed antenna

8.3.7 Using a four-port feeder

The final design of Jerusalem cross antenna was simulated using a four port feeder, as shown in Fig. 8-11 with time-phase delays of 0, 90, 180 and 270 degrees.

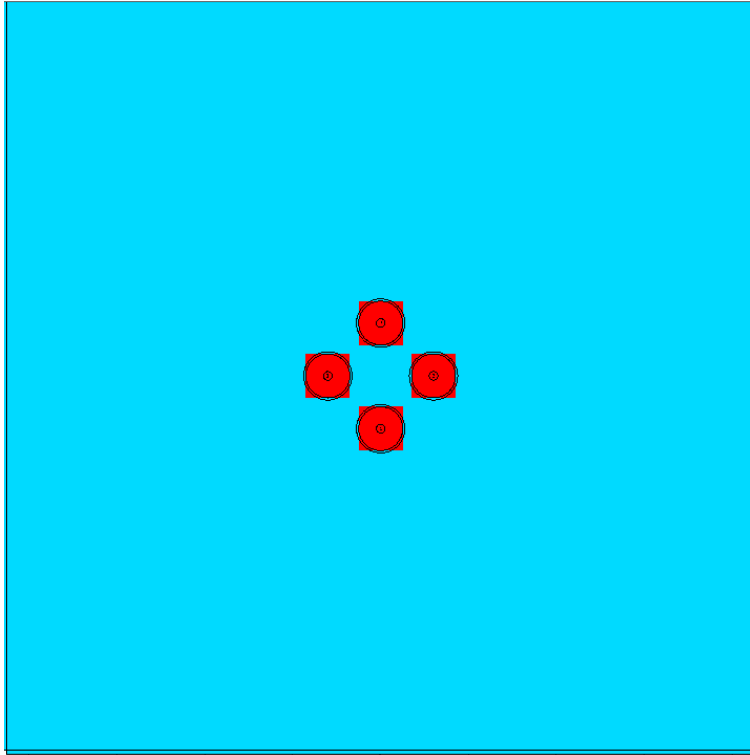


Fig. 8-11: Four port feed with 0, 90, 180- and 270-degree time phase shift delays

Simulations were done and the antenna with a 50 mm patch and an 85 mm ground plane resonated at 862.7 MHz with the following results are tabled in Table 8-1

Table 8-1: Simulated results for a four-port Jerusalem cross fractal antenna

Resonant frequency (MHz)	Return loss S11 (dB)	Directivity (dBi)	VSWR	3dB Beamwidth at phi=0 degrees	3dB Beamwidth at phi=90 degrees
862.7	-10.2041	4.391	1.8938	105.3	105.3

A four-port feeding resulted in providing a symmetric circular polarised beam. A 3-dimensional N-way Wilkinson divider may be used to feed this 4-port feeder with quarter, half and three-quarter wavelength additional lengths to obtain $T/4$, $T/2$, $3T/4$ time phase shifts for an effective circular polarisation of the antenna.

REFERENCES

- [1] A. Lozano-Nieto, *RFID design fundamentals and applications*. CRC press, 2017.
- [2] M. Mladineo, I. Ve, S. Jurc, and I. Znaor, "Performance analysis of the RFID-enabled Manufacturing Execution System," in *International Conference Mechanical Technologies and Structural Materials 2017*, 2017.
- [3] BBC, "NHS misplaced half a million patient documents," Feb 2017. [Online]. Available: <https://www.bbc.co.uk/news/health-39101489>
- [4] T. Guardian, "NHS accused of covering up huge data loss that put thousands at risk," Feb 2017. [Online]. Available: <https://www.theguardian.com/society/2017/feb/26/nhs-accused-of-covering-up-huge-data-loss-that-put-thousands-at-risk>
- [5] E. Standard, "NHS patients at risk after 700,000 medical records and documents lost in huge blunder," June 2017. [Online]. Available: <https://www.standard.co.uk/news/health/700000-medical-records-and-documents-lost-in-huge-nhsblunder-a3573801.html>
- [6] A. Rimmer, "NHS England handling of 102 000 lost medical records is, say MPs," *BMJ*, vol. 359, 2017. [Online]. Available: [10.1136/bmj.j5546](https://doi.org/10.1136/bmj.j5546)
- [7] K. Afifi-Sabet, "The NHS lost almost 10,000 patient records last year," Aug 2018. [Online]. Available: <https://www.itpro.co.uk/security/31745/the-nhs-lost-almost-10000-patient-records-last-year>
- [8] B. Heather, "Health Secretary Jeremy Hunt grilled on missing confidential NHS data," Feb 2017. [Online]. Available: <https://www.digitalhealth.net/2017/02/half-million-nhs-records-lost/>
- [9] bibliotheca, "bibliotheca RFID gate™ premium." [Online]. Available: https://www.bibliotheca.com/wp-content/uploads/GLBDA1333NA_002_RFID_gate_premium_datasheet_LR.pdf
- [10] bibliotheca, "bibliotheca selfCheck™ 500." [Online]. Available: https://www.bibliotheca.com/wp-content/uploads/2017/10/GLBDA1354NA_001_selfCheck_500_datasheet_LR.pdf
- [11] Nordid, "Handheld readers." [Online]. Available: <https://www.nordid.com/devices/handheld-readers/>
- [12] Intellident, "Quarterportal." [Online]. Available: http://www.intellident.co.uk/wp-content/uploads/2018/01/G-FSDA1005_multiportal_500.pdf
- [13] C. Evans and A. Moore, "Using RFID technology at University of Sussex," *SCONUL Focus*, vol. 59, pp. 13–15, 2013.
- [14] bibliotheca, "bibliothecasmartShelf™ range." [Online]. Available: https://www.bibliotheca.com/wp-content/uploads/GLBBR1168UK_001_smartShelf_range_brochure_LR.pdf

- [15] bibliotheca, "bibliotheca flex AMH™return + sorting solutions." [Online]. Available: https://www.bibliotheca.com/wpcontent/uploads/G-LBBR1171NA_001_flex_AMH_brochure_LR.pdf
- [16] D. M. Dobkin, *The rf in RFID: uhf RFID in practice*. Newnes, 2012.
- [17] D. H. Werner and S. Ganguly, "An overview of fractal antenna engineering research," *IEEE Antennas and propagation Magazine*, vol. 45, no. 1, pp. 38–57, 2003.
- [18] W. J. Krzysztofik, "Fractal Geometry in Electromagnetics Applications—from Antenna to Metamaterials." *Microwave Review*, vol. 19, no. 2, 2013.
- [19] M. V. Berry, "DiffRACTALS," *Journal of Physics A: Mathematical and General*, vol. 12, no. 6, p. 781, 1979.
- [20] O. I. Yordanov and K. Ivanova, "Kirchhoff diffractals," *Journal of Physics A: Mathematical and General*, vol. 27, no. 17, p. 5979, 1994.
- [21] C. A. Vélez, M. Lehman, and M. Garavaglia, "Two-dimensional fractal gratings with variable structure and their diffraction," *Optik*, vol. 112, no. 5, pp. 209–217, 2001.
- [22] P. Parthiban, B.-C. Seet, and X. J. Li, "Low-cost scalable UHF RFID reader antenna with no surface dead zones," in *2016 IEEE Asia-Pacific Conference on Applied Electromagnetics (APACE)*, 2016, pp. 24–29.
- [23] J. Zhang, Z. Xie, S. Lai, and Z. Wu, "A design of RF receiving circuit of RFID reader," in *ICMMT 4th International Conference on, Proceedings Microwave and Millimeter Wave Technology, 2004.*, 2004, pp. 406–409.
- [24] H. Dai, S. Lai, X. Lai, and Z. Xie, "An enhanced RF receiving circuitry design for UHF RFID reader," in *2006 IET International Conference on Wireless, Mobile and Multimedia Networks*, 2006, pp. 1–3.
- [25] J.-Y. Hung, "Improving Reader Performance of an UHF RFID System Using Frequency Hopping Techniques," 2009.
- [26] G. A. O. Tek, "GAO Tek RFID Dock Door Portal Series." [Online]. Available: <https://gaotek.com/product/gao-tek-rfiddock-door-portal-series/>
- [27] K. V. S. Rao, "An overview of backscattered radio frequency identification system (RFID)," in *1999 Asia Pacific Microwave Conference. APMC'99. Microwaves Enter the 21st Century. Conference Proceedings (Cat. No. 99TH8473)*, vol. 3, 1999, pp. 746–749.
- [28] B. Glover and H. Bhatt, "RFID essentials."
- [29] N. Prabhu, *Design and Construction of an RFID-enabled Infrastructure: The Next Avatar of the Internet*. CRC Press, 2013.
- [30] GS1, "© GS1 2020Regulatory status for using RFID in the EPC Gen2 (860 to 960 MHz) band of the UHF spectrum," Feb 2020. [Online]. Available: https://www.gs1.org/docs/epc/uhf_regulations.pdf
- [31] GS1, "EPC™ Radio-Frequency Identity ProtocolsGeneration-2 UHF RFIDSpecification for RFID Air InterfaceProtocol for Communications at 860 MHz – 960 MHzVersion 2.0.1 Ratified," Apr 2015. [Online]. Available: https://www.gs1.org/sites/default/files/docs/epc/Gen2_Protocol_Standard.pdf

- [32] W. Alsalihi, K. Ali, and H. Hassanein, "Optimal distance-based clustering for tag anti-collision in RFID systems," in *2008 33rd IEEE Conference on Local Computer Networks (LCN)*, 2008, pp. 266–273.
- [33] X. Deng, M. Rong, T. Liu, Y. Yuan, and D. Yu, "Tag count frame slotted aloha: A novel anti-collision protocol in RFID systems," in *VTC Spring 2008-IEEE Vehicular Technology Conference*, 2008, pp. 2666–2670.
- [34] A. Ferdous, N. G. Jeevarathnam, and I. Uysal, "Comparative analysis of tag estimation algorithms on RFID EPC Gen-2 performance," in *2017 IEEE International Conference on RFID Technology & Application (RFID-TA)*, 2017, pp. 186–190.
- [35] D. Kuester and Z. Popovic, "How good is your tag?: RFID backscatter metrics and measurements," *IEEE Microwave Magazine*, vol. 14, no. 5, pp. 47–55, 2013.
- [36] R. Weinstein, "RFID: a technical overview and its application to the enterprise," *IT professional*, vol. 7, no. 3, pp. 27–33, 2005.
- [37] X. Chen, F. Lu, and T. Y. Terry, "The "weak spots" in stacked UHF RFID tags in NFC applications," in *2010 IEEE International Conference on RFID (IEEE RFID 2010)*, 2010, pp. 181–186.
- [38] J. Guo, H. Lan, and Y. Yin, "A near-field UHF RFID reader antenna without dead zones," in *2018 International Conference on Microwave and Millimeter Wave Technology (ICMMT)*, 2018, pp. 1–3.
- [39] C. H. Loo, A. Z. Elsherbeni, F. Yang, and D. Kajfez, "Experimental and simulation investigation of RFID blind spots," *Journal of Electromagnetic Waves and Applications*, vol. 23, no. 5-6, pp. 747–760, 2009.
- [40] C. A. Balanis, *Antenna theory: analysis and design*. John Wiley & sons, 2016.
- [41] L. V. Blake and M. W. Long, *Antennas: Fundamentals, design, measurement*. SciTech Publishing, 2009, vol. 2.
- [42] I. J. Bahl, "A Designer's Guide to Microstrip Line." 1977.
- [43] K. Carver and J. Mink, "Microstrip antenna technology," *IEEE transactions on antennas and propagation*, vol. 29, no. 1, pp. 2–24, 1981.
- [44] R. Waterhouse, *Microstrip patch antennas: a designer's guide*. Springer Science & Business Media, 2013.
- [45] J. B. Hagen, *Radio-frequency electronics: circuits and applications*. Cambridge University Press, 2009.
- [46] M. Elsdon, "An investigation of reduced size planer fed microstrip patch antennas," 2005.
- [47] A. Khan and R. Nema, "Analysis of five different dielectric substrates on microstrip patch antenna," *International journal of computer applications*, vol. 55, no. 14, 2012.
- [48] M. V. Schneider, "Dielectric loss in integrated microwave circuits," *Bell System Technical Journal*, vol. 48, no. 7, pp. 2325–2332, 1969.
- [49] K. S. Alam, "Influence of Dielectric Embedding on Antenna Performance."
- [50] R. Salama and S. Kharkovsky, "An embeddable microwave patch antenna module for civil engineering applications," in *2013 IEEE International Instrumentation and Measurement Technology Conference (I2MTC)*, 2013, pp. 27–30.

- [51] B. B. Mandelbrot, "The fractal geometry of nature/Revised and enlarged edition," *whf*, 1983.
- [52] K.-L. Wong, *Compact and broadband microstrip antennas*. John Wiley & Sons, 2004, vol. 168.
- [53] P. Borys, "ON THE RELATION BETWEEN LACUNARITY AND FRACTAL DIMENSION." *Acta physica polonica B*, vol. 40, no. 5, 2009.
- [54] C. P. Baliarda, C. B. Borau, M. N. Rodero, and J. R. Robert, "An iterative model for fractal antennas: application to the Sierpinski gasket antenna," *IEEE Transactions on Antennas and Propagation*, vol. 48, no. 5, pp. 713–719, 2000.
- [55] J. A. G. W. Blajer and M. Krawczyk, "The Inverse Simulation Study of Aircraft Flight Path Reconstruction," *Transport*, vol. XVII, no. 3, pp. 103–107, 2002.
- [56] J. Romeu and Y. Rahmat-Samii, "Fractal FSS: A novel dual-band frequency selective surface," *IEEE Transactions on antennas and propagation*, vol. 48, no. 7, pp. 1097–1105, 2000.
- [57] K. Meelarpkit, M. Chongcheawchamnan, C. Phongcharoenpanich, M. Krairiksh, L. B. Lok, and I. D. Robertson, "Dualband microstrip-to-coplanar strip balun transition and loop antenna application," *IET Microwaves, Antennas & Propagation*, vol. 2, no. 8, pp. 823–829, 2008.
- [58] J. K. Ali and A. S. Jalal, "A Miniaturized multiband Minkowski-like pre-fractal patch antenna for GPS and 3g IMT-2000 Handsets," *Asian Journal of Information Technology*, vol. 6, no. 5, pp. 584–588, 2007.
- [59] J. K. Ali, "A new compact size microstrip patch antenna with irregular slots for handheld GPS application," *Engineering and Technology Journal*, vol. 26, no. 10, pp. 1241–1246, 2008.
- [60] N. Abdullah, M. A. Arshad, E. Mohd, and S. A. Hamzah, "Design of minskowski fractal antenna for dual band application," in *2008 International Conference on Computer and Communication Engineering*, 2008, pp. 352–355.
- [61] M. F. Hasan, "A new compact dual band GPS patch antenna design based on minkowski-like pre-fractal geometry," *Engineering and Technology Journal*, vol. 27, no. 7, pp. 1370–1375, 2009.
- [62] P. Hazdra and M. Mazánek, "The miniature fractal patch antenna," in *Radioelektronika 2005 Conference Proceedings*, 2005, pp. 207–210.
- [63] J. A. G. W. Blajer and M. Krawczyk, "The Inverse Simulation Study of Aircraft Flight Path Reconstruction," *Transport*, vol. XVII, no. 3, pp. 103–107, 2002.
- [64] J. S. Colburn and Y. Rahmat-Samii, "Patch antennas on externally perforated high dielectric constant substrates," *IEEE Transactions on Antennas and Propagation*, vol. 47, no. 12, pp. 1785–1794, 1999.
- [65] K. C. Hwang, "Broadband circularly-polarised Spidron fractal slot antenna," *Electronics letters*, vol. 45, no. 1, pp. 3–4, 2009.
- [66] S. N. Sinha and M. Jain, "A self-affine fractal multiband antenna," *IEEE Antennas and Wireless Propagation Letters*, vol. 6, pp. 110–112, 2007.

- [67] P. W. Tang and P. F. Wahid, "Hexagonal fractal multiband antenna," *IEEE antennas and wireless propagation letters*, vol. 3, no. 1, pp. 111–112, 2004.
- [68] A. Azari and J. Rowhani, "Ultra-wideband fractal microstrip antenna design," *Progress In Electromagnetics Research*, vol. 2, pp. 7–12, 2008.
- [69] B. Mukherjee, P. Patel, and J. Mukherjee, "Hemispherical dielectric resonator antenna based on apollonian gasket of circles—a fractal approach," *IEEE Transactions on Antennas and Propagation*, vol. 62, no. 1, pp. 40–47, 2013.
- [70] J. R. James and P. S. Hall, *Handbook of microstrip antennas*. IET, 1989, vol. 1.
- [71] K. Falconer, *Fractal geometry: mathematical foundations and applications*. John Wiley & Sons, 2004.
- [72] G. Monti, L. Catarinucci, and L. Tarricone, "Compact microstrip antenna for RFID applications," *Progress In Electromagnetics Research*, vol. 8, pp. 191–199, 2009.
- [73] L. Ukkonen, L. Sydänheimo, and M. Kivikoski, "Read range performance comparison of compact reader antennas for a handheld UHF RFID reader," in *2007 IEEE International Conference on RFID*, 2007, pp. 63–70.
- [74] G. I. McKerricher and J. S. Wight, "Quadrifilar Helix antenna for UHF RFID," in *2010 IEEE Antennas and Propagation Society International Symposium*, 2010, pp. 1–4.
- [75] A. Farswan, A. K. Gautam, B. K. Kanaujia, and K. Rambabu, "Design of Koch fractal circularly polarized antenna for handheld UHF RFID reader applications," *IEEE Transactions on antennas and propagation*, vol. 64, no. 2, pp. 771–775, 2015.
- [76] P. Sittithai, T. Lertwiriyaprapa, and K. Phaebua, "Study of multiple repeater antennas for high frequency (HF) RFID reader," in *2017 International Symposium on Antennas and Propagation (ISAP)*, pp. 1–2.
- [77] M. Lalkota, G. Gupta, V. K. Pandit, and A. R. Harish, "UHF reader antenna system for near and far-field RFID operation," *IEEE Journal of Radio Frequency Identification*, vol. 3, no. 1, pp. 14–24, 2018.
- [78] I. Khadhraoui, T. B. Salah, and T. Aguil, "Dual-band pre-fractal antenna multi-objective optimization design," in *2017 13th International Wireless Communications and Mobile Computing Conference (IWCMC)*, 2017, pp. 840–844.
- [79] K.-S. Kim, G. Kim, S.-C. Chae, H.-W. Jo, J.-W. Yu, and H. L. Lee, "A compact circular polarization antenna using folded ground elements," *IEEE Transactions on Antennas and Propagation*, vol. 67, no. 5, pp. 3472–3477, 2019.
- [80] M. A. Solutions, "PN6-915 RFID Panel Antenna." [Online]. Available: <https://www.mobilemark.com/product/pn6-915/>
- [81] iDTRONIC A8060, "Door Frame Antenna." [Online]. Available: https://www.idtronic-rfid.com/d/1278380/d/door_frame_antenna_a8060_0.pdf
- [82] T7Antennas, "CIRCULARLYPOLARIZED UHF ANTENNASlimLine -A4030C." [Online]. Available: https://www.times-7.com/A4030C%20Datasheet_v2.0.pdf

- [83] Abracon, "ARRKP7059-S915B." [Online]. Available: <https://abracon.com/datasheets/ARRKP7059-S915B.pdf>
- [84] Abracon, "ARRKP4065-S915A ." [Online]. Available: <https://abracon.com/datasheets/ARRKP4065-S915A.pdf>
- [85] Abracon, "ARRKP5062-S915B." [Online]. Available: <https://www.mouser.co.uk/datasheet/2/3/ARRKP5062-S915B1314072.pdf>
- [86] P. Pagel, "Technical Correspondence." [Online]. Available: <http://www.setileague.org/articles/ham/mstrip.pdf>
- [87] Rogers_Corp, "Calculate Microwave Impedance with Transmission-Line Modeling Tool." [Online]. Available: <https://blog.rogerscorp.com/2018/07/12/calculate-microwave-impedance-with-transmission-line-modeling-tool/> [88] N. C. Barford, "Experimental measurements: precision, error and truth," 1967.
- [89] TheTelegraph, "NHS drug errors may be causing up to 22,000 deaths every year ," Feb 2018. [Online]. Available: <https://www.telegraph.co.uk/news/2018/02/23/nhs-drug-errors-may-causing-22000-deaths-every-year/>
- [90] A. Matthews-King, "NHS medication errors contribute to as many as 22,000 deaths a year, major report shows," Feb 2018. [Online]. Available: <https://www.independent.co.uk/news/health/nhs-medication-errors-deaths-prescription-drugsjeremy-hunt-york-university-health-a8224226.html>
- [91] M. S. Donaldson, J. M. Corrigan, and L. T. Kohn, *To err is human: building a safer health system*. National Academies Press, 2000, vol. 6.
- [92] R. C. of Physicians, "Supporting junior doctors in safe prescribing," 2017.
- [93] Y. Álvarez López, J. Franssen, G. Álvarez Narciandi, J. Pagnozzi, I. G.-P. Arrillaga, and F. L.-H. Andrés, "RFID Technology for management and tracking: e-health applications," *Sensors*, vol. 18, no. 8, p. 2663, 2018.
- [94] M. M. Pérez, G. V. González, and C. Dafonte, "Evaluation of a tracking system for patients and mixed intravenous medication based on rfid technology," *Sensors*, vol. 16, no. 12, p. 2031, 2016.
- [95] idox, "East Yorkshire Trust successfully implements fast-tracking system from Idox Health." [Online]. Available: <https://www.idoxgroup.com/east-yorkshire-trust-successfully-implements-fast-tracking-system-from-idox-health/>
- [96] J. Robinson, "Requesting, Locating and Tracking Patient Records Policy ," Mar 2015. [Online]. Available: <https://www.dbth.nhs.uk/wp-content/uploads/2017/07/CORP-REC-4-v-5-Requesting-Locating-and-TrackingPatient-Records-Policy-Final.pdf>
- [97] RestoreRecordsManagement, "Complete records management for the Healthcare Sector." [Online]. Available: <https://www.restore.co.uk/Records/Sectors/NHS>
- [98] O. Hughes, " Belfast trust green-lights digital tagging system for tracking patient records," Nov 2017. [Online]. Available:

- <https://www.digitalhealth.net/2017/11/belfast-trust-greenlights-digital-tagging-system/>
- [99] L. Stevens, "NHS Forth Valley saves thousands of pounds by tracking equipment," Jun 2017. [Online]. Available: <https://www.digitalhealth.net/2017/06/nhs-forth-valley-saves-thousands-of-pounds-by-tracking-equipment/>
- [100] RFID_Discovery, "Using RFID technology to support theatre inventory management can optimise stock holding, minimise waste and free up time for clinical staff." [Online]. Available: <https://www.rfiddiscovery.com/en/solutions/theatre-inventory-management>
- [101] P. Fuhrer and D. Guinard, *Building a smart hospital using RFID technologies: use cases and implementation*. Department of Informatics-University of Fribourg Fribourg, Switzerland, 2006.
- [102] G. Ewers, "Transforming pathology with RFID could save the NHS millions." [Online]. Available: <https://www.europeanpharmaceuticalreview.com/article/128361/transforming-pathology-with-rfid-could-save-the-nhs-millions/>
- [103] WHO, "GLOBAL INFLUENZA STRATEGY 2019-2030 Prevent. Control. Prepare," 2019. [Online]. Available: <https://apps.who.int/iris/bitstream/handle/10665/311184/9789241515320-eng.pdf>
- [104] RAPIDUSA, "RAPID USA (Rapid Aseptic Packaging of Injectable Drugs): providing rapid population-scale packaging of vaccines and therapeutics in prefilled syringes with real-time reporting of all injections." [Online]. Available: https://static1.squarespace.com/static/5e9a07ad0242040c343c5884/t/5eb5692a78683d6a181c80d6/1588947245085/70318_U.S.+RAPID+Bklt_93.pdf
- [105] Bazian and NHS, "Human test of implanted medicine chips," Feb 2012. [Online]. Available: <https://www.nhs.uk/news/medication/human-test-of-implanted-medicine-chips/>
- [106] M. Swain, "New microchip will let doctor administer drugs into your body over the phone," Feb 2012. [Online]. Available: <https://www.mirror.co.uk/news/technology-science/science/new-microchip-will-let-doctor-administer-drugs-688673>
- [107] J. Laurance, "'Wireless medicine' helps solve one of doctors' biggest problems - getting patients to take drugs," Feb 2012. [Online]. Available: <https://www.independent.co.uk/voices/commentators/jeremy-laurance-wireless-medicinhelps-solve-one-doctors-biggest-problems-getting-patients-take-drugs-6989041.html>
- [108] S. Connor, "Dawn of the age of wireless medicine," Feb 2012. [Online]. Available: <https://www.independent.co.uk/lifestyle/health-and-families/health-news/dawn-age-wireless-medicine-6989042.html>
- [109] ID2020, "Alliance partners share the belief that identity is a human right and that individuals must have "ownership" over their own identity." [Online]. Available: <https://id2020.org/manifesto>

- [110] S. C. Alliance, "Proximity mobile payments: Leveraging NFC and the contactless financial payments infrastructure," *Smart Card Alliance*, 2007.
- [111] UKFinance, "Contactless limit in UK to be increased to £45," Mar 2020. [Online]. Available: <https://www.ukfinance.org.uk/press/press-releases/contactless-limit-uk-be-increased-45>
- [112] J. Johnson, "Sainsbury's rolls out till-free contactless payments in more than 100 stores," Jul 2020. [Online]. Available: <https://www.express.co.uk/life-style/life/1317207/sainsburys-news-contactless-smart-shop-mobile-pay-app>
- [113] S. Sattel, "Amazon Go & RFID – The Automation Dilemma." [Online]. Available: <https://www.autodesk.com/products/eagle/blog/amazon-go-rfid-automation-dilemma/>
- [114] X. Liu, Y. Jiang, K.-H. Kim, and R. Govindan, "Grab: Fast and Accurate Sensor Processing for Cashier-Free Shopping," *arXiv preprint arXiv:2001.01033*, 2020.
- [115] A. Atanasiu and M. I. Mihailescu, "Biometric passports (ePassports)," in *2010 8th International conference on communications*, 2010, pp. 443–446.
- [116] S. Trochu and O. Touret, "Managing the Border, Smartly," in *2013 European Intelligence and Security Informatics Conference*, 2013, pp. 281–284.
- [117] E. Elbasani, P. Siriporn, and J. S. Choi, "A Survey on RFID in Industry 4.0," pp. 1–16, 2020.
- [118] smart TEC, "Industry 4.0." [Online]. Available: <https://www.smart-tec.com/en/auto-id-world/industry-4.0>
- [119] AdvancedmobileGROUP, "RFID's Role in Industry 4.0," Mar 2017. [Online]. Available: <https://www.advancedmobilegroup.com/blog/rfids-role-in-industry-4.0>
- [120] J. A. G. W. Blajer and M. Krawczyk, "The Inverse Simulation Study of Aircraft Flight Path Reconstruction," *Transport*, vol. XVII, no. 3, pp. 103–107, 2002.
- [121] B. Gao, C. H. Cheng, M. M. Yuen, and R. D. Murch, "Low cost passive UHF RFID packaging with electromagnetic band gap (EBG) substrate for metal objects," in *2007 Proceedings 57th Electronic Components and Technology Conference*, 2007, pp. 974–978.
- [122] EnvironmentAgency, N. R. Cymru, ScottishEnvironmentProtectionAgency(SEPA), and NorthernIrelandEnvironmentAgency(NIEA), "Guidance on the classification and assessment of waste (1st Edition v1.1) Technical Guidance WM3," May 2018. [Online]. Available: https://assets.publishing.service.gov.uk/government/uploads/system/uploads/attachment_data/file/719394/Waste-classification-technical-guidance-WM3.pdf

ORCER RF-60A

RoHS and WEEE Compliant
Exceptional Interlaminar Bonds
Low Moisture Absorption
Enhanced Dimensional Stability
Low Z-Axis Expansion
Stable Dk Over Frequency
Increased Flexural Strength

TACONIC

An ISO 9001:2000 Registered Company

Petersburgh, NY: Tel: 800-833-1805 Fax: 518-658-3988

Europe: Tel: +353-44-9395600 Fax: +353-44-9344369 Asia: Tel: +82-31-704-1858 Fax: +82-31-704-1857
www.taconic-add.com

APPLICATIONS

Power Amplifiers
Filters and Couplers
Passive Components
Antennas

RF-60A

RF-60A is an organic-ceramic laminate in the ORCER family of Taconic products. It is based on woven glass reinforcement. RF-60A is a result of Taconic's expertise in both ceramic fill technology and in coated PTFE fiberglass.

RF-60A exhibits exceptional interlaminar bond strength and solder resistance. RF-60A's proprietary composition results in low moisture absorption and uniform electrical properties.

RF-60A's woven glass reinforcement ensures excellent dimensional stability and enhances flexural strength. The RF-60A laminate exhibits low Z-axis expansion allowing for plated-through-hole reliability in extreme thermal environments.

RF-60A laminates are in complete compliance with RoHS and WEEE directives and are compatible with the temperatures required for the new lead free solders.

RF-60A laminates can be sheared, drilled, milled and plated using standard methods for PTFE-woven fiberglass materials.

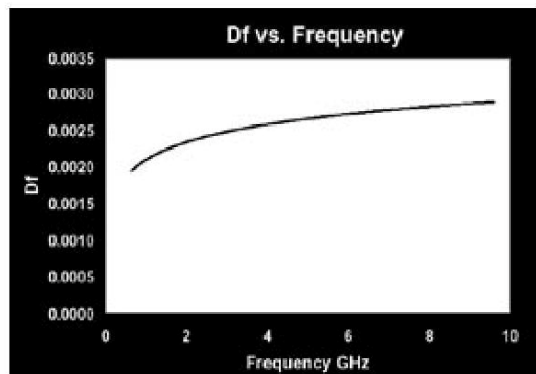
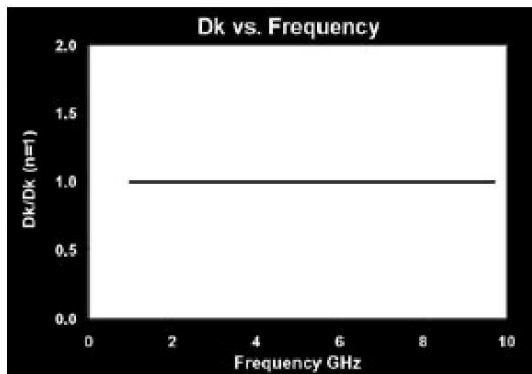
RF-60A laminates are generally ordered clad on both sides. Various panel sizes are available. Contact our customer service department for more information.

RF-60A laminates meet the requirements of IPC-4103 and are tested in accordance with IPC-TM 650. A certificate of compliance containing lot-specific test data accompanies each shipment.

See "How To Order" on back page for a complete product listing.

RF-60A Typical Values					
Property	Test Method	Unit	Value	Unit	Value
Dielectric Constant	IPC-TM-650 2.5.5.6		6.15		6.15
Dissipation Factor @ 10 GHz	IPC-TM-650 2.5.5.5.1		0.0028		0.0028
Moisture Absorption	IPC-TM-650 2.6.2.1	%	0.02	%	0.02
Dielectric Breakdown	IPC-TM-650 2.5.6	kV	53	kV	53
Dielectric Strength	ASTMD 149	V/mil	880	V/mm	34,646
Volume Resistivity	IPC-TM-650 2.5.17.1 (Humidity Conditioning)	Mohm/cm	9.0×10^8	Mohm/cm	9.0×10^8
Surface Resistivity	IPC-TM-650 2.5.17.1 (Humidity Conditioning)	Mohm	2.28×10^8	Mohm	2.28×10^8
Arc Resistance	IPC-TM-650 2.5.1	Seconds	193	Seconds	193
Flexural Strength (MD)	ASTMD 790	psi	18,300	N/mm ²	126.2
Flexural Strength (CD)	ASTMD 790	psi	14,600	N/mm ²	100.7
Tensile Strength (MD)	ASTMD 3039	psi	19,500	N/mm ²	134.4
Tensile Strength (CD)	ASTMD 3039	psi	16,300	N/mm ²	112.4
Young's Modulus	ASTMD 3039	kpsi	15,300	N/mm ²	10,549
Poisson's Ratio	ASTMD 3039		0.068		0.068
Compressive Modulus	ASTMD 695 (23°C)	kpsi	338	N/mm ²	2,330
Peel Strength (1 oz ED)	IPC-TM-650 2.4.8 Sec. 5.2.2 (Thermal Stress)	lbs/linear inch	8	N/mm	1.4
Dimensional Stability (MD)	IPC-TM-650 2.4.39 Sec. 5.4 (After Bake)	mils/in	0.68	mm/M	0.68
Dimensional Stability (CD)	IPC-TM-650 2.4.39 Sec. 5.4 (After Bake)	mils/in	1.05	mm/M	1.05
Density (Specific Gravity)		g/cm ³	2.81	g/cm ³	2.81
Thermal Conductivity	ASTM F433	W/m/K	0.539	W/m/K	0.539
CTE (x)	ASTMD 3386 (-30°C - 125°C)	ppm/°C	9	ppm/°C	9
CTE (y)	ASTMD 3386 (-30°C - 125°C)	ppm/°C	8	ppm/°C	8
CTE (z)	ASTMD 3386 (-30°C - 125°C)	ppm/°C	69	ppm/°C	69
Outgassing (% TML)	ASTME 595*	%	0.02	%	0.02
Outgassing (% CVCM)	ASTME 595*	%	0.00	%	0.00
Outgassing (% WVR)	ASTME 595*	%	0.01	%	0.01
Flammability Rating	UL 94		V-0		V-0

*As reported by NASA. See http://outgassing.nasa.gov/og_disclaimer.html.



All reported values are typical and should not be used for specification purposes. In all instances, the user shall determine suitability in any given application.

How To Order

Designation	Dielectric Constant	Typical Thicknesses ¹		Available Sheet Sizes ²	
RF-60A	6.15 +/- 0.25	0.0100"	0.25 mm	12" x 18"	304 mm x 457 mm
		0.0250"	0.64 mm		
		0.0310"	0.79 mm	16" x 18"	406 mm x 457 mm
		0.0500"	1.27 mm		
		0.0600"	1.52 mm		
0.1250"	3.18 mm	18" x 24"	457 mm x 610 mm		

¹Other thicknesses may be available. Please call for information.

²Our standard sheet size is 18" x 24" (457 mm x 610 mm). Please contact our customer service department for availability of other sizes.

Available Copper Cladding						
Designation	Weight	Copper Thickness		R _{MS} Treated Side		Description
RH	1/2 oz / ft ²	~0.0007"	~18 μm	16 μin	0.4 μm	Rolled annealed
R1	1 oz / ft ²	~0.0014"	~35 μm	11 μin	0.3 μm	Rolled annealed
CVH (CH)	1/2 oz / ft ²	~0.0007"	~18 μm	27 μin	0.7 μm	Very low profile / Electrodeposited
CV1 (C1)	1 oz / ft ²	~0.0014"	~35 μm	25 μin	0.6 μm	Very low profile / Electrodeposited
C2	2 oz / ft ²	~0.0028"	~70 μm	77 μin	2.0 μm	Electrodeposited

Heavy metal claddings (aluminum, brass & copper) may also be available upon request. Please call for information.

An example of our part number is: **RF-60A-0600-CV1/CV1 - 18" x 24" (457 mm x 610 mm)**

TACONIC

An ISO 9001:2000 Registered Company
 Petersburg, NY: Tel: 800-833-1805 Fax: 518-658-3988
 Europe: Tel: +353-44-9395600 Fax: +353-44-9344369 Asia: Tel: +82-31-704-1858 Fax: +82-31-704-1857
www.taconic-add.com

6/06:100-19

APPENDIX B

School of Creative Arts and Engineering: Risk Assessment Department of Design and Engineering	Notes: (please leave blank)
Name:	Supervisor:
E-mail address:	Telephone no. (not mandatory)
Activity: Testing Antennae on a wooden doorframe with a volunteer walking through carrying RFID tagged objects.	People involved in activity: Researcher and Volunteer

Risk Map

	High Risk <i>12 ≤ Score < 25 High Risk</i>			Medium Risk <i>6 ≤ Score < 12 Medium Risk</i>		Low Risk <i>1 ≤ Score < 6 Low Risk</i>	
Probability →	Highly Unlikely (1)	Unlikely (2)	Possible (3)	Likely (4)	Highly Likely (5)		
Severity ↓							
Minor injury (1)	1	2	3	4	5		
Lost time and/or damage to health (2)	2	4	6	8	10		
Major injury >7 days (3)	3	6	9	12	15		
Permanent disability (4)	4	8	12	16	20		
Fatality/Multiple fatality (5)	5	10	15	20	25		

Identified Hazards	Task	People at Risk	Potential risk probability	Severity of Risk	Controls, Procedures, Key Behaviours	Score (Probability x Severity)
Mechanical injuries, dust and debris	Installation of antenna	Researcher, Installation staff	Possible (3)	Lost time and/or damage to health (2)	All staff to wear appropriate PPE during installation. Safety glasses, gloves, face masks, safety steel toe cap shoes All equipment to be visually checked before use and safety guarding to be used where provided	6
Potential eye strain	Data entry	Researcher	Highly Unlikely (1)	Minor (1)	Regular 15 minute breaks every hour	1
Slips and trips	Testing (walking)	Volunteer	Unlikely (2)	Lost time and/or damage to health (2)	Removal of trip hazards. All areas well lit. No trailing cables or leads left in walkways.	4
Exhaustion, frustration, boredom	Testing (walking)	Volunteer	Unlikely (2)	Minor (1)	Regular 15 minute breaks every hour + 20 minute maximum break per work day	2
Slips and trips, collision with chairs/people	General setup	Staff, student, visitors, trespassers	Unlikely (2)	Lost time and/or damage to health (2)	Signage displayed at test site. Test set up in a low foot traffic area.	4
Electromagnetic energy effects on health	Testing and general setup	Volunteer, staff, students, visitors, trespassers	Highly Unlikely (1)	Minor (1)	Operate at 2 Watt ERP maximum energy at 870MHz ETSI according to GS1 regulations. Not using participants with pacemakers, weak hearts, epilepsy or nerve disorder, cochlear implants, insulin pumps, hearing aids or other medically related electronic devices.	1
Electrocution	Operating RFID Reader	Researcher	Highly Unlikely (1)	Fatality/Multiple fatality (5)	Ensure all equipment has current PAT Test compliance and operating at 240 Volts maximum. Follow operation manual procedures for all equipment. Restrict access to equipment.	5

PhD Supervisor		Date:	18 th June 2019
Signature:			
Technical Skills Specialist		Date:	
Signature:			
Researcher		Date:	18 th June 2019
Signature:			

Information Sheet

Version: 1.0

Date: 14.06.2019

Researcher:

Supervisor:

Test: Testing Antennae on a wooden doorframe with a test subject walking through carrying RFID tagged objects.

1. The test subject will be walking in a closed circuit at a regular walking speed through a wooden doorframe on which an active RFID antenna/antennae will be mounted for the purpose of reading RFID tagged objects in the possession of the test subject.
2. The test subject will be carrying an RFID tagged object/objects (up to a reasonable amount which he/she could comfortably carry).
3. The test subject will be requested to walk the closed circuit carrying RFID tagged objects in all three orientations (XY, YZ and XZ in a typical X, Y, Z coordinate space)
4. The test subject will be walking an n number of routes (where n is a positive integer) per each test variable and maybe be requested by the researcher to re-do a test route again for validation if an interference or electrical noise is observed in the system.
5. All tests will be repeated for each antenna designs k . (where k is a positive integer) The number of designs k to be tested is determined by the researcher.
6. As a minimum the test subject will have a 10-minute break for every hour the test is performed and a 20 minute break per every 6 hour work day.

Version 1, 14.06.2019
Supervisor:
Principal Investigator:
Test subject Identification Number for this trial: 01

CONSENT FORM

**Testing Antennae on a wooden doorframe with the test subject walking through
carrying RFID tagged objects.**

Please Initial Box

1. I confirm that I have read and understand the Information Sheet dated Version 1, 14.06.2018 for the above study. I have had the opportunity to consider the information, ask questions and have had these answered satisfactorily.
2. I understand that my participation is voluntary and that I am free to withdraw at any time without giving any reason, and without my medical care or legal rights being affected.
3. I agree to have my personal data stored confidentially on a secure University server or a non-networked computer, for the purposes of contacting you only (compliant with Data Protection Act).
4. I understand my personal data will be deleted after the completion of the study but this consent form will be stored for 10 years at Staffordshire University and my anonymised data including measurements taken as part of this study will be stored with Staffordshire University. I understand that published data will be anonymised.
5. I understand data taken as part of this research study will be stored at Staffordshire University.
6. I agree to take part in the above study.

Full Name of Participant Date Signature

Name of person taking consent Date Signature

APPENDIX C

Random number table generated from www.random.org

1 TAG	2 TAGS		3 TAGS			4 TAGS			
73	99	68	74	78	11	27	34	75	26
9	20	80	65	1	12	47	25	57	37
56	80	3	83	1	14	65	45	53	99
21	41	11	64	56	5	10	19	52	74
82	47	44	23	17	82	32	27	51	38
29	38	19	31	65	56	2	7	73	1
71	26	16	11	61	25	83	9	90	68
57	20	49	18	20	90	18	28	52	33
39	47	31	72	37	33	40	13	91	37
8	74	17	38	30	62	11	48	51	8